

博士論文

**Development of Novel Chalcogenide-Based
Photocathodes and Construction of Reaction Systems
for Water Splitting**

(新規カルコゲナイド系光電極の開発及び水分解反応系構築に関する研究)

兼古 寛之
(Hiroyuki Kaneko)

Department of Chemical System Engineering,
School of Engineering, The University of Tokyo
2019 Doctoral Thesis

Acknowledgements

The author, Hiroyuki Kaneko, would like to express deep gratitude to Prof. Kazunari Domen (Department of Chemical System Engineering, The University of Tokyo) for guiding the study with helpful suggestions, profound discussion and tremendous encouragement.

The author would also like to offer his special thanks to members in The Domen Group; Assoc. Prof. Tsutomu Minegishi kindly gave the author countless numbers of insightful comments, meaningful guidance and experimental techniques. Assoc. Prof. Masao Katayama made enormous contribution to constructing experimental equipment, managing the laboratory and analysing experimental data. Assis. Prof. Tomohiro Higashi has been extraordinarily tolerant and supportive of the study concerning photoelectrochemistry, which greatly helped to establish the thesis. Ms. Mamiko Nakabayashi (Institute of Engineering Innovation, School of Engineering, The University of Tokyo) has been greatly tolerant and supportive of the measurements by using electron microscopy techniques.

The author is particularly grateful for the collaborative researches kindly supported by Assoc. Prof. Lydia Helena Wong (School of Materials Science and Engineering, Nanyang Technological University) and her group members: Mr. Tay Ying Fan, Dr. Prince Saurabh Bassi, Mr. Stener Lie and Mr. Li Wenjie for analyzing the semiconductor properties of the novel thin-film materials using AC Hall measurement, Dr. Ayako Kubo (Nissan Chemical Corporation) for conducting first principle calculations and the fellows in Japan Technological Research Association of Artificial Photosynthetic Chemical Process: Dr. Taro Yamada, Dr. Yongbo Kuang, Dr. Miao Zhong, Mr. Atsushi Ohnishi, Mr. Hiroyuki Kobayashi, Mr. Yusuke Muramatsu and Ms. Yoshie Nagatsuma for meaningful discussion and technical helps.

The author has received financial supports by the Japan Society for the Promotion of Science (JSPS) through the Program for Leading Graduate Schools (MERIT) and the Grant-in-Aid for JSPS Research Fellow. Finally, the author would like to show my greatest appreciation to his family, friends and colleagues for their encouragement and kindness.

January 16, 2019 Hiroyuki Kaneko

Table of Contents

Table of Contents

Chapter 1	General Introduction	1
1-1	Research Background	2
1-2	Systems for Solar-Hydrogen Conversion.....	5
1-2-1	Water Electrolysis Coupled with Solar Cells	5
1-2-2	Photocatalytic Water Splitting Using Powdered Semiconductors	6
1-2-3	Photoelectrochemical Water Splitting Using Semiconductor Electrodes	8
1-3	Fundamentals of Photoelectrodes for Photoelectrochemical Cells.....	9
1-3-1	Electronic Properties of Semiconductor Materials	9
1-3-2	Potential Changes at Semiconductor Interfaces	12
1-3-3	Photoelectrochemical Reaction under Light Irradiation.....	15
1-3-4	Energy Conversion Efficiency and Stability of Photoelectrochemical Cells..	21
1-4	Candidates for Semiconductor Photoelectrode Materials and Surface Modifiers	25
1-4-1	Photoelectrode Materials	25
1-4-2	Techniques and Materials for Surface Modification on Photoelectrodes.....	28
1-4-3	Demonstrations and Challenges of Photoelectrochemical cells	34
1-5	Cu-Chalcopyrite-Based Photocathodes	38
1-5-1	Features as Photocathode Materials.....	38
1-5-2	Challenges and Motivation for Modifications	46
1-6	Objectives of This Thesis	48
	References	51
Chapter 2	Development of ZnSe:Cu(In,Ga)Se₂ Photocathodes.....	64
2-1	Introduction.....	65
2-2	Experimental Section.....	65
2-3	Results and Discussion	70
2-3-1	Effects of ZnSe Introduction into Cu(In,Ga)Se ₂ on the Physical Properties ..	70

Table of Contents

2-3-2	Effects of the Amount of Cu Flux on the Semiconductor Property	74
2-3-3	Effects of Preparation Conditions of ZnSe:Cu(In,Ga)Se ₂ Thin Films onto Their Photoelectrochemical Properties	80
2-3-4	Overall Water Splitting using the ZnSe:Cu(In,Ga)Se ₂ Photocathode and a BiVO ₄ Photoanode	88
2-4	Conclusions.....	91
	References	92
Chapter 3	Enhancement of Charge Separation Efficiency and Visualization of the Separation Fields in ZnSe:Cu(In,Ga)Se₂ Photocathodes.....	95
3-1	Introduction.....	96
3-2	Experimental Section.....	97
3-3	Results and Discussion	100
3-3-1	Effects of Composition Gradient in the ZnSe:Cu(In,Ga)Se ₂ Thin Films onto Their Photoelectrochemical Properties	100
3-3-2	Visualization of Charge Separation Fields Using Mapping of Electron-Beam-Induced Current Signals.....	111
3-3-3	Overall Water Splitting using the Bilayer ZnSe:Cu(In,Ga)Se ₂ Photocathode and a BiVO ₄ Photoanode	118
3-4	Conclusions.....	121
	References	122
Chapter 4	Development of Flexible ZnSe:Cu(In,Ga)Se₂ Photocathodes for Construction of Stirring-Free Photoelectrochemical Cells.....	124
4-1	Introduction.....	125
4-2	Experimental Section.....	126
4-3	Results and Discussion	130
4-3-1	Effects of Substrates onto the Photoelectrochemical Properties of the ZnSe:Cu(In,Ga)Se ₂ Photocathodes	130
4-3-2	Effects of Chemical Bath Deposition of In ₂ S ₃ onto the Photoelectrochemical	

Table of Contents

Properties of the ZnSe:Cu(In,Ga)Se ₂ Photocathodes	137
4-3-3 Construction of a Comb-Like Photoelectrochemical Cell Composed of the ZnSe:Cu(In,Ga)Se ₂ Photocathode and a BiVO ₄ Photoanode	140
4-4 Conclusions.....	148
References	148
Chapter 5 Effects of RuO₂-Coating onto the Durability of the ZnSe:Cu(In,Ga)Se₂ Photocathode.....	151
5-1 Introduction.....	152
5-2 Experimental Section.....	153
5-3 Results and Discussion	157
5-3-1 Characterization of the Photoelectrodeposited RuO ₂ Layers.....	157
5-3-2 Photoelectrochemical Properties of RuO ₂ -Coated ZnSe:Cu(In,Ga)Se ₂ Photocathodes.....	163
5-3-3 Analysis of the RuO ₂ Layers Using Angle-Resolved X-ray Photoelectron Spectroscopy	170
5-3-4 Overall Water Splitting Using the RuO ₂ -Coated ZnSe:Cu(In,Ga)Se ₂ Photocathode and a BiVO ₄ Photoanode.....	174
5-4 Conclusions.....	176
References	177
Chapter 6 Control of Cation Impurities in the Electrolyte for Long-Term Operation of Photoelectrochemical Cells	180
6-1 Introduction.....	181
6-2 Experimental Section.....	182
6-3 Results and Discussion	186
6-3-1 Effects of Chelating Resin Dispersion onto the Stability of the Photoelectrochemical Cells	186
6-3-2 Effects of an Anion-Conductive Ionomer Layer onto the Stability of the Photoelectrochemical Cells	192

Table of Contents

6-4	Conclusions.....	199
	References	200
Chapter 7	Summary and Outlook.....	202
7-1	General Conclusions of This Thesis	203
7-2	Future Prospects	205
	References	208
	List of Publications (Peer Reviewed Papers)	209
	List of Publications (Review Articles - Related to Chapter 1).....	211
	List of Publications (Books).....	212

Chapter 1

General Introduction

1-1 Research Background

Heavy usage of fossil fuels in our current society possesses two big problems: finiteness of each resource and environmental pollution. The consumption of fossil fuels by human being was reported to be 12 billion tonnes oil equivalent in 2016.^[1] On the other hand, reserve-to-production ratios (RPRs) of oil, natural gas and coal in 2016 are estimated to be 51, 53 and 153 years, respectively. This suggests that oil and natural gas are going to be exhausted in the 21st century. Furthermore, the universal oil consumption has been continuously growing with an annual rate of 2-3% as exhibited in Figure 1-1-1. Under the situation, exhaustion of fossil fuels will come earlier than the current RPRs.

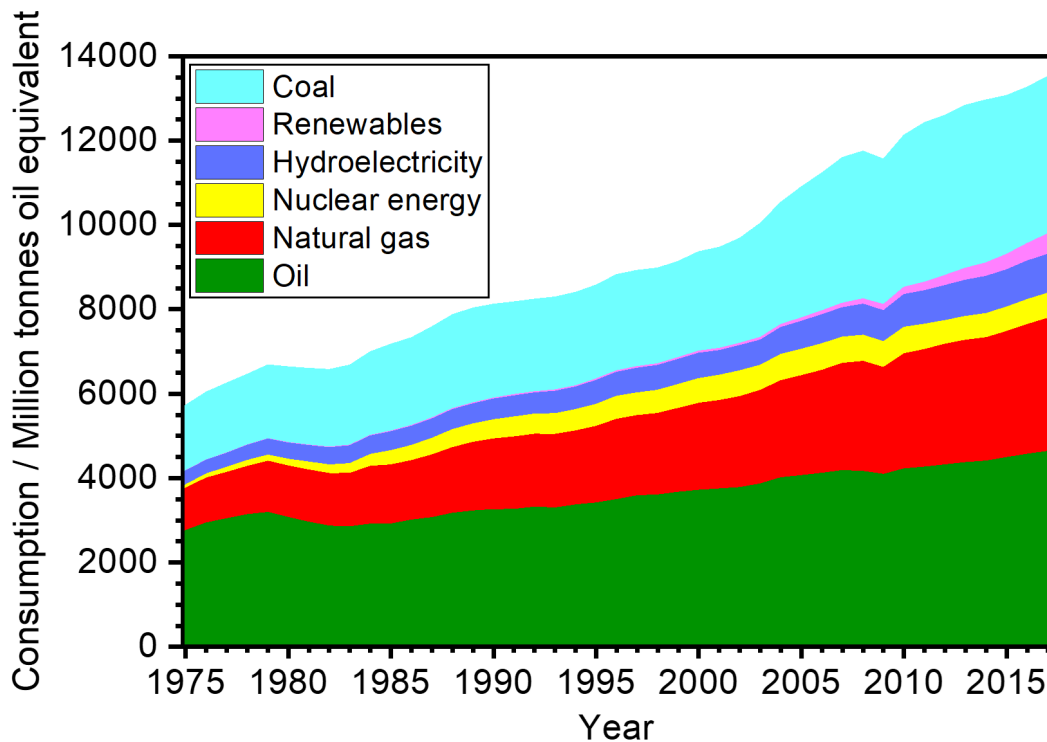


Figure 1-1-1. The growth of world primary energy consumption by each energy resource.^[1]

The usage of fossil fuels has also caused serious environmental problems. Combustion of them can release sulfur- and nitrogen-based compounds into air, resulting in the necessity of removal equipment to prevent severe air pollution as experienced in the modern society. Acid rain in Europe

Chapter 1. General Introduction

and Yokkaichi-asthma are typical issues concerning fossil fuel combustion. Another large concern is the global warming and climate change by the greenhouse effect. CO_2 is a product of fossil fuel combustion and is pointed out as a greenhouse gas. The global emission of CO_2 was 33.5 billion tons in 2010, which is 3.5 times larger than that in 1960,^[2] and the concentration of atmospheric CO_2 showed a remarkable increase by 20% in the corresponding period.^[3] Such a rapid increase in the greenhouse gas concentration in the atmosphere is believed to alter heat transfer on earth and facilitate the abnormal climate change.

More than 90% of the demand on fossil fuels is related to energy source.^[4,5] Therefore, transfer of global energy supply system to renewable energy source is a promising way to resolve the problems introduced above. It should be noted that most of the remaining is consumed in petrochemical industry and that studies on production of sustainable plastics such as CO_2 -based plastics and bioplastics have been intentionally conducted.^[6–8] Among many kinds of renewable energy resources, sunlight has gathered significant attention mainly due to its abundancy and permanency.^[5]

According to calculations, just 0.01% of solar energy entering the earth's surface is equivalent to the energy demand by the human society.^[9,10] Hence, covering a part of the surface with energy conversion facilities is a promising tactic. For example, Mojave Solar Project, which is located in Mojave Desert, USA, with an area of 7.1 km^2 , possesses the maximum rated capacity of 280 MW. Considering the consumption on a worldwide basis of 18 TW,^[9] a land of $456,000 \text{ km}^2$, which is just 5% of Sahara Desert, can meet the demand. This example explains the potential of sunlight-based energy supply system.

However, the sunlight-based system requires two costly devices for its practical use: storage and transportation devices. Large and unremitting fluctuation of sunlight intensity due to a change in the weather condition, rotation of the earth and season's transition causes the necessity of storage devices such as a storage battery to buffer the fluctuation. Furthermore, because the sunlight intensity becomes small in proportion as the location of facility gets far from the equator as shown in Figure 1-

1-2,^[9] mass transportation devices such as superconducting cable are indispensable for worldwide introduction.^[11]

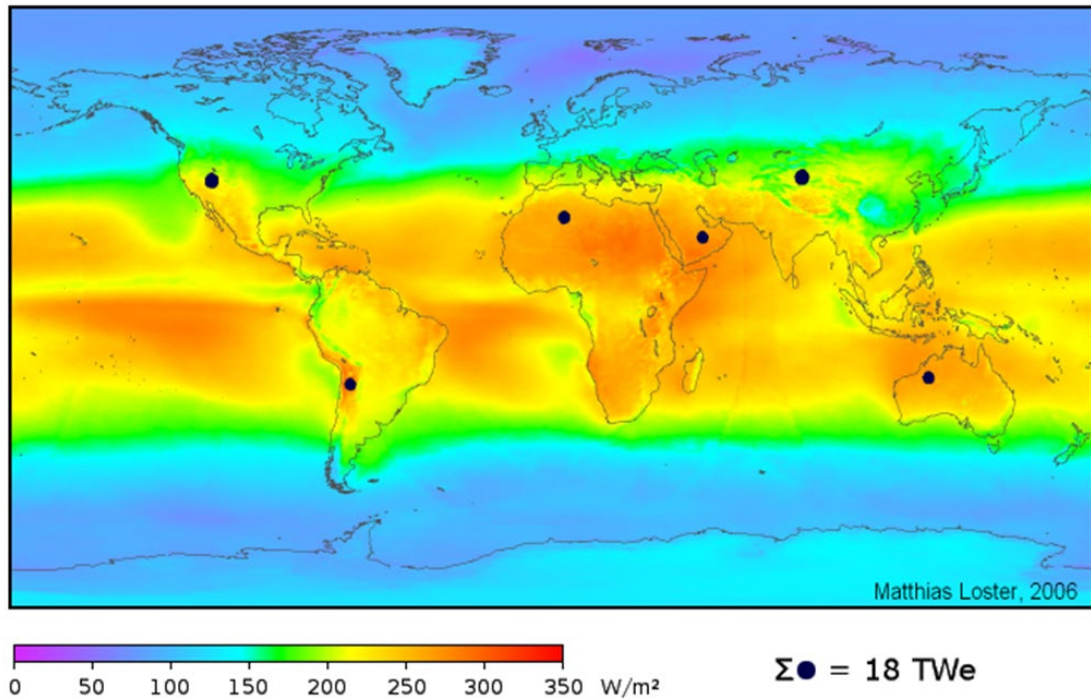


Figure 1-1-2. The distribution of solar irradiance averaged for three years including nights and cloud coverage. Given equipping solar cells with the conversion efficiency of 8% at the regions marked as the six dark disks, the electricity produced in these places statistically can compensate for the world primary energy consumption. Image by Matthias Loster on Wikimedia Commons, CC-BY 3.0.

A solution to avoid the cost issue is solar-to-fuel conversion, in which light energy in sunlight is converted into chemical energy in the form of gas or liquid fuels.^[12] Fuels can be stored in a simple tank or pool instead of expensive battery without natural discharge phenomenon. Moreover, they are transportable by using conventional tankers and pipelines. Among many kinds of fuels, hydrogen is an attractive media thanks to the relatively high energy density per weight (120 MJ kg^{-1}) and a possibility of construction of carbon-free substance circulation system, although it should be noted that presence of nitrogen can generate NO_x during hydrogen combustion in a high temperature. Also,

hydrogen can be utilized as a source of ammonia and methane, which are important commodity chemicals for the modern society.

Therefore, development of efficient and scalable solar-to-fuel system is an important key to realize the sunlight-based energy supply system. In the next chapter, candidates as solar-to-fuel conversion devices are introduced and discussed.

1-2 Systems for Solar-Hydrogen Conversion

1-2-1 Water Electrolysis Coupled with Solar Cells

A probable method composed of a combination of conventional technologies is water electrolysis in conjunction with the electricity generated by solar cells. The scheme is illustrated in Figure 1-2-1. Many kinds of demonstration have been reported so far,^[13,14] and a stand-alone supply system for electricity and heat equipped with solar cells, hydrogen/oxygen tanks and fuel cells has already been commercially available.^[15] It also should be noted that the electricity-based device is compatible with smart grid system.^[16]

Unfortunately, photovoltages of commercially-available photovoltaic (PV) cells such as Si (band gap energy of 1.1 eV), Cu(In,Ga)Se₂ (1.1 eV) and CdTe (1.4 eV) are much less than the required voltage for water splitting reaction, 1.23 V. The low photovoltage means significant losses in the photon energy by relaxation of photoexcited carriers.^[17] Hence, such solar cells are required to connect in a series to obtain a photovoltage high enough to drive overall water splitting, but the serialization results in a serious decrease in the current density of the device. For example, demonstrations of using an electrolyzer and a series of three polycrystalline Cu(In,Ga)Se₂- or Si-based solar cells each showed the solar-to-hydrogen conversion efficiency (STH) of around 10%, while both of the solar cells are capable of showing power conversion efficiencies of 17 to 18%.^[18,19]

Achievement of a low capital expenditure and operation cost can compensate the decreased energy conversion efficiency. However, it is unfortunate that the process cost of the wiring over each cell as well as the necessity of an electrolyzer including costly electrocatalysts makes the system expensive for its energy conversion efficiency.^[20–23] Although development of tandem-type solar cells using a stack of a wide and narrow band gap semiconductors can break the efficiency limitation, it may make the fabrication cost even higher.

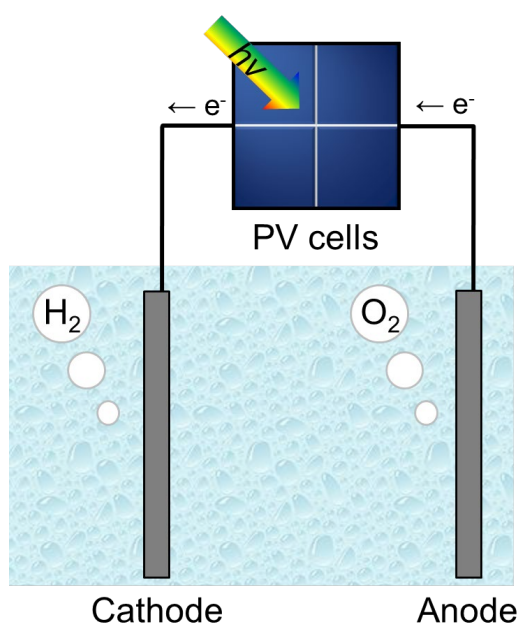


Figure 1-2-1. A scheme for water electrolysis system coupled with PV cells.

1-2-2 Photocatalytic Water Splitting Using Powdered Semiconductors

Employment of powdered photocatalysts dispersed in a solution or embedded onto a monolithic sheet as displayed in Figure 1-2-2 is expected to become the most scalable and cost-effective device thanks to their simplicity.^[21,24–26] The first demonstration of direct photocatalytic overall water splitting was reported in 1970's to 1980's by using particulate metal oxides such as TiO_2 and SrTiO_3 .^[27,28] The photocatalytic reaction is directly driven on the surface of the semiconductor by electrons and holes generated by photoexcitation process. Although the oxides mentioned above can

absorb only ultraviolet light, it performs energy conversion of solar-to-hydrogen in the same way as the combination of PV cells and electrolyzer, and the system is much simpler than that. Since then, development of visible-light-responsive photocatalyst has been addressed so as to achieve meaningful STHs. As the results, GaN:ZnO ($E_g = 450\text{--}480\text{ nm}$), TaON (510 nm) and LaMg_{1/3}Ta_{2/3}O₂N (600 nm) have been found to drive overall water splitting reaction under visible light irradiation to date.^[29–32] Band gaps of these semiconductor photocatalysts are reflected to driving force for the water splitting reaction by themselves. Therefore, the reaction rate (i.e. STH) tends to decline as the band gap of the photocatalyst becomes narrow in spite of the increased production rate of photoexcited electrons and holes.

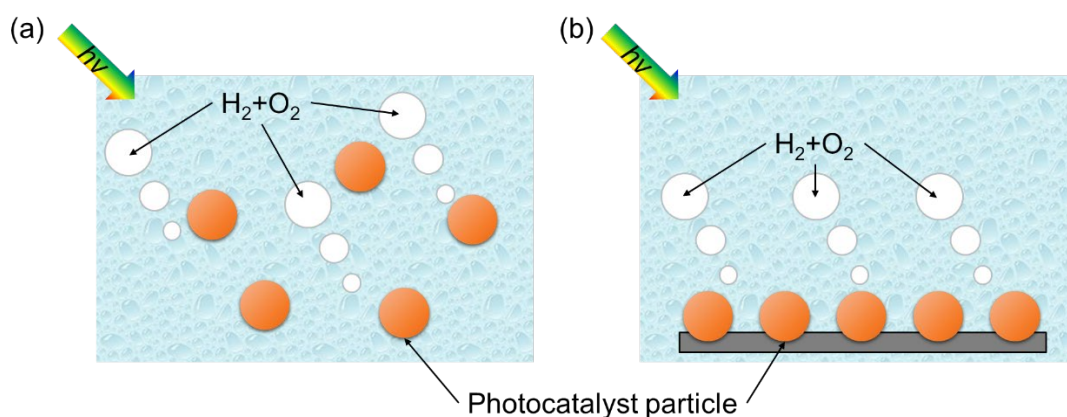


Figure 1-2-2. Schemes of photocatalytic overall water splitting using the powder dispersion (a) and the particles embedded onto a sheet/panel (b).

Photocatalytic reaction using two-step photoexcitation process is often called as Z-scheme photocatalytic system.^[33–37] The system employs two kinds of semiconductor photocatalysts which show high overpotentials for either a water reduction or oxidation potential, so it is expected to drive overall water splitting with a higher STH than that of one-step photoexcitation system. For example, a photocatalyst sheet which embeds SrTiO₃:La,Rh and BiVO₄:Mo powders has been recorded to show a relatively high STH of 1.2% at 331 K at 10 kPa.^[38]

A critical problem for photocatalyst system is separation of hydrogen and oxygen gases. Because the mixture of them can easily explode just by a small spark, they need to be separated immediately after the production by using a separation membrane.^[39]

1-2-3 Photoelectrochemical Water Splitting Using Semiconductor Electrodes

Another promising system using the two-step photoexcitation process is a photoelectrochemical (PEC) cell, which employs two kinds of semiconductor electrodes: photocathode and photoanode for HER and OER, respectively.^[40–44] Figure 1-2-3 shows a scheme for the PEC cell, where these electrodes are often called as photoelectrodes. As the case of Z-scheme photocatalytic system, the photoelectrodes need to possess a band edge potential which is energetically higher than the reduction or oxidation potential of water. The HER and OER sites can be located far from each other like an electrolyzer as shown in Figure 1-2-1, so the system can avoid the necessity of separation process mentioned above. Employment of metallic layers as back contacts for semiconductor layers can be adapted to direct electrolysis under application of external bias voltage.

Another advantage of separating HER and OER sites is realization of appropriate surface modifications to each semiconductor. Recent reports have revealed that surface modification process onto semiconductor photoelectrodes and photocatalysts significantly improves their performances such as charge separation efficiency and stability.^[45–49] The separation of reaction sites is advantageous for execution of selective modification process onto the photocathode and photoanode. Therefore, the PEC cell is a promising system to realize efficient and stable overall water splitting using semiconductor materials.

In the next chapter, fundamentals of the photoelectrodes are discussed in detail. It is indispensable to understand the behavior of electrons in semiconductor photoelectrodes because that is essentially related to photoexcitation, transfer and electrochemical reaction during the PEC process.

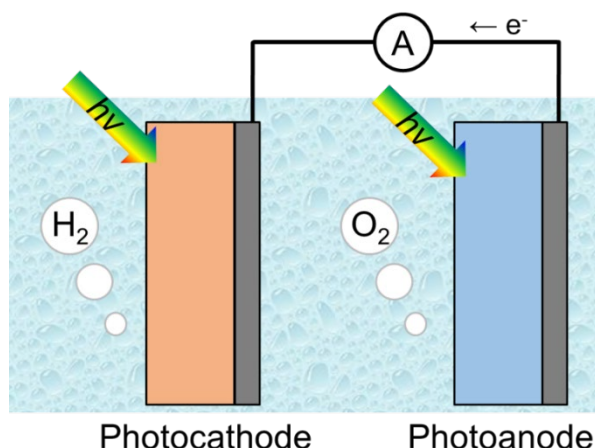


Figure 1-2-3. A scheme for a PEC cell.

1-3 Fundamentals of Photoelectrodes for Photoelectrochemical Cells

1-3-1 Electronic Properties of Semiconductor Materials

In the bulk of an intrinsic semiconductor, where atoms form a pattern of ordered arrangement, energy levels of each molecular orbital get together to build widespread states of electrons, which is called a band.^[50] The band filled with valence electrons is defined as a valence band, while that filled with no electrons (at absolute zero) and located next to the valence band is defined as a conduction band. The gap between the valence band maximum (VBM) and conduction band maximum (CBM) is called band gap. Figure 1-3-1 shows calculated band structure of AgGaSe₂ described as energy distribution of density of states as an example.^[51] The calculation suggests that the states in the vicinity of VBM are attributed to Ag *d* and Se *p* orbitals while those of CBM mainly consist of Ga *s* orbitals. Also, the result suggests that the band gap energy of AgGaSe₂ is around 1.8 eV.

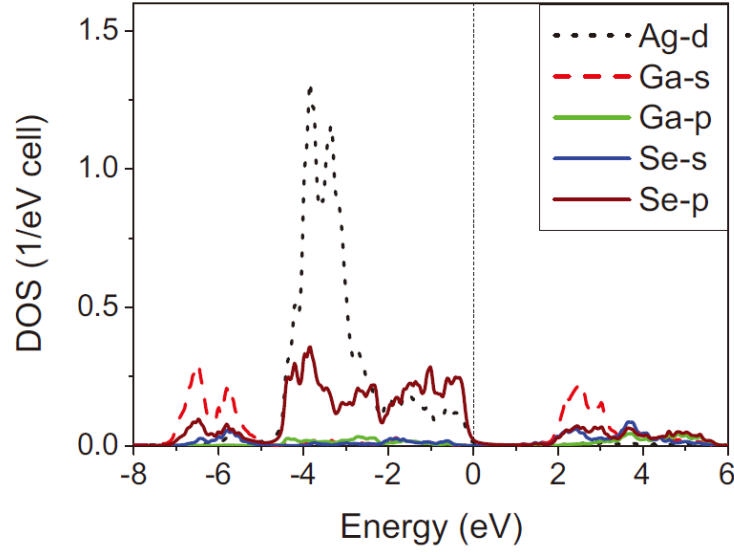


Figure 1-3-1. Density of states of AgGaSe₂ with the VBM set to 0 eV. Reprinted with permission of IOP Publishing Ltd from ref. [51].

Because electrons in a solid act as fermions, their distribution can be described by the Fermi function as

$$f(E) = \frac{1}{1 + e^{\frac{E - E_F}{kT}}} \quad (1-1)$$

in which E stands for energy levels, $f(E)$ is occupation probability by an electron, and kT is the Boltzmann's constant times temperature.^[52] E_F is the Fermi level: the chemical potential of the electrons at absolute zero. Given the absolute zero, electrons occupy all the states from the lowest energy level according to Pauli exclusion principle without any vacancy because no excitation occurs. Considering the limit as T approaches 0 in Eq. (1-1), the Fermi distribution function can be described as

$$\lim_{T \rightarrow 0} f(E) = \begin{cases} 1 & (E < E_F) \\ \frac{1}{2} & (E = E_F) \\ 0 & (E > E_F) \end{cases} \quad (1-2)$$

where E_F is equal to the energy level at which the probability of an occupied state is a half. Even in the case of $T > 0$ K, it is convenient to roughly consider that the energy states lower and higher than E_F are occupied and unoccupied by electrons, respectively.^[53]

Chapter 1. General Introduction

Defects and/or impurities in the crystal can form shallow donor or acceptor levels as shown in Figure 1-3-2.^[50] Consequently, thermally excited electrons or vacancies of electrons, holes, exist in conduction band or valence band, respectively. If both exist, they compensate each other, which is called charge compensation. As shown in Figure 1-3-2 (b), the order of magnitude of carrier concentration strongly depends on the energy level of defects. A semiconductor with the CBM partially occupied by the electrons is called as an n-type semiconductor and its Fermi level is located near the CBM. On the other hand, a semiconductor with the VBM partly occupied by the holes is called as a p-type semiconductor and its Fermi level is located near the VBM. The relationship between the concentrations of hole, p , and donor, n , and E_F can be described as

$$p = N_V e^{\frac{E_V - E_F}{kT}} \quad (1-3a)$$

and

$$n = N_C e^{-\frac{E_C - E_F}{kT}} \quad (1-3b)$$

where N_V and N_C stand for density of states in VB and CB, respectively, and E_V and E_C mean each band-edge potential. The depth of defect levels and formation energy of each defect type strongly affect the carrier concentration (i.e. p- or n-type property of the semiconductor). In the next section, behaviors of these semiconductors at around the interfaces with a different semiconductor or an electrolyte are explained in detail.

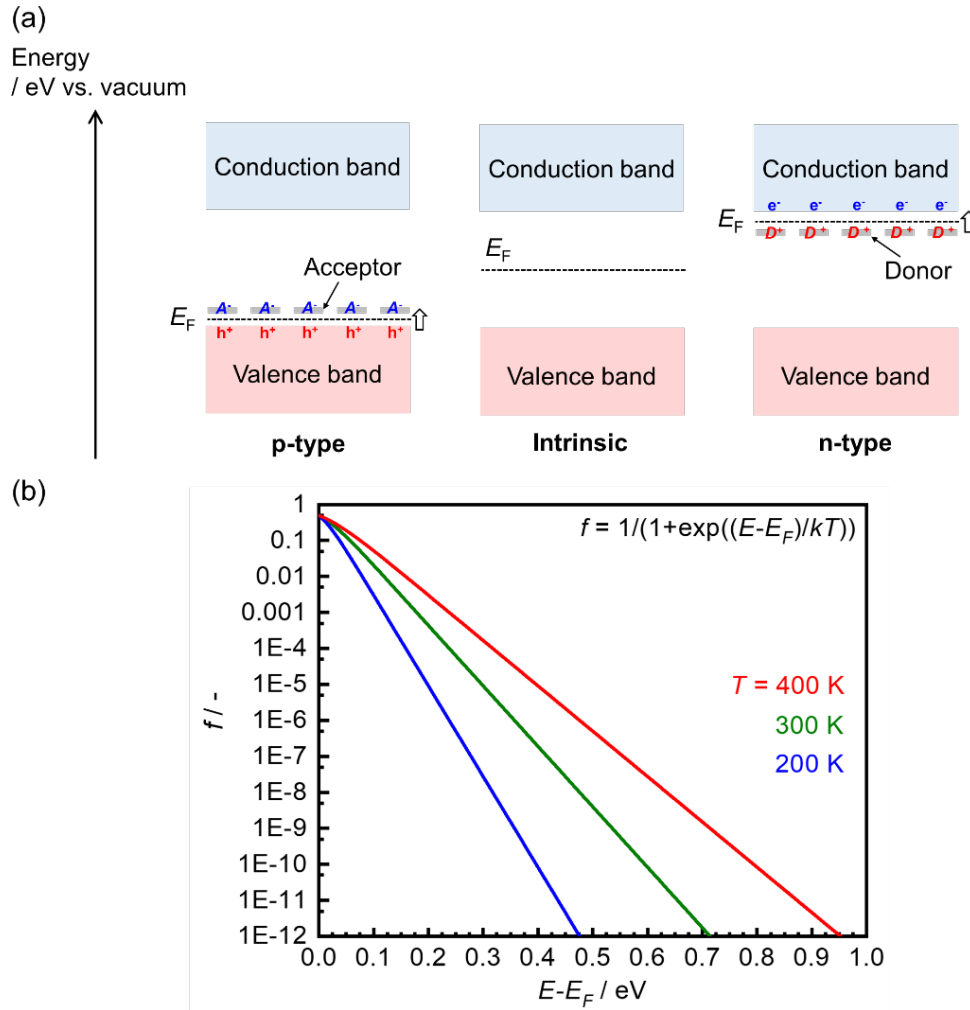


Figure 1-3-2. (a) Fermi levels and activated donor/acceptor levels in semiconductors, and (b) Fermi function at several values of temperature.

1-3-2 Potential Changes at Semiconductor Interfaces

This section considers the situations that a semiconductor is in contact with another semiconductor or an electrolyte. The difference in the Fermi levels between the two semiconductor materials forms a built-in electric field.^[43,54,55] The electric field can be described as bending of bands as shown in Figure 1-3-3, and is attributed to diffusion and recombination of holes and electrons at around the interface. Because the thermally excited electrons and holes mentioned in the previous section diffuse into the interface, the region gets short of charge carrier, which is called a depletion layer.

Chapter 1. General Introduction

The distribution of band bending, (i.e. width of depletion layer) depends on Poisson's equation, written as

$$\frac{d^2\varphi}{dx^2} = \frac{eN_A}{\varepsilon_r\varepsilon_0} \quad (1-4a)$$

for a p-type semiconductor and

$$\frac{d^2\varphi}{dx^2} = -\frac{eN_D}{\varepsilon_r\varepsilon_0} \quad (1-4b)$$

for an n-type semiconductor. Herein, φ means the electric potential (i.e. Fermi level) at position x . e , ε_r and ε_0 stand for the elementary charge, the relative permittivity and the vacuum permittivity, respectively. N_A and N_D stand for the concentrations of ionized acceptors and donors, respectively. Given a junction between a p- and n-type semiconductor, the Eqs. (1-4a) and (1-4b) can be solved by considering boundary conditions, and we can have the widths of band bending (x_p and x_n for the p- and n-type semiconductor, respectively) as

$$x_p = \sqrt{\frac{2\varepsilon_r\varepsilon_0 N_D}{eN_A(N_A+N_D)}\Delta E} \quad (1-5)$$

for the p-type semiconductor and

$$x_n = \sqrt{\frac{2\varepsilon_r\varepsilon_0 N_A}{eN_D(N_A+N_D)}\Delta E} \quad (1-6)$$

for the n-type semiconductor. ΔE is the absolute value of Fermi level difference between the two semiconductors. In more complicated situations, sequential calculation is employed to obtain the distribution of the depletion layer.

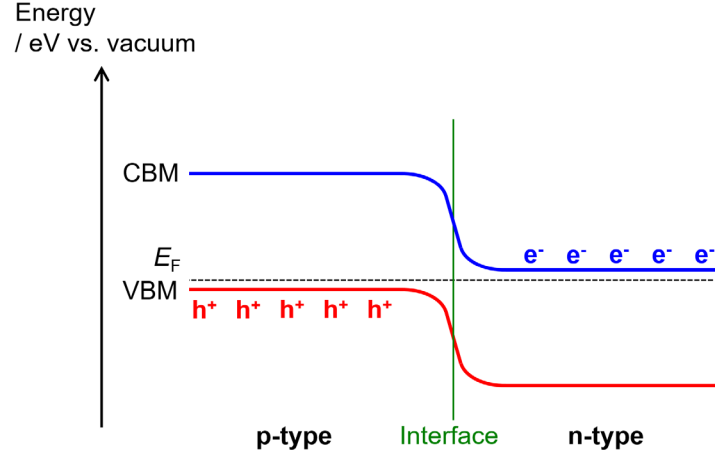


Figure 1-3-3. A schematic band alignment at a p-n junction.

In general, the carrier density in a p- or n-type semiconductor is around 10^{14} to 10^{17} cm^{-3} .^[53] It should be noted that the carrier density should be close to the concentration of ionized donors or acceptors after compensation between each other. On the other hand, the carrier density in the electrolyte which has the ion density of 1 M is calculated to be about $6 \times 10^{20} \text{ cm}^{-3}$. That means that the difference in the carrier density is significantly large in the case of semiconductor-electrolyte interface. Therefore, the Eqs. (1-5) and (1-6) can be approximated to be

$$x_p = \sqrt{\frac{2\epsilon_r\epsilon_0}{eN_A} \Delta E'} \quad (1-7)$$

for a p-type semiconductor and

$$x_n = \sqrt{\frac{2\epsilon_r\epsilon_0}{eN_D} \Delta E'} \quad (1-8)$$

for a n-type semiconductor. In the case of semiconductor-electrolyte interface, $\Delta E'$ equals to the potential difference between the Fermi level of the semiconductor and the redox potential of the electrolyte. The built-in electric field at the interface as shown in Figure 1-3-4 is the same as Schottky junction for a semiconductor-metal junction.^[52] Hence, the behavior of electrons can be described analogously to the Schottky junction. A semiconductor-electrolyte interface also forms an electric double layer, where specific ion adsorption onto the semiconductor surface is not considered in the figure, which is often occurred by anion species.

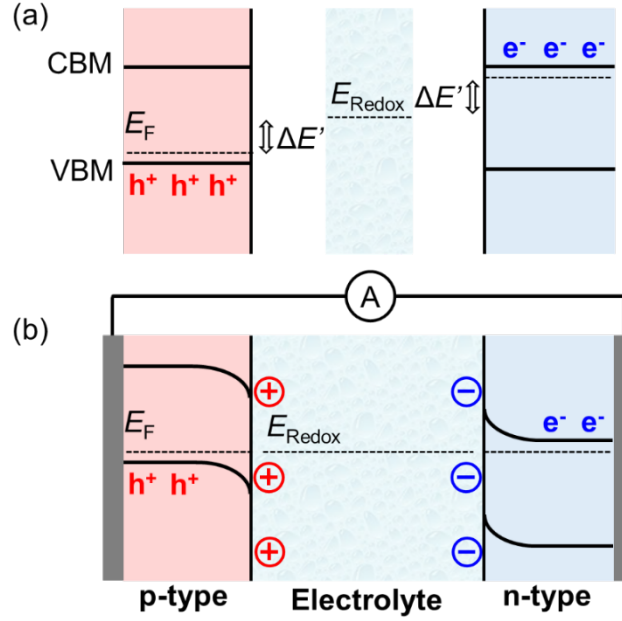


Figure 1-3-4. Band alignments of semiconductors before (a) and after (b) forming contacts with an electrolyte and connection to each other. The interface between each semiconductor and back side electrode is neglected.

1-3-3 Photoelectrochemical Reaction under Light Irradiation

This section considers the principles of photoexcitation, charge separation and electrochemical reaction, which establish the PEC reaction process on photoelectrodes. The intensity of incident light in an absorbing medium exponentially decreases with the increase of transmission distance, known as Lambert-Beer's law. The probability of photoexcitation depends on the absorption coefficient α , defined as

$$\alpha = \frac{1}{d} \ln \frac{I_0}{I} \quad (1-9)$$

where d is the thickness of the absorbing material, and I and I_0 are the transmitted and the incident light intensities, respectively.^[52] In a semiconductor material, the relationship between α and the energy of incident photon, $h\nu$, can be expressed as

$$\alpha = \frac{A(h\nu - E_g)^m}{h\nu} \quad (1-10)$$

Chapter 1. General Introduction

where A is a constant, E_g is the band gap energy, and m is 1/2 and 2 for a direct and indirect band gaps, respectively.^[54] Figure 1-3-5 shows examples of α vs. $h\nu$ for several semiconductor materials. Except for the vicinity of absorption edge, Si shows ten times smaller α compared with the other semiconductor materials exhibited in the figure. This is because phonon emission or absorption needs to be accompanied in the case of indirect band gap semiconductors such as Si so as to satisfy the change in the momentum between the CBM and VBM.^[52] On the other hand, direct band gap semiconductors show high probability of light absorption due to the unnecessary of momentum change, although it also leads to relatively high probability of radiative recombination to decrease external quantum efficiency (QE). Figure 1-3-6 shows calculated absorbance of incident light in depth according to the Lambert-Beer's law. A direct band gap semiconductor with α of 10^5 cm^{-1} requires a path length of only 500 nm to absorb 99% of incident light while an indirect band gap semiconductor with α of 10^4 cm^{-1} can absorb only about 40% in the path length. Considering the typical thickness of the depletion layer formed at the semiconductor-electrolyte interface described below, a direct band gap semiconductor material is preferable for a photoelectrode in a viewpoint of efficient light collection.

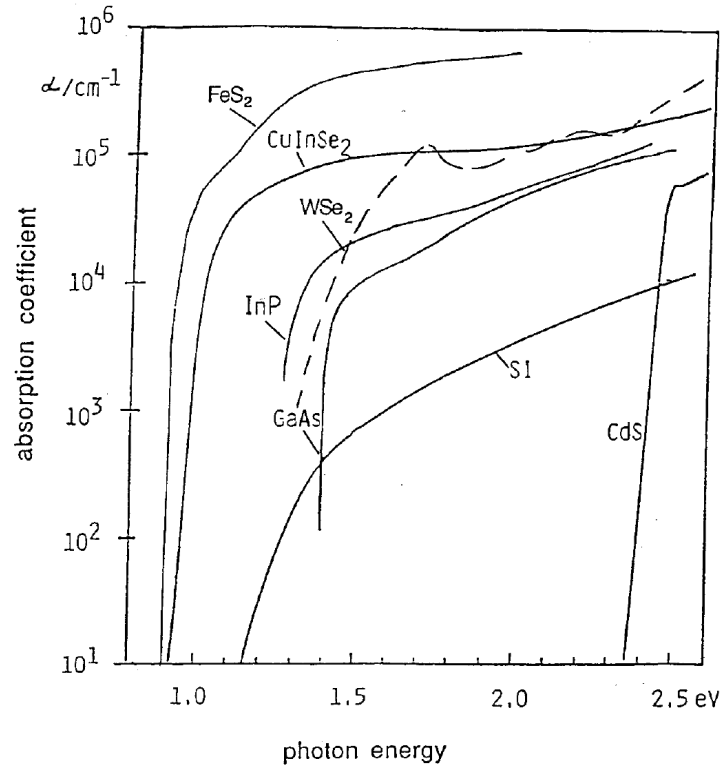


Figure 1-3-5. Absorption spectra of various semiconductors. Reprinted with permission from ref. [52]. Copyright 2001 Wiley-VCH.

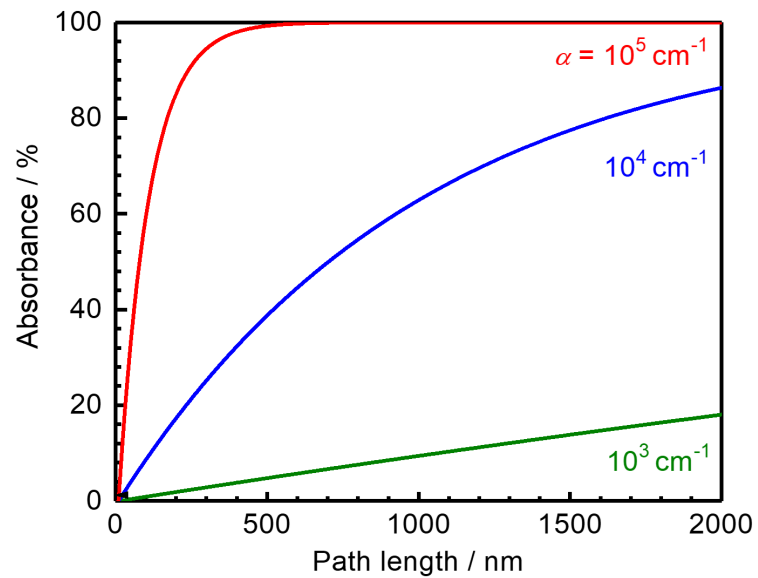


Figure 1-3-6. Calculated absorbance as a function of path length according to Lambert-Beer's law.

Chapter 1. General Introduction

The lifetime of photoexcited electrons in a direct band gap semiconductor is generally less than $1 \mu\text{s}$.^[56,57] In other words, the recombination of photoexcited electrons occurs on a time scale of nanoseconds. Hence, the photoexcited electrons/holes need be quickly separated and transferred to active sites for electrochemical reaction within the lifetime. The built-in electric field formed at a semiconductor-electrolyte interface plays an important role in the charge separation. For instance, the thickness of depletion layer x_p in Eq. (1-7) is calculated to be 235 nm by assuming ϵ_r , N_A and $\Delta E'$ as 10, 10^{16} cm^{-3} and 0.5 V, which corresponds to the electric field strength, E , of 2 MV cm^{-1} . Such a strong electric field separates the photoexcited carriers to generate drift current before their recombination. The drift current value, J , under existence of an electric field is given as

$$J = en\mu E \quad (1-11)$$

where n and μ is the density and the mobility of the corresponding charge carrier, respectively.

Successful separation of the photoexcited carriers results in generation of photocurrent flowing toward the electrolyte side. In real cases, some of the carriers recombine via the surface recombination sites to decrease the photocurrent value, but in this section such surface recombination is neglected. At the semiconductor-electrolyte junction, the relationship between the voltage and the current value doesn't follow Ohm's law but can be expressed in the same manner as a semiconductor-metal junction (see also the section 1-3-2). The Shockley diode equation plus photocurrent is described as

$$J = J_{sc} - J_D = J_{sc} - J_0 \left(e^{\frac{eV}{kT}} - 1 \right) \quad (1-12)$$

where V stands for the voltage externally applied to the photoelectrode, and J_{sc} means the photocurrent under light irradiation under short-circuit condition without any resistance or potential barrier. J_0 is the leakage current in dark condition and called dark saturation current, given as

$$J_0 = \frac{eDn_i^2}{n_0L} \quad (1-13)$$

D and L are the diffusion constant and length of the minority carrier, n_i is the intrinsic carrier density and n_0 is the carrier density in thermal equilibrium.^[52] When the circuit between the

working electrode and the counter electrode is open and the total current is zero, called rest condition, the separated carriers are accumulated at the interface to generate a photovoltage across the junction.

The photovoltage in the rest condition, V_{ph} , can be expressed as

$$V_{ph} = \frac{kT}{e} \ln\left(\frac{J_{sc}}{J_0} + 1\right) \quad (1-14)$$

because J and J_{sc} are zero in this condition.

Consequently, the dependency of current vs. applied potentials for a model photoelectrode following Eqs. (1-12) to (1-14) is drawn in Figure 1-3-7.

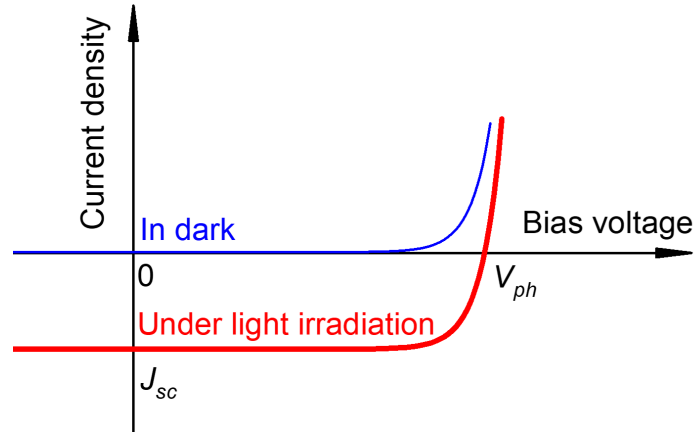


Figure 1-3-7. Calculated current-voltage curves for a photocathode in dark condition and under light irradiation using Eq. (1-12).

These descriptions have ignored existence of activation energy at the semiconductor-to-electrolyte charge transfer. Unlike the semiconductor-metal interface, an additional potential difference is required to drive electrochemical reaction (i.e. charge transfer from semiconductor to electrolyte) in a practical rate. The relationship between J and overpotential η in a half reaction $R \rightarrow Ox + ne^-$, called Butler-Volmer equation, can be derived from Arrhenius equation and given as

$$J = J_+ + J_- = J^0 \left[\left(\frac{C_R^s}{C_R^b} \right) e^{\frac{\alpha_+ e n \eta}{kT}} - \left(\frac{C_{Ox}^s}{C_{Ox}^b} \right) e^{\frac{\alpha_- e n \eta}{kT}} \right] \quad (1-15)$$

where C_R and C_{Ox} are the concentrations of R and Ox , respectively, and n stands for the number of electrons transferred in the reaction. The superscripts s and b stand for the concentrations at the

electrode surface and the bulk electrolyte, respectively.^[53] J_+ and J_- indicate the current densities of the oxidation (forward) and reduction (reverse) reaction, respectively. α_+ and α_- are called transfer coefficient and the sum of each other is one. J^o is the exchange current density, which is given as

$$J^o = nek^oC \quad (1-16)$$

under the condition of $C_R = C_{Ox} = C$, where k^o is called the standard rate constant. All of the constants α_+ , α_- and k^o are classified as the kinetic parameters, and they are specific to the combination of the electrolyte and reaction site. In real cases, reaction catalysts are often deposited onto the photoelectrode surface because they are effective to decrease the η to obtain a certain J . Figure 1-3-8 shows a simulated current-potential curve.

This section discussed the current-potential property of photoelectrodes. It is noteworthy that Eqs. (1-12) and (1-15) should be true for a photoelectrode when the rate-determining step is the extraction of photoexcited carriers to the reaction site and electrochemical reaction, respectively.

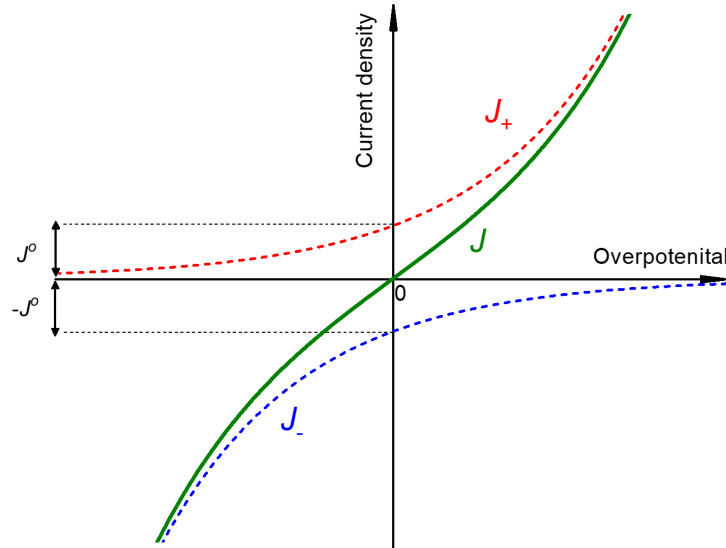


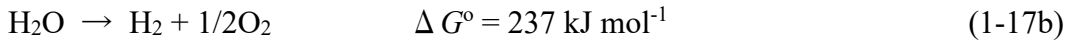
Figure 1-3-8. A calculated current-potential curve using the Butler-Volmer equation assuming $\alpha_+ = \alpha_- = 0.5$ and $\frac{C_R^S}{C_R^b} = \frac{C_{Ox}^S}{C_{Ox}^b} = 1$, where neither photoexcitation process nor charge separation process are considered.

1-3-4 Energy Conversion Efficiency and Stability of Photoelectrochemical Cells

The STH of energy conversion system introduced in the section 1-2 without external bias voltage is described as

$$STH = \frac{1.23 \text{ [V]} \times J}{P_{sun}} \quad (1-17a)$$

for the water splitting reaction



where P_{sun} is the energy of incident sunlight, J is the photocurrent density attributed to water splitting reaction and ΔG° stands for the standard Gibbs free energy of formation, corresponding to 1.23 eV.^[42] ASTM International establishes the standards of sunlight spectra such as AM1.5D.^[58] The AM1.5D spectrum, where D means “direct”, corresponds to that obtained at the solar zenith angle of 48.2° at the sea level, and so it considers light absorption by molecules in the atmosphere. Another reference spectrum shown in Figure 1-3-9, AM1.5G, reflects scattered light from the surroundings, where G stands for global. The total energy of AM1.5G spectrum is 100 mW cm⁻². In this work, simulated sunlight of AM1.5G is employed to evaluate photoelectrodes and PEC cells.

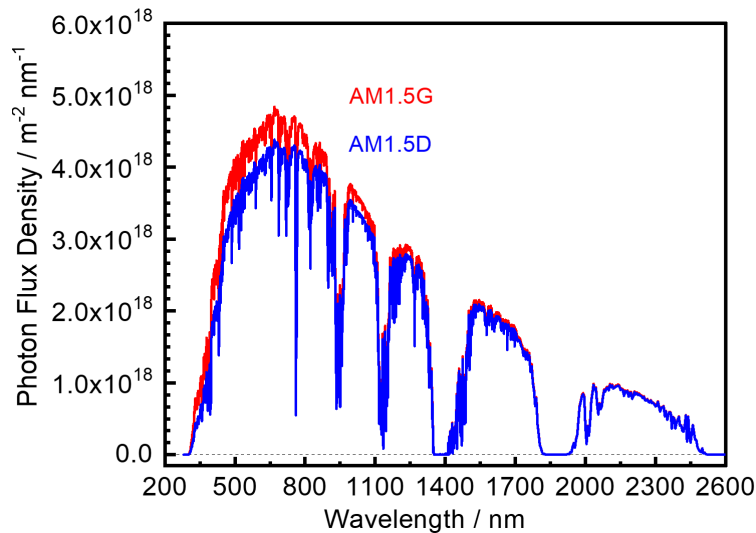


Figure 1-3-9. Spectra of photon numbers in AM1.5G and AM1.5D.

Eq. (1-17) is a simple and convenient standard to evaluate energy conversion efficiency. However, it is impossible to apply to a half cell in a three-electrode cell connected to a potentiostat. Hisatomi et al. established the half-cell STH (HC-STH) so as to evaluate a single photoelectrode under application of external bias voltage,^[40] which is defined as

$$HC - STH = \begin{cases} \frac{|J| \times (E_{RHE} - E_{H^+/H_2})}{P_{sun}} & \text{(for photocathodes)} \\ \frac{|J| \times (E_{O_2/H_2O} - E_{RHE})}{P_{sun}} & \text{(for photoanodes)} \end{cases} \quad (1-18)$$

where E_{RHE} , E_{O_2/H_2O} and E_{H^+/H_2} stand for the applied potential vs. reverse hydrogen potential (RHE), the oxidation potential (1.23 V_{RHE}) and the reduction potential of water (0 V_{RHE}), respectively. In the case of a PEC cell composed of a couple of photoelectrodes, the working current, J , is obtained as an intersection point of current-potential curves of the photocathode and photoanode as shown in Figure 1-3-10. The corresponding potential at the crossing point is called a working potential.

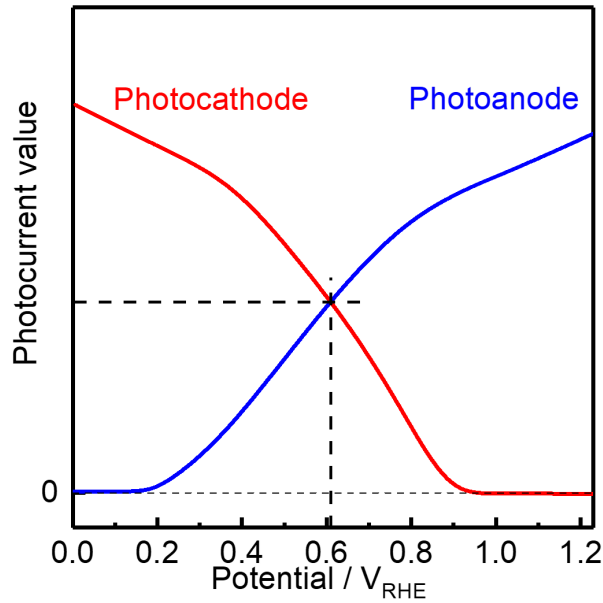


Figure 1-3-10. Current-potential curves for a virtual photocathode and photoanode.

Figure 1-3-11 shows the relationship between the band gap and STH assuming several QEs up to the band gap. For example, a photoelectrode having its band gap of 700 nm is theoretically able to

show a photocurrent density of 20 mA cm^{-2} , which corresponds to the STH of 11.9% in a 2-step photoexcitation system. However, it is difficult to realize such a high STH due to the losses in PEC process described below.

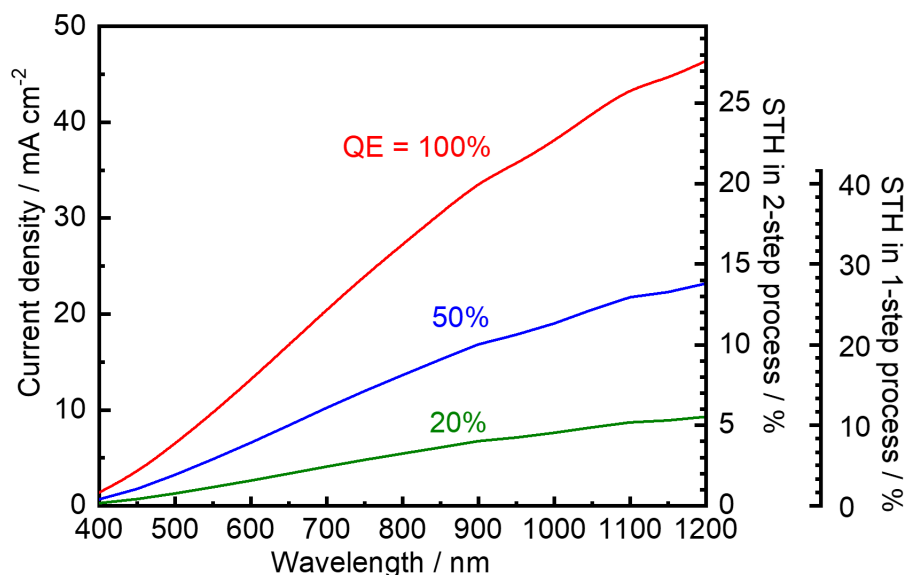


Figure 1-3-11. Relationship between absorption edge wavelength of photoelectrodes, photocurrent density with several assumption of QEs and corresponding STHs.

Crystal defects in a semiconductor material are indispensable for generation of electrons/holes as illustrated in Figure 1-3-2. On the other hand, these defects act as recombination sites for photoexcited carriers, resulting in a decrease in the external QE.^[59] Investigations of experimental detection by using photoluminescence have revealed existence of defect levels in the band gap and transition between the defect level and the band.^[60–63]

Defects also exist at the semiconductor surface consisting of dangling bonds and interface, which can also contain dangling bonds originated by the structural and lattice mismatch and heterovalency at the junction. They cause significant recombination of photoexcited carriers to decrease photovoltage and loss in the photovoltage.^[64–69] Furthermore, a high concentration of surface states has been reported to cause a significant loss in the photovoltage.^[69] Because such states behave as like a

Chapter 1. General Introduction

capacitor, electrochemical impedance spectroscopy has been known as an effective method to evaluate these states.^[70–72]

The potential at which the band bending disappears is called flat-band potential E_{FB} , and the relationship between E_{FB} and surface capacitance follows the Mott-Schottky equation given as

$$\frac{1}{C_{SC}^2} = \left(\frac{2}{\epsilon \epsilon_0 e n} \right) \left(E - E_{FB} - \frac{kT}{e} \right) \quad (1-19)$$

where C_{SC} is the capacitance of the electrode.^[54] This relationship enables assumption of E_{FB} and carrier density n by measuring C_{SC} at each potential.^[73]

Influence of mass transfer on the electrolyte side can also affect the cell efficiency.^[74,75] Behavior of reactants and products under the condition that solute diffusion is the rate-determining step can be calculated by using Fick's laws of diffusion. A commonly-known particular solution of the Fick's law is the Cottrell equation, which is given as

$$J = \frac{nFC_R^0 \sqrt{D_R}}{\sqrt{\pi t}} \quad (1-20)$$

where F , C_R^0 and D_R stand for the Faradaic constant, the concentration and the diffusion coefficient of reductant, respectively, in a half reaction of $R \rightarrow Ox + ne^-$. Eq. (1-20) doesn't consider the convection of solution, which allows the diffusion layer to grow up to the infinite thickness. In real cases, however, the diffusion layer thickness is finite (0.1 to several millimeters) due to existence of convection layer, so the J gradually becomes steady.^[76] Numerical simulations reported by Singh et al. have suggested that a pH gradient as the potential drop (i.e. polarization loss) of about 30 mV can occur in a 1 M buffered electrolyte of pH 7 if the current density and the thickness of the diffusion boundary layer are 10 mA cm⁻² and 2 mm, respectively.^[77]

In addition to these factors, instability of a photoelectrode can also cause a severe decrease in the efficiency. The photoexcited carriers are potentially reactive, so they can react with the photoelectrode surface instead of splitting water. This process is known as photocorrosion and can thermodynamically occur if the self-decomposition reaction is more positive or negative than the reduction or the oxidation reaction of water, respectively.^[46,78–80] Such decomposition often results

in degradation of the cell performance. Because the rate of photocorrosion reaction depends on the chemical composition including pH of the electrolyte, condition of electrolyte as well as chemical compound of the photoelectrode surface is an important factor for photoelectrodes to drive PEC reaction stably.

For the sake of construction of efficient and stable PEC cells, various kinds of photoelectrodes have been developed. In the next chapter, remarkable semiconductor materials and modification techniques for photoelectrodes are introduced in detail.

1-4 Candidates for Semiconductor Photoelectrode Materials and Surface Modifiers

1-4-1 Photoelectrode Materials

Since the photoanode surface is exposed to highly anodic atmosphere, many of photoanodes are composed of metal oxides.^[45,81–85] The first demonstration of spontaneous water splitting has been reported by Honda and Fujishima, who employed TiO_2 as the photoanode.^[86] TiO_2 shows a relatively large band gap of 3.2 eV and is chemically stable. Hence, the TiO_2 photoelectrode is capable of durable splitting water via 1-step photoexcitation process. However, the large band gap limits the theoretical maximum of the photocurrent to less than 2 mA cm^{-2} (see Figure 1-3-10) under AM1.5G illumination.

BiVO_4 is a promising metal oxide material because it can absorb visible light. This ternary oxide shows the band gap energy of 2.4 eV, which corresponds to the absorption edge wavelength of 510–520 nm in wavelength. Furthermore, the reported onset of photocurrent (called onset potential) is around $0.2 V_{\text{RHE}}$, which enables to obtain an intersection point with a photocathode at a wide range of potentials.^[87–90] Because electron mobility of BiVO_4 crystal is relatively low, nanoworm- or nanoporous-like morphology of the BiVO_4 photoelectrode is often fabricated to facilitate charge

Chapter 1. General Introduction

transfer.^[91,92] A nanorod-shape BiVO₄ photoanode has been reported to show a relatively high photocurrent value of 6.7 mA cm⁻² at 1.23 V_{RHE} under simulated sunlight. It is remarkable that the incident photon-to-current conversion efficiency (IPCE) reached >90% up to 470 nm under the condition.^[93] α -Fe₂O₃, which is often called hematite, has also attracted considerable attention because it shows a relatively narrow band gap of 2.1 eV, while the onset potential is more positive than that of typical BiVO₄ photoanodes by about 0.2 V.^[83,92,94] Unfortunately, the difficulty in preparing less-defective hematite crystals has caused low IPCEs.^[95–98] Therefore, additional modification is required to passivate such defects on the hematite crystal, which is introduced in the next section in detail.

The wide band gap of metal oxides is attributed to O 2p orbitals in their VBMs. (Oxy)nitride materials whose O is partially substituted by N show relatively narrow band gaps such as 1.9 eV for BaTaO₂N and 1.8 eV for BaNbO₂N.^[99,100] The theoretical maximum of their photocurrent values reaches around 20 mA cm⁻² under AM1.5G according to the small band gap energies. A challenge for these oxynitride materials is improvement of their onset potentials, which are limited to 0.5–0.6 V_{RHE}. In addition, poor durability due to self-oxidation of N³⁻ anions has also been observed.^[101–103] Hence, surface modifications including alternation of the built-in electric field and the chemical stability of the photoelectrode surface have still been taken on.^[104,105]

In the cases of photocathodes, the photoelectrode surface is kept in reductive atmosphere during PEC reaction. Hence, non-oxide materials can be utilized for a photocathode. Si shows a remarkably small band gap of 1.1 eV and therefore the reported photocurrent values have reached higher than 30 mA cm⁻².^[106–109] However, the onset potential is more negative than 0.5 V_{RHE}, which makes the combination with a photoanode relatively difficult. Also, the indirect transition in the Si crystal requires a large thickness of several hundred micrometers in order to maximize the IPCE.

Among III-V compounds, InP ($E_g = 1.35$ eV) photocathodes fabricated from the single-crystal wafers are also attractive because they show a large photocurrent value of ~ 25 mA cm⁻² and onset

Chapter 1. General Introduction

potential of 0.8 V_{RHE}.^[110,111] A demonstration of overall water splitting in conjunction with a tandem PV cell and a metal electrode showed an STH of 12%, which is the highest value of STH with employment of a photoelectrode.^[112] The critical disadvantage of III-V wafers and the epitaxial thin films is the high fabrication cost; in general, metal organic chemical vapor deposition onto a clean and monocrystalline substrate needs to be employed in fabrication process.^[113]

On the other hand, copper-based materials have attracted great attention as earth-abundant compounds. Polycrystalline Cu₂O-based photocathodes have been reported to show a considerable photocurrent and a relatively high onset potential of 1.0 V_{RHE} after surface modifications with several kinds of metal oxides by using atomic layer deposition (ALD) method.^[114–117] La₅Ti₂CuS₅O₇-based photocathodes also show high onset potentials of around 1.0 V_{RHE} without employment of complicated surface modifications.^[118,119] However, the band gaps of these two materials are less than 660 nm, which has limited the reported photocurrent values up to about 2 mA cm⁻². Cu₄ZnSnS₄ ($E_g = 1.45$ eV) is a notable material because it consists of only earth-abundant and less-expensive elements. In addition, electrodeposition method and spin-coating method to fabricate Cu₄ZnSnS₄ thin films is expected as cost-effective process. Unfortunately, the photocurrent value of a Cu₄ZnSnS₄ photocathode is less than 12 mA cm⁻² due to the low IPCEs (<50%), and the onset potential is limited to 0.7 V_{RHE}.^[120–123]

Except for these materials and Cu-chalcopyrite materials discussed below, there are many kinds of other photocathode materials have been reported such as SiC, amorphous Si, CdTe and CuFeO₂.^[124–128] However, further investigations on development of novel photocathode materials have still been required because few materials could meet all of the requirements including the photocurrent, onset potential and fabrication cost, which are indispensable to realize an efficient and durable PEC cell in a practical way. Following introduction of surface modification methods and demonstrations of PEC cells, Cu-chalcopyrite materials are introduced as a promising material to satisfy those conditions.

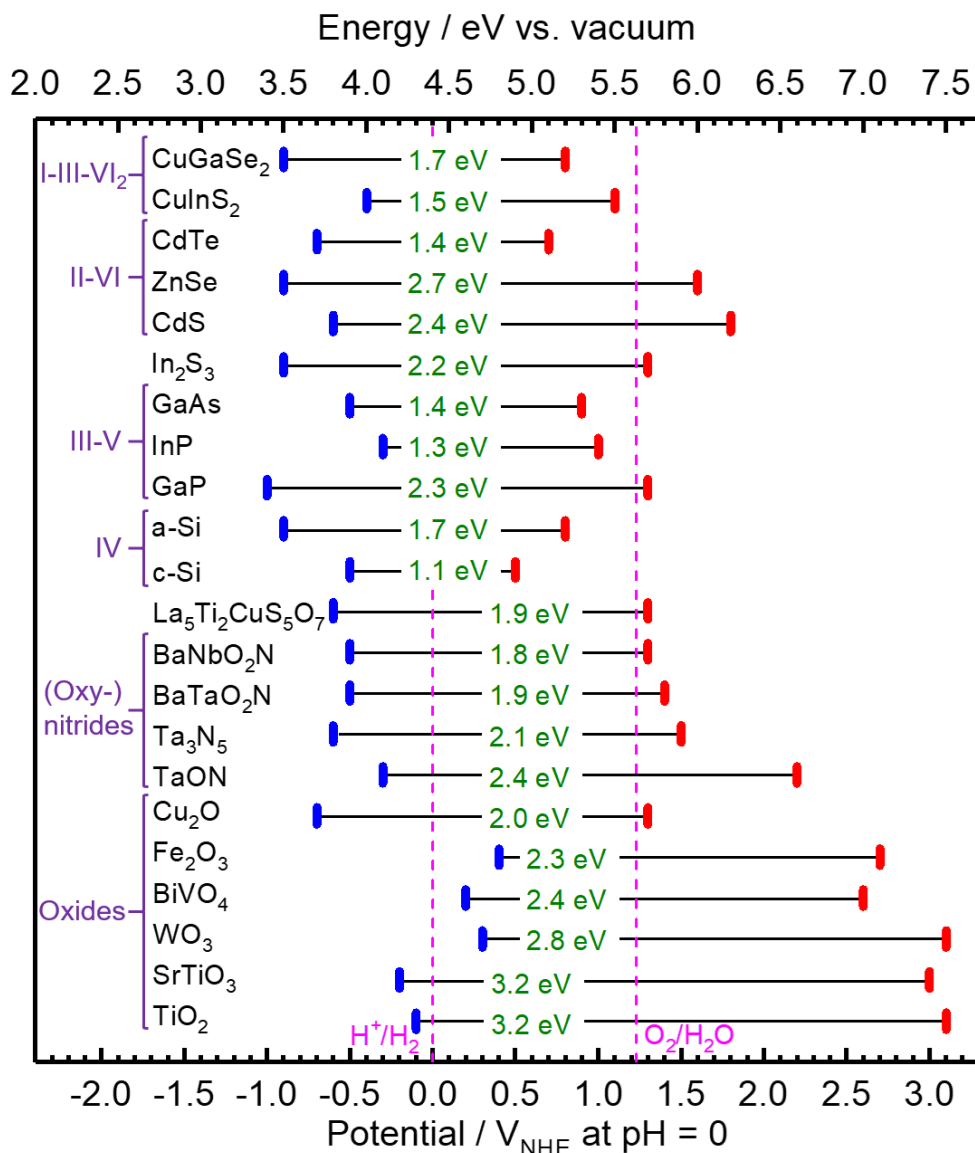


Figure 1-4-1. Reported VBM (red) and CBM (blue) potentials of various photoelectrode materials and their band gaps (green).^[42,48,65,99,129–133]

1-4-2 Techniques and Materials for Surface Modification on Photoelectrodes

Control of built-in potential can facilitate the charge separation at the semiconductor-electrolyte interface. The control can be achieved by fabricating laminated structure with another semiconductor layer which has a different flat-band potential.^[46,134,135] Impurity doping is often employed to change the p- or n-type property of a semiconductor to construct a homo-type p-n junction.^[134,136] Deposition

Chapter 1. General Introduction

of another semiconductor material, classified as a hetero-type junction, can also give the similar effect, although the lattice mismatch between the two layers should be considered to suppress formation of interfacial defects. Also, the band edge potentials should be aligned with a potentially downward gradient so as to transfer photoexcited charge carriers smoothly. Metal sulfide materials such as CdS with a thickness in a scale of nanometers deposited by chemical bath deposition (CBD) method have been reported as a good surface modifier for p-type photoelectrodes.^[120,123,137,138] Although CBD method limits the choice of available materials, the process is of merit in terms of the film conformality, the process simplicity, the easiness of thickness control, the etching effect onto impurity phases and the mild condition.^[139] Metal oxides such as TiO₂ and Ga₂O₃ are also employed and typically deposited by ALD method, which is advantageous in respect of availability of various materials in addition to the thickness control and the film conformality.^[116,140,141] As shown in Figure 1-4-2 (a), introduction of these junctions has been found to increase the photocurrent and shift the onset potential.^[135] Calculation of the built-in electric field by using Poisson's equations (see Eqs. (1-3) and (1-4)) presented in Figure 1-4-2 (b) has also suggested the increase in depletion layer width at a certain potential.

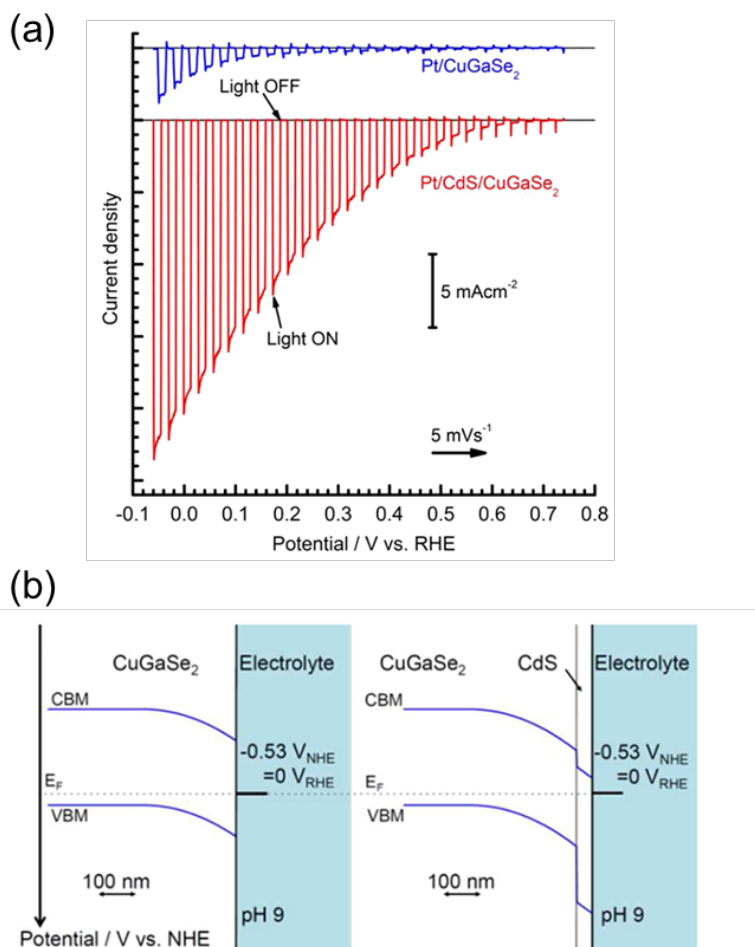


Figure 1-4-2. (a) Current-potential curves for CuGaSe₂ photocathodes modified with only Pt and both of CdS and Pt under chopped irradiation of the Xe lamp. A 0.1 M Na₂SO₄ (pH 9) was used as the electrolyte. (b) Calculated band alignment at semiconductor-electrolyte interfaces of CuGaSe₂ and CdS-modified CuGaSe₂. Reprinted with permission from ref. [135]. Copyright 2013 American Chemical Society.

Defect states in a band gap brought by surface defects cause significant recombination and a low photovoltage as discussed in section 1-3-4. Formation of a hetero-type junction has been reported to passivate such defects.^[54,68,94,96,97,108,142,143] A noteworthy work is NiFeO_x deposition onto a hematite photoanode.^[96] Figure 1-4-3 shows current-potential curves for the photoanodes under AM1.5G or 830 nm light illumination. The bare hematite photoanode showed a photoresponse under the NIR

light illumination, which suggests optical transition between the surface state and the band. On the other hand, the passivated photoanode showed almost no photoresponse due to the small density of surface states. Consequently, the photoanode showed an onset potential more negative than the bare photoanode by 0.4 V. It is interesting that the optimum thickness of these passivation layers is only 0.5 to 2 nm,^[97,144] which means the passivation layer affects only the surface states.

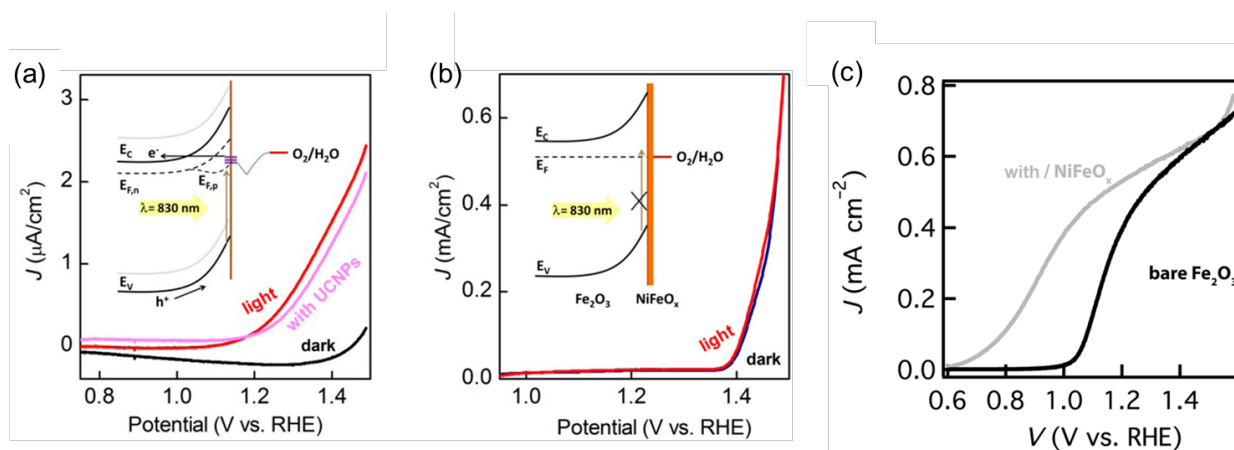


Figure 1-4-3. Current–potential curves for (a) bare and (b) NiFeO_x -modified hematite photoanodes under dark conditions and 830 nm IR illumination. Also shown is the curve obtained under 830 nm illumination following modification of the hematite with rare-earth-based up-conversion nanoparticles (UCNPs) that harvest photons at 980 nm and emit at 520 and 550 nm. Inset: proposed mechanism for a prohibited transition with an energy change smaller than the band gap. (c) Current–potential curves for bare and NiFeO_x -modified hematite photoanodes under AM1.5G illumination. A 1 M NaOH solution was used as the electrolyte. Reproduced with permission from refs. [68, 96]. Copyrights 2014 American Chemical Society and 2013 Wiley-VCH.

Another effect of a surface modifier is improvement of surface conductivity. The photoexcited minority carrier needs to transfer from semiconductor bulk to active sites before recombination. Presence of a highly conductive layer has been reported to support the smooth transfer by providing abundant carriers.^[109,145,146] Kumagai et al. demonstrated surface modification of CdS-modified

Cu(In,Ga)Se₂ photocathodes with a metal Mo and Ti bilayer (Mo/Ti) with each thickness of 3 nm deposited by using sputtering method, as shown in Figure 1-4-4.^[145] In the bilayer, Ti forms an intimate contact with the CdS without forming a Schottky barrier while it can easily be oxidized to TiO₂, so reducible Mo is required to keep the outermost surface metallic during HER. The current-potential curves revealed that employment of the Mo/Ti layer gives the largest photocurrent values below the onset potential. Ni has also been reported to function as a conductive layer for a SiC-based photocathode.^[146]

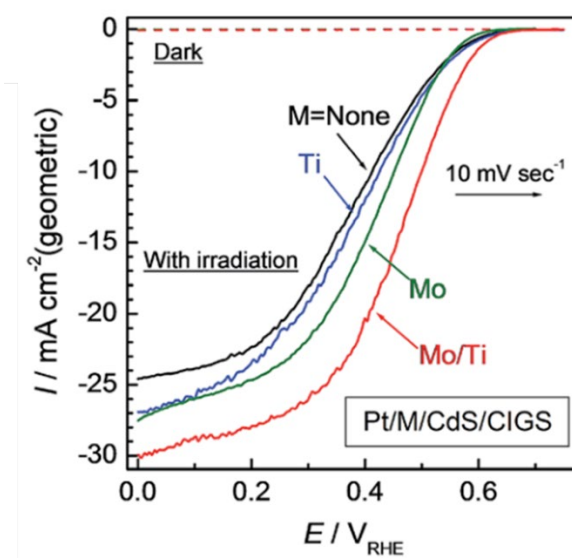


Figure 1-4-4. Current-potential curves for the Cu(In,Ga)Se₂ photocathodes modified with CdS, Ti, Mo and/or Pt under simulated sunlight. A 0.5 M Na₂SO₄ + 0.5 M sodium phosphate buffer solution (pH 6.8) was used as the electrolyte. Reprinted with permission from ref. [145] - Published by The Royal Society of Chemistry.

In general, HER and OER catalysts are deposited on the top of photocathodes and photoanodes, respectively. For HER, Pt is known as the most efficient reaction catalyst,^[147] which is typically deposited by using photoelectrodeposition, sputtering or vacuum evaporation.^[135,148,149] Because Pt is precious and expensive metal, alternative materials such as NiMo and MoS₂ have been developed

Chapter 1. General Introduction

and reported to show comparable HER activity on photocathodes.^[117,150,151] OER catalysts have also been investigated intensively because the four-electron reaction essentially requires relatively high overpotentials.^[152] Among the platinum-group metals, oxides of iridium and ruthenium are often employed as OER catalysts.^[153] Also, oxides (or oxyhydroxides) of nickel, iron and cobalt and combination of them have been reported as not only efficient OER catalyst but also self-generative modifiers.^[88,154] This is because these metal cations can re-deposit onto the photoanode surface via oxidation process (e.g. Ni^{2+} to $\text{Ni}^{3+/4+}$).^[155] Even though the surface catalysts are often suffered from poor durability due to detachment of them, the photoanodes deposited with the self-generative catalysts have shown relatively durable PEC OER for a time scale of hours.

Protection of photoelectrode surface with a chemically stable material has also been developed to establish durable PEC reaction. A TiO_2 layer is the most commonly employed material as the protection layer for both photocathodes and photoanodes.^[78,156,157] For example, Seger et al. prepared an n⁺p Si photocathode coated with TiO_2 with a thickness of 100 nm by using sputtering method followed by heat treatment.^[158] The photocathode showed a highly stable photocurrent for longer than 72 h at 0.3 V_{RHE} under simulated sunlight as shown in Figure 1-4-5. On the other hand, the photocathodes without TiO_2 layer and/or heat treatment showed significant instability during PEC reaction. Similar effects have been reported on amorphous Si, Cu_2O , CuInS_2 photocathodes and so on.^[125,140,159] The deep VBM of TiO_2 is also desirable for photocathodes because it blocks the photoexcited holes to facilitate charge separation. Al_2O_3 and NiO_x layers are also reported as good protection layers.^[160–162] These metal oxides are typically deposited by using sputtering or ALD method. A disadvantage of these process is requirement of heat treatment to crystalize the oxide layers, which can damage the underlying semiconductor layers. Moreover, especially in the case of TiO_2 , the heat treatment can form pinholes in the layer due to density change, which spoils the protection effect.^[70] Hence, further investigation on development of protection layers is still awaited.^[46]

In the next section, experimental demonstrations of PEC cells constructed by using these fabrication techniques and their challenges are introduced.

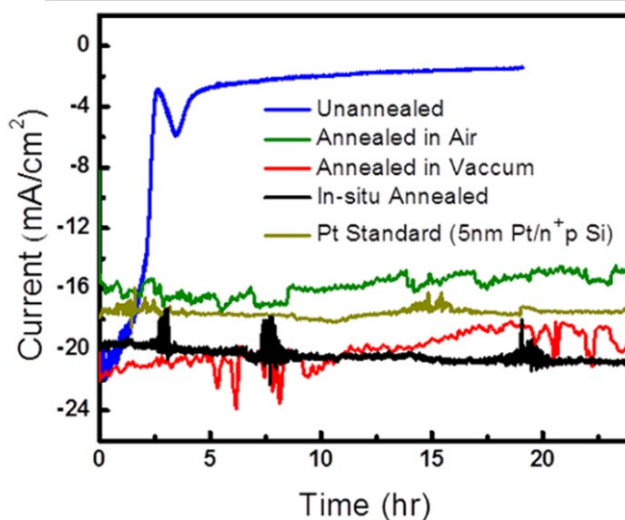


Figure 1-4-5. Current-time curves for the n^+p Si photocathodes modified with Ti, TiO_2 and Pt with various heat treatments at $0.3 V_{\text{RHE}}$ under simulated sunlight. A 1 M HClO_4 solution was used as the electrolyte. Reprinted with permission from ref. [158]. Copyright 2013 American Chemical Society.

1-4-3 Demonstrations and Challenges of Photoelectrochemical cells

Following the Honda and Fujishima's report in 1972,^[86] construction of PEC cells composed of a couple of a photocathode and photoanode has received much attention. In 1976, Nozik reported the first demonstration of PEC cells by employing a monocrystalline p-GaP photocathode and TiO_2 photoanode, which showed an STH of 0.25% without any surface modification.^[163] Ohashi et al. investigated the stability of a PEC cell composed of a monocrystalline p-GaP photocathode and SrTiO_3 photoanode to record no degradation for 13 h.^[164] These monocrystalline photoelectrode materials have shown a promising performance as stated above, but they are known as highly expensive devices.

Chapter 1. General Introduction

For the sake of realizing practical application, construction of a PEC cell using less-expensive materials such as a polycrystalline film was awaited.

In 2014, Yang et al. reported a spontaneous water splitting using a PEC cell composed of quantum dots (QDs) of CdSe and CdS deposited on nanorod-like templates as a photocathode and a photoanode, respectively.^[165] The surfaces of CdSe and CdS QDs were coated with ZnS as passivation layers. Also, nanoparticles of NiS and IrO_x were deposited on the top surface as HER and OER catalyst, respectively. The cell showed an initial STH of 0.17%, which maintained ~70% of the efficiency after 90 minutes from the beginning of reaction. To the best of the author's knowledge, this is the first demonstration of a PEC cell in the absence of expensive single crystals or epitaxial layers. In the same year, a demonstration using a polycrystalline Cu₂O and W:BiVO₄ thin film as a photocathode and photoanode, respectively, were reported by Borno et al.^[166] The photocathode surface was coated with Al:ZnO, TiO₂ and RuO_x as an n-type layer, protection layer and HER catalyst, respectively.^[167] On the other hand, cobalt-phosphate (Co-Pi) was deposited as OER catalyst on the photoanode surface. The cell showed a relatively high STH of approximately 0.4% at the beginning of light irradiation, but a significant degradation was also observed. The authors pointed out that dissolution of Co-Pi catalyst could contribute to the degradation. Ding et al. constructed a PEC cell consisting of a Si-based photocathode, but unfortunately it resulted in a very small STH due to its insufficient onset potential.^[168]

In 2015, Jiang et al. demonstrated a PEC cell consisting of a Cu₂ZnSnS₄ photocathode prepared by less-expensive methods of electrodeposition and sulfurization.^[121] The cell showed relatively a high stability which maintained 90% of initial STH for 2 h. Another cost-effective process for photoelectrode fabrication is particle transfer (PT) method.^[169] Doped La₅Ti₂Ag_xCu_{1-x}S₅O₇ ($x = 0-0.1$) photocathodes and BaTaO₂N photoanodes were known as promising photoelectrodes prepared by PT method, and combinations of both photoelectrodes have shown STHs up to 0.14% after surface modifications.^[102,118] It should be noted that a La₅Ti₂CuS₅O₇ photoelectrode can act as a photoanode

Chapter 1. General Introduction

if contacted with Ti on the back side, so a PEC cell composed of only $\text{La}_5\text{Ti}_2\text{CuS}_5\text{O}_7$ photoelectrodes has also been demonstrated.^[170] A similar configuration was reported on BiVO_4 -based photoelectrodes.^[171] It should be noted that more records for various kinds of device configurations including a PV and metal electrode(s) have recently been reviewed by Ager et al.^[13] Table 1-4-1 presents a summary of overall water splitting focusing on the reports employing a couple of photoelectrodes, and Figure 1-4-6

This overview reveals that the long-term durability in a time scale of days of a PEC cell has not been established yet. It can be pointed out that decomposition (dissolution, self-oxidation/reduction and detachment) of photoelectrode surface has still been a critical issue. As claimed in this and the previous sections, further investigation on stabilization of photoelectrode surface is needed. Plus, although continuous progress in STH has been established, few reports exceeded the value of 1%.^[13,114,172] Demonstrations recorded so far also revealed that the insufficient onset potentials of narrow band gap materials ($E_g < 2$ eV) have limited the operation photocurrent of the cells (see the working potentials in Table 1-4-1). The highest value of STH 3% was achieved by using state-of-the-art Cu_2O and BiVO_4 photoelectrodes,^[114] but employment of these oxide materials tightly limits room for a further increase in their IPCE. Therefore, it is necessary to develop a novel photocathode material which is capable of both a positive onset potential and long absorption edge wavelength. In the next chapter, Cu-chalcopyrite is introduced as promising material system to obtain optimum band edge potentials for use as a photocathode.

Chapter 1. General Introduction

Table 1-4-1. Demonstrations of PEC cells. C/B/A stands for A modified with B and C in the order.

Photocathode (band gap)	Photoanode (band gap)	Initial STH	Electrolyte	Working potential	Stability	Year	Ref.
GaP (2.25 eV)	TiO ₂ (3.0 eV)	0.25%	0.2 M H ₂ SO ₄	N/A	N/A	1976	[163]
GaP (2.25 eV)	SrTiO ₃ (3.8 eV)	0.67%	1 M NaOH	N/A	~100% for 13 h	1977	[164]
NiS/ZnS/CdSe QDs (2.0 eV)	IrO _x /ZnS/CdS QDs (2.46 eV)	0.17%	0.5 M Na ₂ SO ₄ pH 6.8	0.45 V _{RHE}	~70% after 1.5 h	2014	[165]
RuO _x /TiO ₂ /Al:ZnO/ Cu ₂ O (2.0 eV)	Co-Pi/W:BiVO ₄ (2.4 eV)	0.4%	0.5 M Na ₂ SO ₄ + 0.1 M potassium phosphate pH 6	0.5 V _{RHE}	~20% after 1.3 h	2014	[166]
Pt/p-Si (1.1 eV)	FeOOH/Mo:BiVO ₄ (2.4 eV)	0.01%	0.5 M sodium phosphate pH 7	N/A	~100% for 2 h	2014	[168]
Pt/In ₂ S ₃ /CdS/ Cu ₂ ZnSnS ₄ (1.4 eV)	BiVO ₄ (2.4 eV)	0.28%	0.2 M phosphate buffer pH 6.5	0.5 V _{RHE}	~90% after 2 h	2015	[121]
Pt/La ₅ Ti ₂ CuS ₅ O ₇ (1.9 eV)	Co- Pi/La ₅ Ti ₂ CuS ₅ O ₇ (1.9 eV)	N/A	0.1 M Na ₂ SO ₄ pH 12	N/A	~60% after 5 h	2015	[170]
Pt/Al:La ₅ Ti ₂ Cu _{0.9} Ag _{0.1} S ₅ O ₇ (1.8 eV)	Co/BaTaO ₂ N (1.9 eV)	N/A	0.1 M Na ₂ SO ₄ pH 11	0.7 V _{RHE}	~30% after 10 h	2015	[118]
Pt/TiO ₂ /amorphous p-i-n Si (1.7 eV)	NiFeO _x /a-Fe ₂ O ₃ (2.1 eV)	0.91%	0.5 M phosphate buffer pH 11.8	0.7 V _{RHE}	~100% for 10 h	2015	[94]
Pt/CdS/CuGa ₃ Se ₅ /Ag _x Cu _{1-x} GaSe ₂ (x = 6%, 1.7 eV)	NiOOH/FeOOH/ Mo:BiVO ₄ (2.4 eV)	0.67%	0.1 M potassium phosphate pH 7	0.48 V _{RHE}	~100% for 2 h	2016	[173]
Pt/TiO ₂ /Al:La ₅ Ti ₂ Cu _{0.9} Ag _{0.1} S ₅ O ₇ (1.8 eV)	Ir/Co/BaTaO ₂ N (1.9 eV)	0.14%	0.1 M sodium phosphate pH 13	0.7 V _{RHE}	~40% after 6 h	2016	[102]
Pt/Bi ₄ V ₂ O ₁₁ /BiVO ₄ (2.4 eV)	NiOOH/FeOOH/ Bi ₄ V ₂ O ₁₁ /W:BiVO ₄ (2.4 eV)	N/A	0.5 M Na ₂ SO ₄ pH 6.6	N/A	N/A	2017	[171]
RuO _x /TiO ₂ /Ga ₂ O ₃ / Cu ₂ O (2.0 eV)	NiFeO _x /Mo:BiVO ₄ (2.4 eV)	3.00%	0.2 M potassium borate pH 9.0	0.6 V _{RHE}	~90% after 12 h	2018	[114]
Pt/HfO ₂ /CdS/ Cu ₂ ZnSnS ₄ (1.4 eV)	NiFeO _x /BiVO ₄ (2.4 eV)	1.05%	0.2 M sodium phosphate pH 6.5	0.57 V _{RHE}	~90% after 10 h	2018	[172]

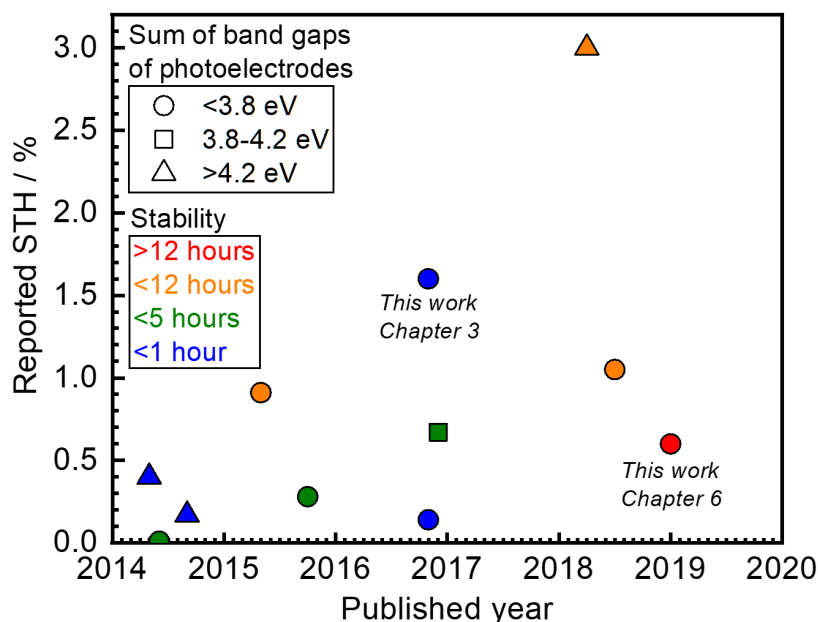


Figure 1-4-6. Reported initial STH values as a function of published year by PEC cells extracted from Table 1-4-1 and this thesis. The color represents the period during which each cell maintained 90% of the initial STH, and the shape corresponds to the sum of band gaps of the photocathode and photoanode materials.

1-5 Cu-Chalcopyrite-Based Photocathodes

1-5-1 Features as Photocathode Materials

CuFeS₂, chalcopyrite, shows a crystal structure as shown in Figure 1-5-1. Its basic structure is equal to the diamond structure and zinc blende structure, but the Cu⁺ and Fe³⁺ are ordered to in the period of two original unit cells. Therefore, the *c*-axis is twice as long as the other axes. This type of crystal is called “chalcopyrite structure” and reported to show direct band gaps thanks to the structure (see also Figure 1-3-5).^[52] Because copper vacancies (V_{Cu}) are the major crystal defects and act as acceptors, Cu-chalcopyrites generally show p-type semiconductor property.^[174]

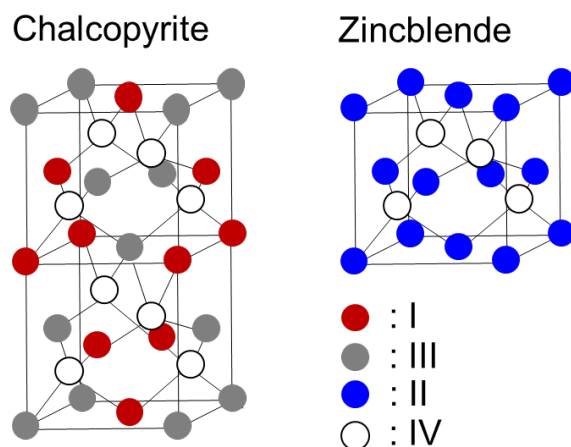


Figure 1-5-1. Crystal structures of chalcopyrite and zinc blende.

An important feature of this crystal is that various kinds of alloys can be prepared with keeping the structure as summarized in Figure 1-5-2.^[175] The band gap energies of $\text{Cu}(\text{Al,Ga,In})(\text{S,Se})_2$ alloys range from 1.0 to 3.5 eV. In the case of Cu-chalcopyrite, the orbitals of CBM are mainly attributed to s orbitals of III element (s) and p orbitals of VI element (s), and those of VBM are d orbitals of Cu and p orbitals of VI element (s). This feature is suitable for engineering of band edge potentials to obtain an optimum semiconductor property for its application.^[137] It should be noted that the contribution of Cu $3d$ orbitals to VBM of sulfide is larger than that of selenide as shown in Figure 1-5-3 (b) and (c).^[62,176,177] In other words, VBM potentials of Cu-III-IV₂ compounds are kept relatively negative due to interaction with Cu $3d$ orbitals. Chen et al. employed first-principle calculations to obtain band edge potentials of various semiconductors including Cu- and Ag-chalcopyrites as shown in Figure 1-5-4.^[132] The VBMs of Cu-chalcopyrites are significantly higher than those of other related materials. They considered that repulsion between Cu $3d$ orbitals and p orbitals of S/Se also contributes to the shallow VBMs of Cu-chalcopyrites.

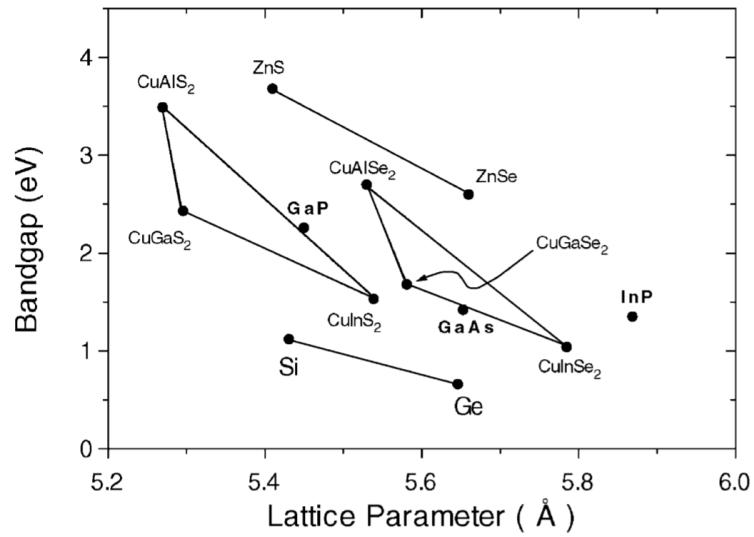


Figure 1-5-2. The relationships between band gaps and lattice constants including alloys of I-III-VI₂ semiconductor materials. Reprinted ref. [175], Copyright 2001, with permission from Elsevier.

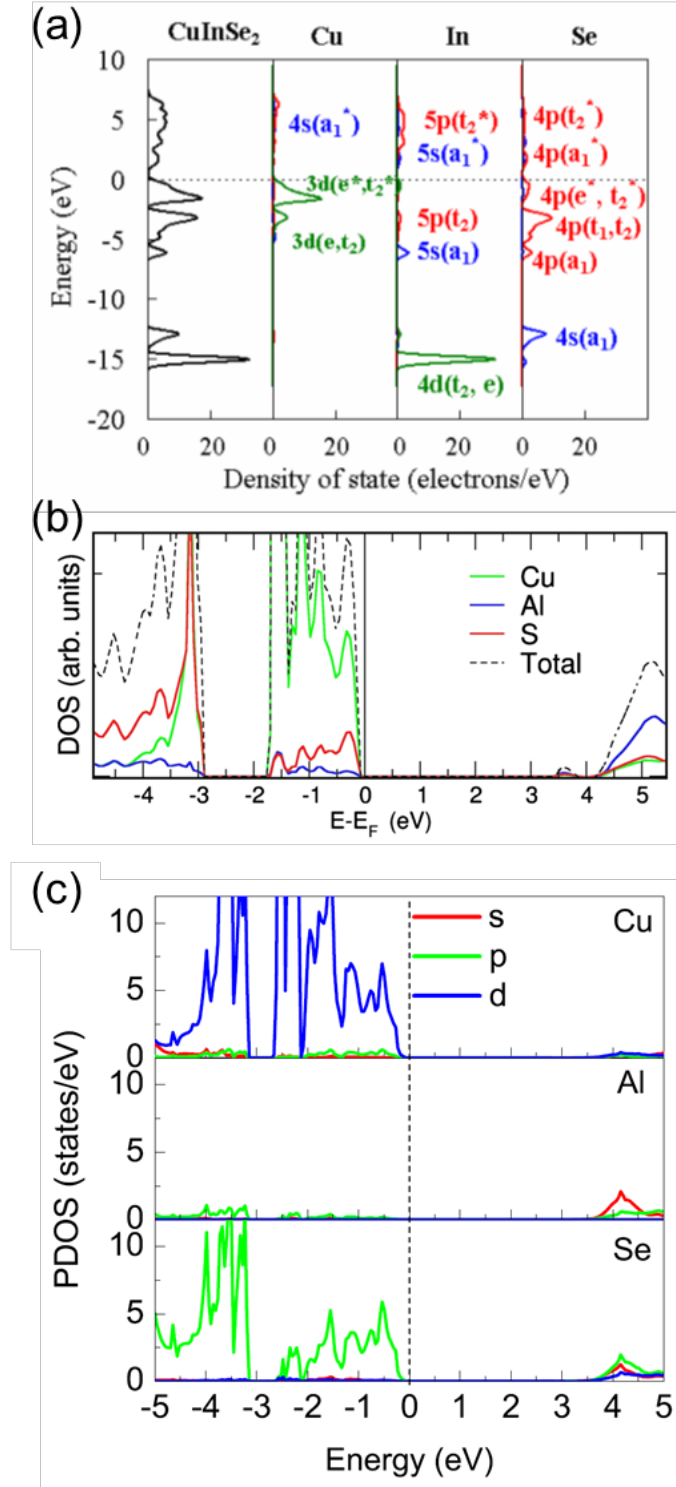


Figure 1-5-3. Distribution of density of states of CuInSe_2 (a), CuAlS_2 (b) and CuAlSe_2 (c). Reprinted with permission of AIP Publishing, Wiley-VCH and IOP Publishing Ltd, from refs. [62, 176, 177], respectively; permission conveyed through Copyright Clearance Center, Inc.

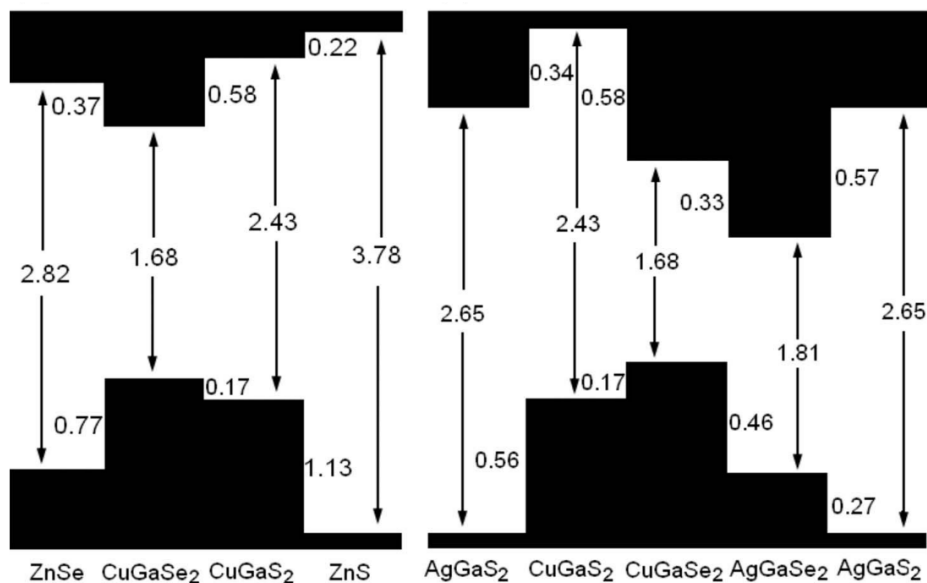


Figure 1-5-4. Calculated offsets in band edge potentials of various I-III-VI₂ and II-VI compounds. Reprinted with permission from ref. [132]. Copyright 2007 by the American Physical Society.

Another notable feature of the Cu-chalcopyrites is that it doesn't require monocrystalline state to obtain a high QE when utilized as PVs and photoelectrodes.^[178,179] The origin of the high QE (i.e. low rate of recombination) is still under discussion, but several reports have suggested that the vicinity of grain boundaries is Cu-rich and produces downward band bending to act as a good electron collection layer,^[180] and that alkali-metals diffused from a glass substrate can contribute to passivation of interfacial defects.^[181] In any cases, the polycrystalline film doesn't require a high temperature or long fabrication time, which makes the material cost-competitive. Consequently, Cu(In,Ga)(S,Se₂)-based solar cells have already been widespread to the market.^[182]

Cu-chalcopyrites have been applied to not only PVs but also photocathodes. Table 1-5-1 summarizes the existing reports on PEC properties of Cu-chalcopyrite-based photocathodes. The first investigation was reported by Valderrama et al.,^[183] who demonstrated PEC HER using a bare Cu(In,Ga)Se₂ photocathode with a band gap energy of 1.1 eV in an acidic electrolyte. Yokoyama et al. investigated effects of pH on the PEC property of Pt-modified Cu(In,Ga)Se₂ photocathodes.^[184] They found that weak-alkaline condition is the optimum electrolyte condition due to the balance

Chapter 1. General Introduction

between the total concentration of H^+ and OH^- , flat-band potential and chemical stability; low pH shifts the flat-band potential to negative vs. RHE, a neutral solution easily forms gradient in concentration and extreme pHs cause corrosion. This dilemma was alleviated by Kumagai et al., who found that employment of a neutral phosphate buffer solution resulted in the significant increase in the photocurrent value at 0 V_{RHE} by four times (5 $mA\ cm^{-2}$ in pH 9.5 Na_2SO_4 to 25 $mA\ cm^{-2}$ in a pH 6.8 phosphate buffer solution).^[145] This is because the buffer solution can keep the H^+ concentration around Pt relatively stable during PEC reaction.

Chapter 1. General Introduction

Table 1-5-1. PEC properties of Cu-chalcopyrite photocathodes. C/B/A stands for A modified with B, and C in the order. The onset potential was defined as the photocurrent density of -0.05 mA cm^{-2} .

Photocathode	Photocurrent at 0 V_{RHE} (light source)	Onset potential	Maximum HC-STH (potential)	Electrolyte	Stability at 0 V_{RHE}	Year	Ref.
Cu(In,Ga)Se ₂	-5 mA cm^{-2} (halogen lamp)	N.A.	N.A.	0.5 M H ₂ SO ₄	Unstable	2005	[183]
Pt/CdS/ Cu(In,Ga)Se ₂	-12 mA cm^{-2} (Xe lamp)	0.6 V_{RHE}	N.A.	0.1 M Na ₂ SO ₄ pH 9.5	Unstable	2010	[184]
Pt/ZnS/CuGa ₃ Se ₅	-4.4 mA cm^{-2} (AM1.5G)	0.4 V_{RHE}	0.25% (0.1 V_{RHE})	0.1 M Na ₂ SO ₄ pH 9.5	25 h (0.1 V_{RHE})	2012	[185]
Pt/CdS/CuGaSe ₂	-7.5 mA cm^{-2} (AM1.5G)	0.7 V_{RHE}	0.83% (0.2 V_{RHE})	0.1 M Na ₂ SO ₄ pH 9	>10 days	2013	[135]
Pt/CdS/Cu-Ga-Se (powder, Ga/Cu=2)	-2.4 mA cm^{-2} (AM1.5D)	0.7 V_{RHE}	N.A.	0.1 M Na ₂ SO ₄ pH 9.5	16 h (0.1 V_{RHE})	2014	[186]
Pt/CdS/ Ag _x Cu _{1-x} GaSe ₂ ($x = 5.9\%$)	-8.1 mA cm^{-2} (AM1.5G)	0.7 V_{RHE}	1.22% (0.3 V_{RHE})	0.1 M Na ₂ SO ₄ pH 9.5	55 h	2014	[187]
Pt/In ₂ S ₃ /CuInS ₂	-15 mA cm^{-2} (AM1.5G)	0.8 V_{RHE}	1.97% (0.28 V_{RHE})	0.1 M Na ₂ SO ₄ pH 9	N.A.	2014	[120]
Pt/TiO ₂ /CdS/ CuInS ₂	-13 mA cm^{-2} (AM1.5G)	0.7 V_{RHE}	1.82 % (0.36 V_{RHE})	0.1 M Na ₂ HPO ₄ pH 10	1 h	2014	[159]
Pt/CdS/CuGa ₃ Se ₅ / Ag _x Cu _{1-x} GaSe ₂ ($x = 6\%$)	-8.8 mA cm^{-2} (AM1.5G)	1.0 V_{RHE}	1.81% (0.36 V_{RHE})	0.1 M Na ₂ HPO ₄ pH 10	20 days	2015	[188]
Pt/Mo/Ti/ Cu(In,Ga)Se ₂	-30 mA cm^{-2} (AM1.5G)	0.7 V_{RHE}	8.5% (0.38 V_{RHE})	0.5 M Na ₂ SO ₄ + 0.5 M sodium phosphate pH 6.8	10 days	2015	[145]

Surface modification with thin n-type layers with the thickness of less than 100 nm has been found to facilitate the charge separation at the semiconductor-electrolyte interface. CdS, ZnS and In₂S₃

Chapter 1. General Introduction

have often been employed as the n-type layers because of the small lattice mismatch, band edge potentials suitable for HER and mild condition to deposit them by CBD method. The first investigation on the surface modification was shown in the report by Yokoyama et al.^[184] The onset potential of the Cu(In,Ga)Se₂ photocathode was raised by 0.3 V and the photocurrent value at 0 V_{RHE} increased by twice after CdS deposition. A further examination including simulation of the band alignment was reported by Moriya et al.^[135] They also found that surface modification of a CuGaSe₂ photocathode with CdS significantly increase the photocurrent value and shift the onset potential as shown in Figure 1-4-2. Furthermore, they calculated the band alignment at the semiconductor-electrolyte interface using the Poisson's equation. The depletion layer depth of the bare CuGaSe₂ at 0 V_{RHE} was estimated to be 250 nm. On the other hand, that of CdS-modified CuGaSe₂ was revealed to show a larger depth of the depletion layer by 70 nm. The enhanced band bending can facilitate charge separation of photoexcited carriers. In addition, the deep VBM potential in the band diagram can block diffusion of photoexcited holes to the surface side, resulting in suppression of charge recombination. Cu(In,Ga)Se₂ photocathodes modified with CdS, a Mo/Ti binary (see section 1-4-2) and Pt (Pt/Mo/Ti/CdS/CIGS) showed a photocurrent value of 30 mA cm⁻² at 0 V_{RHE} under simulated sunlight,^[145] which is the highest value among various photocathodes composed of polycrystalline materials.

The durability of Cu-chalcopyrite-based photocathodes at around 0 V_{RHE} has been reported to be notably high. As shown in table 1-5-1, some of them are able to endure the long-term stability test for the time scale of days. The longest period of stability test was reported by Zhang et al.^[188] As shown in Figure 1-5-5, there was no meaningful decrease in photocurrent observed for 20 days, which is the longest period of PEC HER among photocathodes to the best of the author's knowledge. Hence, the material system can be concluded to be a promising candidate as photocathodes for efficient and durable PEC cells.

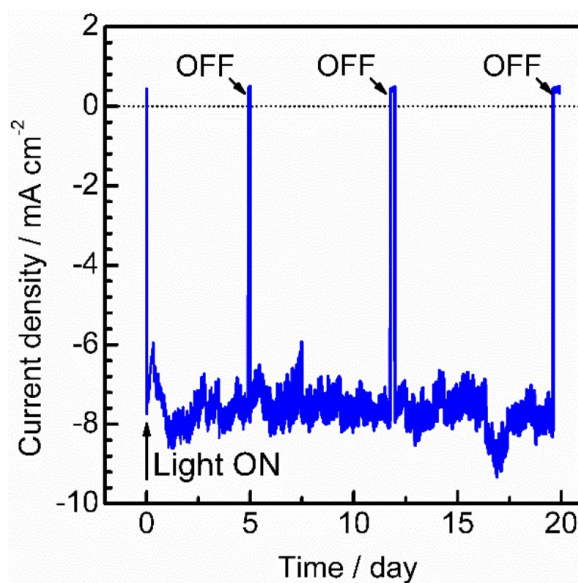


Figure 1-5-5. Current-time curves for $\text{Ag}_x\text{Cu}_{1-x}\text{GaSe}_2$ ($x = 6\%$) photocathodes modified with CuGa_3Se_5 , CdS and Pt at 0 V_{RHE} under irradiation of the Xe lamp. A 0.1 M potassium phosphate buffer solution ($\text{pH } 7$) was used as the electrolyte. Reprinted with permission from ref. [188] - Published by The Royal Society of Chemistry.

1-5-2 Challenges and Motivation for Modifications

However, these reports have also revealed critical challenges concerning their onset potentials and durability at a positive potential. As shown in Table 1-5-1, most photocathodes show onset potentials more negative than $0.8 \text{ V}_{\text{RHE}}$. Exceptionally, the photocathode modified with a 100 nm -thick CuGa_3Se_3 layer on the $\text{Ag}_x\text{Cu}_{1-x}\text{GaSe}_2$ layer showed the onset potential of $1.0 \text{ V}_{\text{RHE}}$,^[188] but the photocurrent value at $0.6\text{--}0.9 \text{ V}_{\text{RHE}}$ is no more than 1 mA cm^{-2} and a severe and less-reproducible deposition condition is often required to fabricate such a multilayer structure. These photocathodes showed maximum HC-STHs at more negative than $0.4 \text{ V}_{\text{RHE}}$ due to the insufficient onset potentials. Considering reduction and oxidation potentials of water, a plausible working potential of a PEC cell without external bias voltage is expected to be around $0.6 \text{ V}_{\text{RHE}}$. Therefore, it is highly necessary to modify the Cu-chalcopyrite material to shift the onset potential to more positive.

Chapter 1. General Introduction

Because the Fermi level of p-type semiconductor is located in the vicinity of VBM, modification of VBM potential can control the flat-band potential (i.e. onset potential). As mentioned above, existence of Cu 3*d* orbitals are the main reason for the shallow VBM potential of Cu-chalcopyrite materials. Substitution of Cu to Ag has already been investigated by the author to obtain a deep VBM.^[137] However, Ag-chalcopyrite materials were found to be unsuitable as photocathodes due to the difficulty in obtaining p-type semiconductor, although a considerable shift in the onset potential was observed as expected. Decreasing the fraction of Cu to form ordered-defect chalcopyrites such as CuGa₃Se₅ has also been investigated by Kim et al, and they reported that a CuGa₃Se₅ showed a deeper VBM potential than CuGaSe₂ due to the decreased influence of Cu 3*d* orbitals onto the VBM.^[189] Moreover, the photocathode showed cathodic photoresponses up to 1.1 V_{RHE}. Unfortunately, the disadvantage of CuGa₃Se₅ is the small grain size. Further modification of deposition condition has been required when it is fabricated.^[185]

Another means to modify the VBM potential is alloying it with II-VI compounds such as ZnSe. As shown in Figure 1-5-4, ZnSe shows much deeper VBM potential than CuGaSe₂ by 0.8 eV. There has been no report on the PEC property of a Cu-chalcopyrite materials alloyed with II-VI compounds, so it can be said that there is a strong motivation to investigate the preparation of the alloyed compounds. In addition, substitution of group III elements with Zn is a promising technology because it can reduce the consumption of rare metals, In and Ga.

As noted, the working potential of a PEC cell will be around 0.6 V_{RHE}. Unfortunately, the photocathodes based on Cu-chalcopyrite materials have been reported to show poor durability at the potential. Figure 1-5-6 shows a time course of photocurrent for the Cu(In,Ga)Se₂-based photocathode at various applied potentials.^[145] The decrease in the photocurrent became clearer with the increase of applied potentials. This kind of degradation is attributed to oxidative corrosion of surface sulfides (for example, $\text{CdS} + 2\text{h}^+ \rightarrow \text{Cd}^{2+} + \text{S}$) accompanied with detachment HER catalysts.^[190] As introduced in the section 1-4-2, surface coating with an oxide material has

commonly been employed for stabilization. However, conventional oxide materials require heat treatment to stabilize itself, which not only forms pinholes but also influences the underlying sulfides and selenides.^[70,158] This dilemma in modification process has caused the difficulty in the protection of Cu-chalcopyrite-based photocathodes. Hence, a novel technique for deposition of a protection layer in a mild and conformal way, which is suitable for non-oxide photoelectrodes, should be developed.

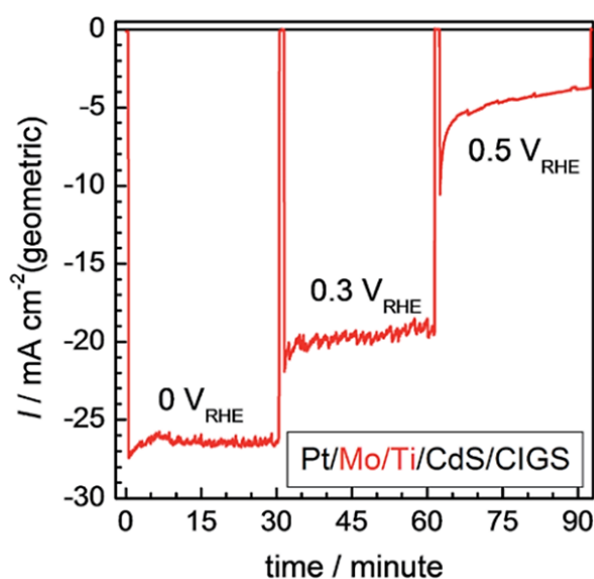


Figure 1-5-6. Current-time curves for the Pt/Mo/Ti/CdS/Cu(In,Ga)Se₂ photocathode at various potentials under simulated sunlight. A 0.5 M Na₂SO₄ + 0.5 M sodium phosphate buffer solution (pH 6.8) was used as the electrolyte. Reprinted with permission from ref. [145] - Published by The Royal Society of Chemistry.

1-6 Objectives of This Thesis

As described in the previous section, the conventional photocathodes have shown insufficient onset potentials, photocurrent values and durability at the expected working potential of PEC cells. Considering the background, the objectives of this thesis are set to development of an NIR-responsive

Chapter 1. General Introduction

photocathode having an onset potential of higher than 0.8 V_{RHE} (**Chapters 2-4**) and sufficient durability for >10 h at 0.6 V_{RHE} (**Chapter 5**), including demonstration of overall water splitting using the PEC cell composing of the novel photocathode in conjunction with control of catalyst poisoning (**Chapter 6**).

In **Chapter 1**, the social and global background, the needs of energy conversion system from sunlight to hydrogen gas, and the potential of Cu-chalcopyrite-based photocathodes were described. A PEC cell is a promising candidate as solar-to-hydrogen conversion system thanks to its simplicity and expected efficiency. Cu-chalcopyrite materials have been expected to be a suitable photocathode material because of usability in a polycrystalline state, stable semiconductor property and easiness in band position engineering. However, they have been suffering from the insufficient onset potential and poor durability.

In **Chapter 2**, composition modification of $\text{Cu}(\text{In,Ga})\text{Se}_2$ by alloying with ZnSe was investigated so as to obtain an optimum VBM potential and onset potential. As discussed in section 1-5-1, ZnSe shows a deeper VBM potential than CuGaSe_2 (as well as CuInSe_2) by 0.8 eV due to absence of Cu 3d orbitals. Hence, partial substitution with ZnSe was expected to deepen the VBM potential of $\text{Cu}(\text{In,Ga})\text{Se}_2$. Co-evaporation in a high vacuum chamber was employed to fabricate $(\text{ZnSe})_x(\text{Cu}(\text{In,Ga})\text{Se}_2)_{1-x}$ thin films. Consequently, $(\text{ZnSe})_{0.85}(\text{Cu}(\text{In,Ga})\text{Se}_2)_{0.15}$ (abbreviated as $(\text{ZnSe})_{0.85}(\text{CIGS})_{0.15}$ herein) was found to show a deeper VBM potential than $\text{Cu}(\text{In,Ga})\text{Se}_2$ by 0.17 eV, resulting in successful achievement of the onset potential of 0.89 V_{RHE} , while it exhibits a relatively narrow band gap of 1.4 eV. This onset potential is the most positive among those obtained by Cu-chalcopyrite-based photocathodes responsive to NIR light.

In **Chapter 3**, assessment and improvement of charge separation efficiency of the $(\text{ZnSe})_{0.85}(\text{CIGS})_{0.15}$ photocathodes were investigated. For the sake of visualization of active area for charge separation in cross-section, a modified electron-beam-induced current mapping was newly developed and applied to the photocathodes. The measurement succeeded in visualization of the

Chapter 1. General Introduction

active area and revealed that creation of the composition gradient in In and Ga forms a preferable distribution of the area. A PEC cell composed of the $(\text{ZnSe})_{0.85}(\text{CIGS})_{0.15}$ photocathode and BiVO_4 photoanode showed an STH of 1.6%, which was the highest value among reported at that time.

In **Chapter 4**, effects of substrates for the $(\text{ZnSe})_{0.85}(\text{CIGS})_{0.15}$ photocathodes onto their PEC properties were investigated. $(\text{ZnSe})_{0.85}(\text{CIGS})_{0.15}$ was also found to require Na species in the substrate for expression of strong p-type property as reported in $\text{Cu}(\text{In,Ga})\text{Se}_2$ -based solar cells. On receiving the result, a flexible $(\text{ZnSe})_{0.85}(\text{CIGS})_{0.15}$ photocathode was successfully fabricated on a Ti-foil deposited with a nanolayer of soda-lime glass. Because the photocathode can be readily handled and manipulated, it was realized to fabricate a PEC cell consisting of comb-shaped photocathodes and photoanodes with the width of less than 1 mm. The performance of the PEC cell was expected not to decrease with increasing the size, and the cell showed a STH of 1.0% without stirring the electrolyte solution, which can contribute to development of a practical PEC cell.

In **Chapter 5**, stabilization of the $(\text{ZnSe})_{0.85}(\text{CIGS})_{0.15}$ photocathodes was investigated through the development of novel surface coating. The photocathodes showed insufficient durability especially at positive potentials such as 0.6 V_{RHE} due to corrosion of the photocathode surface as pointed out in **Chapter 1**. In this chapter, a RuO_2 nanolayer was employed as a multi-functional modifier: a protective layer, an HER catalyst and a surface conductor. The RuO_2 , which is a stable oxide material, itself can provide active sites for HER, and act as a good mediator for electrons. Therefore, no additional deposition of HER catalyst or a conductive layer was required. Moreover, PEC deposition of RuO_2 via a RuO_4^- precursor could deposit a conformal and pinhole-free RuO_2 layer without applying a heat treatment which can damage to the underlying layers. The RuO_2 -coated $(\text{ZnSe})_{0.85}(\text{CIGS})_{0.15}$ photocathode showed a high durability at 0.6 V_{RHE} in not only a neutral condition but also a strong alkaline electrolyte. Hence, the newly developed photocathode can be employed in combinations with various kinds of PEC cells.

Chapter 1. General Introduction

In **Chapter 6**, a PEC cell consisting of the RuO₂-coated (ZnSe)_{0.85}(CIGS)_{0.15} photocathode and a BiVO₄ photoanode was constructed and investigated in detail. Because both photoelectrodes showed high durability in a three-electrode cell, the PEC cell was also expected to show the high durability. However, the PEC cell showed a clear decrease in photocurrent within 1 h, and surface analyses revealed that a severe catalyst poisoning occurred on the photocathode due to deposition of Bi species, which eluted from the photoanode. This discovery called on the needs to develop a technique to suppress the surface poisoning. Firstly, coating of the photoanode surface with an anion-conductive ionomer was found to prevent Bi³⁺ species to elute into the bulk electrolyte. Secondly, dispersing a chelating resin beads into the electrolyte was also found to adsorb the eluted metal cations effectively. These two techniques realized a stable overall water splitting over the PEC cell for hours.

In **Chapter 7**, the results described in Chapters 2-6 were summarized, and the contributions and meanings of the thesis for the research field of PEC water splitting were discussed in conjunction with future prospects concerning the system.

References

- [1] BP, *Statistical Review of World Energy 2017*; 2017.
- [2] H. Ritchie, M. Roser, CO₂ and other Greenhouse Gas Emissions. *OurWorldInData.org* **2018**.
- [3] T. F. Stocker, D. Qin, G.-K. Plattner, M. Tignor, J. B. S.K. Allen, A. Nauels, Y. Xia, V. Bex, P. M. Midgley, *Climate Change 2013: The Physical Science Basis. Contribution of Working Group I to the Fifth Assessment Report of the Intergovernmental Panel on Climate Change*; 2013.
- [4] M. Weiss, M. Neelis, K. Blok, M. Patel, *Clim. Change* **2009**, 95, 369.
- [5] *IEA Key world energy statistics 2016*; International Energy Agency, 2016.
- [6] Y. Qin, X. Wang, *Biotechnology J.* **2010**, 5, 1164.

- [7] M. Brodin, M. Vallejos, M. T. Opedal, M. C. Area, G. Chinga-Carrasco, *J. Clean. Prod.* **2017**, *162*, 646.
- [8] A. Soroudi, I. Jakubowicz, *Eur. Polym. J.* **2013**, *49*, 2839.
- [9] M. Loster, Total Primary Energy Supply — From Sunlight.
http://www.ez2c.de/ml/solar_land_area/ **2010**.
- [10] I. Colak, E. Hossain, R. Bayindir, J. Hossain, *2016 IEEE Int. Power Electron. Motion Control Conf.* **2016**, 372.
- [11] L. Trevisani, M. Fabbri, F. Negrini, *Fuel Process. Technol.* **2006**, *87*, 157.
- [12] S. Clegg, P. Mancarella, *IEEE Trans. Sustain. Energy* **2015**, *6*, 1234.
- [13] J. W. Ager, M. R. Shaner, K. A. Walczak, I. D. Sharp, S. Ardo, *Energy Environ. Sci.* **2015**, *8*, 2811.
- [14] H. Döscher, J. L. Young, J. F. Geisz, J. A. Turner, T. G. Deutsch, *Energy Environ. Sci.* **2016**, *9*, 74.
- [15] R. Mohtadi, S. Orimo, *Nat. Rev. Mater.* **2016**, *2*, 16091.
- [16] A. Keyhani, *Design of Smart Power Grid Renewable Energy Systems*; 1st ed.; Wiley-IEEE Press, 2011.
- [17] W. Shockley, H. J. Queisser, *J. Appl. Phys.* **1961**, *32*, 510.
- [18] C. R. Cox, J. Z. Lee, D. G. Nocera, T. Buonassisi, *Proc. Natl. Acad. Sci.* **2014**, *111*, 14057.
- [19] J. T. Jacobsson, *Energy Environ. Sci.* **2018**, *11*, 1977.
- [20] C. A. Rodriguez, M. A. Modestino, D. Psaltis, C. Moser, *Energy Environ. Sci.* **2014**, *7*, 3828.
- [21] B. A. Pinaud, J. D. Benck, L. C. Seitz, A. J. Forman, Z. Chen, T. G. Deutsch, B. D. James, K. N. Baum, G. N. Baum, S. Ardo, H. Wang, E. Miller, T. F. Jaramillo, *Energy Environ. Sci.* **2013**, *6*, 1983.
- [22] C. Wadia, A. P. Alivisatos, D. M. Kammen, *Environ. Sci. Technol.* **2009**, *43*, 2072.
- [23] K. Sivula, *J. Phys. Chem. Lett.* **2015**, *6*, 975.

- [24] T. Hisatomi, T. Yamamoto, Q. Wang, T. Nakanishi, T. Higashi, M. Katayama, T. Minegishi, K. Domen, *Catal. Sci. Technol.* **2018**, 8, 3918.
- [25] Y. Goto, T. Hisatomi, Q. Wang, T. Takata, T. Yamada, K. Domen, T. Higashi, K. Ishikiriya, T. Maeda, Y. Sakata, S. Okunaka, H. Tokudome, M. Katayama, S. Akiyama, H. Nishiyama, Y. Inoue, T. Takewaki, T. Setoyama, T. Minegishi, *Joule* **2017**, 2, 1.
- [26] A. Xiong, G. Ma, K. Maeda, T. Takata, T. Hisatomi, T. Setoyama, J. Kubotaa, K. Domen, *Catal. Sci. Technol.* **2014**, 4, 325.
- [27] K. Domen, A. Kudo, T. Onishi, N. Kosugi, H. Kuroda, *J. Phys. Chem.* **1986**, 90, 292.
- [28] G. N. Schrauzer, T. D. Guth, *J. Am. Chem. Soc.* **1977**, 99, 7189.
- [29] K. Maeda, T. Takata, M. Hara, N. Saito, Y. Inoue, H. Kobayashi, K. Domen, *J. Am. Chem. Soc.* **2005**, 127, 8286.
- [30] K. Maeda, K. Teramura, D. Lu, T. Takata, N. Saito, Y. Inoue, K. Domen, *Nature* **2006**, 440, 295.
- [31] K. Maeda, D. Lu, K. Domen, *Chem. Eur. J.* **2013**, 19, 4986.
- [32] C. Pan, T. Takata, M. Nakabayashi, T. Matsumoto, N. Shibata, Y. Ikuhara, K. Domen, *Angew. Chemie Int. Ed.* **2015**, 54, 2955.
- [33] J. Li, N. Wu, *Catal. Sci. Technol.* **2015**, 5, 1360.
- [34] Q. Wang, T. Hisatomi, M. Katayama, T. Takata, T. Minegishi, A. Kudo, T. Yamada, K. Domen, *Faraday Discuss.* **2017**, 197, 491.
- [35] H. Suzuki, S. Nitta, O. Tomita, M. Higashi, R. Abe, *ACS Catal.* **2017**, 7, 4336.
- [36] K. Maeda, R. Abe, K. Domen, *J. Phys. Chem. C* **2011**, 115, 3057.
- [37] Q. Wang, T. Hisatomi, Q. Jia, H. Tokudome, M. Zhong, C. Wang, Z. Pan, T. Takata, M. Nakabayashi, N. Shibata, Y. Li, I. D. Sharp, A. Kudo, T. Yamada, K. Domen, *Nat. Mater.* **2016**.

Chapter 1. General Introduction

- [38] Q. Wang, T. Hisatomi, Y. Suzuki, Z. Pan, J. Seo, M. Katayama, T. Minegishi, H. Nishiyama, T. Takata, K. Seki, A. Kudo, T. Yamada, K. Domen, *J. Am. Chem. Soc.* **2017**, *139*, 1675.
- [39] N. W. Ockwig, T. M. Nenoff, *Chem. Rev.* **2007**, *107*, 4078.
- [40] T. Hisatomi, J. Kubota, K. Domen, *Chem. Soc. Rev.* **2014**, *43*, 7520.
- [41] Y. Chen, X. Feng, M. Liu, J. Su, S. Shen, *Nanophotonics* **2016**, *5*, 524.
- [42] M. G. Walter, E. L. Warren, J. R. McKone, S. W. Boettcher, Q. Mi, E. A. Santori, N. S. Lewis, *Chem. Rev.* **2010**, *110*, 6446.
- [43] M. Grätzel, *Nature* **2001**, *414*, 338.
- [44] B. O. Hansen, B. Seger, P. C. K. Vesborg, I. Chorkendorff, *Science* **2015**, *350*, 1030.
- [45] F. F. Abdi, S. P. Berglund, *J. Phys. D Appl. Phys* **2017**, *50*, 193002.
- [46] H. Kaneko, T. Minegishi, K. Domen, *Chem. Eur. J.* **2018**, *24*, 5697.
- [47] C. Ding, J. Shi, Z. Wang, C. Li, *ACS Catal.* **2017**, *7*, 675.
- [48] T. Yao, H. Han, J. Q. Chen, C. Li, *Adv. Energy Mater.* **2018**, *8*, 1800210.
- [49] R. Liu, Z. Zheng, J. Spurgeon, X. Yang, *Energy Environ. Sci.* **2014**, *7*, 2504.
- [50] P. A. Cox, *The electronic Structure and Chemistry of Solids*; Oxford University Press, 1987.
- [51] D. Huang, C. Persson, Z. Ju, M. Dou, C. Yao, J. Guo, *EPL* **2014**, *105*, 37007.
- [52] R. Memming, *Semiconductor Electrochemistry*; 1st ed.; Wiley-Vch, 2001.
- [53] Y. Nakato, *Denki Kagaku*; 1st ed.; Tokyo Kagaku Dojin, 2016.
- [54] D. Wang, G. Cao, *Nanomaterials for Energy Conversion and Storage*; 1st ed.; World Scientific, 2018.
- [55] P. Cendula, S. D. Tilley, S. Gimenez, J. Bisquert, M. Schmid, M. Grätzel, J. O. Schumacher, M. Gra, *J. Phys. Chem. C* **2014**, *118*, 29599.
- [56] A. T. Barrows, R. Masters, A. J. Pearson, C. Rodenburg, D. G. Lidzey, *Sol. Energy Mater. Sol. Cells* **2016**, *144*, 600.
- [57] Y. Yamada, Y. Yamaji, M. Imada, *Phys. Rev. Lett.* **2015**, *115*, 197701.

Chapter 1. General Introduction

- [58] NREL, 2000 ASTM Standard Extraterrestrial Spectrum Reference E-490-00.
<https://www.nrel.gov/grid/solar-resource/spectra-astm-e490.html>.
- [59] T. Hisatomi, T. Minegishi, K. Domen, *Bull. Chem. Soc. Jpn.* **2012**, 85, 647.
- [60] J. Bekaert, R. Saniz, B. Partoens, D. Lamoen, *Phys. Chem. Chem. Phys.* **2014**, 16, 22299.
- [61] S. Ishizuka, H. Shibata, A. Yamada, P. Fons, K. Sakurai, K. Matsubara, S. Niki, M. Yonemura, H. Nakanishi, *J. Appl. Phys.* **2006**, 100, 98.
- [62] L. M. Liborio, C. L. Bailey, G. Mallia, S. Tomić, N. M. Harrison, *J. Appl. Phys.* **2011**, 109, 023519.
- [63] D. A. R. Barkhouse, O. Gunawan, T. Gokmen, T. K. Todorov, D. B. Mitzi, *Prog. Photovoltaics Res. Appl.* **2012**, 20, 6.
- [64] T. Nishimura, S. Toki, H. Sugiura, K. Nakada, A. Yamada, *Appl. Phys. Express* **2016**, 9, 092301.
- [65] W. A. Smith, I. D. Sharp, N. C. Strandwitz, J. Bisquert, *Energy Environ. Sci.* **2015**, 8, 2851.
- [66] X. An, T. Li, B. Wen, J. Tang, Z. Hu, L.-M. Liu, J. Qu, C. P. Huang, H. Liu, *Adv. Energy Mater.* **2016**, 6, 1502268.
- [67] X. Chen, Y. Li, S. Shen, *J. Phys. D. Appl. Phys.* **2018**, 51, 163002.
- [68] C. Du, M. Zhang, J. Jang, Y. Liu, G. Liu, D. Wang, *J. Phys. Chem. C* **2014**, 118, 17054.
- [69] X. Yang, C. Du, R. Liu, J. Xie, D. Wang, *J. Catal.* **2013**, 304, 86.
- [70] L. Kavan, L. Steier, M. Grätzel, *J. Phys. Chem. C* **2017**, 121, 342.
- [71] P. S. Bassi, R. P. Antony, P. P. Boix, Y. Fang, J. Barber, L. H. Wong, *Nano Energy* **2016**, 22, 310.
- [72] E. S. Kim, N. Nishimura, G. Magesh, J. Y. Kim, J. W. Jang, H. Jun, J. Kubota, K. Domen, J. S. Lee, *J. Am. Chem. Soc.* **2013**, 135, 5375.
- [73] R. van de Krol, A. Goossens, J. Schoonman, *J. Electrochem. Soc.* **1997**, 144, 1723.
- [74] T. Shinagawa, M. T.-K. Ng, K. Takanabe, *ChemSusChem* **2017**, 10, 4155.

Chapter 1. General Introduction

- [75] M. A. Modestino, S. M. H. Hashemi, S. Haussener, *Energy Environ. Sci.* **2016**, 9, 1533.
- [76] T. Watanabe, *Denki Kagaku*; Maruzen Publishing Co., Ltd., 2009.
- [77] M. R. Singh, C. Xiang, N. Lewis, *Sustain. Energy Fuels* **2017**, 1, 458.
- [78] S. Hu, N. S. Lewis, J. W. Ager, J. Yang, J. R. McKone, N. C. Strandwitz, *J. Phys. Chem. C* **2015**, 119, 24201.
- [79] Y. Tang, X. Hu, C. Liu, *Phys. Chem. Chem. Phys.* **2014**, 16, 25321.
- [80] Y. Yang, Y. Ling, G. Wang, T. Liu, F. Wang, T. Zhai, Y. Tong, Y. Li, *Nano Lett.* **2015**, 15, 7051.
- [81] Y. Kuang, T. Yamada, K. Domen, *Joule* **2017**, 1, 290.
- [82] D. Kang, T. W. Kim, S. R. Kubota, A. C. Cardiel, H. G. Cha, K.-S. Choi, *Chem. Rev.* **2015**, 115, 12839.
- [83] Y. Lin, G. Yuan, S. Sheehan, S. Zhou, D. Wang, *Energy Environ. Sci.* **2011**, 4, 4862.
- [84] M. D. Bhatt, J. S. Lee, *J. Mater. Chem. A* **2015**, 3, 10632.
- [85] Z. Li, W. Luo, M. Zhang, J. Feng, Z. Zou, *Energy Environ. Sci.* **2013**, 6, 347.
- [86] A. Fujishima, K. Honda, *Nature* **1972**, 238, 37.
- [87] K. Ding, B. Chen, Z. Fang, Y. Zhang, Z. Chen, A. Manuscript, *Phys. Chem. Chem. Phys.* **2014**, 16, 13465.
- [88] Y. Kuang, Q. Jia, G. Ma, T. Hisatomi, T. Minegishi, H. Nishiyama, M. Nakabayashi, N. Shibata, T. Yamada, A. Kudo, K. Domen, *Nat. Energy* **2016**, 2, 16191.
- [89] M. Zhong, T. Hisatomi, T. Minegishi, H. Nishiyama, M. Katayama, T. Yamada, K. Domen, *J. Mater. Chem. A* **2016**, 4, 9858.
- [90] T. W. Kim, K.-S. Choi, *Science* **2014**, 343, 990.
- [91] W. Zhang, D. Yan, J. Li, Q. Wu, J. Cen, L. Zhang, A. Orlov, H. Xin, J. Tao, M. Liu, *Chem. Mater.* **2018**, 30, 1677.

- [92] Y. Kuang, Q. Jia, H. Nishiyama, T. Yamada, A. Kudo, K. Domen, *Adv. Energy Mater.* **2016**, 6, 1501645.
- [93] Y. Pihosh, I. Turkevych, K. Mawatari, J. Uemura, Y. Kazoe, S. Kosar, K. Makita, T. Sugaya, T. Matsui, D. Fujita, M. Tosa, M. Kondo, T. Kitamori, *Sci. Rep.* **2015**, 5, 11141.
- [94] J.-W. Jang, C. Du, Y. Ye, Y. Lin, X. Yao, J. Thorne, E. Liu, G. McMahon, J. Zhu, A. Javey, J. Guo, D. Wang, *Nat. Commun.* **2015**, 6, 7447.
- [95] K. G. Upul Wijayantha, S. Saremi-Yarahmadi, L. M. Peter, *Phys. Chem. Chem. Phys.* **2011**, 13, 5264.
- [96] C. Du, X. Yang, M. T. Mayer, H. Hoyt, J. Xie, G. McMahon, G. Bischooping, D. Wang, *Angew. Chemie - Int. Ed.* **2013**, 52, 12692.
- [97] X. Yang, R. Liu, C. Du, P. Dai, Z. Zheng, D. Wang, *ACS Appl. Mater. Interfaces* **2014**, 6, 12005.
- [98] O. Zandi, A. R. Schon, H. Hajibabaei, T. W. Hamann, *Chem. Mater.* **2015**, 29, 7760.
- [99] J. Seo, H. Nishiyama, T. Yamada, K. Domen, *Angew. Chemie Int. Ed.* **2018**, 57, 2.
- [100] J. Seo, Y. Moriya, M. Kodera, T. Hisatomi, T. Minegishi, M. Katayama, K. Domen, *Chem. Mater.* **2016**, 28, 6869.
- [101] K. Ueda, T. Minegishi, J. Clune, M. Nakabayashi, T. Hisatomi, H. Nishiyama, M. Katayama, N. Shibata, J. Kubota, T. Yamada, K. Domen, *J. Am. Chem. Soc.* **2015**, 137, 2227.
- [102] T. Higashi, Y. Shinohara, A. Ohnishi, J. Liu, K. Ueda, S. Okamura, T. Hisatomi, M. Katayama, H. Nishiyama, T. Yamada, T. Minegishi, K. Domen, *ChemPhotoChem* **2017**, 1, 167.
- [103] M. Kodera, H. Urabe, M. Katayama, T. Hisatomi, T. Minegishi, K. Domen, *J. Mater. Chem. A* **2016**, 4, 7658.
- [104] M. Zhong, T. Hisatomi, Y. Sasaki, S. Suzuki, K. Teshima, M. Nakabayashi, N. Shibata, H. Nishiyama, M. Katayama, T. Yamada, K. Domen, *Angew. Chemie Int. Ed.* **2017**, 56, 4739.

Chapter 1. General Introduction

- [105] Y. Li, T. Takata, D. Cha, K. Takanabe, T. Minegishi, J. Kubota, K. Domen, *Adv. Mater.* **2013**, 25, 125.
- [106] N. Y. Labrador, X. Li, Y. Liu, H. Tan, R. Wang, J. T. Koberstein, T. P. Moffat, D. V. Esposito, *Nano Lett.* **2016**, 16, 6452.
- [107] L. Ji, M. D. McDaniel, S. Wang, A. B. Posadas, X. Li, H. Huang, J. C. Lee, A. A. Demkov, A. J. Bard, J. G. Ekerdt, E. T. Yu, *Nat. Nanotechnol.* **2015**, 10, 84.
- [108] R. Fan, C. Tang, Y. Xin, X. Su, X. Wang, M. Shen, *Appl. Phys. Lett.* **2016**, 109, 233901.
- [109] D. V Esposito, I. Levin, T. P. Moffat, A. A. Talin, *Nat. Mater.* **2013**, 12, 562.
- [110] M. H. Lee, K. Takei, J. Zhang, R. Kapadia, M. Zheng, Y. Z. Chen, J. Nah, T. S. Matthews, Y. L. Chueh, J. W. Ager, A. Javey, *Angew. Chemie - Int. Ed.* **2012**, 51, 10760.
- [111] Y. Lin, R. Kapadia, J. Yang, M. Zheng, K. Chen, M. Hettick, X. Yin, C. Battaglia, I. D. Sharp, J. W. Ager, A. Javey, *J. Phys. Chem. C* **2015**, 119, 2308.
- [112] O. Khaselev, J. A. Turner, *Science* **2013**, 425.
- [113] M. Hettick, M. Zheng, Y. Lin, C. M. Sutter-Fella, J. W. Ager, A. Javey, *J. Phys. Chem. Lett.* **2015**, 6, 2177.
- [114] L. Pan, J. H. Kim, M. T. Mayer, M.-K. Son, A. Ummadisingu, J. S. Lee, A. Hagfeldt, J. Luo, M. Grätzel, *Nat. Catal.* **2018**, 1, 412.
- [115] J. Luo, L. Steier, M.-K. Son, M. Schreier, M. T. Mayer, M. Grätzel, *Nano Lett.* **2016**, 16, 1848.
- [116] C. Li, T. Hisatomi, O. Watanabe, M. Nakabayashi, N. Shibata, K. Domen, J.-J. Delaunay, *Appl. Phys. Lett.* **2016**, 109, 033902.
- [117] C. G. Morales-Guio, S. D. Tilley, H. Vrubel, M. Grätzel, X. Hu, *Nat. Commun.* **2014**, 5, 3059.
- [118] T. Hisatomi, S. Okamura, J. Liu, Y. Shinohara, K. Ueda, T. Higashi, M. Katayama, T. Minegishi, K. Domen, *Energy Environ. Sci.* **2015**, 8, 3354.

Chapter 1. General Introduction

- [119] J. Liu, T. Hisatomi, G. Ma, A. Iwanaga, T. Minegishi, Y. Moriya, M. Katayama, J. Kubota, K. Domen, *Energy Environ. Sci.* **2014**, 7, 2239.
- [120] Gunawan, W. Septina, S. Ikeda, T. Harada, T. Minegishi, K. Domen, M. Matsumura, *Chem. Commun.* **2014**, 50, 8941.
- [121] F. Jiang, Gunawan, T. Harada, Y. Kuang, T. Minegishi, K. Domen, S. Ikeda, *J. Am. Chem. Soc.* **2015**, 137, 13691.
- [122] S. Huang, W. Luo, Z. Zou, *J. Phys. D. Appl. Phys.* **2013**, 46, 235108.
- [123] D. Yokoyama, T. Minegishi, K. Jimbo, T. Hisatomi, G. Ma, M. Katayama, J. Kubota, H. Katagiri, K. Domen, *Appl. Phys. Express* **2010**, 3, 101202.
- [124] I. A. Digdaya, L. Han, T. Buijs, M. Zeman, B. Dam, A. H. M. Smets, W. Smith, *Energy Environ. Sci.* **2015**, 8, 1585.
- [125] Y. Lin, C. Battaglia, M. Boccard, M. Hettick, Z. Yu, C. Ballif, J. W. Ager, A. Javey, *Nano Lett.* **2013**, 13, 5615.
- [126] W. Qin, N. Wang, T. Yao, S. Wang, H. Wang, Y. Cao, S. Liu, C. Li, *ChemSusChem* **2015**, 8, 3987.
- [127] Y. J. Jang, Y. B. Park, H. E. Kim, Y. H. Choi, S. H. Choi, J. S. Lee, *Chem. Mater.* **2016**, 28, 6054.
- [128] J. Su, T. Minegishi, K. Domen, *J. Mater. Chem. A* **2017**, 5, 13154.
- [129] A. Kudo, Y. Miseki, *Chem. Soc. Rev.* **2009**, 38, 253.
- [130] G. Ma, J. Liu, T. Hisatomi, T. Minegishi, Y. Moriya, M. Iwase, H. Nishiyama, M. Katayama, T. Yamada, K. Domen, *Chem. Commun.* **2015**, 51, 4302.
- [131] Y. Li, S. Luo, Z. Wei, D. Meng, M. Ding, C. Liu, *Phys. Chem. Chem. Phys.* **2014**, 16, 4361.
- [132] S. Chen, X. G. Gong, S. H. Wei, *Phys. Rev. B* **2007**, 75, 205209.
- [133] S.-H. Wei, A. Zunger, *J. Appl. Phys.* **1995**, 78, 3846.

- [134] L. Gao, Y. Cui, R. H. J. Vervuurt, D. van Dam, R. P. J. van Veldhoven, J. P. Hofmann, A. A. Bol, J. E. M. Haverkort, P. H. L. Notten, E. P. A. M. Bakkers, E. J. M. Hensen, *Adv. Funct. Mater.* **2015**, 26, 679.
- [135] M. Moriya, T. Minegishi, H. Kumagai, M. Katayama, J. Kubota, K. Domen, *J. Am. Chem. Soc.* **2013**, 135, 3733.
- [136] Y. Lin, Y. Xu, M. T. Mayer, Z. I. Simpson, G. McMahon, S. Zhou, D. Wang, *J. Am. Chem. Soc.* **2012**, 134, 5508.
- [137] H. Kaneko, T. Minegishi, K. Domen, *Coatings* **2015**, 5, 293.
- [138] Y. Chen, Z. Qin, T. Chen, J. Su, X. Feng, M. Liu, *RSC Adv.* **2016**, 6, 58409.
- [139] L. Rovelli, S. D. Tilley, K. Sivula, *ACS Appl. Mater. Interfaces* **2013**, 5, 8018.
- [140] C. Li, T. Hisatomi, O. Watanabe, M. Nakabayashi, N. Shibata, K. Domen, J.-J. Delaunay, *Energy Environ. Sci.* **2015**, 8, 1493.
- [141] A. Azarpira, M. Lublow, A. Steigert, P. Bogdanoff, D. Greiner, C. A. Kaufmann, M. Krüger, U. Gernert, R. van de Krol, A. Fischer, T. Schedel-Niedrig, *Adv. Energy Mater.* **2015**, 5, 1402148.
- [142] J. E. Thorne, S. Li, C. Du, G. Qin, D. Wang, *J. Phys. Chem. Lett.* **2015**, 6, 4083.
- [143] C. P. Muzzillo, *Sol. Energy Mater. Sol. Cells* **2017**, 172, 18.
- [144] L. Xi, S. Y. Chiam, W. F. Mak, P. D. Tran, J. Barber, S. C. J. Loo, L. H. Wong, *Chem. Sci.* **2013**, 4, 164.
- [145] H. Kumagai, T. Minegishi, N. Sato, T. Yamada, J. Kubota, K. Domen, *J. Mater. Chem. A* **2015**, 3, 8300.
- [146] I. A. Digdaya, P. Perez Rodriguez, M. Ma, G. Adhyaksa, E. Garnett, A. H. M. Smets, W. A. Smith, *J. Mater. Chem. A* **2016**, 4, 6842.
- [147] J. Mahmood, F. Li, S.-M. Jung, M. S. Okyay, I. Ahmad, S.-J. Kim, N. Park, H. Y. Jeong, J.-B. Baek, *Nat. Nanotechnol.* **2017**, 12, 441.

- [148] H. Kobayashi, N. Sato, M. Orita, Y. Kuang, H. Kaneko, T. Minegishi, T. Yamada, K. Domen, *Energy Environ. Sci.* **2018**, *11*, 3003.
- [149] R. Fan, W. Dong, L. Fang, F. Zhenga, M. Shen, *J. Mater. Chem. A* **2015**, *5*, 18744.
- [150] M. R. Shaner, J. R. McKone, H. B. Gray, N. S. Lewis, *Energy Environ. Sci.* **2015**, *2*, 2977.
- [151] J. Gu, J. A. Aguiar, S. Ferrere, K. X. Steirer, Y. Yan, C. Xiao, J. L. Young, M. Al-Jassim, N. R. Neale, J. A. Turner, *Nat. Energy* **2017**, *2*, 1.
- [152] C. C. L. McCrory, S. Jung, J. C. Peters, T. F. Jaramillo, *J. Am. Chem. Soc.* **2013**, *135*, 16977.
- [153] H. Over, *Chem. Rev.* **2012**, *112*, 3356.
- [154] D. A. Lutterman, Y. Surendranath, D. G. Nocera, *J. Am. Chem. Soc.* **2009**, *131*, 3838.
- [155] D. Friebe, M. W. Louie, M. Bajdich, K. E. Sanwald, Y. Cai, A. M. Wise, M. J. Cheng, D. Sokaras, T. C. Weng, R. Alonso-Mori, R. C. Davis, J. R. Bargar, J. K. Nørskov, A. Nilsson, A. T. Bell, *J. Am. Chem. Soc.* **2015**, *137*, 1305.
- [156] S. Hu, M. R. Shaner, J. A. Beardslee, M. Lichterman, B. S. Brunschwig, N. S. Lewis, *Science* **2014**, *344*, 1005.
- [157] Y. Lu, S. Guan, L. Hao, H. Yoshida, *Coatings* **2015**, *5*, 425.
- [158] B. Seger, T. Pedersen, A. B. Laursen, P. C. K. Vesborg, O. Hansen, I. Chorkendor, *J. Am. Chem. Soc.* **2013**, *135*, 1057.
- [159] J. Zhao, T. Minegishi, L. Zhang, M. Zhong, Gunawan, M. Nakabayashi, G. Ma, T. Hisatomi, M. Katayama, S. Ikeda, N. Shibata, T. Yamada, K. Domen, *Angew. Chemie Int. Ed.* **2014**, *53*, 11808.
- [160] M. J. Choi, J.-Y. Jung, M.-J. Park, J.-W. Song, J.-H. Lee, J. H. Bang, *J. Mater. Chem. A* **2014**, *2*, 2928.
- [161] R. Fan, W. Dong, L. Fang, F. Zheng, X. Su, S. Zou, J. Huang, X. Wang, M. Shen, *Appl. Phys. Lett.* **2015**, *106*, 013902.
- [162] M. J. Kenney, M. Gong, Y. Li, J. Z. Wu, J. J. Feng, M. Lanza, H. Dai, *Science* **2013**, *342*, 836.

- [163] A. J. Nozik, *Appl. Phys. Lett.* **1976**, 29, 150.
- [164] K. Ohashi, J. McCann, J. O. Bockris, *Nature* **1977**, 266, 610.
- [165] H. Bin Yang, J. Miao, S. Hung, F. Huo, H. M. Chen, B. Liu, *ACS Nano*. **2014**, 8, 10403.
- [166] P. Borno, F. F. Abdi, S. D. Tilley, B. Dam, R. van de Krol, M. Graetzel, K. Sivula, *J. Phys. Chem. C* **2014**, 118, 16959.
- [167] S. D. Tilley, M. Schreier, J. Azevedo, M. Stefiak, M. Grätzel, *Adv. Funct. Mater.* **2014**, 24, 303.
- [168] C. Ding, W. Qin, N. Wang, G. Liu, Z. Wang, P. Yan, J. Shi, C. Li, *Phys. Chem. Chem. Phys.* **2014**, 16, 15608.
- [169] T. Minegishi, N. Nishimura, J. Kubota, K. Domen, *Chem. Sci.* **2013**, 4, 1120.
- [170] G. Ma, Y. Suzuki, R. B. Singh, A. Iwanaga, Y. Moriya, T. Minegishi, J. Liu, T. Hisatomi, H. Nishiyama, M. Katayama, K. Seki, A. Furube, T. Yamada, K. Domen, *Chem. Sci.* **2015**, 6, 4513.
- [171] W. S. dos Santos, M. Rodriguez, J. M. O. Khoury, L. A. Nascimento, R. J. P. Ribeiro, J. P. Mesquita, A. C. Silva, F. G. E. Nogueira, M. C. Pereira, *ChemSusChem* **2018**, 11, 589.
- [172] D. Huang, K. Wang, L. Yu, T. H. Nguyen, S. Ikeda, F. Jiang, *ACS Energy Lett.* **2018**, 3, 1875.
- [173] J. H. Kim, H. Kaneko, T. Minegishi, J. Kubota, K. Domen, J. S. Lee, *ChemSusChem* **2015**, 9, 61.
- [174] Y. J. Zhao, C. Persson, S. Lany, A. Zunger, *Appl. Phys. Lett.* **2004**, 85, 5860.
- [175] H. Metzner, T. Hahn, *J. Cryst. Growth* **2001**, 225, 354.
- [176] T. Maeda, T. Wada, *Phys. Status Solidi C* **2009**, 6, 1312.
- [177] T. Wang, X. Li, W. Li, L. Huang, C. Ma, Y. Cheng, J. Cui, H. Luo, G. Zhong, C. Yang, *Mater. Res. Express* **2016**, 3, 045905.
- [178] U. P. Singh, S. P. Patra, *Int. J. Photoenergy* **2010**, 2010, 468147.

Chapter 1. General Introduction

- [179] S. Niki, M. Contreras, I. Repins, M. Powalla, K. Kushiya, S. Ishizuka, K. Matsubara, *Prog. Photovoltaics Res. Appl.* **2010**, *18*, 453.
- [180] M. Raghuwanshi, B. Thöner, P. Soni, M. Wuttig, R. Wuerz, O. Cojocaru-Miredin, *ACS Appl. Mater. Interfaces* **2018**, *10*, 14759.
- [181] B. L. Kronik, D. Cahen, H. W. Schock, *Adv. Mater.* **1998**, *10*, 31.
- [182] K. Kushiya, *Sol. Energy Mater. Sol. Cells* **2014**, *122*, 309.
- [183] R. C. Valderrama, P. J. Sebastian, J. P. Enriquez, S. A. Gamboa, *Sol. Energy Mater. Sol. Cells* **2005**, *88*, 145.
- [184] D. Yokoyama, T. Minegishi, K. Maeda, M. Katayama, J. Kubota, A. Yamada, M. Konagai, K. Domen, *Electrochem. Commun.* **2010**, *12*, 851.
- [185] J. Kim, T. Minegishi, J. Kubota, K. Domen, *Energy Environ. Sci.* **2012**, *5*, 6368.
- [186] H. Kumagai, T. Minegishi, Y. Moriya, J. Kubota, K. Domen, *J. Phys. Chem. C* **2014**, *118*, 16386.
- [187] L. Zhang, T. Minegishi, J. Kubota, K. Domen, *Phys. Chem. Chem. Phys.* **2014**, *16*, 6167.
- [188] L. Zhang, T. Minegishi, M. Nakabayashi, Y. Suzuki, K. Seki, N. Shibata, J. Kubota, K. Domen, *Chem. Sci.* **2015**, *6*, 894.
- [189] J. Kim, T. Minegishi, J. Kubota, K. Domen, *Jpn. J. Appl. Phys.* **2012**, *51*, 015802.
- [190] R. Williams, *J. Chem. Phys.* **1960**, *32*, 1505.

Chapter 2

Development of ZnSe:Cu(In,Ga)Se₂ Photocathodes

2-1 Introduction

As mentioned in chapter 1, Cu-chalcopyrite materials have been reported to show insufficient onset potentials due to their shallow valence band maximum (VBM) potentials attributing to Cu 3*d* orbitals. Substitution of Cu by ZnSe is expected to deepen them. It should be noted that the alloying of these elements has already been reported by Li et al and Yamamoto et al. in the morphology of nanocrystals and thin-film photovoltaics, respectively.^[1,2] However, investigation on neither VBM potentials or photoelectrochemical (PEC) properties of alloys has not been reported yet.

In this work, co-evaporation of each element in a high vacuum chamber is employed to prepare polycrystalline thin films of (ZnSe)_x(CuIn_{0.7}Ga_{0.3}Se₂)_{1-x}, which is abbreviated as (ZnSe)_x(CIGS)_{1-x} herein. This method is preferable for this purpose thanks to the relatively small amount of impurities, easiness in adjusting feed rates of each element, availability of in-depth composition gradient and so on.^[3-5] Because Kumagai et al, have already established the sufficient surface modifications and electrolyte condition to facilitate smooth PEC hydrogen evolution reaction (HER), which are a binary Mo/Ti nanolayer on a CdS layer and a neutral phosphate buffer solution, respectively,^[6] the current work follows these conditions expect for the light-absorbing layers. In the next section, experimental conditions concerning the investigation on (ZnSe)_x(CIGS)_{1-x} photocathodes are described in detail.

2-2 Experimental Section

Preparation of (ZnSe)_x(CIGS)_{1-x} Thin Films

(ZnSe)_x(CIGS)_{1-x} thin films were deposited on substrates of Mo-coated soda-lime glass. The substrates were fabricated by RF magnetron sputtering of a Mo target (99.9%, Kojundo) onto each soda-lime glass plate heated at 573 K. Prior to the Mo deposition, a 30 nm thick Ti was deposited by the sputtering of a Ti target (99.9%, Kojundo) so as to improve the adhesion. The thickness of Mo and Ti are about 500 and 30 nm, respectively.

Chapter 2. Development of ZnSe:Cu(In,Ga)Se₂ Photocathodes

The substrate was loaded into a deposition chamber equipped with Knudsen cells containing elemental Cu, In, Ga, Zn and Se (99.9999%, Asahi Metal or Furuuchi Chemical). The substrate temperature was set at 623 K for 5 min and then reset to 623-823 K for 35 min. The typical deposition rates for Cu, In, Ga, Zn and Se were 0.042, 0.048, 0.014, 0-0.5 and 1 nm s⁻¹ unless otherwise noted. The rates were monitored by using a quartz crystal microbalance sensor (Q-POD, INFICON). The pressure in the chamber was kept at $<2 \times 10^{-5}$ Pa during deposition.

KCN Etching

After deposition, the samples were immersed into an etching solution containing 0.1 M KCN (98.0%, FUJIFILM Wako Pure Chemical) and 0.8 M KOH (8 M, FUJIFILM Wako Pure Chemical) for 1 min in room temperature. This etching process removed excess Cu from the (ZnSe)_x(CIGS)_{1-x} thin films. Energy dispersive X-ray spectroscopy (EDS; EMAX-7000, Horiba) analysis revealed that the atomic ratio of Cu/(In+Ga) was 0.9 to 1.0 after the process.

Characterization

The (ZnSe)_x(CIGS)_{1-x} thin film samples were analyzed using X-ray diffraction (XRD; RINT-Ultima3, Rigaku), photoelectron spectroscopy in air (PESA; AC-3, Riken Keiki), UV-vis reflectance spectroscopy (V-670, JASCO), scanning electron microscopy (SEM; Hitachi), (scanning) transmission electron microscopy ((S)TEM; JEM-2800, JEOL) and X-ray photoelectron spectroscopy (XPS; JPS-9000, JEOL) equipped with an Ar ion gun.

Surface Modification with an CdS Layer

A CdS layer was formed on the surface of each (ZnSe)_x(CIGS)_{1-x} thin film using chemical bath deposition (CBD) method.^[6-8] The CBD solution with a volume of 50 mL contained 14 wt% ammonia (28 wt%, FUJIFILM Wako Pure Chemical), 25 mM of Cd(CH₃COO)₂ (98.0%, FUJIFILM Wako Pure Chemical) and 0.375 M of SC(NH₂)₂ (98.0%, Kanto Chemical). The bath temperature was gradually increased from room temperature to 325-326 K over the span of about 8 min. The

samples were taken out from the bath and immediately washed with pure water 14 min after the initiation of heating, followed by annealing at 473 K for 1 min in air.

Surface Modification with Thin Metal Layers

A binary of Mo/Ti with each thickness of 3 nm was deposited by successive RF magnetron sputtering of a Ti and Mo target in room temperature.^[6] Subsequently, a Pt layer with a thickness of a few nanometers was deposited on it by thermal evaporation of Pt wire (99.98%, Nilaco) in a high vacuum of $<4 \times 10^{-3}$ Pa.

After these surface modifications, the (ZnSe)_x(CIGS)_{1-x} thin film samples were connected with a lead wire using indium at the Mo substrate exposed by polishing. The region not intended for measurement was coated with epoxy resin (Araldite Rapid, Nichiban), resulting in the geometric surface areas of specimens of 0.1-0.3 cm².

Preparation of NiFeO_x-Bi/BiVO₄ Photoanodes

A BiOI precursor was prepared on an indium tin oxide (ITO)-coated soda-lime glass substrate (0051, Geomatec) by electrodeposition method in a three-electrode cell with an Ag/AgCl reference electrode in a saturated aqueous KCl solution and with a Pt wire counter electrode. Subsequently, a dimethyl sulfoxide solution containing VO(C₅H₇O₂)₂ (98%, Sigma-Aldrich) was drop-cast onto the precursor, followed by calcination at 723 K for 1 h in air. As oxygen evolution reaction (OER) catalyst, NiFeO_x-Bi was deposited onto the prepared BiVO₄ electrode (NiFeO_x-Bi/BiVO₄) by photoelectrodeposition method.^[9] The potential of the electrode was held at -0.16 V vs. Ag/AgCl until saturation of the photocurrent (typically requiring 10-20 min) under simulated sunlight (XES-40S2-CE, SAN-EI Electric) in a 0.5 M aqueous potassium borate solution containing 4 μM NiSO₄ (99.9%, FUJIFILM Wako Pure Chemical) and 40 μM FeSO₄ (99%, FUJIFILM Wako Pure Chemical) with the pH adjusted to 9.5 by KOH addition. It should be noted that a previous report describes the fabrication process of the BiVO₄-based photoanode in more detail.^[10]

Photoelectrochemical Measurements

A three-electrode cell equipped with a magnetic stirrer under an Ar atmosphere using an aqueous solution of 1.0 M potassium phosphate buffer solution (pH 7.0) as the electrolyte was set up and connected to a potentiostat (HSV-110, Hokuto Denko), unless otherwise noted. A solar simulator (XES-70S1 or XES-40S2-CE, SAN-EI Electric) producing AM1.5G was employed as the light source. In the current-potential measurements, the applied potential, expressed relative to a reversible hydrogen electrode (RHE), was swept at 5 mV s⁻¹ from 0 V_{RHE} under intermittent irradiation with a period of 6 s.

The wavelength dependence of the incident photon-to-current conversion efficiency (IPCE) was evaluated under monochromatic light from a 300 W Xe lamp equipped with a monochromator (CT-10, JASCO), where the light intensity was measured using a Si photodiode (S2281-01, Hamamatsu Photonics).

Analysis of the evolved gases was conducted using an airtight and Ar-purged glass cell connected to a gas chromatograph (3000 Micro GC Gas Analyzer, Agilent Technologies) and a potentiostat.

First Principle Calculations

The model of (ZnSe)_{0.85}(CIGS)_{0.15} crystal structure was set as shown in Figure 2-2-2, which has been reported as the most stable arrangement of cations as it satisfies the Octet rule.^[11,12] The model cell contains 192 atoms with the atomic Zn/(Cu+Zn) ratio of 0.86. The formation energy of each defect is defined as

$$E_f(D^q) = E(D^q) - E_p - \sum n_i \mu_i + q(E_{VBM} + E_F) \quad (2-1)$$

where $E_f(D^q)$ is the total energy of the defect model with charge q , E_p is the total energy of the bulk structure motel, n_i is the number of reduced or added atoms of element i , μ_i is the chemical potential of element i , and E_F is the Fermi level vs. the VBM potential, (E_{VBM}). The band gap energy of (ZnSe)_{0.85}(CIGS)_{0.15} was set to 1.4 eV. μ_i is obtained from the phase diagram shown in

Figure 2-1 or can be estimated from the partial pressure (i.e. the feed rate) and the definition of chemical potential, which is described as

$$\mu_i = \Delta_f G_i^o - TS^o + RT \ln \frac{p_i}{p^o} \quad (2-2)$$

where $\Delta_f G_i^o$ is the standard molar Gibbs energy of element i ,^[13] p^o and p_i are the total pressure under the standard condition and the partial pressure of element i , respectively. T stands for the temperature, S^o is the entropy under the standard condition and R means the gas constant. Accordingly, $\mu_{\text{Cu}}, \mu_{\text{In}}, \mu_{\text{Ga}}, \mu_{\text{Zn}}$ and μ_{Se} at 723 K were calculated to 1.1, 0.1, 0.3, -0.9 and 0.0 eV, respectively. Compared with the phase diagram shown in Figure 2-1, the chemical potentials at the point A ($\mu_{\text{Cu}}, \mu_{\text{In}}, \mu_{\text{Ga}}, \mu_{\text{Zn}}, \mu_{\text{Se}} = (0.0, -1.1, -1.4, -1.0, -0.6)$) were employed.

The calculations were conducted by using the means of density functional theory with the projector augmented wave method and the localized density approximation for the exchange-correlation energy. For Cu, In, Ga and Zn, electrons in the s and p orbitals at the outermost shell and d electrons just under these electrons were treated as valence states, while $4s$ and $4p$ electrons were treated as valence states for Se. The k -point sampling and the cutoff energy were set to $2 \times 2 \times 1$ and 400 eV, respectively. The onsite Coulomb potentials of Zn ($U = 7.0$ eV), Cu (6.0 eV), In (7.0 eV) and Ga (9.0 eV) were added so as to describe the electrons in the d -electrons nearby the defects more precisely. The detailed information about the calculations has already published elsewhere.^[12]

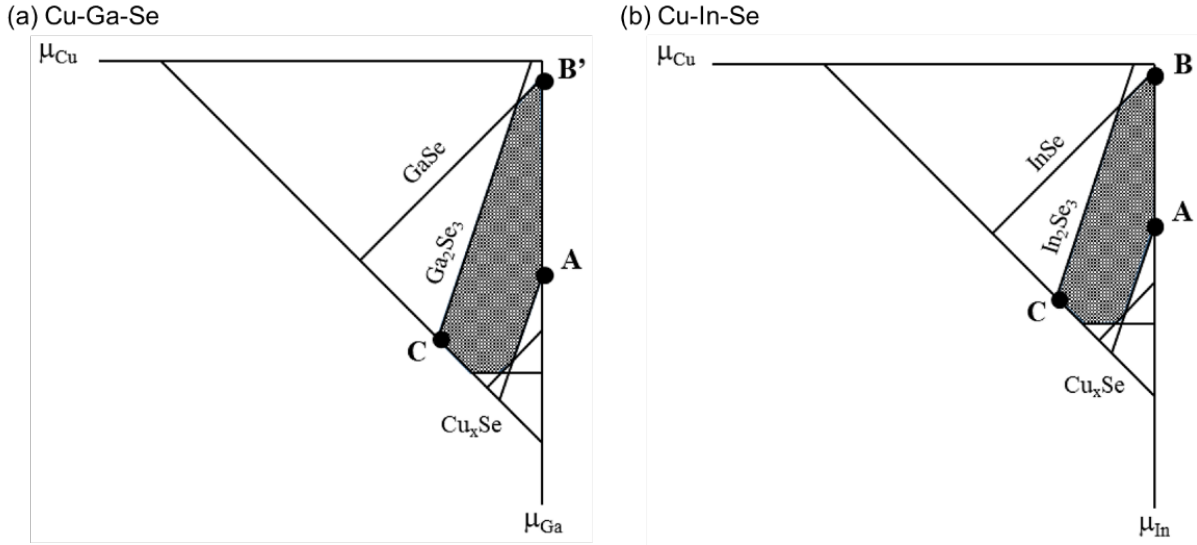


Figure 2-1. Phase diagrams of Cu-Ga-Se (a) and Cu-In-Se (b).^[12] Reprinted with permission from ref. [12].

2-3 Results and Discussion

2-3-1 Effects of ZnSe Introduction into Cu(In,Ga)Se₂ on the Physical Properties

(ZnSe)_x(CIGS)_{1-x} thin films with various x were prepared, and their XRD patterns were shown in Figure 2-1-1. These samples were prepared at the substrate temperature of 723 K during deposition, and flux ratio of Cu to In and Ga ($J_{\text{Cu}}/J_{\text{In}}+J_{\text{Ga}}$) was fixed to approximately 1.4. The patterns revealed that all of the thin films are composed of pure (ZnSe)_x(CIGS)_{1-x}, oriented to the (111) and (112) planes in zincblende and chalcopyrite, respectively. The common crystal structures of ZnSe are zinc blende and wurtzite, and the patterns revealed that only zinc blende phase was formed in the current deposition condition. Furthermore, a meaningful shift in the corresponding peak was observed due to the change in lattice constant by substitution. Except for the peaks attributed to the substrates, no impurity phase or phase separation was observed in the pattern. Figure 2-1-2 shows PESA spectra for the samples, where the onset of photoelectrons is equal to the VBM potentials based on photoelectric effect.^[14,15] It should be noted that the onset is estimated from extrapolation of the yield to the power of 0.33

relative to the energy of incident photons. The spectra also showed a meaningful shift in the VBMs as ZnSe was introduced into CuIn_{0.7}Ga_{0.3}Se₂.

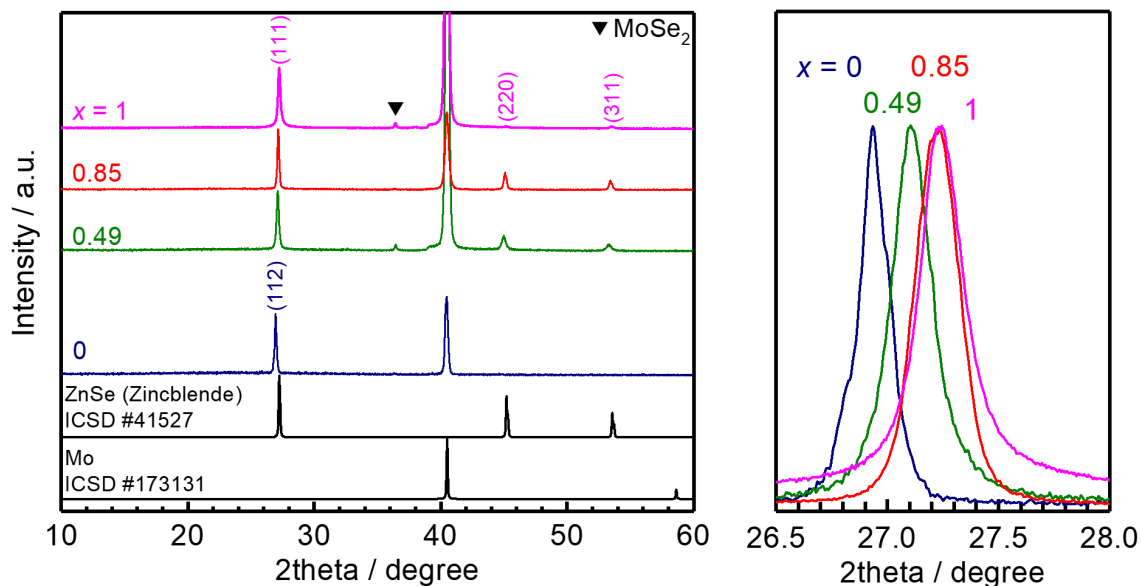


Figure 2-1-1. XRD patterns for $(\text{ZnSe})_x(\text{CIGS})_{1-x}$ thin films ($x = 0, 0.49, 0.85, \text{ and } 1$). Reference peak positions of MoSe₂ are shown. (ICSD #16948)

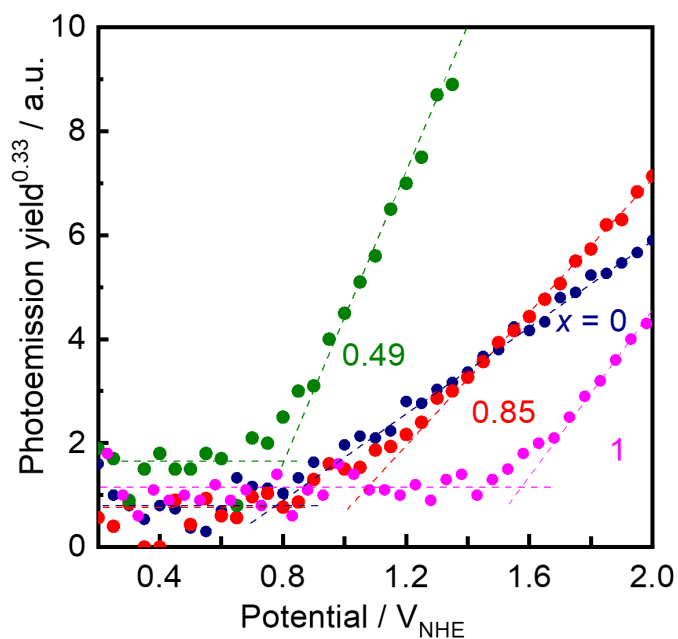


Figure 2-1-2. PESA spectra for $(\text{ZnSe})_x(\text{CIGS})_{1-x}$ thin films ($x = 0, 0.49, 0.85 \text{ and } 1$).

The lattice parameter calculated from the peak positions at about 27° in Figure 2-1-1 and the VBM potentials directly determined by Figure 2-1-2 were summarized in Figure 2-1-3. As shown in the figure, the mismatch between the α -axis lengths of chalcopyrite CuIn_{0.7}Ga_{0.3}Se₂ and zincblende ZnSe is just 1%, which enabled formation of the uniform alloy at all range of ZnSe mole fractions. On the other hand, the difference in VBM potentials was significant, approximately 0.8 eV, which is similar to the reported value of 0.77 eV (between ZnSe and CuGaSe₂) using first principle calculation shown in Figure 1-5-4.^[16] In the case of VBM potentials, the change showed a significant nonlinearity with x . The similar tendency was also reported by Li et al. and Quintans et al. on (ZnSe) _{x} (CuInSe₂)_{1- x} and (ZnS) _{x} (CuGaSe₂)_{1- x} alloys, respectively.^[1,17] These reports suggest that there is a relatively large band gap bowing of such material systems, possibly due to the large interaction by Cu 3d orbitals. After all, ZnSe mole fraction of 0.7-0.9 resulted in the shift of VBM potential by 0.2-0.3 eV.

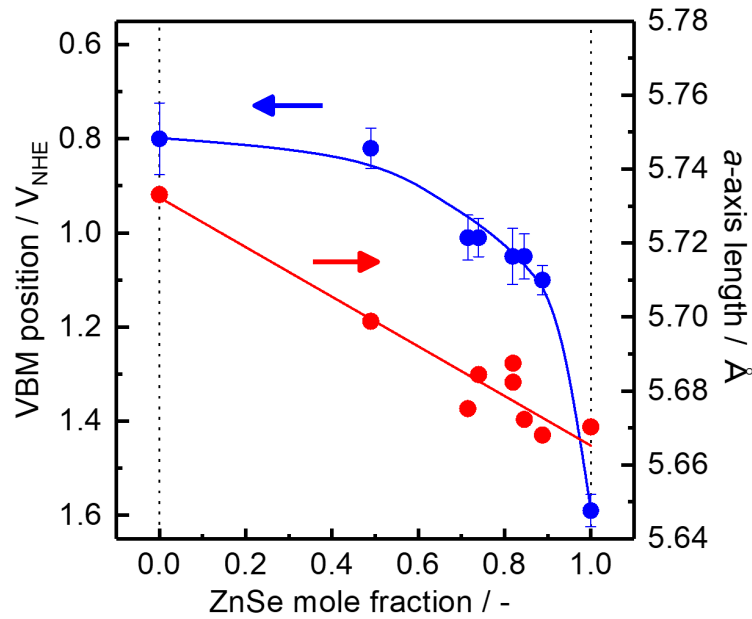


Figure 2-1-3. Dependence of α lattice parameter and VBM potential for (ZnSe) _{x} (CIGS)_{1- x} . The ZnSe mole fraction x corresponds to the atomic ratio of Zn/(Zn+In+Ga) obtained by EDS.

Figure 2-1-4 shows SEM images of (ZnSe) _{x} (CIGS)_{1- x} thin films after etching with KCN. All samples show polycrystalline and dense films with the thickness of 2 to 3 μ m. Compared with

Cu(In,Ga)Se₂ thin films prepared by three-stage method,^[18] the grain size is relatively small and a few voids can be observed, possibly due to the relatively low substrate temperature. Effects of substrate temperature during deposition are discussed below in detail. Current-potential curves for the (ZnSe)_x(CIGS)_{1-x} photocathodes are compared in Figure 2-1-5, where the substrate temperature was set to 823 K and 723 K for the samples with $x = 0$ and the others, respectively. Obviously, the increase in x resulted in a positive shift in the onset potential, which is attributed to the shift in the VBM potential. On the other hand, the samples with the large ratios of ZnSe showed relatively small photocurrent values due to the widened band gaps and the small grain sizes as shown in Figure 2-1-4. Under these contradictory factors, the sample with $x = 0.85$ showed the highest photocurrent value at 0.6 V_{RHE} of approximately 2.5 mA cm⁻².

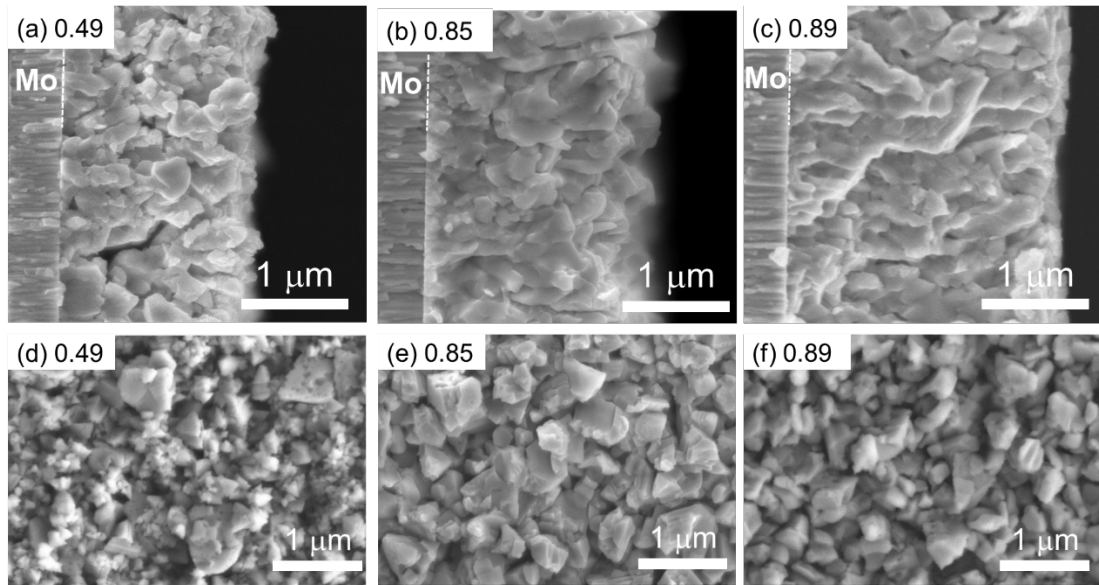


Figure 2-1-4. Cross-sectional (a-c) and surface (d-f) SEM images of (ZnSe)_x(CIGS)_{1-x} thin films with $x = 0.49$ (a, d), 0.85 (b, e) and 0.89 (c, f).

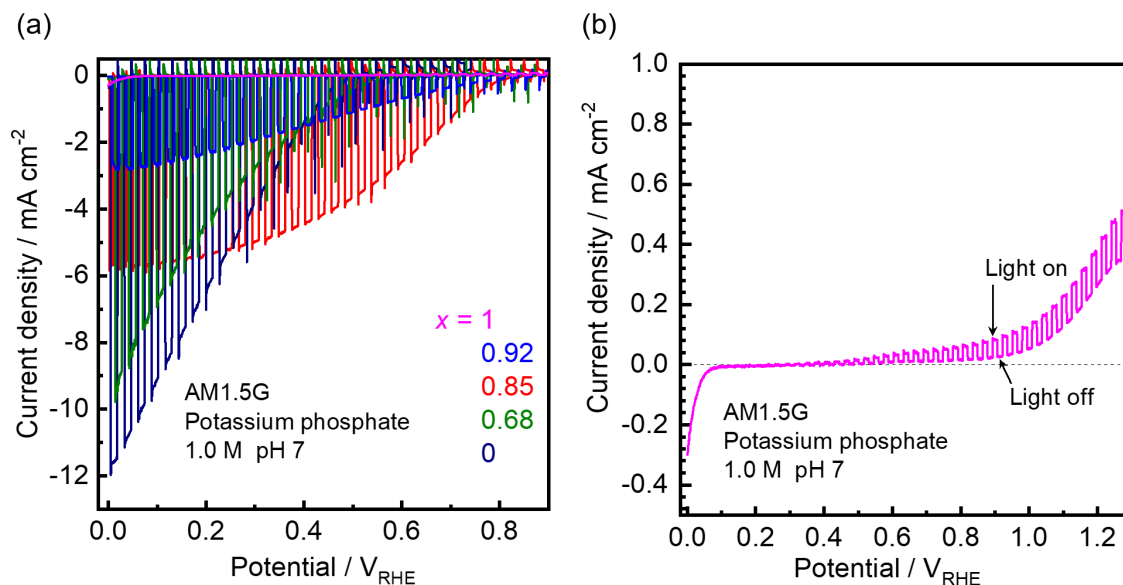


Figure 2-1-5. Current-potential curves for (ZnSe)_x(CIGS)_{1-x} photocathodes modified with CdS, Ti, Mo and Pt prepared with various kinds of x (a) and only $x = 1$ (b).

2-3-2 Effects of the Amount of Cu Flux on the Semiconductor Property

In the case of Cu-chalcopyrite-based semiconductors, it has been known that the atomic ratio of Cu/III should be slightly less than one by several percent.^[5,19,20] This is because vacancies of copper, V_{Cu} , function as acceptors. However, when II elements coexist with V_{Cu} in the crystal, they can form antisite defects of II_{Cu} , which act as donors. In fact, recent reports have shown that introduction of Zn or Cd into Cu(In,Ga)Se₂ crystals changes their semiconductor property from p-type to n-type.^[21–24] Hence, the atomic ratio of Cu/III should dramatically affect the semiconductor property of (ZnSe)_x(CIGS)_{1-x}. Moreover, there is also another possibility that the type of dominant acceptor-type defects of (ZnSe)_x(CIGS)_{1-x} is different from that of Cu(In,Ga)Se₂.

Figure 2-2-1 shows current-potential curves for (ZnSe)_x(CIGS)_{1-x} ($x = 0.7-0.9$) photocathodes prepared with various flux ratios. After film preparation, the etching process with KCN removed the excess Cu_xSe, so the samples prepared in Cu-rich conditions show the atomic ratio of Cu/(In+Ga) of 0.9-1.0, which was confirmed by EDS analyses. On the other hand, it is highly possible that the Cu-

deficient sample contains V_{Cu} and/or Zn_{Cu} defects. It should be noted that Cu-chalcopyrites have been known to tolerate large range of anion to cation off-stoichiometry with forming ordered defect compounds such as CuGa_3Se_5 , which are possibly present in the Cu-deficient sample.^[25] Following the etching process, the surfaces of photocathodes were modified with CdS and Pt. The sample prepared with the ratio of 0.78 showed a significantly smaller photocurrent than the others. Furthermore, anodic photoresponses were also observed (see Figure 2-2-1 (b)) at the potential higher than 0.55 V_{RHE} . Figure 2-2-2 shows current potential curves in a Na_2SO_3 aqueous solution as a reducible reagent.^[26] The Cu-deficient $(\text{ZnSe})_x(\text{CIGS})_{1-x}$ photoelectrode showed anodic photoresponse at potentials of higher than 0.2 V_{RHE} due to oxidation by photoexcited holes migrating to photoelectrode surface, which suggests that the semiconductor property of the Cu-deficient $(\text{ZnSe})_x(\text{CIGS})_{1-x}$ is closer to n-type. On the other hand, the $(\text{ZnSe})_x(\text{CIGS})_{1-x}$ photoelectrode prepared in Cu-rich condition exhibited no anodic photoresponse but large oxidation current in dark at potentials of higher than 0.6 V_{RHE} . The difference in the dark current can be explained by considering the semiconductor-electrolyte interface as a Schottky barrier diode; the sweep toward a positive potential is equal to application of forward and negative bias for the p-type and n-type semiconductor electrodes, respectively. Moreover, the threshold potential of approximately 0.9 V_{RHE} is quite consistent with the onset potential as a photocathode.

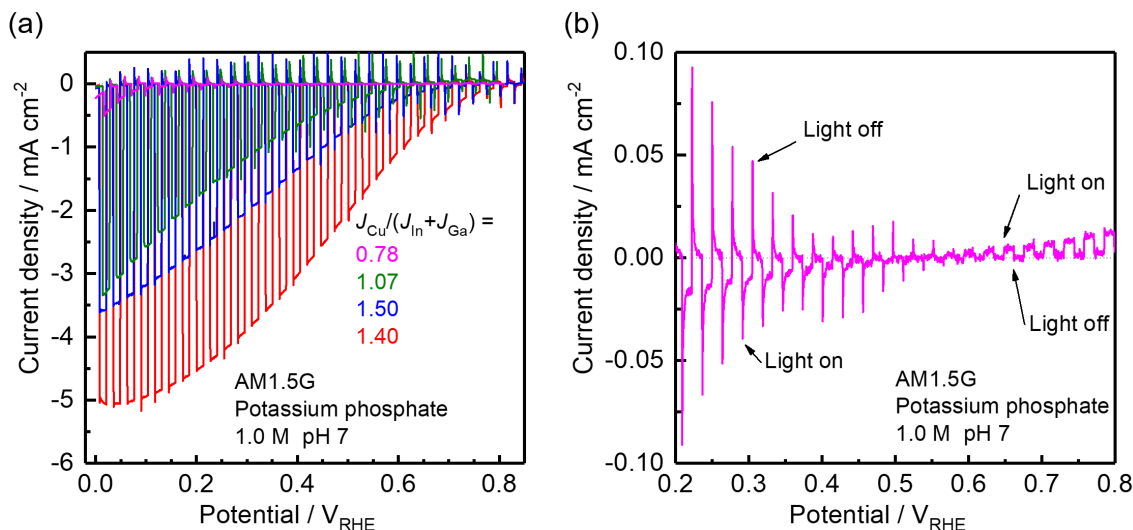


Figure 2-2-1. Current-potential curves for (ZnSe)_x(CIGS)_{1-x} ($x = 0.7-0.9$) photocathodes modified with CdS and Pt prepared with various kinds of Cu/(In + Ga) flux ratio during film deposition (a) and only 0.78 (b).

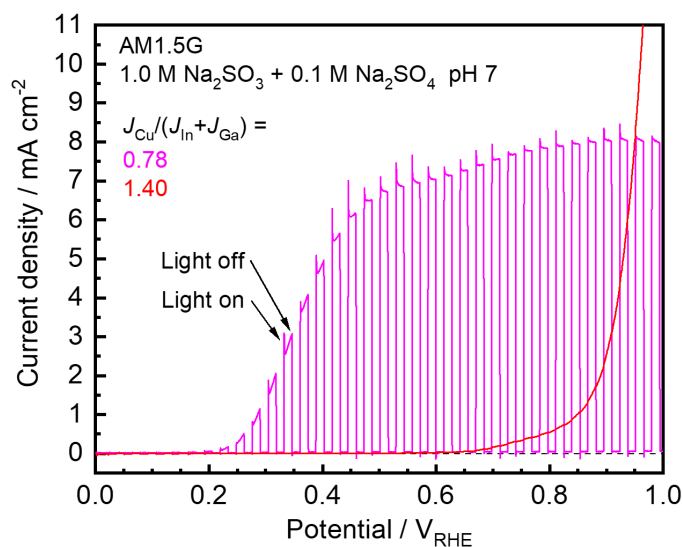


Figure 2-2-2. Current-potential curves for bare (ZnSe)_x(CIGS)_{1-x} ($x = 0.7-0.9$) photoelectrodes prepared with Cu/(In + Ga) flux ratios of 0.78 and 1.40 followed by the etching process. A 1.0 M Na₂SO₃ + 0.1 M Na₂SO₄ solution (pH adjusted to 7 by H₂SO₄ addition) was used as the electrolyte.

Chapter 2. Development of ZnSe:Cu(In,Ga)Se₂ Photocathodes

First principle calculations were performed for the sake of obtaining information concerning major defect species in (ZnSe)_{0.85}(CIGS)_{0.15} crystal. It is noted that the results have already been published elsewhere.^[12] The detailed conditions on calculations were explained in the experimental section. Figure 2-2-3 shows the model of crystal structure and formation energies of vacancy, antisite and interstitial defects in the band gap of (ZnSe)_{0.85}(CIGS)_{0.15} crystals deposited in the condition of $J_{\text{Cu}}/J_{\text{In}}+J_{\text{Ga}} = 1.4$. Antisite defects have been found to show the lowest formation energies. Especially, it is likely that Cu_{Zn} and Zn_{III} (III = In, Ga) are major acceptors and that Zn_{Cu} and III_{Zn} are major donors. The intersection of these energies shown as an arrow in the Figure 2-2-3 (c) indicates the estimated Fermi level. Because the arrow is near the VBM, the calculation supports the p-type property of (ZnSe)_{0.85}(CIGS)_{0.15}. Figure 2-2-4 and 2-2-5 shows formation energies of antisite defects accompanied with their dependency on chemical potentials of Cu (μ_{Cu}) and Zn (μ_{Zn}), respectively. The change in each chemical potential can be assumed to that in the feed. In the case of Cu, the estimated Fermi level showed a meaningful sensitivity to μ_{Cu} ; the increase and decrease in μ_{Cu} resulted in the shifts of the Fermi level to VBM and CBM side, respectively. In other words, decreasing the atomic ratio of Cu to the other metals in the feed is suggested to alter the semiconductor property of (ZnSe)_{0.85}(CIGS)_{0.15} to n-type. On the other hand, the Fermi level of (ZnSe)_{0.85}(CIGS)_{0.15} didn't show a clear sensitivity to μ_{Zn} because defect formation energy was not affected by the change in μ_{Zn} as shown in Figure 2-2-5.

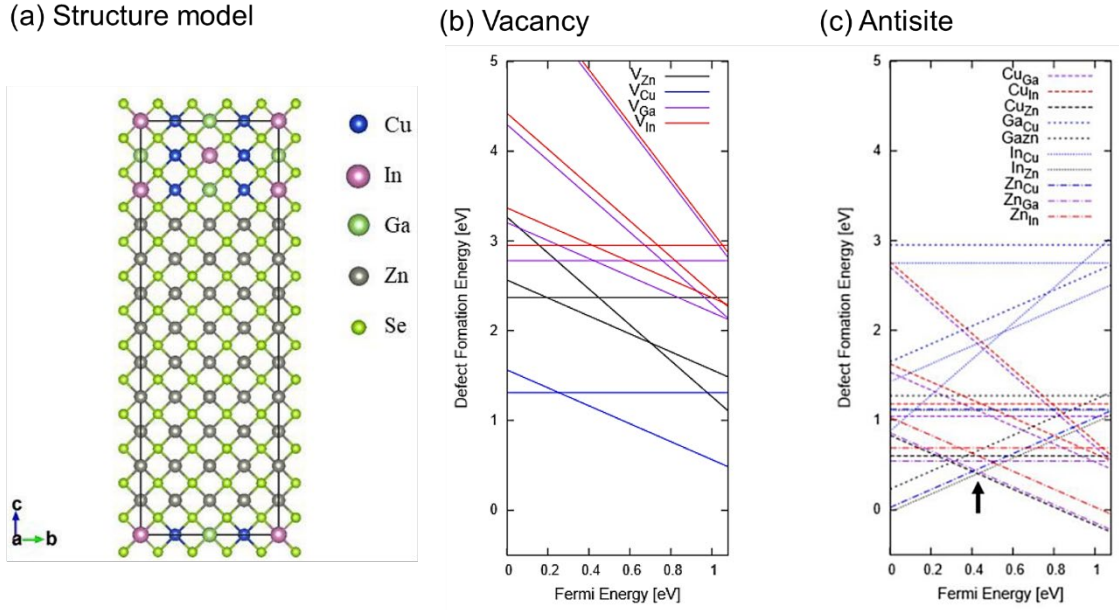


Figure 2-2-3. (a) The structural model for $(\text{ZnSe})_{0.85}(\text{CIGS})_{0.15}$ crystal. (b, c) Comparison of defect formation energies in $(\text{ZnSe})_{0.85}(\text{CIGS})_{0.15}$ crystals. The VBM potential was set to zero. Reprinted with permission from ref. [12].

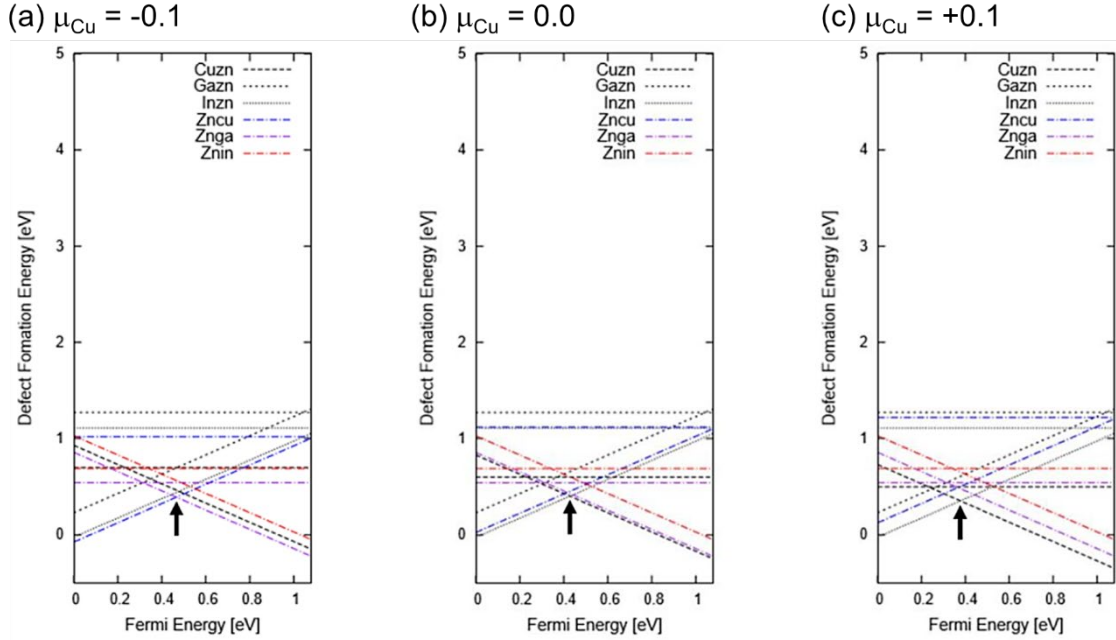


Figure 2-2-4. Comparison of formation energies of antisite defects in $(\text{ZnSe})_{0.85}(\text{CIGS})_{0.15}$ crystals with various μ_{Cu} . Reprinted with permission from ref. [12].

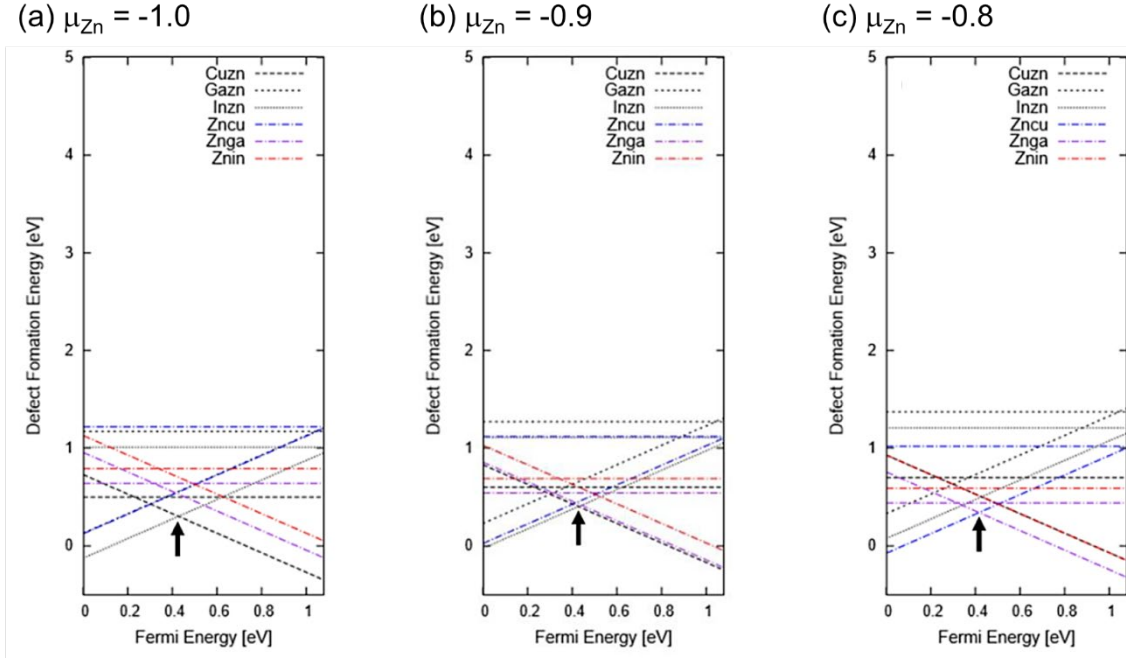


Figure 2-2-5. Comparison of formation energies of antisite defects in (ZnSe)_{0.85}(CIGS)_{0.15} crystals with various μ_{Zn} . Reprinted with permission from ref. [12].

These experimental and computation results have also suggested a difficulty in development of multi-stage deposition process. For example, so-called three-stage method is a commonly employed to deposit polycrystalline Cu(In,Ga)Se₂ thin films.^[5,18,27] This method at first forms Cu-absent layer on the substrate, then introduces an excess amount of Cu so as to grow large grains using Cu_xSe as a flux, and finally adjusts the stoichiometry to slightly Cu-deficient Cu(In,Ga)Se₂. Such a method dramatically affects p- and n-type character of (ZnSe)_x(CIGS)_{1-x} thin films in depth, so it is not preferable to simply apply it into the material system. Even though, multistage deposition process should be indispensable because it can form composition gradient which is often preferable for crystal growth and/or charge separation. Development of the multistage process suitable for (ZnSe)_{0.85}(CIGS)_{0.15} is discussed in chapter 3.

2-3-3 Effects of Preparation Conditions of ZnSe:Cu(In,Ga)Se₂ Thin Films onto Their Photoelectrochemical Properties

The previous sections revealed that deposition in the Cu-rich deposition is indispensable for (ZnSe)_{0.85}(CIGS)_{0.15} thin films to work as efficient photocathodes. Herein, effects of deposition temperature onto their PEC properties are mainly investigated in order to optimize the performance as a photocathode suitable for the usage in a PEC cell. Figure 2-3-1 shows XRD patterns and surface SEM images of (ZnSe)_{0.85}(CIGS)_{0.15} thin films deposited at various substrate temperature. The sample deposited at a relatively low temperature of 623 K showed a peak attributed to wurtzite structure, which can provide recombination sites between the boundary of the two different phases. Also, the grain size obtained from the SEM image is relatively small and not uniform. The other sample deposited at 823 K showed a relatively grain size, and the peak intensity of Mo substrate is relatively small possibly due to the relatively high density of the crystal grains. However, the edge is relatively rounded possibly due to re-evaporation of Zn species, which can cause a high density of crystal defects as recombination sites. This is because the vapor pressure of Zn is relatively higher than the other metals. Consequently, the optimum substrate temperature for deposition of (ZnSe)_{0.85}(CIGS)_{0.15} thin films was determined to be about 723 K, which is >100 K lower than that of Cu(In,Ga)Se₂.^[5,18,27] Figure 2-3-2 shows a high-resolution TEM image of the single grain of (ZnSe)_{0.85}(CIGS)_{0.15} deposited at 723 K. The continuous lattice fringes suggest the grain to be a single crystal.

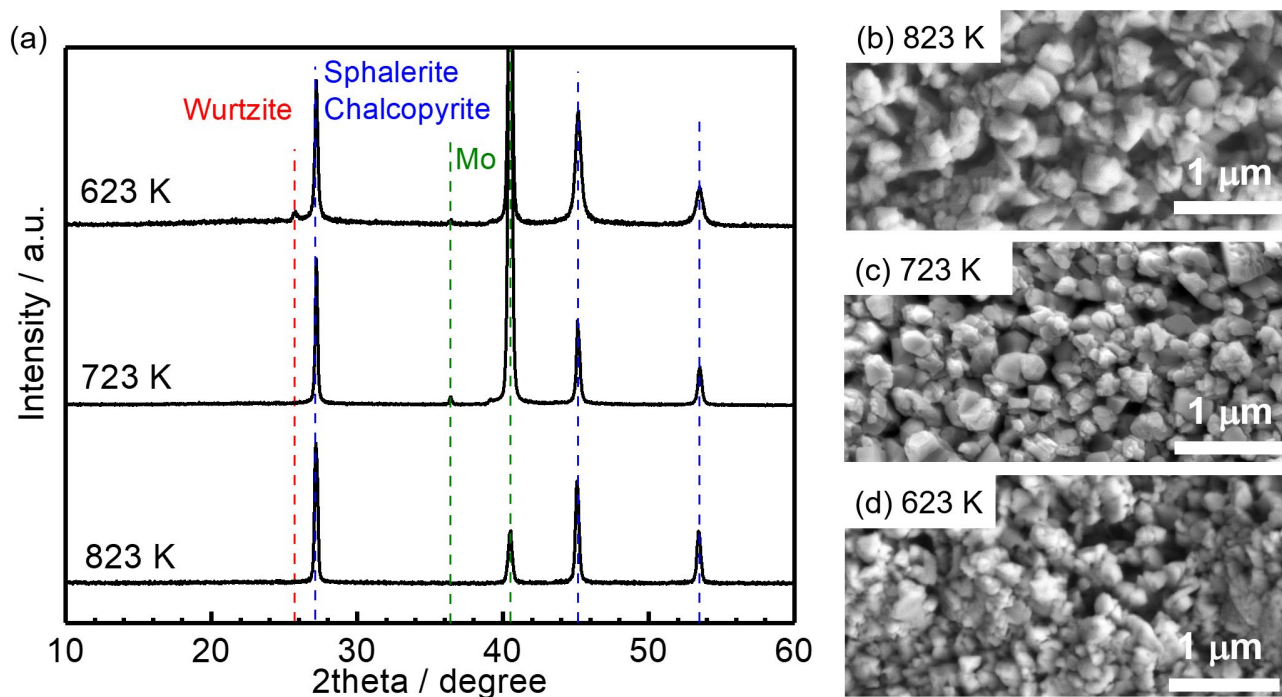


Figure 2-3-1. XRD patterns (a) and surface SEM images (b-d) of (ZnSe)_{0.85}(CIGS)_{0.15} thin films prepared at various substrate temperature during deposition. The intensities for the XRD patterns are normalized to the peak intensity at around 27° of the sample deposited at 723 K.

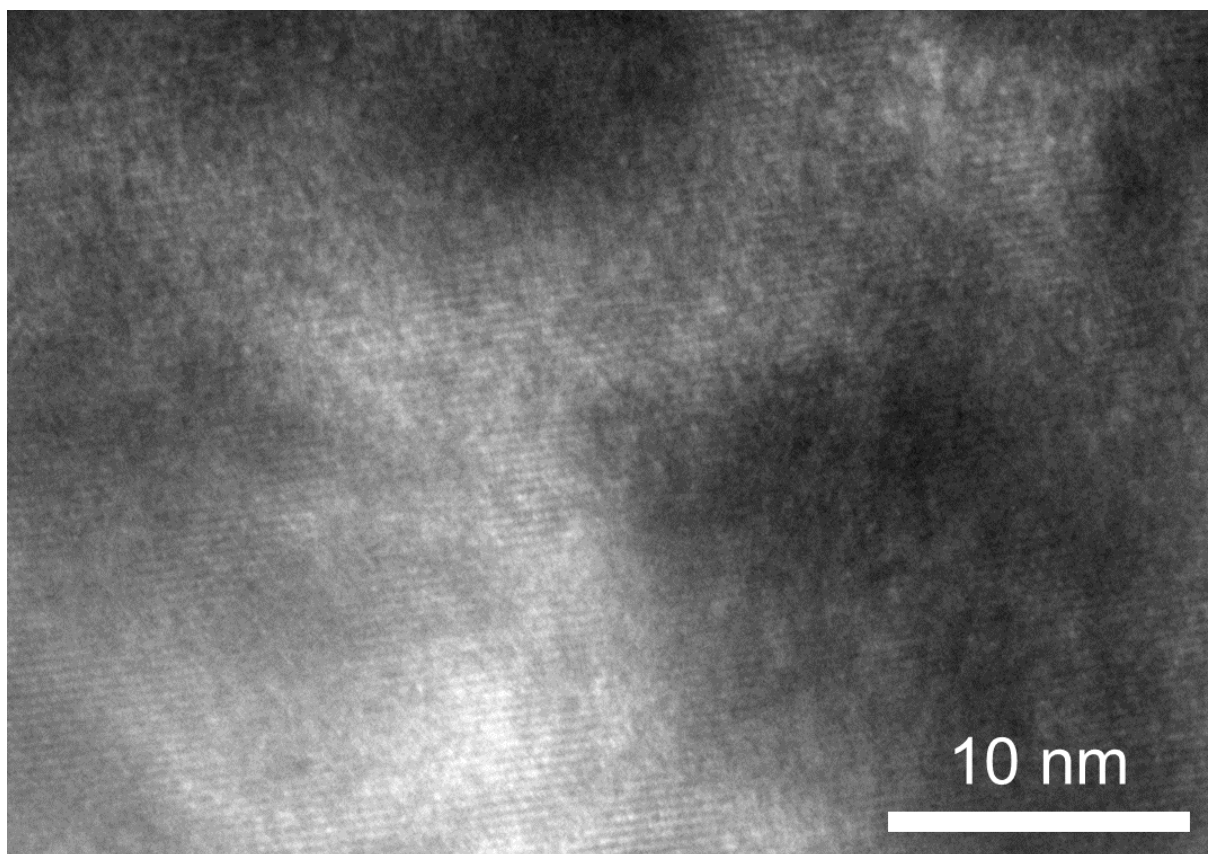


Figure 2-3-2. A high-resolution TEM image of single grain of (ZnSe)_{0.85}(CIGS)_{0.15} prepared at 723 K.

The current-potential curves shown in Figure 2-3-3 revealed that the sample deposited at 723 K showed the largest photocurrent and the highest onset potential among them. Hence, it can be concluded that the relatively low temperature of about 723 K is the optimum condition for deposition of (ZnSe)_{0.85}(CIGS)_{0.15} thin films for photocathodes.

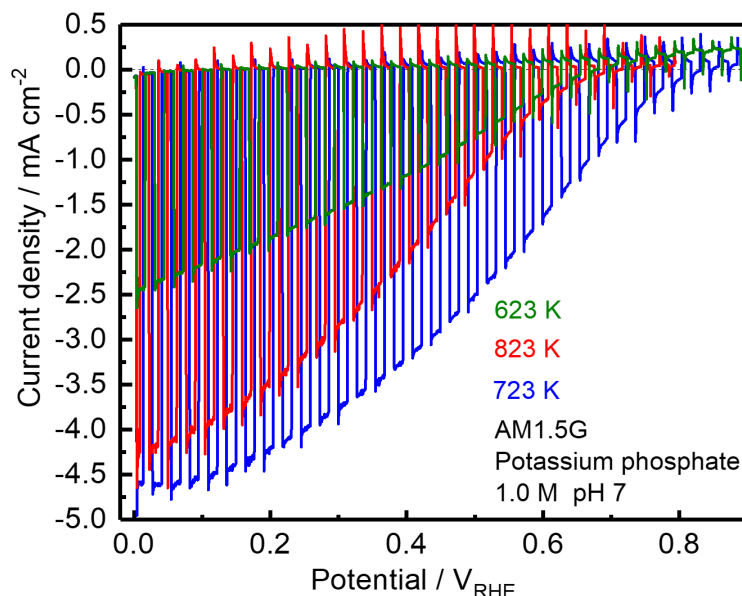


Figure 2-3-3. Current-potential curves for (ZnSe)_{0.85}(CIGS)_{0.15} photocathodes prepared at various substrate temperature during deposition of (ZnSe)_{0.85}(CIGS)_{0.15} thin films. The surface of each photocathode was modified with CdS and Pt.

Figure 2-3-4 compares current-potential curves for the (ZnSe)_{0.85}(CIGS)_{0.15} photocathodes with various kinds of surface modifications. Deposition of CdS (Pt/CdS/(ZnSe)_{0.85}(CIGS)_{0.15}) clearly improves both of the photocurrent and onset potential, while deposition of Pt alone (Pt/(ZnSe)_{0.85}(CIGS)_{0.15}) resulted in very small photoresponses as a photocathode. The deposition of an n-type CdS layer has been reported to promote the charge separation at the semiconductor-electrolyte interface by altering built-in potential as discussed in chapter 1. Moreover, deposition of a Mo/Ti binary (Pt/Mo/Ti/CdS/(ZnSe)_{0.85}(CIGS)_{0.15}) increased the photocurrent value around the onset potential. The layer has been known as a good mediator of electrons between CdS and the active sites, Pt.^[6] As discussed in the same chapter, Ti alleviates a Schottky barrier between CdS and Pt, and forms an intimate contact at the interface with CdS. Although the surface of Ti can be easily oxidized, Mo stably works stably in a metallic state, resulting in the increase in the photocurrent.

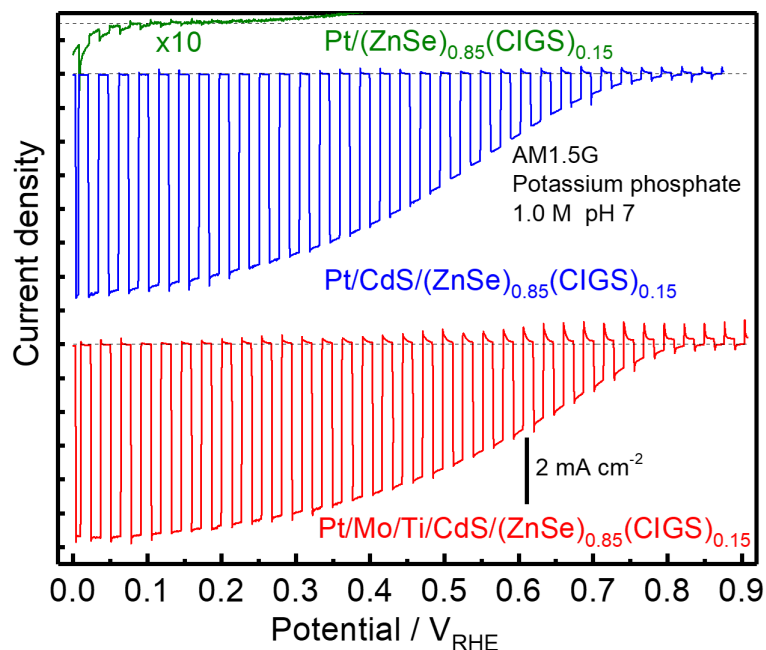


Figure 2-3-4. Current-potential curves for $(\text{ZnSe})_{0.85}(\text{CIGS})_{0.15}$ photocathodes with various kinds of surface modification. The thin film was deposited at 723 K.

As pointed out above, the high vapor pressure of Zn can form defects such as V_{Zn} , especially at the surface of $(\text{ZnSe})_{0.85}(\text{CIGS})_{0.15}$ crystal, which often provide recombination sites. In order to avoid the formation of Zn-deficient surface, effects of a postdeposition treatment (PDT) with Zn were investigated. While the $(\text{ZnSe})_{0.85}(\text{CIGS})_{0.15}$ thin film was being cooled from 723 to 573 K after deposition, the film was exposed to Zn and Se vapor. The deposition rates were same as those during film deposition. Figure 2-3-5 (a) shows in-depth relative peak intensity of Zn, where the outermost surface was not measured because of the influence of the chemical etching using KCN. Without PDT, the continuous decrease of the relative intensity of Zn toward the outermost surface was observed, possibly due to re-evaporation of Zn during the cooling process. On the other hand, the sample with PDT showed a slight increase in the Zn peak intensity. These results suggest that the PDT effectively alleviates the decrease of Zn species from the film surface by feeding additional Zn onto the surface. Consequently, the $\text{Pt}/\text{Mo}/\text{Ti}/\text{CdS}/(\text{ZnSe})_{0.85}(\text{CIGS})_{0.15}$ photocathode showed a meaningful increase in the photocurrent as shown in Figure 2-3-5 (b). The photocurrent value at 0 V_{RHE} recorded 7.1 mA

cm⁻², which is clearly smaller than that of the Cu(In,Ga)Se₂ photocathode (see Figure 1-4-4). However, the onset potential (defined as a cathodic photocurrent of 0.05 mA cm⁻²) reached 0.89 V_{RHE}, which is more positive than not only the Cu(In,Ga)Se₂ photocathode but also any other Cu-chalcopyrite-based photocathode as shown in Table 1-4-1. To conclude, the (ZnSe)_{0.85}(CIGS)_{0.15} photocathode prepared by an appropriate condition is able to a significantly high onset potential due to its deep VBM potential.

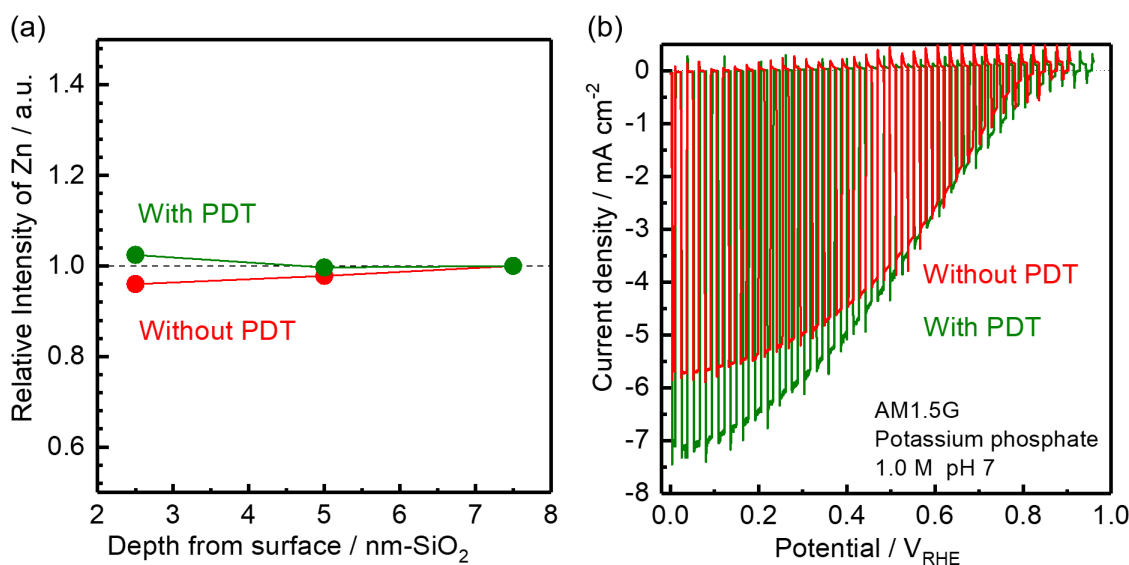


Figure 2-3-5. (a) In-depth relative intensity of Zn 2p_{3/2} XPS peaks obtained from the surface of (ZnSe)_{0.85}(CIGS)_{0.15} thin films with and without PDT. The peak intensity of Se 3d was used as the reference. (b) Current-potential curves for Pt/Mo/Ti/CdS/(ZnSe)_{0.85}(CIGS)_{0.15} photocathodes with and without PDT.

Figure 2-3-6 shows an IPCE spectrum of the (ZnSe)_{0.85}(CIGS)_{0.15} photocathode at 0 V_{RHE}, which indicates that the absorption edge of the photocathode is about 850 to 900 nm. Although that value is smaller than that of CuIn_{0.7}Ga_{0.3}Se₂, about 1100 nm, theoretically it is still able to show a photocurrent value of much higher than 10 mA cm⁻². Given the IPCE of 100% up to 900 nm, the corresponding photocurrent reach 34 mA cm⁻² under simulated sunlight (refer to Figure 1-3-11). The

(ZnSe)_{0.85}(CIGS)_{0.15} photocathode showed IPCEs higher than 40% without employment of multistage deposition process. Hence, there is a high possibility that further modification of the preparation process results in a significant improvement in the photocurrent, which is investigated in chapter 3. It should be noted that the onset of the IPCE spectrum shown in Figure 2-3-6 is relatively gentle, leading to especially small IPCEs at the wavelengths of 750-900 nm. The calculated distribution of density of states (DOS) exhibited in Figure 2-3-7 suggests that the DOS in the vicinity of CBM of (ZnSe)_{0.85}(CIGS)_{0.15} is obviously small than that of VBM due to the small fraction of In, which is known to compose the orbitals of the CBM of Cu(In,Ga)Se₂.^[28] In contrast, Figure 1-5-3 (a) in chapter 1 exhibits the calculated distribution of DOS for CuInSe₂ crystal, which shows the onset of DOS at CBM clearly steeper than that of (ZnSe)_{0.85}(CIGS)_{0.15}. Figure 2-3-8 shows a diffuse reflectance spectrum for the (ZnSe)_{0.85}(CIGS)_{0.15}. The sample was exfoliated from the thin film to avoid observation of optical interference, and therefore it contains considerable impurities such as MoSe_{2-x}, contributing to the relatively high background. Although the band gap estimated from the extrapolation from the steep was approximately 800 nm, the significant tail at the range of 750-900 nm in wavelength extended the onset of absorbance up to 900 nm. The unique absorbance spectrum is consistent with the IPCE spectrum and distribution of DOS.

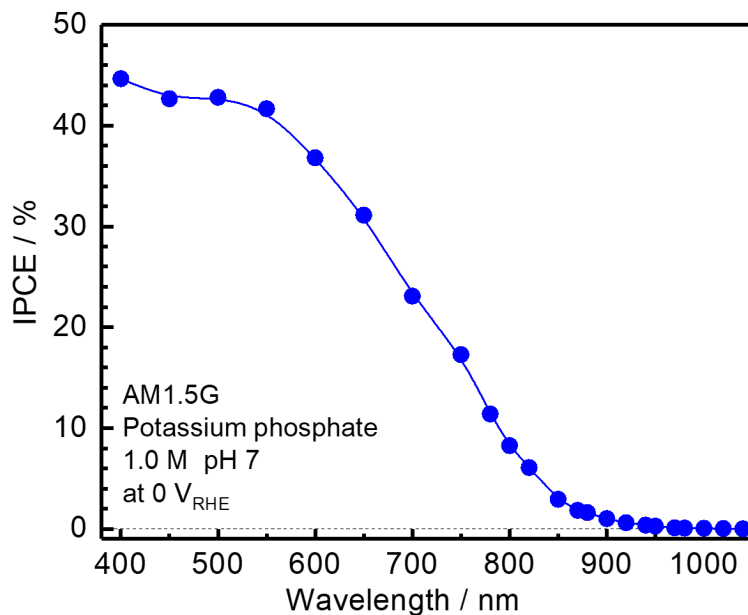


Figure 2-3-6. Wavelength dependence of IPCEs at 0 V_{RHE} for the Pt/CdS/(ZnSe)_{0.85}(CIGS)_{0.15} photocathode.

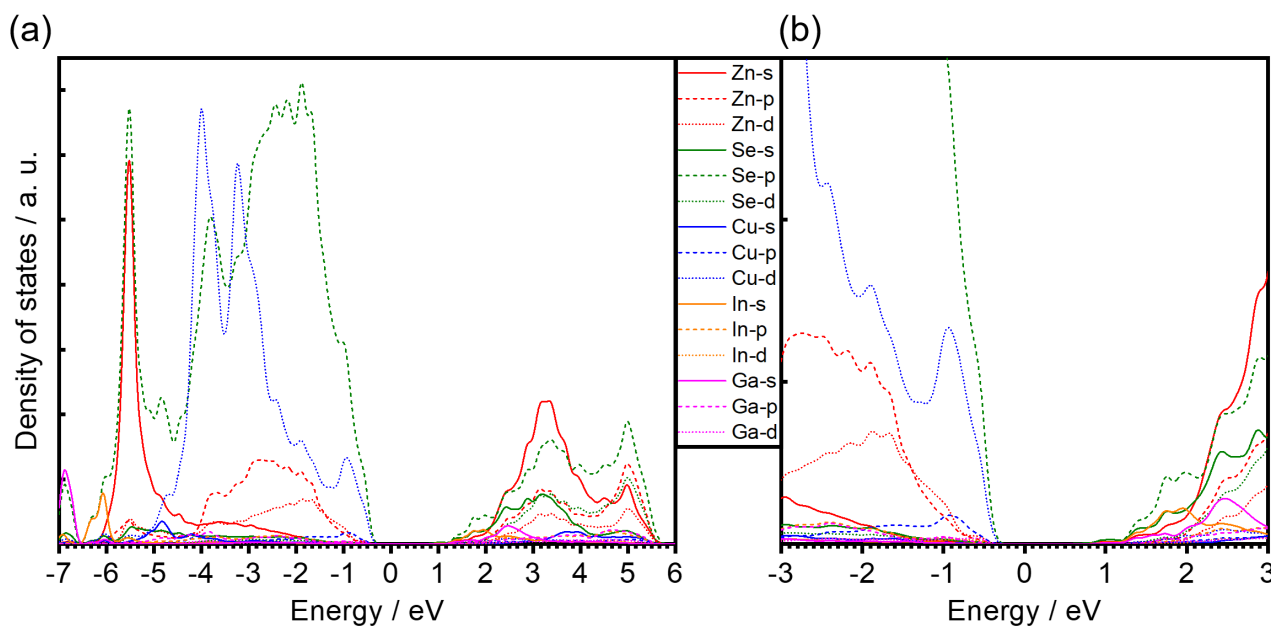


Figure 2-3-7. Distribution of DOS of (ZnSe)_{0.85}(CIGS)_{0.15} calculated by assuming the crystal structure shown in Figure 2-2-2 (a), and the zoom graph in the vicinity of the CBM and VBM (b).

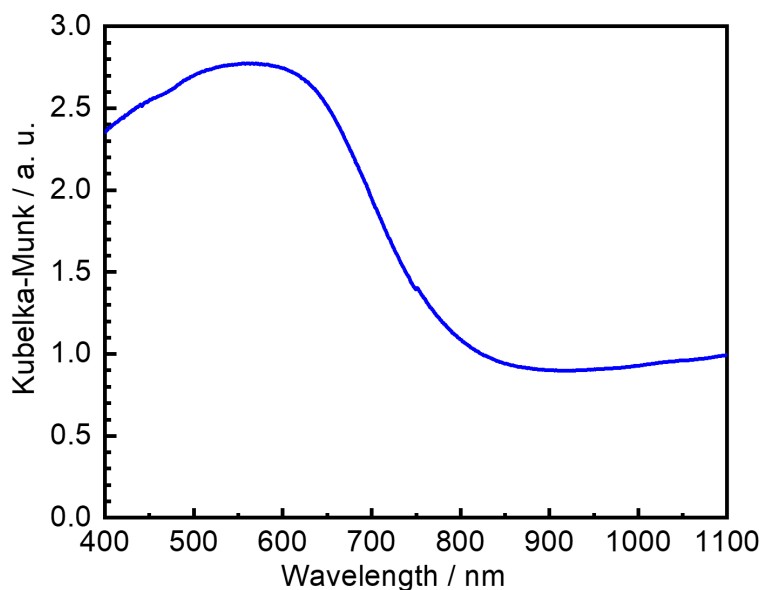


Figure 2-3-8. A diffuse reflectance spectrum of (ZnSe)_{0.85}(CIGS)_{0.15} powder exfoliated from the thin film.

The carrier concentration in the (ZnSe)_{0.85}(CIGS)_{0.15} prepared at $\mu_{\text{Cu}} = 0.0$ was calculated to be $3 \times 10^{16} \text{ cm}^{-3}$ by using the obtained DOS, the Fermi level (0.42 eV), formation energy of each defect and Eqs. (1-3a) and (1-3b).^[12] The value is comparable with that obtained by Mott-Schottky plots and Hall measurements (see chapter 3), supporting the consistency of the DFT calculations.

2-3-4 Overall Water Splitting using the ZnSe:Cu(In,Ga)Se₂ Photocathode and a BiVO₄ Photoanode

The Pt/Mo/Ti/CdS/(ZnSe)_{0.85}(CIGS)_{0.15} photocathode showed a relatively high onset potential of 0.89 V_{RHE}. Accordingly, the PEC cell consisting of the photocathode is expected to show a spontaneous overall water splitting without any external bias voltage. A BiVO₄ photoanode modified with NiFeO_x-Bi (termed as NiFeO_x-Bi/BiVO₄ herein), which is known as efficient OER catalyst in a borate buffer solution,^[9] was employed due to the relatively high IPCEs and stability.^[10] Figure 2-4-1 (a) shows current-potential curves of each photoelectrode in a weak-alkaline 0.5 M potassium borate solution. The electrolyte is a more suitable for the NiFeO_x-Bi/BiVO₄ photoanode, while the

photocathode showed slightly small photocurrent in the electrolyte. The estimated working current and potential of the two-electrode cell were 1.08 mA and 0.55 V_{RHE}, respectively, according to the intersection of each current-potential curve. It should be noted that the employment of the Pt/Mo/Ti/CdS/(ZnSe)_{0.85}(CIGS)_{0.15} photocathode showed a slight but considerable increase in the estimated photocurrent at the working potential compared with the conventional CuIn_{0.7}Ga_{0.3}Se₂-based photocathode in spite of the widened band gap, and that further improvement in the photocurrent is expected by modification of film preparation process as discussed in the next chapter. After the cell was constructed in a parallel scheme using the Pt/Mo/Ti/CdS/(ZnSe)_{0.85}(CIGS)_{0.15} photocathode and the NiFeO_x-Bi/BiVO₄ photoanode, it was irradiated by simulated sunlight and the photocurrent was plotted in Figure 2-4-1 (b). The initial photocurrent was 0.89 mA 30 s after the beginning of light irradiation, which corresponds to the solar-to-hydrogen conversion efficiency (STH) of 0.91%. On the other hand, the STH decreased to 0.72% 30 min after the beginning. Because the XPS peaks of Pt, Mo, Ti, Cd and S became weaker after the reaction as shown in Figure 2-4-2, corrosion of CdS is likely to have caused degradation of the photocathode. The instability of CdS layer is discussed in chapter 5. Furthermore, a reversible decrease of ~5% in the photocurrent was observed when the magnetic stirring was stopped. It suggests the presence of resistance due to mass transport in the electrolyte, which has already been discussed in section 1-3-4. Investigations to address the mass transport limitation are conducted in chapter 4.

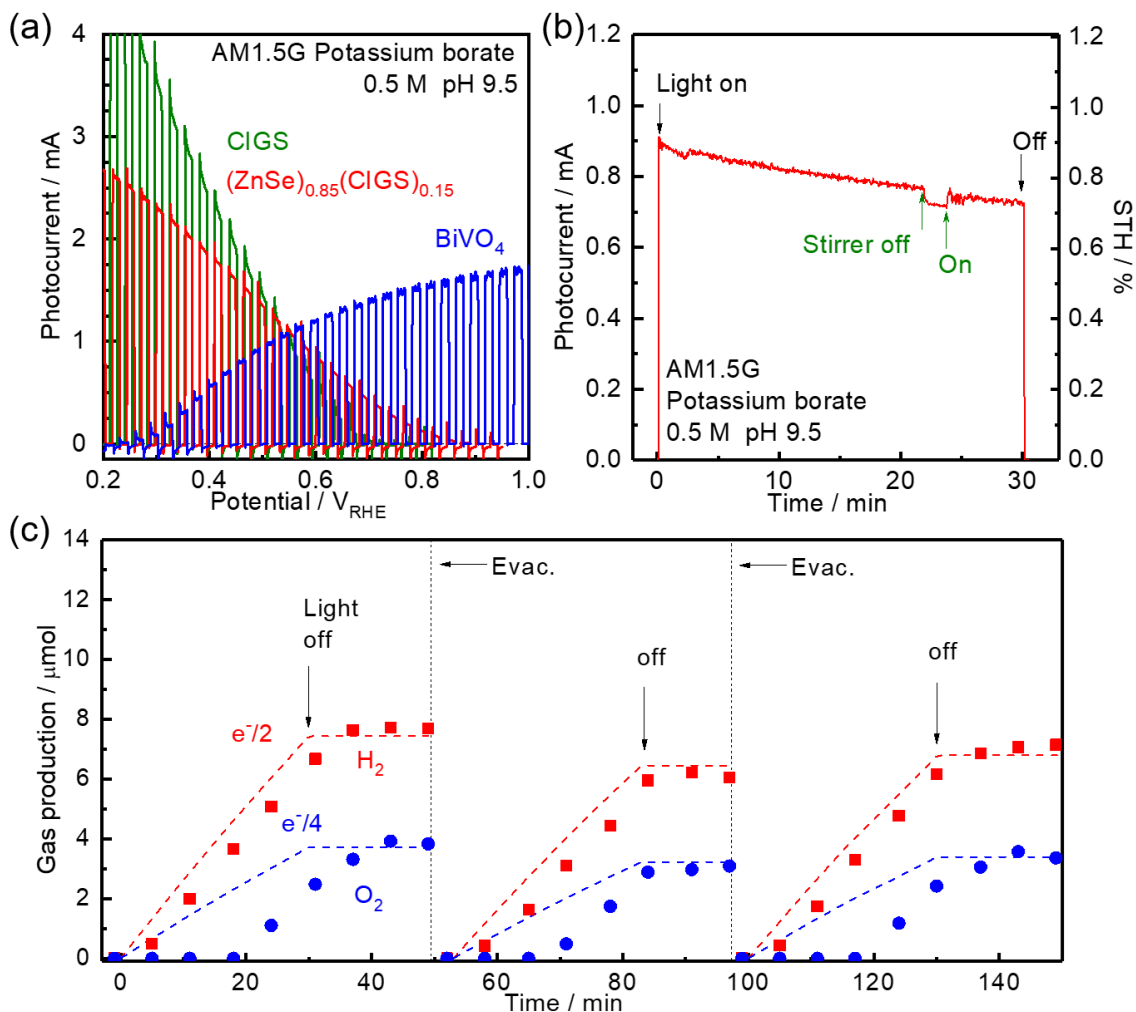


Figure 2-4-1. (a) Current-potential curves for a Pt/Mo/Ti/CdS/(ZnSe)_{0.85}(CIGS)_{0.15} photocathode (red, geometric area of 0.28 cm²) and NiFeO_x-Bi/BiVO₄ photoanode (blue, 0.90 cm²). The green line represents a typical current-potential curve for a CuIn_{0.7}Ga_{0.3}Se₂-based photocathode with a geometric area of 0.28 cm².^[6] (b) A current-time curve for the two-electrode cell under simulated sunlight. (c) The amount of evolved H₂ (red) and O₂ (blue) over the cell. The dashed lines represent the amount expected for a Faradaic efficiency of unity.

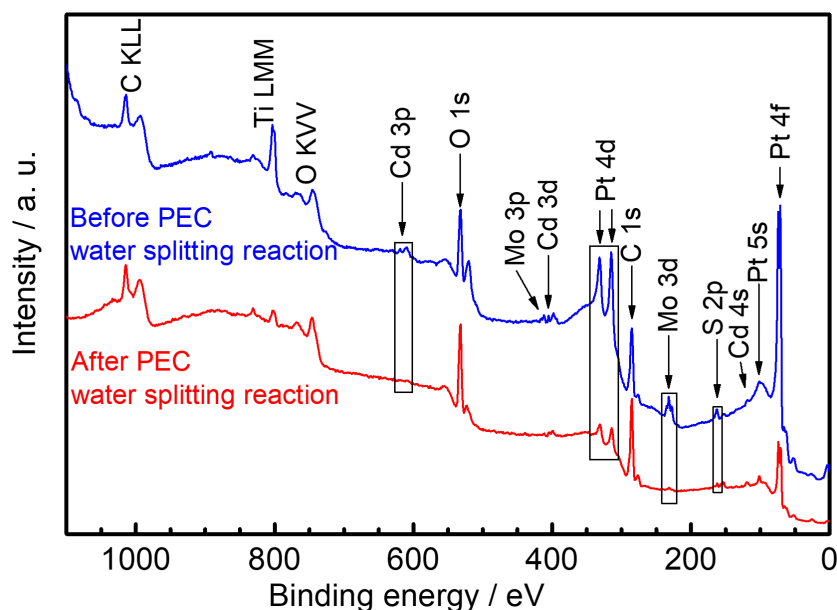


Figure 2-4-2. XPS spectra for the Pt/Mo/Ti/CdS/(ZnSe)_{0.85}(CIGS)_{0.15} photocathodes before and after the overall water splitting reaction shown in Figure 2-4-1.

The time-course of the amount of evolved H₂ and O₂ was measured using gas chromatograph and shown in Figure 2-4-1 (c). Although there were delays for the detection of each gas due to the homogenization time for the gas phase in the cell, the Faradaic efficiency was calculated to be about 100% for three times of measurements. The average STHs of the first, second and third measurements were 0.8%, 0.7% and 0.7%, respectively. The STH values of the PEC cell are higher than those of previous reports (see Table 1-4-1) and even comparable with the state-of-the-art cells employing complicate modifications on coating layers and/or their morphologies.^[29,30]

2-4 Conclusions

Effects of ZnSe introduction into Cu(In,Ga)Se₂ thin films were investigated. The solid solution of ZnSe and Cu(In,Ga)Se₂ deposited at the optimum temperature showed a uniform and dense structure and no phase separation. The ZnSe mole fraction of 70-90% resulted in the deepening of

VBM potentials by 0.2-0.3 eV, and consequently, (ZnSe)_{0.85}(CIGS)_{0.15} photocathodes showed a higher onset potential than the conventional Cu(In,Ga)Se₂ photocathode by 0.17 V.

The deposition condition preferable for (ZnSe)_x(CIGS)_{1-x} thin films is different from that for Cu(In,Ga)Se₂ thin films. A relatively low deposition temperature is required in order to prevent re-evaporation of Zn, which shows higher vapor pressure than many other metals. It is also necessary to employ PDT of Zn after film deposition to compensate the Zn species evaporated from the film surface. Moreover, Cu-rich condition during film deposition is indispensable for (ZnSe)_x(CIGS)_{1-x} to show a sufficient net density of acceptors. This is probably because the density of Zn-related donor defects increases under Cu-poor condition, which is supported by first principle calculations.

A PEC cell composed of the (ZnSe)_{0.85}(CIGS)_{0.15} photocathode and BiVO₄ photoanode showed a relatively high STH of 0.91% without any external bias voltage. On the other hand, a meaningful degradation of the photocathode was observed due to corrosion of the CdS layer. Hence, further investigations on surface protection were needed to address the corrosion problem and to improve durability of the photocathode, which is conducted in chapter 5.

To conclude, the (ZnSe)_{0.85}(CIGS)_{0.15} photocathode was confirmed to be a promising photocathode material due to the relatively high onset potential and long absorption edge wavelength. In the next chapter, further modification of the preparation process so as to improve the photocurrent of the photocathode is investigated.

References

- [1] S. Li, Z. Zhao, Q. Liu, L. Huang, G. Wang, D. Pan, H. Zhang, X. He, *Inorg. Chem.* **2011**, 50, 11958.
- [2] T. Yamamoto, T. Negami, K. Matsubara, S. Niki, *Jpn. J. Appl. Phys.* **2012**, 51, 10NC06.
- [3] H. Kaneko, T. Minegishi, K. Domen, *Coatings* **2015**, 5, 293.

- [4] S. Thiru, M. Asakawa, K. Honda, A. Kawaharazuka, A. Tackeuchi, T. Makimoto, Y. Horikoshi, *AIP Adv.* **2015**, 5, 027120.
- [5] S. Niki, M. Contreras, I. Repins, M. Powalla, K. Kushiya, S. Ishizuka, K. Matsubara, *Prog. Photovoltaics Res. Appl.* **2010**, 18, 453.
- [6] H. Kumagai, T. Minegishi, N. Sato, T. Yamada, J. Kubota, K. Domen, *J. Mater. Chem. A* **2015**, 3, 8300.
- [7] M. Moriya, T. Minegishi, H. Kumagai, M. Katayama, J. Kubota, K. Domen, *J. Am. Chem. Soc.* **2013**, 135, 3733.
- [8] D. Yokoyama, T. Minegishi, K. Maeda, M. Katayama, J. Kubota, A. Yamada, M. Konagai, K. Domen, *Electrochem. Commun.* **2010**, 12, 851.
- [9] A. M. Smith, L. Trotochaud, M. S. Burke, S. W. Boettcher, *Chem. Commun.* **2015**, 51, 5261.
- [10] Y. Kuang, Q. Jia, H. Nishiyama, T. Yamada, A. Kudo, K. Domen, *Adv. Energy Mater.* **2016**, 6, 1501645.
- [11] S. Chen, X. G. Gong, A. Walsh, S.-H. Wei, *Phys. Rev. B* **2009**, 79, 165211.
- [12] A. Kubo, *Ph.D. Thesis*; The University of Tokyo, 2018.
- [13] D. R. Lide, *CRC Handbook Chemistry and Physics*; Lide, D. R., Ed.; 85th Editi.; CRC Press, 2005.
- [14] T. Pan, L. Sun, *Int. J. Electrochem. Sci.* **2012**, 7, 9325.
- [15] E. O. Kane, *Phys. Rev.* **1962**, 127, 131.
- [16] S. Chen, X. G. Gong, S. H. Wei, *Phys. Rev. B* **2007**, 75, 205209.
- [17] C. S. Quintans, H. Kato, M. Kobayashi, H. Kaga, A. Iwase, A. Kudo, M. Kakihana, *J. Mater. Chem. A* **2015**, 3, 14239.
- [18] M. A. Contreras, B. Egaas, K. Ramanathan, J. Hiltner, A. Swartzlander, F. Hasoon, R. Noufi, *Prog. Photovoltaics Res. Appl.* **1999**, 316, 311.

- [19] H. Kumagai, T. Minegishi, Y. Moriya, J. Kubota, K. Domen, *J. Phys. Chem. C* **2014**, *118*, 16386.
- [20] B. Ümsür, W. Calvet, B. Höpfner, A. Steigert, I. Lauermann, M. Gorgoi, K. Prietzel, H. A. Navirian, C. A. Kaufmann, T. Unold, M. C. Lux-Steiner, *Thin Solid Films* **2014**.
- [21] K. Ramanathan, F. S. Hasoon, S. Smith, A. Mascarenhas, H. Al-Thani, J. Alleman, H. S. Ullal, J. Keane, P. K. Johnson, J. R. Sites, *Conf. Rec. Twenty-Ninth IEEE Photovolt. Spec. Conf. 2002*. **2002**.
- [22] Y. Y. I. Choi, **2013**, *1*, 52.
- [23] T. Sugiyama, S. Chaisitsak, A. Yamada, M. Konagai, Y. Kudriavtsev, A. Godnes, A. Villegas, R. Asomoza, *Jpn. J. Appl. Phys.* **2000**, *39*, 4816.
- [24] Y. J. Zhao, C. Persson, S. Lany, A. Zunger, *Appl. Phys. Lett.* **2004**, *85*, 5860.
- [25] M. Grossberg, J. Krustok, S. Siebentritt, J. Albert, *Phys. B Condens. Matter* **2009**, *404*, 1984.
- [26] T. Inoue, *J. Electrochem. Soc.* **1977**, *124*, 719.
- [27] P. Jackson, D. Hariskos, R. Wuerz, O. Kiowski, A. Bauer, T. M. Friedlmeier, M. Powalla, *Phys. status solidi - Rapid Res. Lett.* **2015**, *9*, 28.
- [28] M. Turcu, U. Rau, *Thin Solid Films* **2003**, *431–432*, 158.
- [29] L. Pan, J. H. Kim, M. T. Mayer, M.-K. Son, A. Ummadisingu, J. S. Lee, A. Hagfeldt, J. Luo, M. Grätzel, *Nat. Catal.* **2018**, *1*, 412.
- [30] D. Huang, K. Wang, L. Yu, T. H. Nguyen, S. Ikeda, F. Jiang, *ACS Energy Lett.* **2018**, *3*, 1875.

Chapter 3

Enhancement of Charge Separation Efficiency and Visualization of the Separation Fields in ZnSe:Cu(In,Ga)Se₂ Photocathodes

3-1 Introduction

Through chapter 2, photoelectrochemical (PEC) properties of (ZnSe)_x(CuIn_{0.7}Ga_{0.3}Se₂)_{1-x} photocathodes, especially at $x = 0.85$, were investigated. The (ZnSe)_{0.85}(CuIn_{0.7}Ga_{0.3}Se₂)_{0.15} (abbreviated as (ZnSe)_{0.85}(CIGS)_{0.15} herein) photocathode showed the relatively high onset potential of 0.89 V_{RHE} under simulated sunlight when modified with CdS and a Mo/Ti binary as an n-type layer and surface conductor, respectively. The high fraction of ZnSe to CuIn_{0.7}Ga_{0.3}Se₂ can reduce the use of expensive rare-metals of In and Ga. Furthermore, the absorption edge wavelength is located at around 900 nm, which means that the photocathode can utilize not only visible light but also near infrared light. As a specific example, given an incident photon-to-current conversion efficiency (IPCE) of 100% up to the absorption edge, the theoretically available photocurrent value reaches as high as about 34 mA cm⁻² under simulated sunlight of AM1.5G.

However, the photocurrent value experimentally observed was limited to 7.1 mA cm⁻², and the corresponding IPCEs were less than 45% as exhibited in Figure 2-3-5 and 2-3-6, respectively. The most probable reason for the low photocurrent and IPCE values is the relatively small grain size and rough surface of (ZnSe)_{0.85}(CIGS)_{0.15} thin films. Cu(In,Ga)Se₂ thin film photocathodes composed of smooth surface and the grains with the size of larger than 1 μm show a high IPCE of about 80%.^[1] The small grain size causes charge recombination at the grain boundaries and/or defective interfaces at the CdS-(ZnSe)_{0.85}(CIGS)_{0.15} interface, resulting in the significant loss in the IPCE.

Therefore, structural modification of the (ZnSe)_{0.85}(CIGS)_{0.15} thin film is expected to be an effective way to enhance PEC hydrogen evolution reaction (HER). In the current chapter, modification of film structure of (ZnSe)_{0.85}(CIGS)_{0.15} was investigated by introducing a multistage deposition method to form laminated structure of an In-rich and Ga-rich layer, termed the bilayer method herein. It is noted that the conventional deposition process employed in chapter 2 was termed the monolayer method. Although another multistage deposition process, called the three-stage method, is often employed for

Chapter 3. Enhancement of Charge Separation Efficiency and Visualization of the Separation Fields in ZnSe:Cu(In,Ga)Se₂ Photocathodes

application of Cu(In,Ga)Se₂ thin films into solar cells,^[2,3] the bilayer lamination has hardly been reported on them except for the work done by Lundberg et al.^[4]

Moreover, cross-sectional mapping of electron-beam-induced current (EBIC) was newly developed and conducted into the photocathodes so as to visualize the difference of charge separation efficiency between the two kinds of (ZnSe)_{0.85}(CIGS)_{0.15} thin films. The EBIC measurement has commonly been utilized in the fields related to semiconductor-based devices such as solar cells and transistors.^{[5–}

^{7]} To the best of the author's knowledge, however, this is the first report on its application to a photoelectrode.

3-2 Experimental Section

Preparation of (ZnSe)_x(CIGS)_{1-x} Thin Films

(ZnSe)_{0.85}(CIGS)_{0.15} thin films were deposited on substrates of Mo-coated soda-lime glass. The substrates were fabricated by RF magnetron sputtering of a Mo target (99.9%, Kojundo) onto each soda-lime glass plate heated at 573 K. Prior to the Mo deposition, a 30 nm thick Ti was deposited by the sputtering of a Ti target (99.9%, Kojundo) so as to improve the adhesion. The thickness of Mo and Ti are about 500 and 30 nm, respectively.

The substrate was loaded into a deposition chamber equipped with Knudsen cells containing elemental Cu, In, Ga, Zn and Se (99.9999%, Asahi Metal or Furuuchi Chemical). The substrate temperature was set at 623 K for 5 min and then reset to 723 K for 35 min. In the case of the monolayer method, the typical deposition rates for Cu, In, Ga, Zn and Se were 0.042, 0.048, 0.014, 0.4 and 1 nm s⁻¹, respectively, and all of the elements were evaporated simultaneously over the course of 40 min. In the case of the bilayer method, the typical deposition rates for Cu, In, Ga, Zn and Se were 0.042, 0.095, 0.028, 0.4 and 1 nm s⁻¹, respectively. In and Ga were absent for the first and last 20 min, respectively, followed by 10 min-annealing in a Se atmosphere. The rates were monitored by using

Chapter 3. Enhancement of Charge Separation Efficiency and Visualization of the Separation Fields in ZnSe:Cu(In,Ga)Se₂ Photocathodes

a quartz crystal microbalance sensor (Q-POD, INFICON). The pressure in the chamber was kept at $<2 \times 10^{-5}$ Pa during deposition. Following the film deposition processes, each sample was cooled from 723 to 573 K with exposure to Zn and Se vapor to alleviate the formation of a Zn-poor surface.

KCN Etching

After deposition, the samples were immersed into an etching solution containing 0.1 M KCN (98.0%, FUJIFILM Wako Pure Chemical) and 0.8 M KOH (8 M, FUJIFILM Wako Pure Chemical) for 1 min in room temperature. This etching process removed excess Cu from the (ZnSe)_{0.85}(CIGS)_{0.15} thin films. Energy dispersive X-ray spectroscopy (EDS; EMAX-7000, Horiba) analysis revealed that the atomic ratio of Cu/(In+Ga) was 0.9 to 1.0 after the process.

Characterization

The (ZnSe)_{0.85}(CIGS)_{0.15} thin film samples were analyzed using X-ray diffraction (XRD; RINT-Ultima3, Rigaku), photoelectron spectroscopy in air (PESA; AC-3, Riken Keiki), scanning electron microscopy (SEM; Hitachi), (scanning) transmission electron microscopy ((S)TEM; JEM-2800, JEOL) equipped with an SDD detector for STEM-EDS mapping (X-Max 100 TLE, Oxford Instruments), electron backscattering diffraction mapping (EBSD; JEM-7000F, JEOL) and EBIC mapping conducted together with SEM (JSM-7000F, JEOL) at an acceleration voltage of 5 kV. Prior to the EBIC measurement, a 100 nm-thick Mo layer was additionally deposited onto the surface of (ZnSe)_{0.85}(CIGS)_{0.15} photocathodes modified with CdS and a Mo/Ti binary. Hall measurement of the thin films exfoliated from the substrate was performed using a rotating parallel dipole line system, which was previously reported by O. Gunawan et al. in detail.^[8]

Surface Modification with an CdS Layer

A CdS layer was formed on the surface of each (ZnSe)_{0.85}(CIGS)_{0.15} thin film using chemical bath deposition (CBD) method.^[9–11] The CBD solution with a volume of 50 mL contained 14 wt% ammonia (28 wt%, FUJIFILM Wako Pure Chemical), 25 mM of Cd(CH₃COO)₂ (98.0%, FUJIFILM Wako Pure Chemical) and 0.375 M of SC(NH₂)₂ (98.0%, Kanto Chemical). The bath temperature

Chapter 3. Enhancement of Charge Separation Efficiency and Visualization of the Separation Fields in ZnSe:Cu(In,Ga)Se₂ Photocathodes

was gradually increased from room temperature to 325-326 K over the span of about 8 min. The samples were taken out from the bath and immediately washed with pure water 14 min after the initiation of heating, followed by annealing at 473 K for 1 min in air.

Surface Modification with Thin Metal Layers

A binary of Mo/Ti with each thickness of 3 nm was deposited by successive RF magnetron sputtering of a Ti and Mo target in room temperature.^[9] Subsequently, a Pt layer with a thickness of a few nanometers was deposited on it by thermal evaporation of Pt wire (99.98%, Nilaco) in a high vacuum of $<4 \times 10^{-3}$ Pa.

After these surface modifications, the (ZnSe)_{0.85}(CIGS)_{0.15} thin film samples were connected with a lead wire using indium at the Mo substrate exposed by polishing. The region not intended for measurement was coated with epoxy resin (Araldite Rapid, Nichiban), resulting in the geometric surface areas of specimens of 0.1-0.3 cm².

Preparation of NiFeO_x-Bi/BiVO₄ Photoanodes

A BiOI precursor was prepared on an indium tin oxide (ITO)-coated soda-lime glass substrate (0051, Geomatec) by electrodeposition method in a three-electrode cell with an Ag/AgCl reference electrode in a saturated aqueous KCl solution and with a Pt wire counter electrode. Subsequently, a dimethyl sulfoxide solution containing VO(C₅H₇O₂)₂ (98%, Sigma-Aldrich) was drop-cast onto the precursor, followed by calcination at 723 K for 1 h in air. As oxygen evolution reaction (OER) catalyst, NiFeO_x-Bi was deposited onto the prepared BiVO₄ electrode (NiFeO_x-Bi/BiVO₄) by photoelectrodeposition method.^[12] The potential of the electrode was held at -0.16 V vs. Ag/AgCl until saturation of the photocurrent (typically requiring 10-20 min) under simulated sunlight (XES-40S2-CE, SAN-EI Electric) in a 0.5 M aqueous potassium borate solution containing 4 μM NiSO₄ (99.9%, FUJIFILM Wako Pure Chemical) and 40 μM FeSO₄ (99%, FUJIFILM Wako Pure Chemical) with the pH adjusted to 9.5 by KOH addition. It should be noted that a previous report describes the fabrication process of the BiVO₄-based photoanode in more detail.^[13]

Chapter 3. Enhancement of Charge Separation Efficiency and Visualization of the Separation Fields in ZnSe:Cu(In,Ga)Se₂ Photocathodes

Photoelectrochemical Measurements

A three-electrode cell equipped with a magnetic stirrer under an Ar atmosphere using an aqueous solution of 1.0 M potassium phosphate buffer solution (pH 7.0) as the electrolyte was set up and connected to a potentiostat (HSV-110, Hokuto Denko), unless otherwise noted. A solar simulator (XES-70S1 or XES-40S2-CE, SAN-EI Electric) producing AM1.5G was employed as the light source. In the current-potential measurements, the applied potential, expressed relative to a reversible hydrogen electrode (RHE), was swept at 5 mV s⁻¹ from 0 V_{RHE} under intermittent irradiation with a period of 6 s.

The wavelength dependence of the incident photon-to-current conversion efficiency (IPCE) was evaluated under monochromatic light from a 300 W Xe lamp equipped with a monochromator (CT-10, JASCO), where the light intensity was measured using a Si photodiode (S2281-01, Hamamatsu Photonics).

Analysis of the evolved gases was conducted using an airtight and Ar-purged glass cell connected to a gas chromatograph (3000 Micro GC Gas Analyzer, Agilent Technologies) and a potentiostat.

3-3 Results and Discussion

3-3-1 Effects of Composition Gradient in the ZnSe:Cu(In,Ga)Se₂ Thin Films onto Their Photoelectrochemical Properties

(ZnSe)_{0.85}(CIGS)_{0.15} thin films were prepared by using the monolayer and bilayer methods, and their SEM images and XRD patterns are shown in Figure 3-1-1 and 3-1-2, respectively. It has often been reported that the grain size and/or crystal morphology of Cu-chalcopyrite-based materials strongly depends on the growth condition.^[14–16] However, the (ZnSe)_{0.85}(CIGS)_{0.15} thin film showed very small difference in the morphology by usage of the bilayer method, while the surface of the bilayer sample is relatively flat and the grain size is smaller than that of the monolayer sample. The wide-

Chapter 3. Enhancement of Charge Separation Efficiency and Visualization of the Separation Fields in ZnSe:Cu(In,Ga)Se₂ Photocathodes

range XRD patterns revealed that both samples show the prominent peaks associated with the (111) plane of zincblende ZnSe. On the other hand, clear peak separation was observed in the magnified pattern of the bilayer sample. Considering the fact that In-based compounds show larger lattice parameters than Ga-based compounds (e.g. *a*-axis lengths of CuInSe₂ and CuGaSe₂ are 5.8 Å and 5.6 Å, respectively.^[17]), the peaks at 27.1° and 27.3° were assigned to In- and Ga-rich phases, respectively. The two patterns were well-fitted by superposition of two pseudo-Voigt profiles to the observed peak. Therefore, these two phases were suggested to be separated to each other, which was supported by cross-sectional STEM-EDS mapping exhibited in Figure 3-1-3. The signals attributed to Ga and In were clearly separated in-depth. A possible reason for the insignificant diffusion is a small concentration of V_{III} (III = In or Ga) vacancies; Lundberg et al. has reported that interdiffusion of In and Ga between CuInSe₂ and CuGaSe₂ occurs via V_{III} vacancies. However, the (ZnSe)_{0.85}(CIGS)_{0.15} thin film contains relatively small density of such vacancies, which might prevent In and Ga from smooth interdiffusion. Also, the relatively low substrate temperature during film deposition can kinetically suppress the diffusion.

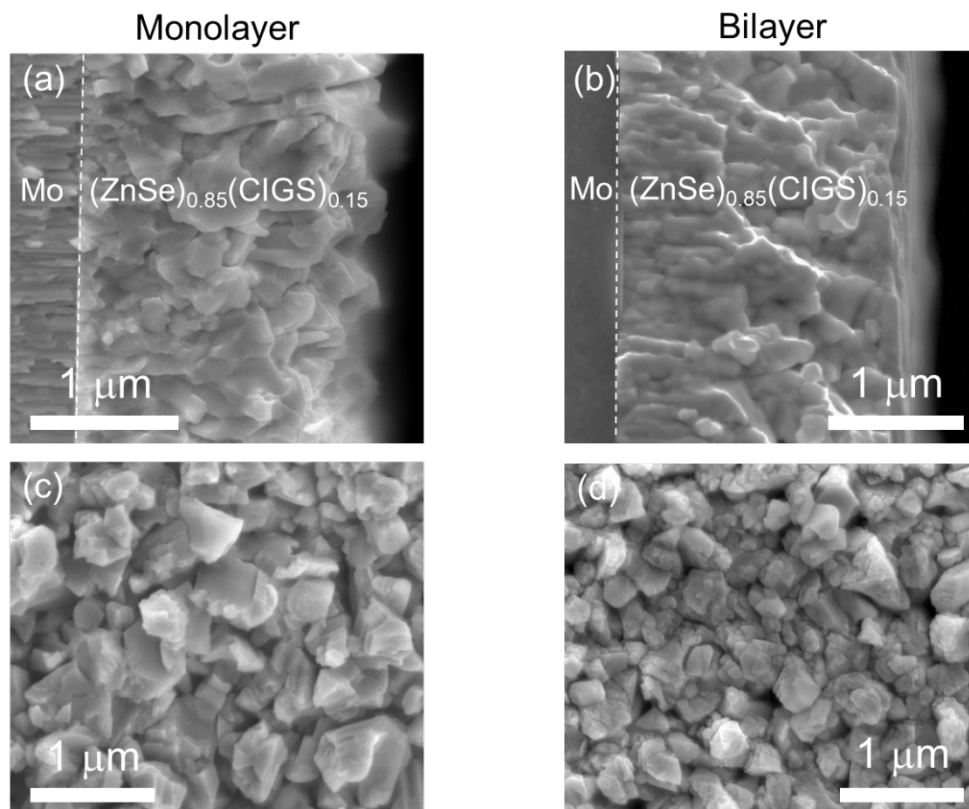


Figure 3-1-1. Cross-sectional (a, b) and surface (c, d) SEM images of $(\text{ZnSe})_{0.85}(\text{CIGS})_{0.15}$ thin films prepared by the monolayer (a, c) and bilayer (b, d) methods.

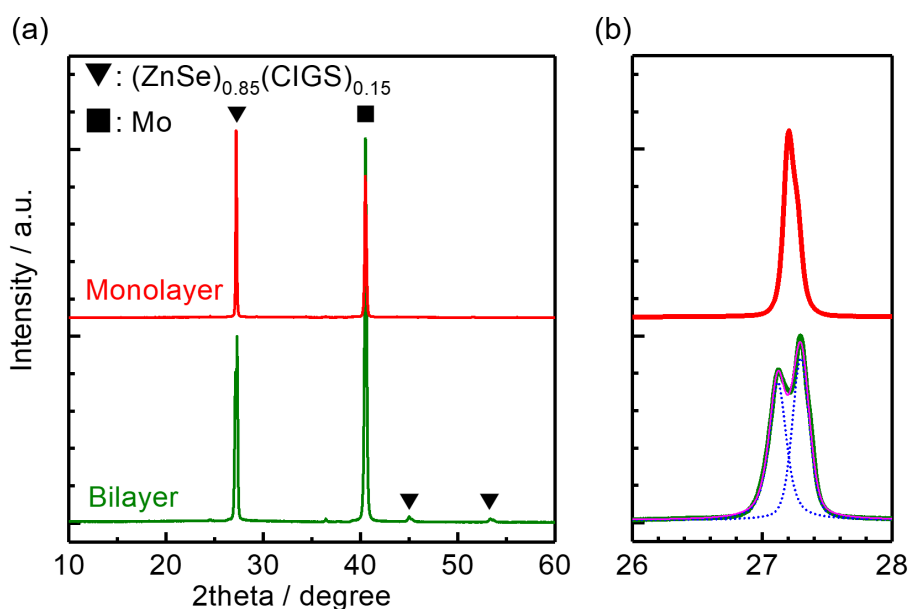


Figure 3-1-2. (a) XRD patterns of $(\text{ZnSe})_{0.85}(\text{CIGS})_{0.15}$ thin films prepared by the monolayer and bilayer methods, and (b) the magnified patterns. The intensities for the XRD patterns are normalized

Chapter 3. Enhancement of Charge Separation Efficiency and Visualization of the Separation Fields in ZnSe:Cu(In,Ga)Se₂ Photocathodes

to each peak intensity at around 27°. Two pseudo-Voigt profiles (blue dots) and their superposition (purple) are shown for the bilayer film.

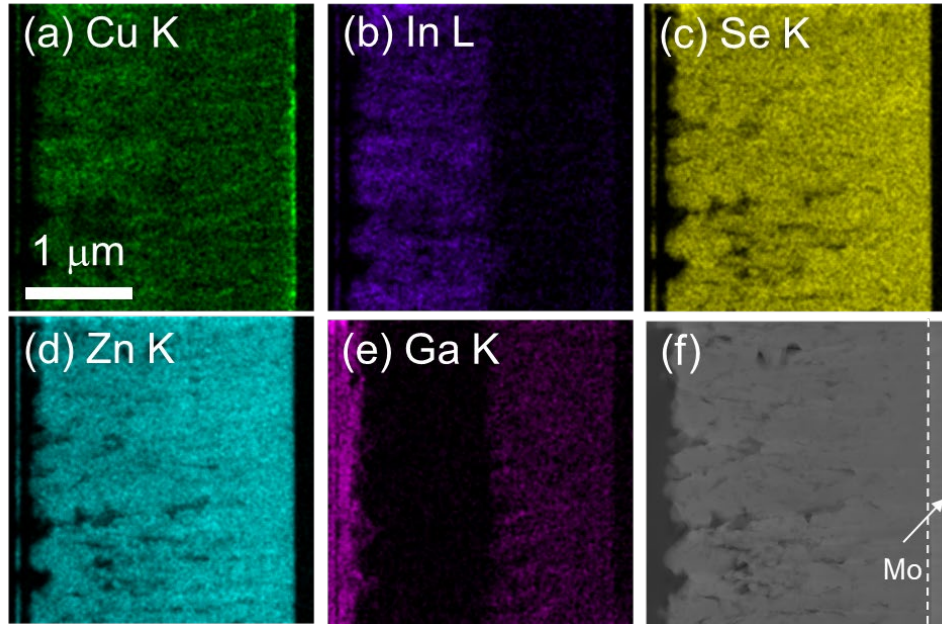


Figure 3-1-3. (a) Cross-sectional STEM-EDS elemental maps for (a) Cu, (b) In, (c) Se, (d) Zn and (e) Ga exhibited with (f) the corresponding STEM image for the (ZnSe)_{0.85}(CIGS)_{0.15} thin film prepared by the bilayer method. Ga was detected on the film surface due to the cross-sectioning process using a focused Ga-ion beam.

The bilayer method employs 10 min-annealing in a Se atmosphere after deposition of the (ZnSe)_{0.85}(CIGS)_{0.15} thin film. This is because the annealing process was found to alleviate existence of Cu_xSe residue as an impurity phase in the film; Figure 3-1-4 exhibits the cross-sectional STEM-EDS elemental maps for the bilayer (ZnSe)_{0.85}(CIGS)_{0.15} thin film without annealing process. In this case, Cu-rich phases (termed as Cu_xSe herein), which often acts as recombination sites,^[18] are significantly evident in the sample, although it showed a relatively large and dense crystals. Hence, the annealing process is important for the photocathode to suppress recombination of photoexcited

Chapter 3. Enhancement of Charge Separation Efficiency and Visualization of the Separation Fields in ZnSe:Cu(In,Ga)Se₂ Photocathodes

electrons and holes at the Cu_xSe region. Successful segregation of Cu_xSe phases by the annealing results in their own removal via the following KCN etching treatment.

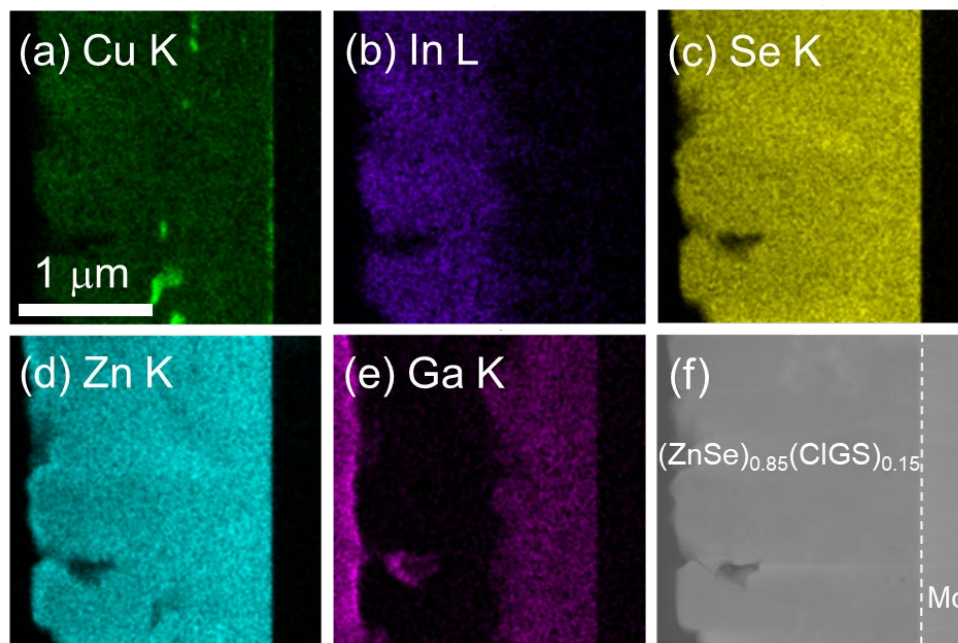


Figure 3-1-4. (a) Cross-sectional STEM-EDS elemental maps for (a) Cu, (b) In, (c) Se, (d) Zn and (e) Ga exhibited with (f) the corresponding STEM image for the (ZnSe)_{0.85}(CIGS)_{0.15} thin film prepared by the bilayer method without the 10 min-annealing process. Ga was detected on the film surface due to the cross-sectioning process using a focused Ga-ion beam.

Figure 3-1-5 shows current-potential curves for the (ZnSe)_{0.85}(CIGS)_{0.15} photocathodes prepared by using the monolayer method (without the annealing), the monolayer method followed by the 10 min-annealing and the bilayer method. The surface of each film was modified with CdS, a Mo/Ti binary and Pt (Pt/Mo/Ti/CdS/(ZnSe)_{0.85}(CIGS)_{0.15}). Employment of the monolayer method significantly increased the photocurrent values from 7.1 to 12 mA cm⁻² at 0 V_{RHE}. Moreover, there is almost no change in the onset potential, resulting in the similar increase in the photocurrent value at 0.6 V_{RHE}: from 2.6 to 4.9 mA cm⁻². On the other hand, the application of the 10 min-annealing to the

Chapter 3. Enhancement of Charge Separation Efficiency and Visualization of the Separation Fields in ZnSe:Cu(In,Ga)Se₂ Photocathodes

monolayer method didn't increase the photocurrent, so the annealing process itself didn't contribute to the improvement in the PEC property.

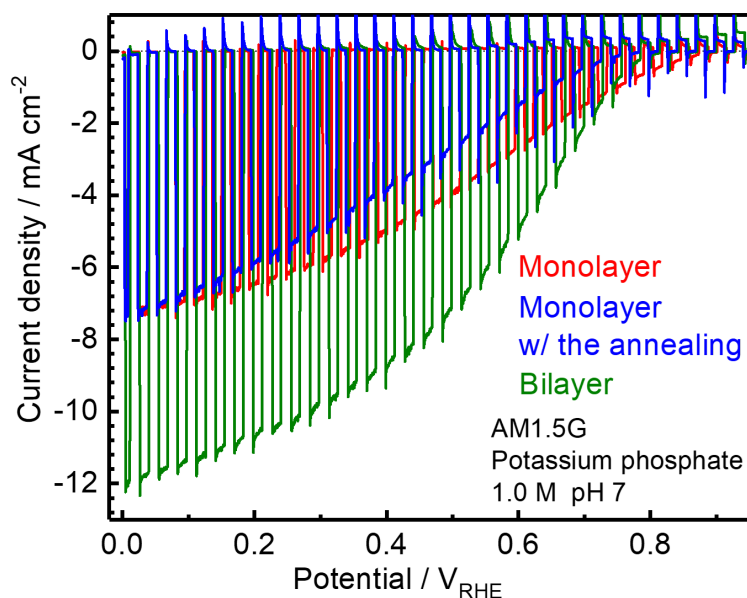


Figure 3-1-5. Current-potential curves for Pt/Mo/Ti/CdS/(ZnSe)_{0.85}(CIGS)_{0.15} photocathodes prepared by the monolayer method (red), the monolayer method (blue) and the bilayer method (green).

Another possible factor for the increase in photocurrent is that In-rich layer itself can show a high quantum efficiency. To reveal that point, an effect of the atomic ratio of Ga/(In+Ga) was also investigated using the monolayer method and exhibited in Figure 3-1-6. The continuous decrease in the photocurrent as the ratio decreased suggested that the employment of just the In-rich layer or the Ga-rich layer cannot result in the large photocurrent as shown in Figure 3-1-5. The significant decrease in the Ga-rich layer is most likely attributed to the widened band gap; CuGaSe₂ shows a larger band gap than CuInSe₂ by 0.6-0.7 eV (see Figure 1-5-2 in chapter 1). Correspondingly, the Ga-rich layer should show a considerably larger band gap than the In-rich layer, resulting in the decrease in the photocurrent. After all, formation of the bilayer was found to be indispensable to exhibit the PEC property, and the reason for the necessity of bilayer structure is discussed in the next section in detail.

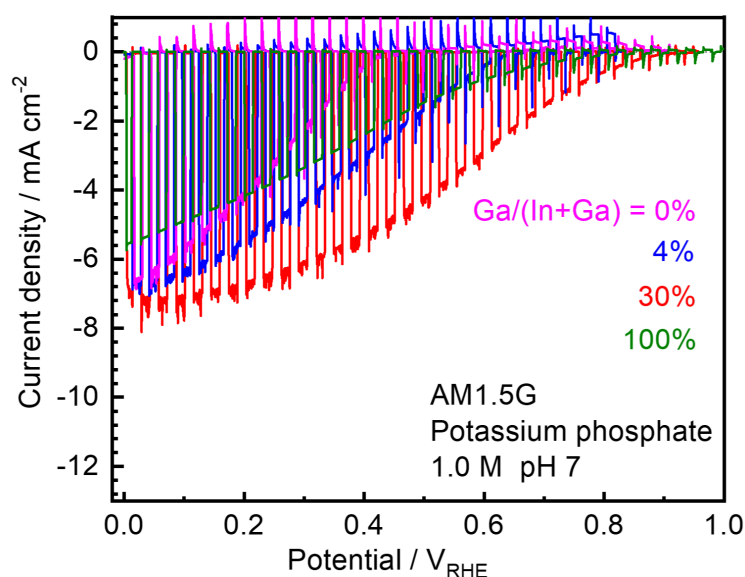


Figure 3-1-6. Current-potential curves for Pt/Mo/Ti/CdS/(ZnSe)_{0.85}(CIGS)_{0.15} photocathodes prepared by the monolayer method using various atomic ratios of Ga/(In+Ga).

Figure 3-1-7 shows the effects of annealing time for the bilayer samples on their current-potential properties. 10 min was found to be the optimum annealing period for the bilayer (ZnSe)_{0.85}(CIGS)_{0.15} photocathode, while a too long period of the annealing can cause severe re-evaporation of Zn species from the thin film as discussed in chapter 2. Difference in the XRD pattern by annealing time is compared in Figure 3-1-8. Although no clear impurity phase appeared after the annealing process, the intensity of the peak attributed to the underlying Ga-rich phase clearly increased, suggesting gradual decomposition of the outermost layer. It should be noted that the fusion of each peak shown in the sample annealed for 60 min suggests interdiffusion between each layer. The cross-sectional STEM-EDS image shown in Figure 3-1-9 clearly revealed the collapse of the In-rich layer. To conclude, the optimum period of annealing time is determined by the speeds of Cu_xSe segregation and re-evaporation of the thin film.

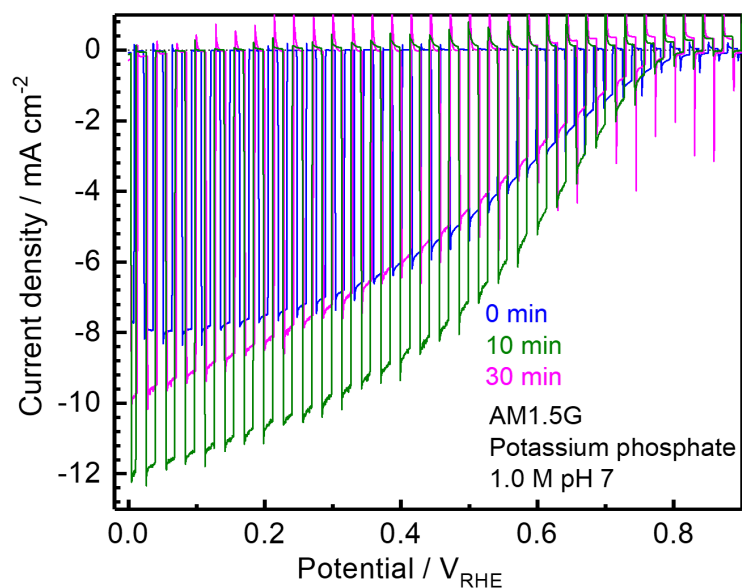


Figure 3-1-7. Current-potential curves for Pt/Mo/Ti/CdS/(ZnSe)_{0.85}(CIGS)_{0.15} photocathodes prepared by the monolayer method (red), the monolayer method (blue) and the bilayer method (green).

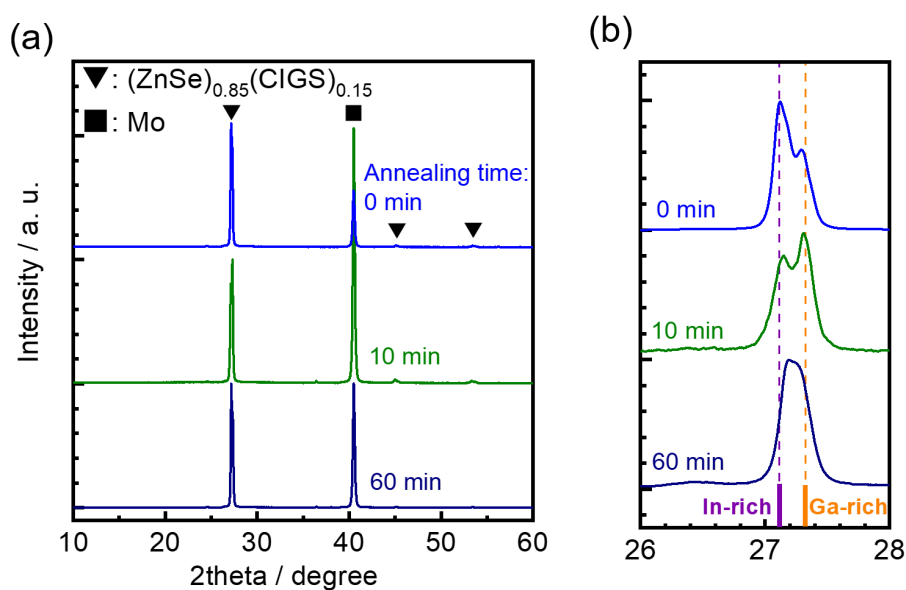


Figure 3-1-8. (a) XRD patterns of (ZnSe)_{0.85}(CIGS)_{0.15} thin films prepared by the bilayer method with various periods of annealing, and (b) the magnified patterns. The intensities for the XRD patterns are normalized to each peak intensity at around 27°.

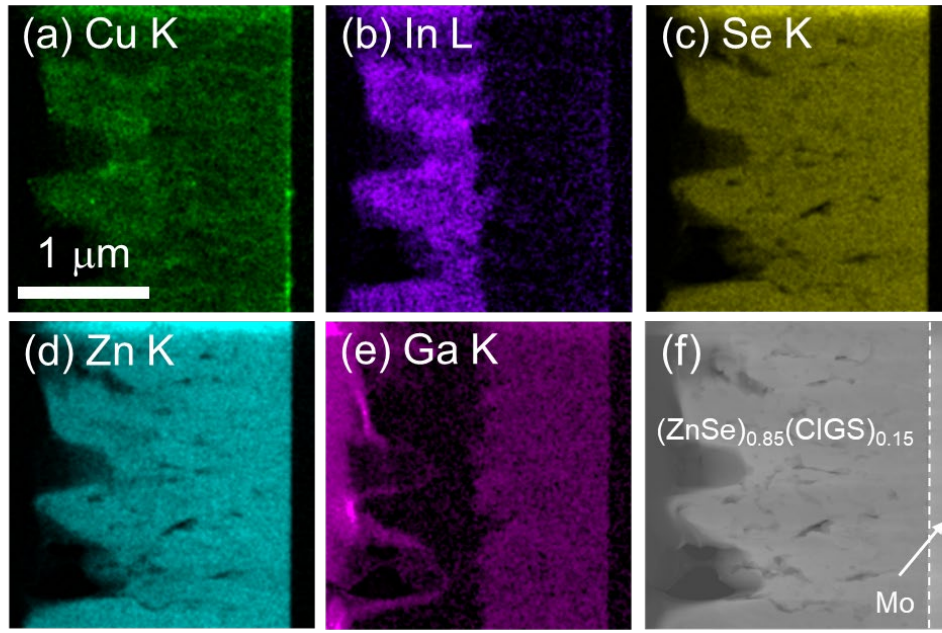


Figure 3-1-9. (a) Cross-sectional STEM-EDS elemental maps for (a) Cu, (b) In, (c) Se, (d) Zn and (e) Ga exhibited with (f) the corresponding STEM image for the (ZnSe)_{0.85}(CIGS)_{0.15} thin film prepared by the bilayer method with the annealing process for 30 min. Ga was detected on the film surface due to the cross-sectioning process using a focused Ga-ion beam.

Herein, half-cell STHs (HC-STHs) of the bilayer (ZnSe)_{0.85}(CIGS)_{0.15} photocathode and a conventional CuIn_{0.7}Ga_{0.3}Se₂ photocathode were plotted in Figure 3-1-10, which was calculated using the photocurrent in Figure 3-1-5 and Eq. (1-18).^[9,19] Both photocathodes employed the same surface modification. At potentials more negative than 0.5 V_{RHE}, the CuIn_{0.7}Ga_{0.3}Se₂ photocathode showed higher HC-STHs than the (ZnSe)_{0.85}(CIGS)_{0.15} photocathode, reaching 8.5% at 0.38 V_{RHE}. On the other hand, the bilayer (ZnSe)_{0.85}(CIGS)_{0.15} photocathode showed relatively high HC-STHs at potentials more positive than 0.5 V_{RHE} due to its high onset potential. The HC-STH at 0.6 V_{RHE} recorded 3.0% with the maximum value of 3.6% at 0.45 V_{RHE}, which is the most positive potential among Cu-chalcopyrite-based photocathodes (see Table 1-5-1). The positive shift in the HC-STH curve is preferable for efficient overall water splitting using a PEC cell. Figure 3-1-11 exhibits a current-time curve for the bilayer (ZnSe)_{0.85}(CIGS)_{0.15} photocathode at 0.45 V_{RHE}. The photocathode

Chapter 3. Enhancement of Charge Separation Efficiency and Visualization of the Separation Fields in ZnSe:Cu(In,Ga)Se₂ Photocathodes

showed very slight decrease in the photocurrent value of only 6% after the total illumination span of 3 h. As the cases of many other Cu-chalcopyrite-based photocathodes,^[10,20,21] the (ZnSe)_{0.85}(CIGS)_{0.15} photocathode is also capable of durable PEC HER at the potential, even though degradation would be observed due to corrosion of CdS layer at relatively positive potentials as discussed in section 1-5-2.

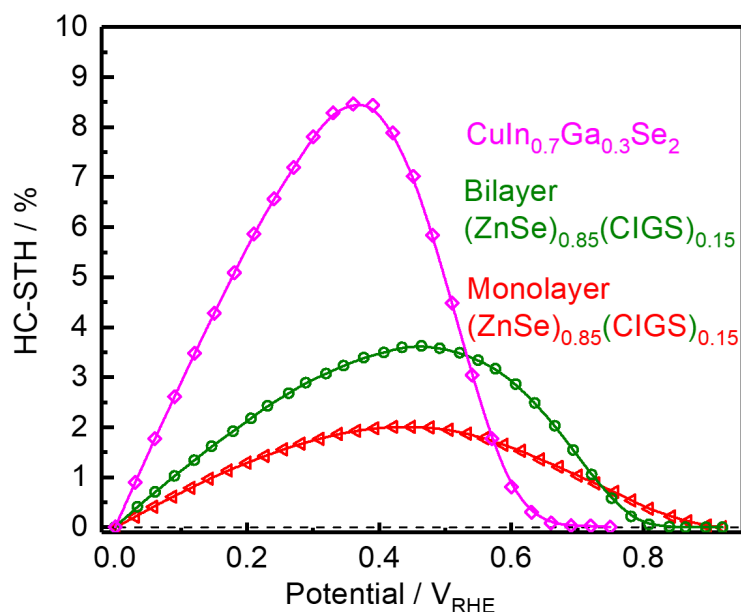


Figure 3-1-10. HC-STHs at each potential for the (ZnSe)_{0.85}(CIGS)_{0.15} photocathodes prepared by the monolayer (red) and bilayer (green) methods, and the CuIn_{0.7}Ga_{0.3}Se₂ photocathode (pink). The photocurrent values were extracted from Figure 3-1-5 and ref. [10] for the bilayer (ZnSe)_{0.85}(CIGS)_{0.15} photocathode and the CuIn_{0.7}Ga_{0.3}Se₂ photocathode, respectively.^[9]

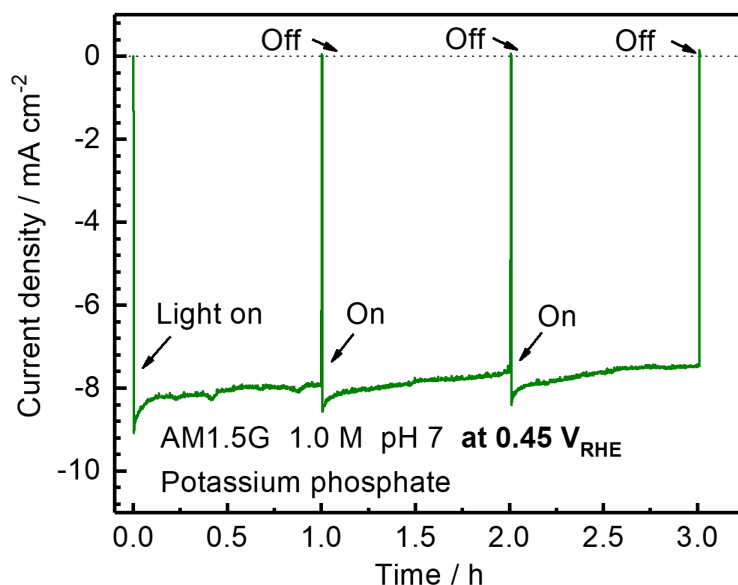


Figure 3-1-11. A current-time curve for Pt/Mo/Ti/CdS/(ZnSe)_{0.85}(CIGS)_{0.15} photocathode at 0.45 V_{RHE} prepared by the bilayer method.

Figure 3-1-12 shows IPCE spectra for the (ZnSe)_{0.85}(CIGS)_{0.15} photocathodes prepared by the monolayer and bilayer methods. Because the In-rich layer is estimated to show a narrower band gap than that of the Ga-rich layer, there was a slight (10-30 nm) shift in the absorption edge at the onset of IPCEs. The most probable reason for the negligible change in the absorption edge is that the orbitals of Ga affects the CBM as shown in Figure 2-3-7; the CBM of (ZnSe)_{0.85}(CIGS)_{0.15} is mainly composed of the orbitals of In and Se, which means that absence of Ga makes almost no difference in the band gap. Despite that, the bilayer sample exhibited a significant increase in the IPCEs at wavelength below 750 nm. The values reached greater than 60% in the 400 to 600 nm range. The significant increase in the IPCEs obviously contributed to the improvement of the PEC property. However, the characterizations obtained so far cannot find any clear difference in the property of the film, so it is difficult to explain the exact reason for the increase in the photocurrent value. In the next chapter, EBIC measurement is conducted to directly observe the active area for charge separation so as to find the reason.

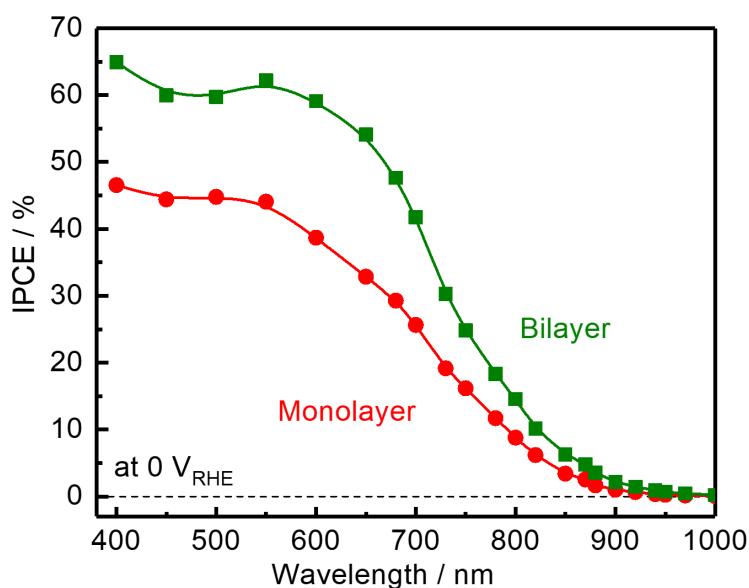


Figure 3-1-12. IPCE spectra at 0 V_{RHE} for the (ZnSe)_{0.85}(CIGS)_{0.15} photocathodes prepared by the monolayer (pink) and bilayer (green) methods.

3-3-2 Visualization of Charge Separation Fields Using Mapping of Electron-Beam-Induced Current Signals

In general, EBIC measurements have been conducted into solid-state devices in a high vacuum chamber.^[5,6] Photoelectrodes, however, generally function in the presence of a semiconductor-electrolyte interface. Therefore, the distribution of band bending can be dramatically different between the conditions in vacuum and an electrolyte. Figure 3-2-1 shows a schematic illustration of the EBIC measurement. By irradiation of highly energetic electrons (accelerated to 5 kV), inelastic collisions excite carriers at the irradiation part. Successful separation of the excited carriers is detected at the ammeter as the EBIC signal. Therefore, mapping of EBIC signals reflects the distribution of the area which is active in charge separation without significant recombination. Furthermore, the work function of the surface electrode metal determines the built-in potential at the metal-semiconductor interface. In this case, Mo and Ti were employed to reproduce the condition because their work functions, 4.45 eV for Mo and 4.33 eV for Ti, are very close to 0 V vs. normal

Chapter 3. Enhancement of Charge Separation Efficiency and Visualization of the Separation Fields in ZnSe:Cu(In,Ga)Se₂ Photocathodes

hydrogen electrode (NHE). It should be noted that the flat-band potential of CdS vs. NHE has been reported not to shift by changing the pH of an electrolyte.^[22] That means the measurement condition is almost equivalent to 0 V_{RHE}. Figure 3-2-2 shows the calculated band alignments at the interfaces composed of Mo/Ti, CdS, (monolayer) (ZnSe)_{0.85}(CIGS)_{0.15} and the substrate layers. The interface at the front-side is the Ohmic-contact for photoexcited electrons, and the depletion layer depth was estimated to be 200-250 nm. There has been a concern that a Schottky barrier is formed at the interface between (ZnSe)_{0.85}(CIGS)_{0.15} ($E_F = 5.3$ eV) and Mo ($\Phi = 4.4$ eV) layers. However, MoSe₂ ($E_F = 5.4$ eV),^[23] which is known to be formed under selenium atmosphere during film deposition, was found to effectively alleviate the Schottky barrier as shown in the right side of the figure.

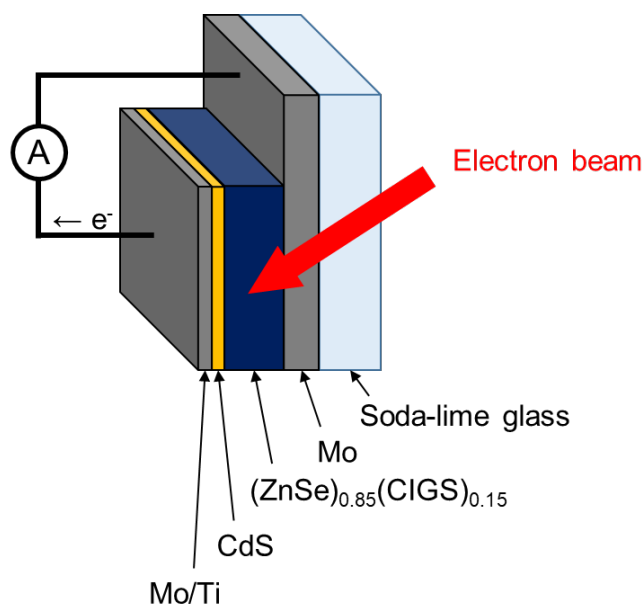


Figure 3-2-1. A scheme of the cross-sectional EBIC measurement.

Chapter 3. Enhancement of Charge Separation Efficiency and Visualization of the Separation Fields in ZnSe:Cu(In,Ga)Se₂ Photocathodes

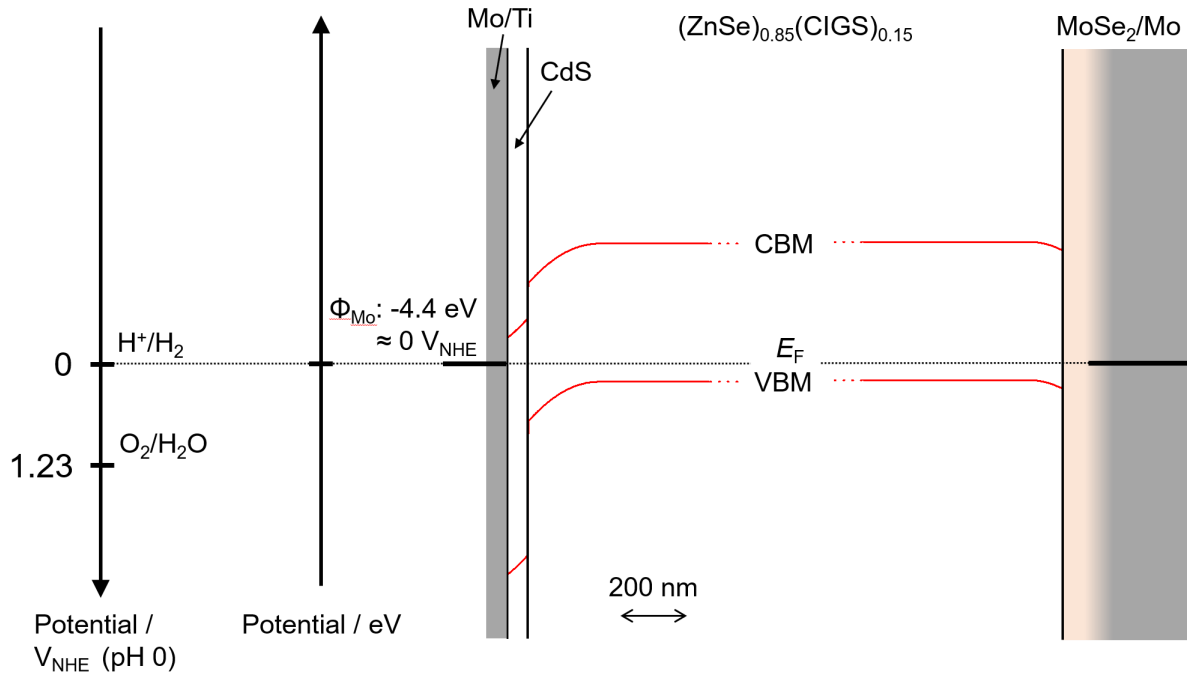


Figure 3-2-2. Calculated band alignments at the interfaces between the front contact (Mo/Ti), CdS, (ZnSe)_{0.85}(CIGS)_{0.15} layers and the substrate (p-type MoSe₂/Mo) based on the Poisson's equation: Eqs. (1-3) and (1-4), where $\varepsilon = 10$, $N_A = N_D = 10^{16} \text{ cm}^{-3}$ were assumed for both semiconductors. Band gap energies of CdS and (ZnSe)_{0.85}(CIGS)_{0.15} were set to 2.4 and 1.4 eV, respectively. Electron affinities of CdS and (ZnSe)_{0.85}(CIGS)_{0.15} were set to 4.45, 4.10 according to the reference and the result in chapter 2, respectively.^[24] The work function of Mo/Ti was set to 4.4 eV. The valence band maximum (VBM) of MoSe₂ was estimated to be 1.14 V_{NHE},^[23] where the offset to that of (ZnSe)_{0.85}(CIGS)_{0.15} (1.05 V_{NHE}) is -0.09 V. The difference in the Fermi level (E_F) and the conduction band minimum (CBM) of CdS, and that between the E_F and the VBM of (ZnSe)_{0.85}(CIGS)_{0.15} and MoSe₂ were both assumed to be 0.2 eV.

Figure 3-2-3 exhibits the results of EBIC mapping without application of any bias voltage between the back- and front-side electrodes. In both cases, the EBIC signals are distributed in the vicinity of CdS-(ZnSe)_{0.85}(CIGS)_{0.15} interfaces. The monolayer sample showed a poor uniformity than the bilayer sample, which suggests that the built-in potential at the region is not uniform. The uncolored

Chapter 3. Enhancement of Charge Separation Efficiency and Visualization of the Separation Fields in $\text{ZnSe}:\text{Cu}(\text{In,Ga})\text{Se}_2$ Photocathodes

region can be considered not to contribute to the PEC reaction, resulting in the relatively low IPCEs. On the other hand, the bilayer sample showed relatively higher uniformity of the EBIC signals. The distribution of the active region should be suitable for efficient separation of photoexcited carriers. The width of the active region is approximately 200-300 nm, which is quite consistent with the width of the depletion layer estimated by calculations such as Figure 3-2-2 and the reference.^[10] The interface between the In- and Ga-rich layers was also expected to be able to separate the excited carriers due to the offset in the band edges, but there was no signal observed. This is likely because the VBM offset between the two layers are so small that the extraction of holes to the back-side is not facilitated, as revealed by PESA spectra shown in Figure 3-2-4.

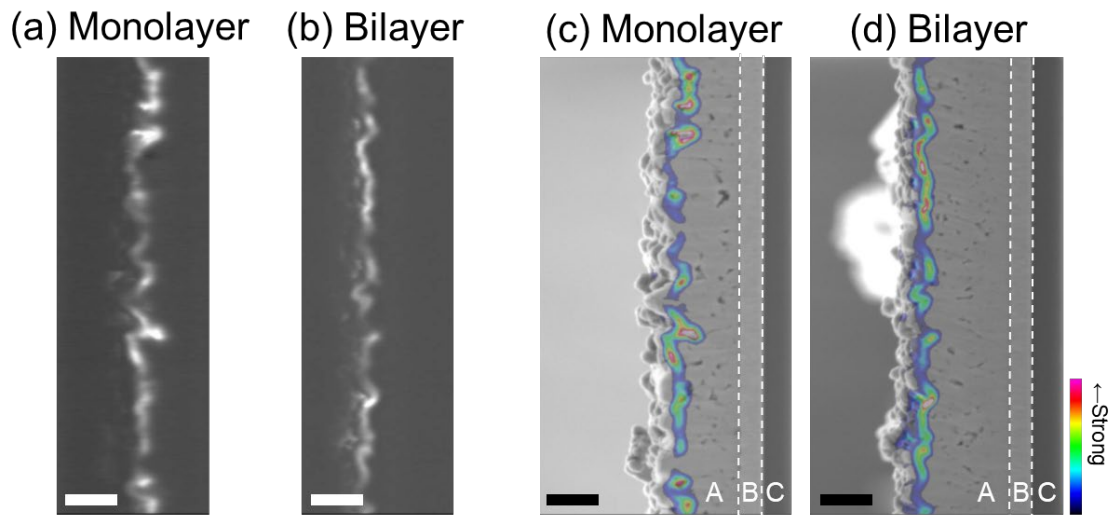


Figure 3-2-3. Maps of EBIC signals for the $(\text{ZnSe})_{0.85}(\text{CIGS})_{0.15}$ photocathodes prepared by the monolayer (a, c) and bilayer (b, d) methods. The signal intensity was normalized in each map (a, b), and then colorized maps (c, d) were generated according to the normalized values. The designations A, B and C stand for the $(\text{ZnSe})_{0.85}(\text{CIGS})_{0.15}$, Mo, and soda-lime glass, respectively. The scale bars are 1 μm .

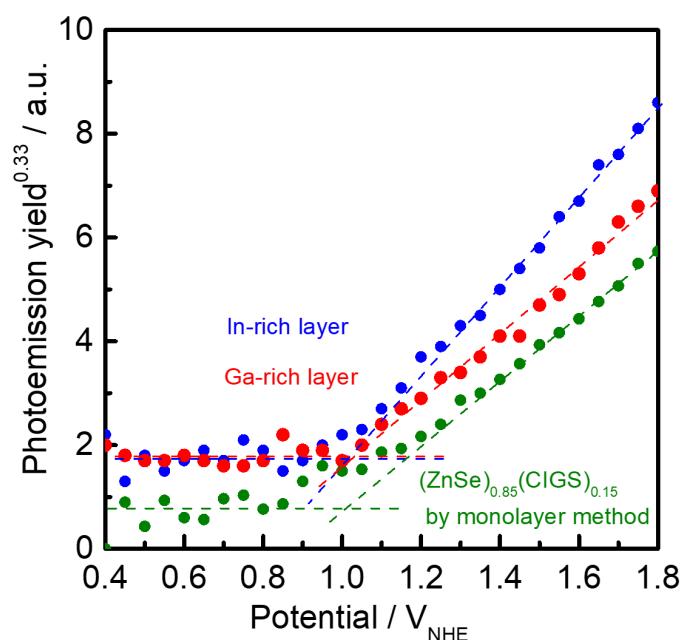


Figure 3-2-4. PESA spectra for the bilayer (ZnSe)_{0.85}(CIGS)_{0.15} thin film (green), the In- (blue) and Ga-rich (red) layers.

Instead, it is highly possible that the improved structure and crystallinity of the thin film contributes to the enhanced charge separation. Figure 3-2-5 exhibits cross-sectional SEM images of each monolayer at the back- and front-sides. In the back-side, the Ga-rich layer shows relatively high density in the middle of thin film, while a considerable number of voids can be found in the In-rich layer, which should form unfavorable built-in potential and act as recombination sites. On the other hand, the front-side of the Ga-rich layer is relatively rough compared with that of the In-rich layer. The smooth surface of the In-rich layer should be suitable for formation of uniform built-in potentials. EBSD mapping revealed that the In-rich phase shows a relatively large grain size, which is meaningfully oriented to the (111) plane of zincblende as shown in Figure 3-2-6. Moreover, the grain size is approximately twice as high as that of the monolayer sample. On the other hand, the region of Ga-rich phase exhibited a relatively low image quality, possibly due to the small grain size. Table 3-2-1 summarized the Hall mobility and carrier concentration of each layer. It is interesting that the Hall mobilities of the layers composing the bilayer sample are one order of magnitude higher than that

Chapter 3. Enhancement of Charge Separation Efficiency and Visualization of the Separation Fields in ZnSe:Cu(In,Ga)Se₂ Photocathodes

of the monolayer sample. A probable origin for the high Hall mobility of the Ga-rich layer is the high carrier concentration; it alleviates the influence of double Schottky barriers formed at grain boundaries as the majority carriers, holes, fill energy states in the vicinity of the band edge. However, the minority carriers, electrons, formed by photoexcitation process are not affected by the phenomenon, meaning that the actual mobility of minority carriers didn't significantly change. On the other hand, it is highly possible that the mobility of minority carriers as well as majority carriers in the In-rich layer was increased as there is no clear difference in the estimated carrier concentration. The high crystallinity of the In-rich layer decreased the density of grain boundaries, alleviating the scattering effect at grain boundaries. In summary, the high carrier concentration of the Ga-rich layer at the back-side is suitable for smooth transfer of holes from the film bulk to Mo substrate, and the high mobility of the In-rich layer at front-side facilitates transportation of photoexcited electrons in the vicinity of the electrode-electrolyte interface.

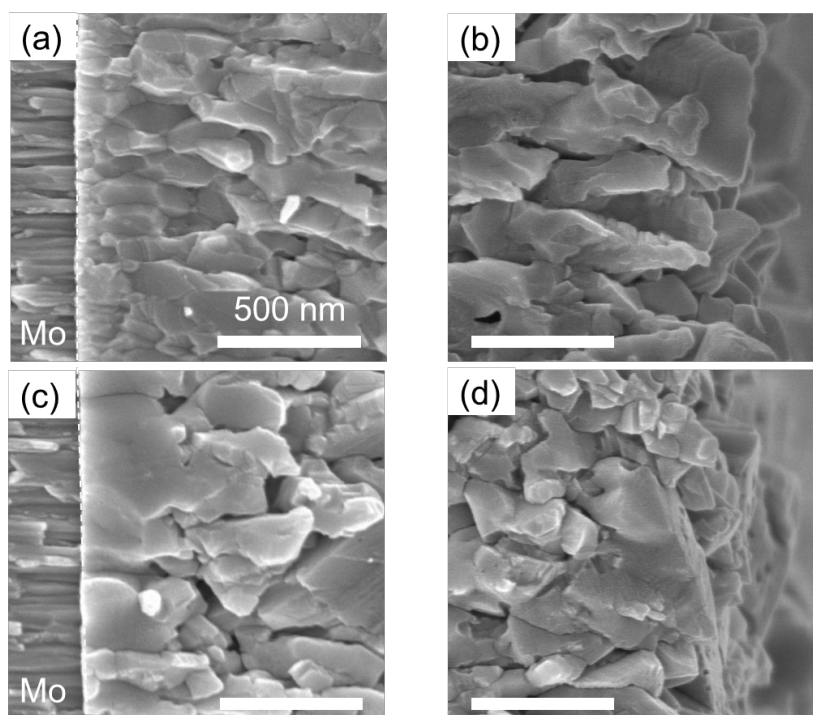


Figure 3-2-5. Cross-sectional SEM images of the Ga-rich (a, b) and In-rich (c, d) monolayers.

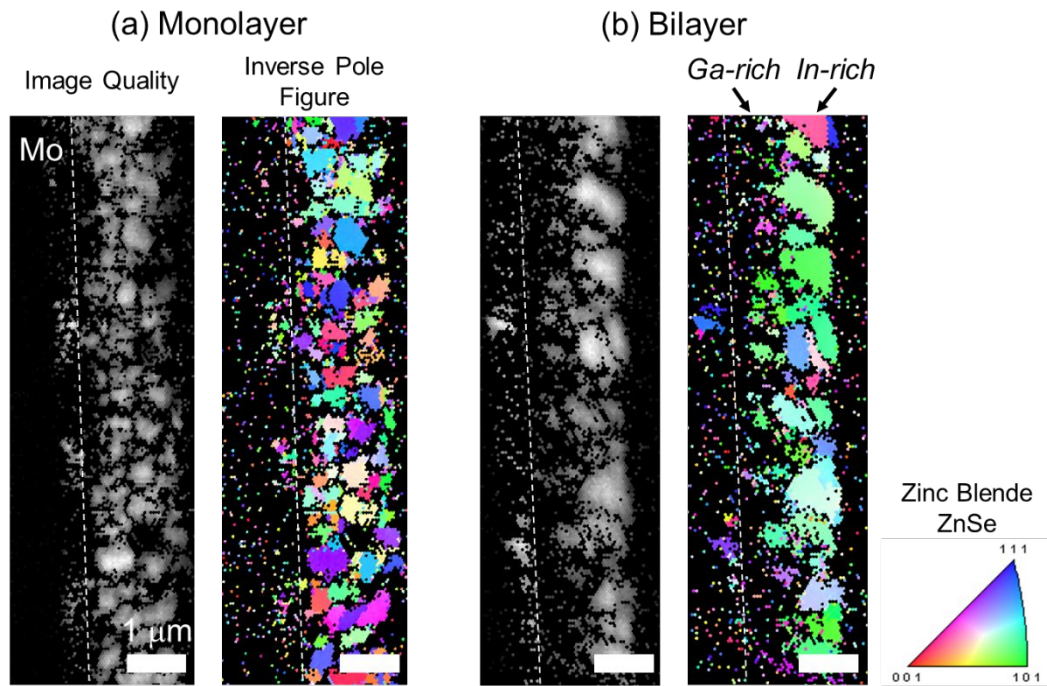


Figure 3-2-6. Cross-sectional EBSD image quality and inverse pole figure maps obtained from the (ZnSe)_{0.85}(CIGS)_{0.15} thin films prepared by the monolayer (a) and bilayer (b) methods.

Table 3-2-1. Hall mobility and carrier concentration for ZnSe:Cu(In,Ga)Se₂ thin films estimated by the Hall measurement.

Material	Hall mobility [cm ² V ⁻¹ s ⁻¹]	Carrier concentration [cm ⁻³]
(ZnSe) _{0.85} (CuIn _{0.7} Ga _{0.3} Se ₂) _{0.15}	1.2 ± 0.3	(5.1 ± 1.5) × 10 ¹⁴
(ZnSe) _{0.85} (CuInSe ₂) _{0.15}	13 ± 2	(4.7 ± 0.6) × 10 ¹⁴
(ZnSe) _{0.85} (CuGaSe ₂) _{0.15}	15 ± 2	(7.3 ± 1.2) × 10 ¹⁵
CuIn _{0.7} Ga _{0.3} Se ₂	6.3 ± 0.6	(1.6 ± 0.1) × 10 ¹⁷

To conclude, the EBIC measurement successfully visualized the region active for charge separation with reproducing the condition of 0 V_{RHE}, and revealed the origin of the difference in PEC property

between the monolayer and bilayer samples: the uniformity of the active area realized by the laminated structure composed of the Ga-rich layer and the In-rich layer.

3-3-3 Overall Water Splitting using the Bilayer ZnSe:Cu(In,Ga)Se₂ Photocathode and a BiVO₄ Photoanode

A PEC cell composed of a Pt/Mo/Ti/CdS/(ZnSe)_{0.85}(CIGS)_{0.15} photocathode prepared by the bilayer method and a NiFeO_x-Bi/BiVO₄ photoanode was constructed again. It should be noted that employment of the potassium borate buffer solution as the electrolyte decreases the photocurrent somewhat as compared in Figure 3-3-1. The decrease in the photocurrent can be attributed to the relatively small conductivity of the borate buffer solution than that of phosphate buffer solution, while the borate buffer solution resulted in a meaningful shift in the onset potential due to a change in the flat-band potential of CdS relative to RHE.^[22,25] Even though, a tandem-type PEC cell could be constructed due to the increased photocurrent of the Pt/Mo/Ti/CdS/(ZnSe)_{0.85}(CIGS)_{0.15} photocathode by the bilayer method and the optimized thickness of BiVO₄ films to increase transmittance of the incident light. The photocathode was laid under the BiVO₄ photoanode, and the transmitted light instead of AM1.5G illuminates the photoanode. Figure 3-3-2 presents the current-potential curves of the photocathodes with and without BiVO₄ filter. It should be noted that the photocurrent values are greatly smaller than the case of Figure 3-1-5 because the electrolyte is different. The absence of the phosphate buffer decreases the conductivity of H⁺ in the vicinity of the photocathode surface as reported by Kumagai et al.^[9] Even though, an intersection of each current-potential curve was obtained, and the estimated working current of about 1.5 mA cm⁻² was clearly larger than the case of monolayer method.

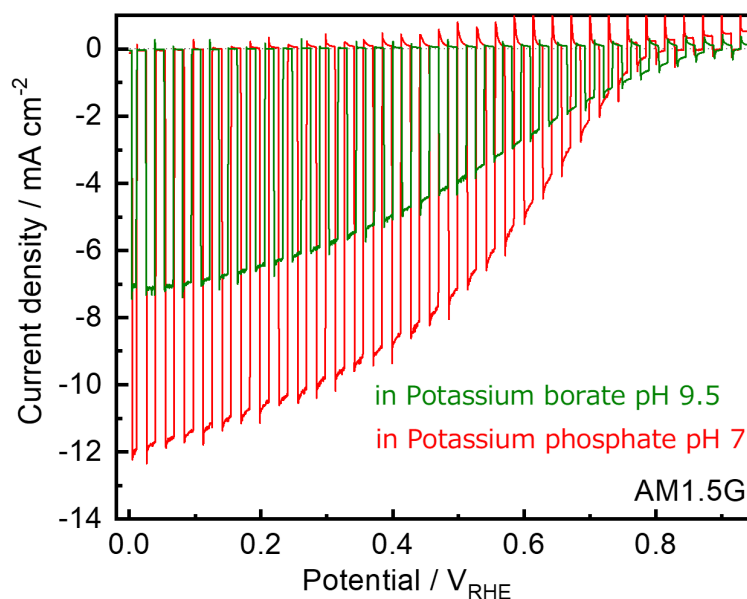


Figure 3-3-1. Current-potential curves for the Pt/Mo/Ti/CdS/(ZnSe)_{0.85}(CIGS)_{0.15} photocathode prepared by the bilayer method in a 1.0 M potassium phosphate (red) and 0.5 M potassium borate (green) solutions at pH 9.5 and 7, respectively.

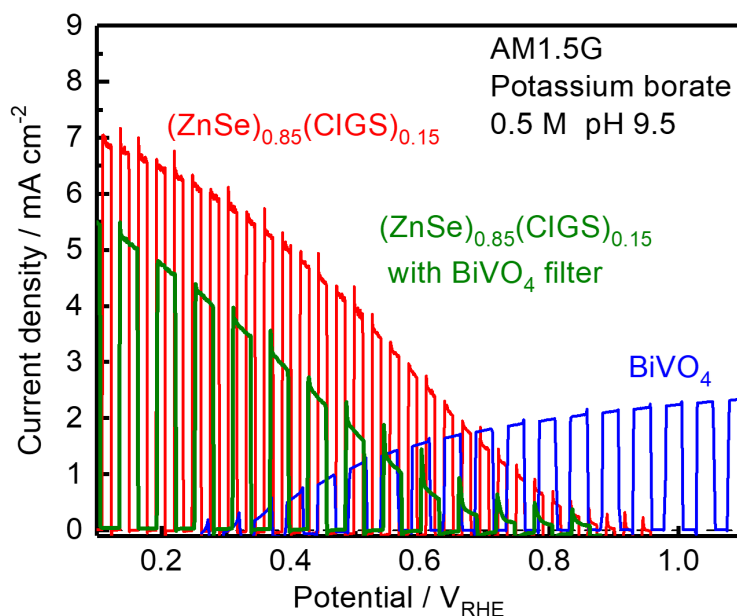


Figure 3-3-2. Current-potential curves for the Pt/Mo/Ti/CdS/(ZnSe)_{0.85}(CIGS)_{0.15} photocathode prepared by the bilayer method (red) and the photocathode under BiVO₄ filter (green) and a NiFeO_x-Bi/BiVO₄ photoanode (blue). The sweep speed of potential was 10 mV s⁻¹ except for the case of the Pt/Mo/Ti/CdS/(ZnSe)_{0.85}(CIGS)_{0.15} photocathode without BiVO₄ filter.

Chapter 3. Enhancement of Charge Separation Efficiency and Visualization of the Separation Fields in ZnSe:Cu(In,Ga)Se₂ Photocathodes

Figure 3-3-3 shows the current-time curve for the tandem cell under simulated sunlight and the corresponding gas detection. 30 s after initiation of light irradiation, the photocurrent value reached 1.41 mA cm⁻², which is equal to 1.68% of STH. The STH value is approximately 1.9 times higher than the report in chapter 2. The detection of evolved gases revealed that the Faradaic efficiency is almost 100%, which means that the photocurrent is attributed to overall water splitting reaction. However, significant degradation of the cell was observed again. After one hour of continuous illumination, the photocurrent decreased to one third. Interestingly, the interval of light irradiation for 8 min recovered the photocurrent to 80% of the initial value. The result suggests the existence of reversible degradation mechanism, which is investigated in detail in chapter 4 and 6.

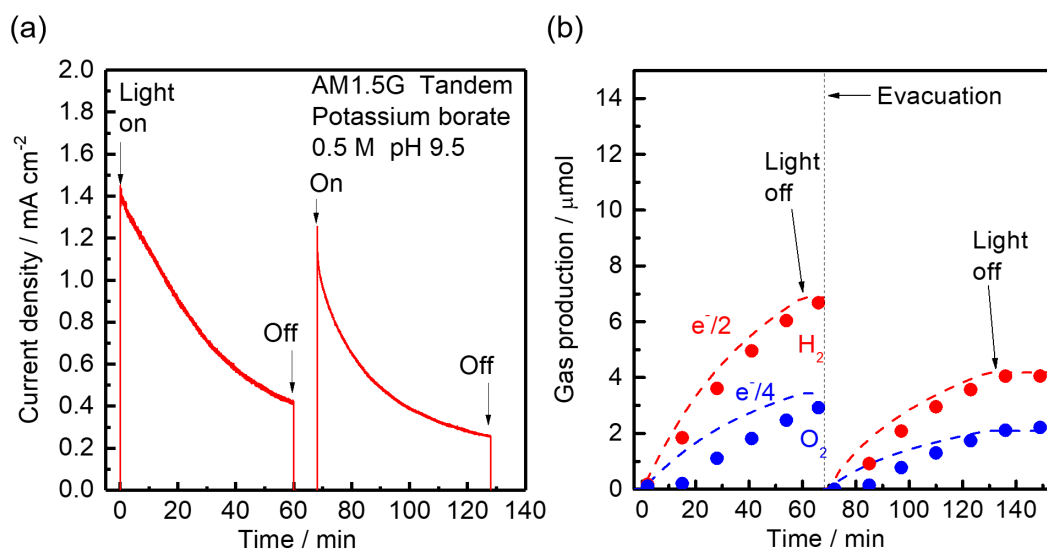


Figure 3-3-3. (a) A current-time curve for the tandem two-electrode cell (geometric area of 0.47 cm²) under simulated sunlight. (b) The amount of evolved H₂ (red) and O₂ (blue) over the cell. The dashed lines represent the amount expected for a Faradaic efficiency of unity.

3-4 Conclusions

Effects of multistage deposition process of $(\text{ZnSe})_{0.85}(\text{CIGS})_{0.15}$ thin films were investigated. The bilayer structure composed of a Ga-rich layer and In-rich layer significantly increased almost twice as large as the conventional monolayer sample. The IPCEs reached greater than 60% at a wide range of wavelength of 400 to 600 nm. Moreover, the photocathode showed good stability for 3 h at a relatively negative potential.

EBIC mapping measurement onto the photoelectrode was newly developed in order to reveal the origin of the increase in IPCEs. The distribution of active region for efficient charge separation was similar to the calculations of built-in potentials at the semiconductor-electrolyte and semiconductor-metal interfaces, which supports the consistency of the EBIC measurement. As a result of comparing the monolayer and bilayer samples, the uniform distribution of the active region was suggested to be the reason for the improvement. The improved charge separation efficiency was attributed to the Ga-rich layer at back-side with dense crystals and relatively high carrier concentration, and the In-rich layer at front-side with relatively large grains, high mobility of carriers and flat surface.

A tandem-type PEC cell was constructed using the bilayer $(\text{ZnSe})_{0.85}(\text{CIGS})_{0.15}$ photocathode and a BiVO_4 photoanode. The initial STH reached 1.68%, which was also almost twice as high as the previous result presented in chapter 2. Even though, a continuous decrease in the photocurrent was still observed accompanied with a considerable recover by interval of the light irradiation.

To conclude, employment of bilayer method greatly improves the PEC property of $(\text{ZnSe})_{0.85}(\text{CIGS})_{0.15}$ photocathodes, while protection of the surface against the degradation has been strongly required. Moreover, EBIC measurement can be applied to photoelectrodes under a modest condition. It is noted that the equipment employed in the current investigation is not capable of applying external bias voltage, but comparing the intensity and distribution of EBIC signals at various

Chapter 3. Enhancement of Charge Separation Efficiency and Visualization of the Separation Fields in ZnSe:Cu(In,Ga)Se₂ Photocathodes

applied biases is also expected to provide important information concerning the charge separation efficiency of photoelectrodes.

In the next chapter, modification of the substrate for the (ZnSe)_{0.85}(CIGS)_{0.15} photoelectrode was investigated toward fabrication of a practical PEC cell which doesn't need to stir the electrolyte.

References

- [1] A. Azarpira, M. Lublow, A. Steigert, P. Bogdanoff, D. Greiner, C. A. Kaufmann, M. Krüger, U. Gernert, R. van de Krol, A. Fischer, T. Schedel-Niedrig, *Adv. Energy Mater.* **2015**, 5, 1402148.
- [2] S. Niki, M. Contreras, I. Repins, M. Powalla, K. Kushiya, S. Ishizuka, K. Matsubara, *Prog. Photovoltaics Res. Appl.* **2010**, 18, 453.
- [3] M. A. Contreras, B. Egaas, K. Ramanathan, J. Hiltner, A. Swartzlander, F. Hasoon, R. Noufi, *Prog. Photovoltaics Res. Appl.* **1999**, 316, 311.
- [4] O. Lundberg, J. Lu, A. Rockett, M. Edoff, L. Stolt, *J. Phys. Chem. Solids* **2003**, 64, 1499.
- [5] T. Sugiyama, S. Chaisitsak, A. Yamada, M. Konagai, Y. Kudriavtsev, A. Godnes, A. Villegas, R. Asomoza, *Jpn. J. Appl. Phys.* **2000**, 39, 4816.
- [6] E. Edri, S. Kirmayer, S. Mukhopadhyay, K. Gartsman, G. Hodes, D. Cahen, *Nat. Commun.* **2014**, 5, 3461.
- [7] H. Takenoshita, *Jpn. J. Appl. Phys.* **1984**, 23, L680.
- [8] O. Gunawan, Y. Virgus, K. F. Tai, *Appl. Phys. Lett.* **2015**, 106, 062407.
- [9] H. Kumagai, T. Minegishi, N. Sato, T. Yamada, J. Kubota, K. Domen, *J. Mater. Chem. A* **2015**, 3, 8300.
- [10] M. Moriya, T. Minegishi, H. Kumagai, M. Katayama, J. Kubota, K. Domen, *J. Am. Chem. Soc.* **2013**, 135, 3733.

Chapter 3. Enhancement of Charge Separation Efficiency and Visualization of the Separation Fields in ZnSe:Cu(In,Ga)Se₂ Photocathodes

- [11] D. Yokoyama, T. Minegishi, K. Maeda, M. Katayama, J. Kubota, A. Yamada, M. Konagai, K. Domen, *Electrochem. Commun.* **2010**, *12*, 851.
- [12] A. M. Smith, L. Trotochaud, M. S. Burke, S. W. Boettcher, *Chem. Commun.* **2015**, *51*, 5261.
- [13] Y. Kuang, Q. Jia, H. Nishiyama, T. Yamada, A. Kudo, K. Domen, *Adv. Energy Mater.* **2016**, *6*, 1501645.
- [14] J. Kim, T. Minegishi, J. Kubota, K. Domen, *Energy Environ. Sci.* **2012**, *5*, 6368.
- [15] J. Kim, T. Minegishi, J. Kubota, K. Domen, *Jpn. J. Appl. Phys.* **2012**, *51*, 015802.
- [16] H. Wang, Y. Zhang, X. L. Kou, Y. A. Cai, W. Liu, T. Yu, J. B. Pang, C. J. Li, Y. Sun, *Semicond. Sci. Technol.* **2010**, *25*, 055007.
- [17] H. Metzner, T. Hahn, *J. Cryst. Growth* **2001**, *225*, 354.
- [18] T. P. Hsieh, C. C. Chuang, C. S. Wu, J. C. Chang, J. W. Guo, W. C. Chen, *Solid. State. Electron.* **2011**, *56*, 175.
- [19] T. Hisatomi, J. Kubota, K. Domen, *Chem. Soc. Rev.* **2014**, *43*, 7520.
- [20] L. Zhang, T. Minegishi, M. Nakabayashi, Y. Suzuki, K. Seki, N. Shibata, J. Kubota, K. Domen, *Chem. Sci.* **2015**, *6*, 894.
- [21] F. Jiang, Gunawan, T. Harada, Y. Kuang, T. Minegishi, K. Domen, S. Ikeda, *J. Am. Chem. Soc.* **2015**, *137*, 13691.
- [22] T. Watanabe, A. Fujishima, K. Honda, *Chem. Lett.* **1974**, *3*, 897.
- [23] K. J. Hsiao, J. D. Liu, H. H. Hsieh, T. S. Jiang, *Phys. Chem. Chem. Phys.* **2013**, *15*, 18174.
- [24] A. Niemegeers, M. Burgelman, R. Herberholz, U. Rau, D. Hariskos, *Prog. Photovoltaics Res. Appl.* **1998**, *6*, 407.
- [25] H. Kobayashi, N. Sato, M. Orita, Y. Kuang, H. Kaneko, T. Minegishi, T. Yamada, K. Domen, *Energy Environ. Sci.* **2018**, *11*, 3003.

Chapter 4

Development of Flexible ZnSe:Cu(In,Ga)Se₂ Photocathodes for Construction of Stirring-Free Photoelectrochemical Cells

4-1 Introduction

Through chapter 3, effects of deposition process of (ZnSe)_{0.85}(CuIn_{0.7}Ga_{0.3}Se₂)_{0.15} (abbreviated as (ZnSe)_{0.85}(CIGS)_{0.15} herein) thin films onto their photoelectrochemical (PEC) properties were investigated. The (ZnSe)_{0.85}(CIGS)_{0.15} photocathode prepared by the bilayer method, which forms a composition gradient of In and Ga in depth, was found to show relatively high photocurrent value due to the improved distribution of active area for charge separation. A PEC cell composed of the bilayer (ZnSe)_{0.85}(CIGS)_{0.15} photocathode and a BiVO₄ photoanode showed a solar-to-hydrogen conversion efficiency (STH) of 1.6% without application of an external bias voltage.

The conventional photoelectrochemical cells composed of plate-type photoelectrodes often require mechanical stirring of the electrolyte to facilitate the mass transfer of reactants; otherwise, chemical bias due to a pH gradient can cause degradation in the STH as discussed in chapter 2. However, such mechanical convection of the electrolyte decreases the net STH because it applies external energy into the system. Hence, it is worth investigating a stirring-free PEC cell, which is advantageous in terms of the net energy conversion efficiency and scalability.

It is important for photoelectrodes to be located near each other so as to minimize the mass transport resistance. Thin photoelectrodes arranged as a striped structure like a comb, called integrated photoelectrodes (*i*-PEs) herein, can practically realize the environment. However, both the (ZnSe)_{0.85}(CIGS)_{0.15} photocathode and BiVO₄ photoanode have conventionally employed glass plates as substrates, which makes fabrication of thin electrodes highly difficult. Hence, it is necessary to employ a flexible metal foil as a substitutive substrate for the (ZnSe)_{0.85}(CIGS)_{0.15} thin film for the glass plate. Given the flexible substrate, the photocathode can be readily cut and manipulated.

Under this concept, fabrication of flexible (ZnSe)_{0.85}(CIGS)_{0.15} photocathodes was investigated in this chapter. Because alkali metal species in the glass substrate have been reported to be indispensable for Cu-chalcopyrite materials to present preferable semiconductor property, addition of

Chapter 4. Development of Flexible ZnSe:Cu(In,Ga)Se₂ Photocathodes for Construction of Stirring-Free Photoelectrochemical Cells

the alkali metal into the substrate was also carried out using soda-lime glass as a stable and safe Na source.^[1–6] Moreover, effects of chemical bath deposition treatment of In₂S₃ onto the durability of the photocathode were also investigated so as to alleviate the significant corrosion of the CdS layer, which had already been reported by Jiang et al using Cu₂ZnSnS₄ photocathodes.^[7] They found that deposition of an In₂S₃ layer on a CdS layer can prevent the CdS layer from photocorrosion, resulting in the stable overall water splitting for 2 h. Hence, the similar effect was expected in the case of (ZnSe)_{0.85}(CIGS)_{0.15} photocathodes. Subsequently, overall water splitting with and without stirring the electrolyte was demonstrated using the integrated PEC cell fabricated from the flexible (ZnSe)_{0.85}(CIGS)_{0.15} photocathode and a BiVO₄ photoanode.

4-2 Experimental Section

Preparation of (ZnSe)_{0.85}(CIGS)_{0.15} Thin Films

(ZnSe)_{0.85}(CIGS)_{0.15} thin films were deposited on substrates of Mo-coated soda-lime glass (SLG) or 20 μm-thick Ti foils (99.5%, Nilaco). The Mo-coated substrates were fabricated by RF magnetron sputtering of a Mo target (99.9%, Kojundo) onto each soda-lime glass plate heated at 573 K. Prior to the Mo deposition, a 30 nm thick Ti was deposited by the sputtering of a Ti target (99.9%, Kojundo) so as to improve the adhesion. The thickness of Mo and Ti are about 500 and 30 nm, respectively. In the case of Ti foils, Ti was not deposited on the surface by the sputtering, but instead a 10 nm-thick SLG layer was deposited by RF magnetron sputtering of an SLG target (Koushi Kougaku) for 20 min, followed by the Mo deposition.

The substrate was loaded into a deposition chamber equipped with Knudsen cells containing elemental Cu, In, Ga, Zn and Se (99.9999%, Asahi Metal or Furuuchi Chemical). The substrate temperature was set at 623 K for 5 min and then reset to 723 K for 35 min. The (ZnSe)_{0.85}(CIGS)_{0.15} thin films were deposited using the bilayer method (see chapter 3); the typical deposition rates for Cu,

Chapter 4. Development of Flexible ZnSe:Cu(In,Ga)Se₂ Photocathodes for Construction of Stirring-Free Photoelectrochemical Cells

In, Ga, Zn and Se were 0.042, 0.095, 0.028, 0.4 and 1 nm s⁻¹, respectively. In and Ga were absent for the first and last 20 min, respectively, followed by 10 min-annealing in a Se atmosphere. The rates were monitored by using a quartz crystal microbalance sensor (Q-POD, INFICON). The pressure in the chamber was kept at $<2 \times 10^{-5}$ Pa during deposition. Following the film deposition processes, each sample was cooled from 723 to 573 K with exposure to Zn and Se vapor to alleviate the formation of a Zn-poor surface.

KCN Etching

After deposition, the samples were immersed into an etching solution containing 0.1 M KCN (98.0%, FUJIFILM Wako Pure Chemical) and 0.8 M KOH (8 M, FUJIFILM Wako Pure Chemical) for 1 min in room temperature. This etching process removed excess Cu from the (ZnSe)_{0.85}(CIGS)_{0.15} thin films. Energy dispersive X-ray spectroscopy (EDS; EMAX-7000, Horiba) analysis revealed that the atomic ratio of Cu/(In+Ga) was 0.9 to 1.0 after the process.

Characterization

The (ZnSe)_{0.85}(CIGS)_{0.15} thin film samples were analyzed using scanning electron microscopy (SEM; Hitachi) equipped with energy dispersive X-ray spectroscopy (EDS; EMAX-7000, Horiba), scanning transmission electron microscopy (STEM; JEM-2800, JEOL) equipped with an SDD detector for STEM-EDS mapping (X-Max 100 TLE, Oxford Instruments), X-ray photoelectron spectroscopy (XPS; JPS-9000, JEOL) and X-ray photoelectron spectroscopy (XPS; JPS-9000, JEOL).

Surface Modification with an CdS Layer

A CdS layer was formed on the surface of each (ZnSe)_{0.85}(CIGS)_{0.15} thin film using chemical bath deposition (CBD) method.^[8–10] The CBD solution with a volume of 50 mL contained 14 wt% ammonia (28 wt%, FUJIFILM Wako Pure Chemical), 25 mM of Cd(CH₃COO)₂ (98.0%, FUJIFILM Wako Pure Chemical) and 0.375 M of SC(NH₂)₂ (98.0%, Kanto Chemical). The bath temperature was gradually increased from room temperature to 325–326 K over the span of about 8 min. The

Chapter 4. Development of Flexible ZnSe:Cu(In,Ga)Se₂ Photocathodes for Construction of Stirring-Free Photoelectrochemical Cells

samples were taken out from the bath and immediately washed with pure water 14 min after the initiation of heating, followed by annealing at 473 K for 1 min in air.

Chemical bath deposition treatment of In₂S₃

The CdS-modified (ZnSe)_{0.85}(CIGS)_{0.15} thin film was treated with additional CBD treatment of In₂S₃.^[7,11] The CBD solution with a volume of 50 mL contained 100 mM of CH₃COOH (99.7%, FUJIFILM Wako Pure Chemical), 25 mM of In₂(SO₄)₂ (FUJIFILM Wako Pure Chemical) and 100 mM of CH₃CSNH₂ (98.0%, FUJIFILM Wako Pure Chemical). The bath temperature was heated at 343 K. The samples were taken out from the bath and immediately washed with pure water 10-30 min after the initiation of heating.

Surface Modification with Thin Metal Layers

A binary of Mo/Ti with each thickness of 3 nm was deposited by successive RF magnetron sputtering of a Ti and Mo target in room temperature.^[8] Subsequently, a Pt layer with a thickness of a few nanometers was deposited on it by thermal evaporation of Pt wire (99.98%, Nilaco) in a high vacuum of $<4 \times 10^{-3}$ Pa. Some samples were deposited with Pt using photoelectrodeposition method; the photocathode was exposed to simulated sunlight (XES-40S2-CE, SAN-EI Electric) for 30 min in a solution containing 10 μ M (98.5%, Kanto) and 0.1 M Na₂SO₄ (99%, FUJIFILM Wako Pure Chemical) at a potential of -0.2 V vs. Ag/AgCl reference electrode in a saturated aqueous KCl solution.

Preparation of BiVO₄ Photoanodes

A Bi precursor was prepared on an indium tin oxide (ITO)-coated soda-lime glass substrate (0051, Geomatec) by electrodeposition method in a three-electrode cell containing a 0.1 M BiNO₃ (99.9%, FUJIFILM Wako Pure Chemical) and a 0.3 M *p*-benzoquinone (98.0%, FUJIFILM Wako Pure Chemical) solution equipped with the Ag/AgCl reference electrode and with a Pt wire counter electrode. Subsequently, a dimethyl sulfoxide solution containing 0.2 M VO(C₅H₇O₂)₂ (98%, Sigma-Aldrich) in a mixture of DMSO and ethanol (1:1 v/v) was drop-cast onto the precursor, followed by calcination at 793 K for 2 h in air. As oxygen evolution reaction (OER) catalyst, CoO_x and NiO were

Chapter 4. Development of Flexible ZnSe:Cu(In,Ga)Se₂ Photocathodes for Construction of Stirring-Free Photoelectrochemical Cells

successively deposited using immersion and atomic layer deposition (ALD) methods, respectively. The BiVO₄ thin films were immersed in an aqueous solution containing 10 mM Co(NO₃)₂ (FUJIFILM Wako Pure Chemical) and 10 mM NH₄OH for 0.5 h to deposit CoO_x, followed by annealing in air at 523 K for 0.5 h. After the surface was cleaned using an ozone plasma for 5 min, the sample was loaded into a vacuum chamber and ALD of NiO for 300 cycles at 533 K was conducted using bis-(2,2,6,6-tetramethylheptane-3,5-dionate) nickel(II) (FUJIFILM Wako Pure Chemical) and water as precursors. It should be noted that a previous report describes the fabrication process of the BiVO₄-based photoanode in more detail.^[12]

Fabrication of Integrated Photoelectrodes

The (ZnSe)_{0.85}(CIGS)_{0.15} photocathodes prepared on Ti foil substrates were processed into sections about 0.1 × 1 cm by mechanical cutting. Each piece was arrayed on the surface of the BiVO₄ photoanodes with photocathode lines approximately 1 mm wide and photoanode lines 2-3 mm wide to form a striped structure. The photocathodes were fixed and the region not intended for measurement was coated using epoxy resin (Araldite Rapid, Nichiban).

Photoelectrochemical Measurements

A three-electrode cell equipped with a magnetic stirrer under an Ar atmosphere using an aqueous solution of 1.0 M potassium phosphate buffer solution (pH 7.0) as the electrolyte was set up and connected to a potentiostat (HSV-110, Hokuto Denko), unless otherwise noted. A solar simulator (XES-40S2-CE, SAN-EI Electric) producing AM1.5G was employed as the light source. In the current-potential measurements, the applied potential, expressed relative to a reversible hydrogen electrode (RHE), was swept at 5 mV s⁻¹ from 0 V_{RHE} under intermittent irradiation with a period of 6 s. Mott-Schottky plots were obtained in the dark using a potentiostat (VersaSTAT 3, Princeton Applied Research) with applied potential perturbation at the amplitude of 20 mV applying the frequency of 2 kHz.

Chapter 4. Development of Flexible ZnSe:Cu(In,Ga)Se₂ Photocathodes for Construction of Stirring-Free Photoelectrochemical Cells

Analysis of the evolved gases was conducted using an airtight and Ar-purged glass cell connected to a gas chromatograph (3000 Micro GC Gas Analyzer, Agilent Technologies) and a potentiostat.

4-3 Results and Discussion

4-3-1 Effects of Substrates onto the Photoelectrochemical Properties of the ZnSe:Cu(In,Ga)Se₂ Photocathodes

Figure 4-1-1 shows surface SEM images of bilayer (ZnSe)_{0.85}(CIGS)_{0.15} thin films deposited on Ti foils. The grain morphology exhibits little difference between presence of the SLG layer; both show dense and polycrystalline (ZnSe)_{0.85}(CIGS)_{0.15} films with the in-plane grain size of 300-500 nm, which suggests that the SLG layer doesn't affect crystal growth. Figure 4-1-2 shows XPS spectra obtained from the surface of the films. The peaks in the spectra were attributed to the elements in (ZnSe)_{0.85}(CIGS)_{0.15} and surface contaminations related to carbon and oxygen. In the case of SLG-introduced substrate, a meaningful peak of Na 1s was also detected at 1071-1072 eV. Hence, it is likely that the Na species diffuses into the (ZnSe)_{0.85}(CIGS)_{0.15} thin films during deposition process. In addition, these results suggest that the Na species doesn't affect crystal growth even though it exists in the film. The amount of Na was quantified using the peak area and the atomic sensitivity factors: 2.51 and 0.48 for Na 1s and Se 3d, respectively.^[13] The estimated atomic Na/Se ratio was approximately 5%, although the distribution of the Na species can be ununiform in the film; many reports have revealed that the Na or K species in Cu-chalcopyrite thin films showed segregation at around the film surface or grain boundaries.^[1,3,4,6] Thus, it is highly possible that the concentration of the Na species in the (ZnSe)_{0.85}(CIGS)_{0.15} thin film is much lower than 5%.

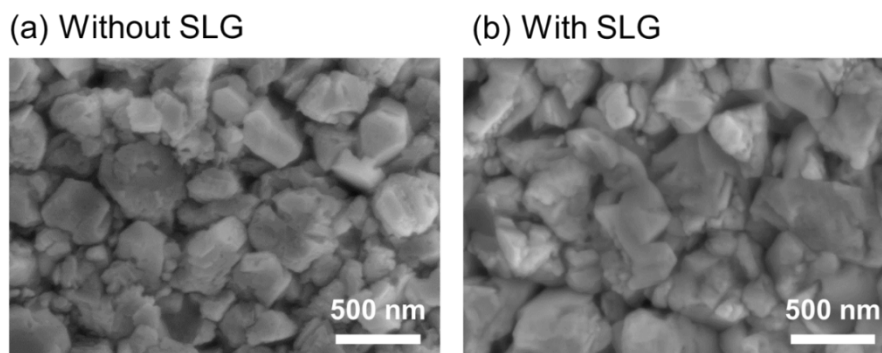


Figure 4-1-1. Surface SEM images of $(\text{ZnSe})_{0.85}(\text{CIGS})_{0.15}$ thin films prepared on Ti foils without (a) and with (b) deposition of SLG.

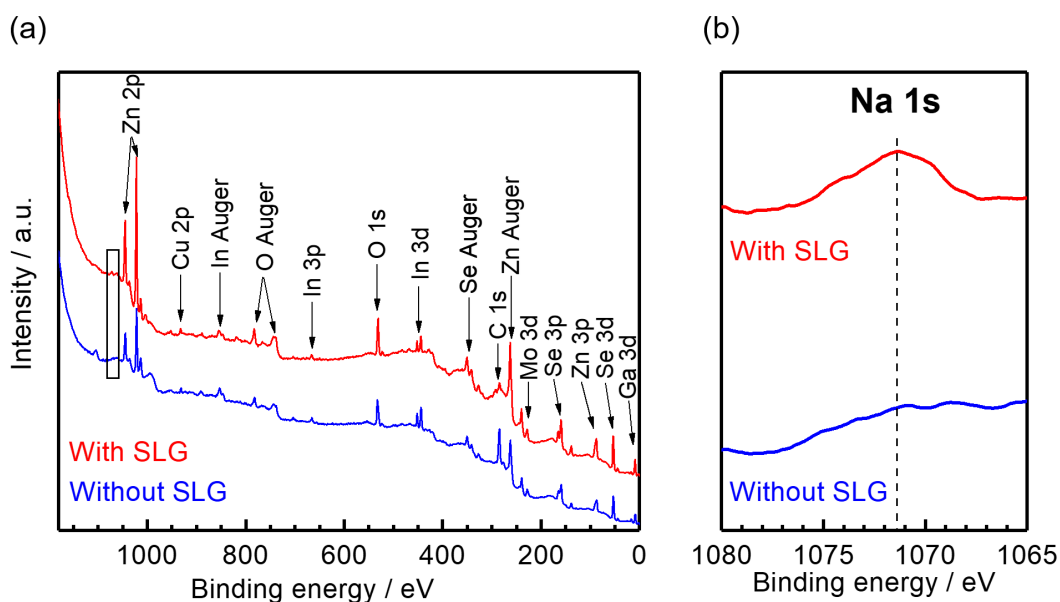


Figure 4-1-2. (a) XPS spectra $(\text{ZnSe})_{0.85}(\text{CIGS})_{0.15}$ thin films prepared on Ti foils without and with deposition of SLG, and (b) magnified spectra.

Flat-band potentials and carrier concentrations of the $(\text{ZnSe})_{0.85}(\text{CIGS})_{0.15}$ thin films prepared on Ti foils were estimated using Mott-Schottky plots and Eq. (1-19), assuming the relative permittivity ϵ_r to 10. It should be noted that the potential range was not the same with each other because the range where straight plots were obtained was different. From the slope of the linear-fitted lines, the carrier concentrations (in the vicinity of the electrode surface) at the samples with the thickness of SLG layers

Chapter 4. Development of Flexible ZnSe:Cu(In,Ga)Se₂ Photocathodes for Construction of Stirring-Free Photoelectrochemical Cells

of 0, 5 and 10 nm were estimated to be 3×10^{16} , 6×10^{16} and 2×10^{17} cm⁻³, respectively. Moreover, the (ZnSe)_{0.85}(CIGS)_{0.15} thin film with the 10 nm-thick SLG layer showed a relatively high flat-band potential of 0.8 V_{RHE}, which was estimated from the extrapolation. Therefore, the SLG layer provides Na dopant into the (ZnSe)_{0.85}(CIGS)_{0.15} thin film to increase the acceptor density without alternating the main semiconductor property. It should be noted that the carrier concentrations estimated by Mott-Schottky plots are almost two orders of magnitude larger than the values obtained by AC Hall measurement (see Table 3-2-1 in chapter 3). This is because Mott-Schottky plots are affected by the depletion layer formed in the vicinity of film surface, where the defect concentration is relatively large.

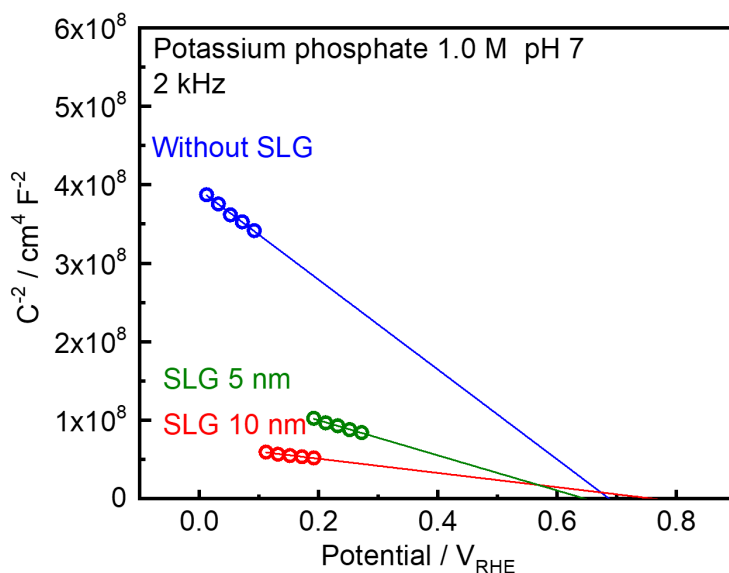


Figure 4-1-3. Mott-Schottky plots for the (ZnSe)_{0.85}(CIGS)_{0.15} photocathodes prepared on Ti foils without and with deposition of 5 nm- and 10 nm-thick SLG layers.

Figure 4-1-4 exhibits current-potential curves for Pt/Mo/Ti/CdS/(ZnSe)_{0.85}(CIGS)_{0.15} photocathodes prepared on various types of substrates. Even though all employed the bilayer method and the same surface modifications, the PEC properties are significantly different from each other. Without SLG layer or substrate, the photocurrent value at 0 V_{RHE} under simulated sunlight was 4 mA cm⁻². In contrast, the other photocathodes showed the photocurrent values of 12 to 14 mA cm⁻² at the

Chapter 4. Development of Flexible ZnSe:Cu(In,Ga)Se₂ Photocathodes for Construction of Stirring-Free Photoelectrochemical Cells

potential. Also, the onset potential (defined as a cathodic photocurrent of 0.05 mA cm⁻²) was 0.70 V_{RHE}, which is 0.1-0.2 V more negative than those with SLG. The difference in the onset potential is consistent with the measurement of flat-band potentials. These results revealed that the Na or perhaps any other alkali metal species is indispensable for (ZnSe)_{0.85}(CIGS)_{0.15} photocathodes to show a sufficient semiconductor property as the cases of Cu(In,Ga)Se₂ solar cells.^[3,6] The photocurrent values of the (ZnSe)_{0.85}(CIGS)_{0.15} photocathode prepared on the Ti foil with the SLG layer at the potentials of >0.4 V_{RHE} is slightly smaller than those of that prepared on the Mo-coated SLG substrate likely due to the mechanical damage by the flexibility. It should be noted that the difference in the thermal expansion coefficient between the Ti foil (1×10^{-5} K⁻¹) and SLG (9×10^{-6} K⁻¹) is negligible, so the (ZnSe)_{0.85}(CIGS)_{0.15} thin film is not strained even when deposited on the Ti foil, which is preferable for prevention of exfoliation.^[14-16]

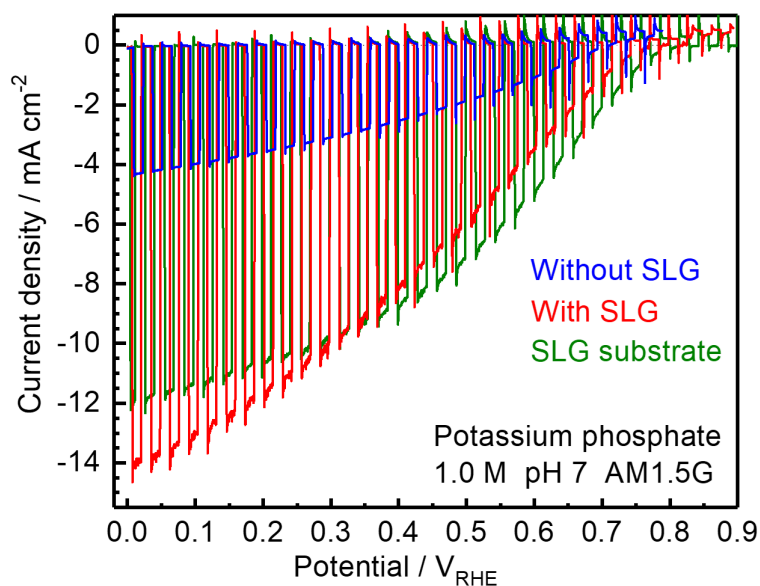


Figure 4-1-4. Current-potential curves for Pt/Mo/Ti/CdS/(ZnSe)_{0.85}(CIGS)_{0.15} photocathodes prepared on a Mo-coated SLG substrate (green) and Ti foils without (blue) deposition of SLG and with (red) a 10 nm-thick SLG layer.

Chapter 4. Development of Flexible ZnSe:Cu(In,Ga)Se₂ Photocathodes for Construction of Stirring-Free Photoelectrochemical Cells

EDX analyses revealed that introduction of SLG led to a slight decrease in the atomic ratio of Cu/(In+Ga) as shown in Figure 4-1-5. With the insufficient amounts of SLG, the fraction of Cu showed relatively large deviation and was close to the stoichiometry. On the other hand, the samples with a large amount of SLG resulted in the decrease by 3-5%. The most probable reason for the relationship between the increased carrier density and the decreased amount of Cu is formation of Na_{Cu} antisites, resulting in suppression of formation of donor-type defects such as Zn_{Cu}. By assuming that all Na_{Cu} substituted Zn_{Cu} and estimating the activation energy of Zn_{Cu} at 0.2 eV as reported by Chen et al. on Cu₂ZnSeS₄,^[17] the decrease in the Cu/(In+Ga) ratio by 3% theoretically causes the decrease in the donor density by $8 \times 10^{16} \text{ cm}^{-3}$ according to the Fermi function (see also Eq. (1-3) in section 1-3-1). The decrease in the donor density should increase the net carrier concentration, and the increase is highly consistent with the value estimated by Mott-Schottky plots as shown in Figure 4-1-3.

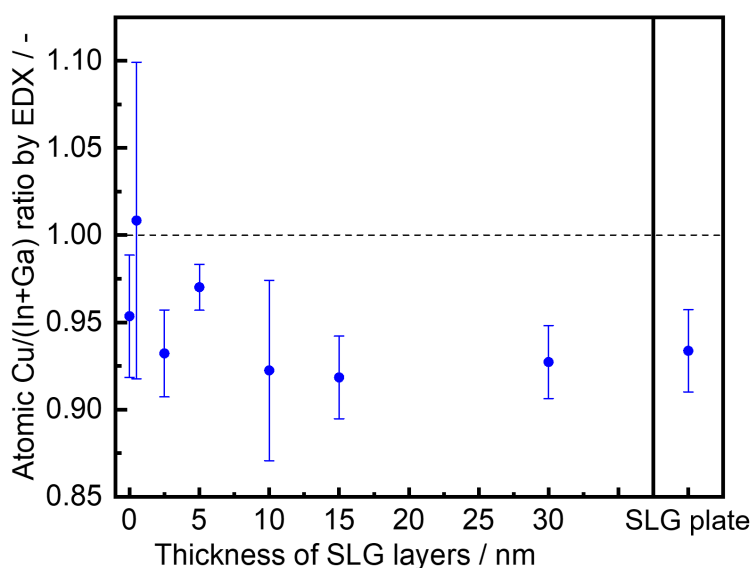


Figure 4-1-5. The relationship between thickness of SLG layers and atomic ratio of Cu/(In+Ga) obtained by using EDX. The error bars stand for standard deviations.

XPS analyses in conjunction with surface etching by Ar⁺ were conducted on each sample to measure the distribution of Na and Cu in-depth. Table 4-1-1 summarizes the atomic ratios of Na/Se

Chapter 4. Development of Flexible ZnSe:Cu(In,Ga)Se₂ Photocathodes for Construction of Stirring-Free Photoelectrochemical Cells

and Cu/In. It should be noted that a small but considerable peak of Na was often detected possibly due to surface contamination. Despite that, the Na peak clearly decreased after Ar⁺ etching and instead the atomic ratio of Cu/In increased, suggesting that the Na species diffuses from the substrate via grain boundaries to reach the film surface as supposed by Blösch et al.^[18] Consequently, the Na species possibly substitutes Cu_{Cu} and/or Zn_{Cu} to form Na_{Cu} antisites.

Table 4-1-1. Peak area ratios in XPS for (ZnSe)_{0.85}(CIGS)_{0.15} thin films prepared on SLG plate and Ti foils with various thickness of SLG layers before and after Ar⁺-etching by 15 nm-SiO₂.

Substrate	Na/Se	Na/Se after etching	Cu/In	Cu/In after etching
Without SLG	0.02	0.01	0.44	0.38
SLG (15 nm)	0.03	0.02	0.60	0.38
SLG (30 nm)	0.1	0.01	0.28	0.42
SLG plate	0.03	0.01	0.23	0.31

The diffusion model also means that the excess amount of Na is not incorporated into the (ZnSe)_{0.85}(CIGS)_{0.15} crystal, which is consistent with the saturation in the Figure 4-1-5, while direct addition of Na into the crystal has been reported to cause stacking faults as reported by Stange et al., who employed NaF evaporation on the Mo layer for CuInSe₂ thin films.^[19] Therefore, introduction of a Na species by thermal diffusion from the substrate following crystal growth is preferable for the absorber layer to modify its semiconductor property without aggravating the crystallinity.

Another possible reason for the enhanced charge separation for the (ZnSe)_{0.85}(CIGS)_{0.15} photocathodes by the presence of a Na species is passivation of V_{Se} with O_{Se}, which is introduced with Na⁺ as reported by Kronik et al.^[5] The passivation of V_{Se} reduces donor-type defects and/or recombination sites at the grain boundaries. It is noteworthy that the co-workers of the author have demonstrated the increase in the amount of O species by addition of Na₂S using (ZnSe)_{0.85}(CIGS)_{0.15}

Chapter 4. Development of Flexible ZnSe:Cu(In,Ga)Se₂ Photocathodes for Construction of Stirring-Free Photoelectrochemical Cells

particles.^[20] Figure 4-1-6 (a) shows the relationship between the amounts of introduced Na₂S and the detected O species, revealing that addition of Na₂S facilitates the incorporation of the O species. The photocathodes introduced with Na₂S showed relatively high photocurrent values even if they were synthesized under Cu-stoichiometric condition as shown in Figure 4-1-6 (b).

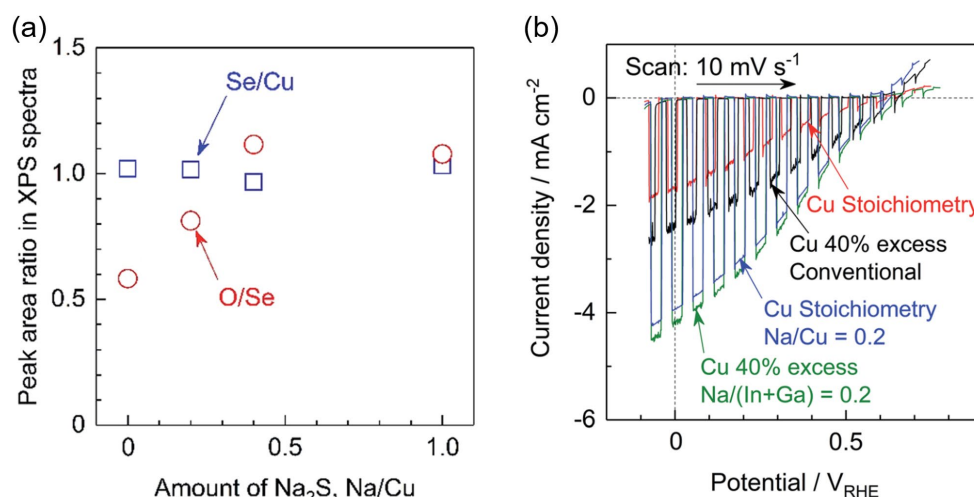


Figure 4-1-6. (a) Ratios of Se/Cu and O/Se peak areas in XPS spectra for (ZnSe)_{0.85}(CIGS)_{0.15} particles as a function of the relative amount of Na₂S used, and (b) current-potential curves for particulate (ZnSe)_{0.85}(CIGS)_{0.15} photocathodes synthesized under stoichiometric or 40% Cu-excess conditions with and without Na₂S. Reprinted with permission from ref. [21] - Published by The Royal Society of Chemistry.

To summarize, introduction of a Na species was found to suppress formation of donor-type defects and/or passivation of recombination sites via forming antisites such as Na_{Cu} and O_{Se}. It was also found that a thin SLG layer with the thickness of 10-20 nm is enough to maximize the effects, and the thickness affects neither electric conductivity or flexibility of the (ZnSe)_{0.85}(CIGS)_{0.15} thin films deposited on the Ti foil. Figure 4-1-7 shows a photographic image of the flexible (ZnSe)_{0.85}(CIGS)_{0.15} photocathode. The photocathode is easy to cut and bend as demonstrated in the image.

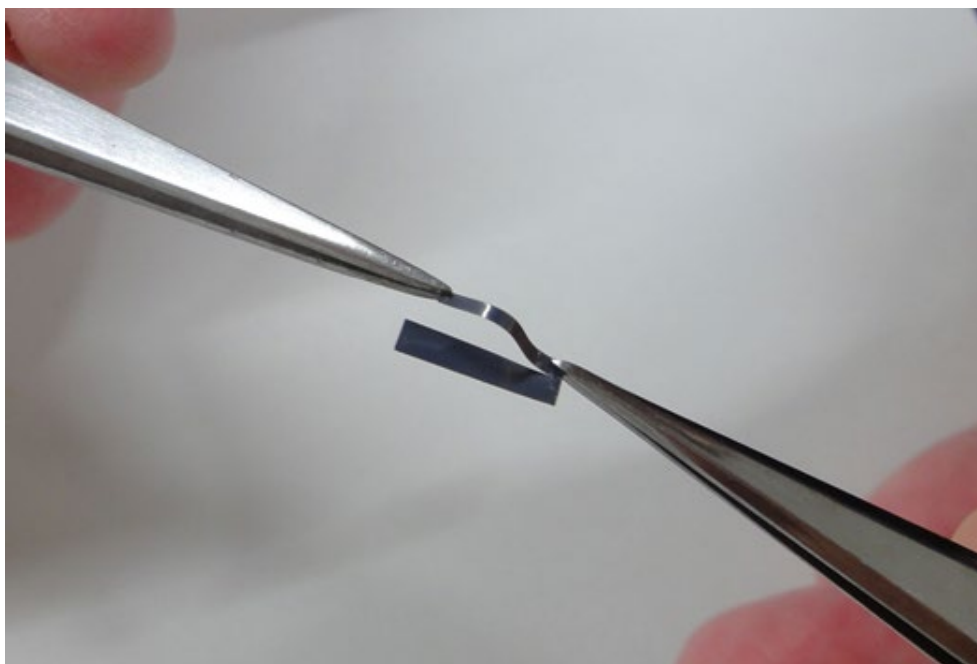


Figure 4-1-7. A photographic image of the Pt/Mo/Ti/CdS/(ZnSe)_{0.85}(CIGS)_{0.15} photocathode prepared on a Ti foil substrate deposited with SLG.

4-3-2 Effects of Chemical Bath Deposition of In₂S₃ onto the Photoelectrochemical Properties of the ZnSe:Cu(In,Ga)Se₂ Photocathodes

Investigation on substrates discussed in section 4-3-1 enabled construction of the *i*-PEs using the Pt/Mo/Ti/CdS/(ZnSe)_{0.85}(CIGS)_{0.15} photocathode. However, the photocathode has shown a significant degradation at positive potentials due to corrosion of CdS, which has made it difficult to conduct long-term measurement as reported in chapter 2 and 3. As noted in the introduction, In₂S₃ has been known to alleviate the corrosion of the CdS layer,^[7] so effects of chemical bath deposition of In₂S₃ onto the durability were investigated in this section. Figure 4-2-1 shows cross-sectional EDS line profile of each element at the interfaces between In₂S₃ (deposited using CBD for 10 min), CdS and (ZnSe)_{0.85}(CIGS)_{0.15}. The CdS layer with the thickness of several tens of nanometers was detected, while diffusion or penetration of CdS into the underlying layer was also observed. On the other hand, it is difficult to find the In₂S₃ layer on the CdS clearly, suggesting that the thickness of the layer is far

Chapter 4. Development of Flexible ZnSe:Cu(In,Ga)Se₂ Photocathodes for Construction of Stirring-Free Photoelectrochemical Cells

below the spatial resolution of STEM-EDS measurement. XPS spectra obtained from the surface were exhibited in Figure 4-2-2. After the CBD treatment of In₂S₃, the peak attributed to In was clearly detected, while that of Zn was not detected, providing the evidence that the peak was not attributed to underlying (ZnSe)_{0.85}(CIGS)_{0.15}.

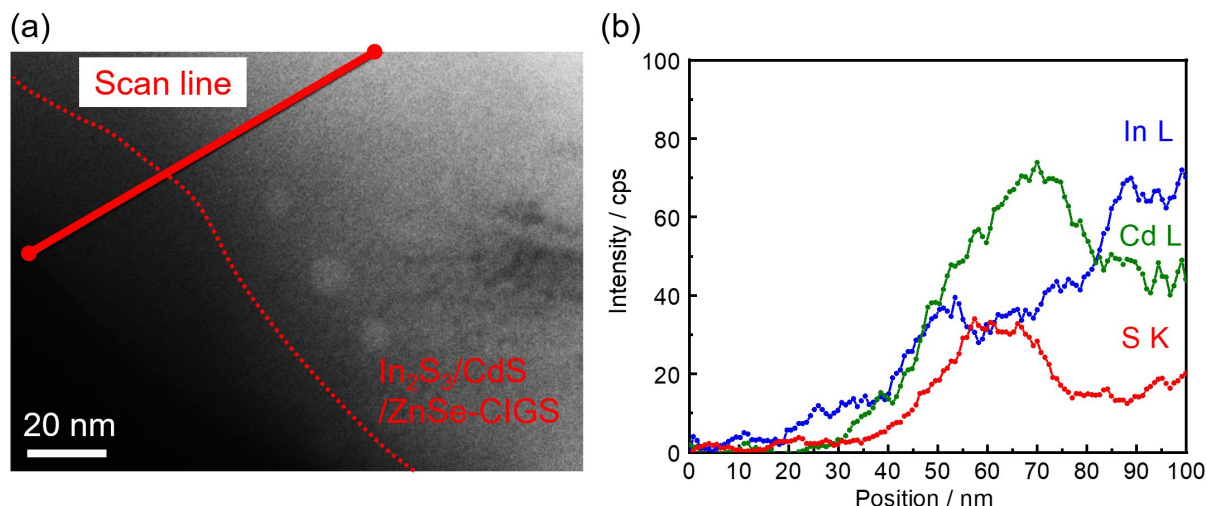


Figure 4-2-1. A cross-sectional STEM image (a) and the corresponding line profiles (b) acquired along the red line at the interfaces between In₂S₃, CdS and (ZnSe)_{0.85}(CIGS)_{0.15}.

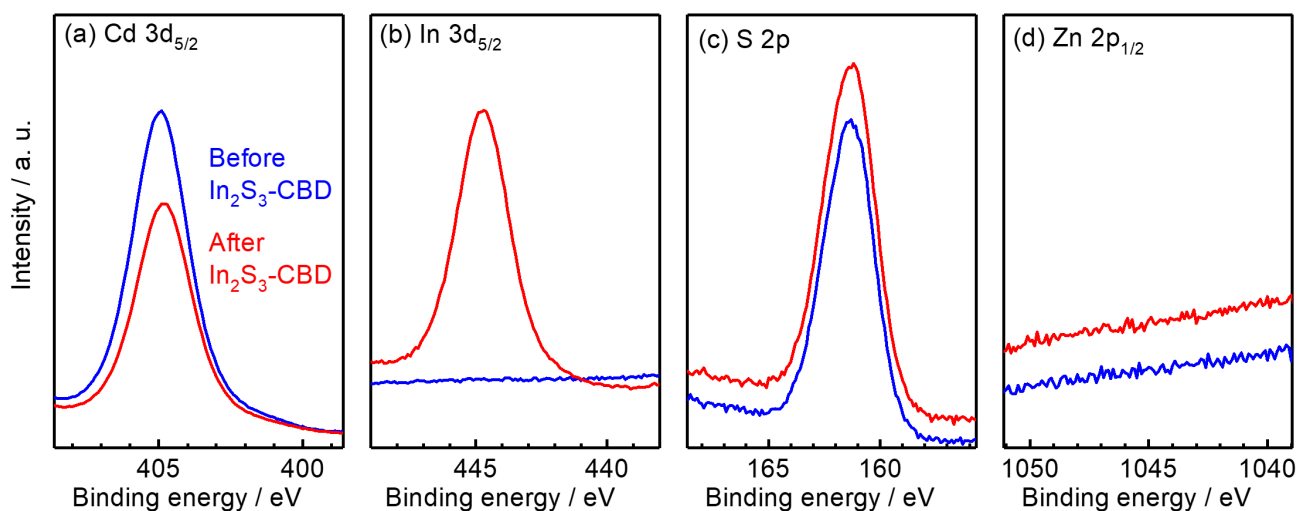


Figure 4-2-2. XPS spectra obtained for Cd (a), In (b), S (c) and Zn (d) from the surface of CdS-modified (ZnSe)_{0.85}(CIGS)_{0.15} thin films before (blue) and after (red) CBD of In₂S₃.

Chapter 4. Development of Flexible ZnSe:Cu(In,Ga)Se₂ Photocathodes for Construction of Stirring-Free Photoelectrochemical Cells

Figure 4-2-3 shows the stability at 0.6 V_{RHE} for the (ZnSe)_{0.85}(CIGS)_{0.15} photocathodes with various conditions of CBD of In₂S₃. The decreases in the photocurrent value from 5 min after initiation of light irradiation to the end of measurement were 39%, 23%, 20% and 40% for the photocathodes without CBD and with CBD for 10 min, 20 min and 30 min, respectively. The deposition time of 30 min was found to be so long that the photocurrent and durability were relatively poor. The improved stability of In₂S₃-deposited photocathode can be explained by the difference in the solubility of hydroxide, which is expected to be formed after oxidation of the sulfide anions. The solubility of Cd(OH)₂ has been reported to be approximately 1 mg L⁻¹, while that of In(OH)₃ has been estimated to be 2 ng L⁻¹ at room temperature.^[21,22] Consequently, although it is not perfect, the (ZnSe)_{0.85}(CIGS)_{0.15} photocathode modified with In₂S₃ for the modest period shows a relatively stable PEC hydrogen evolution reaction (HER) at 0.6 V_{RHE}, which is estimated to be the working potential of a PEC cell. Further investigation on stabilization of the (ZnSe)_{0.85}(CIGS)_{0.15} photocathode is reported in the next chapter.

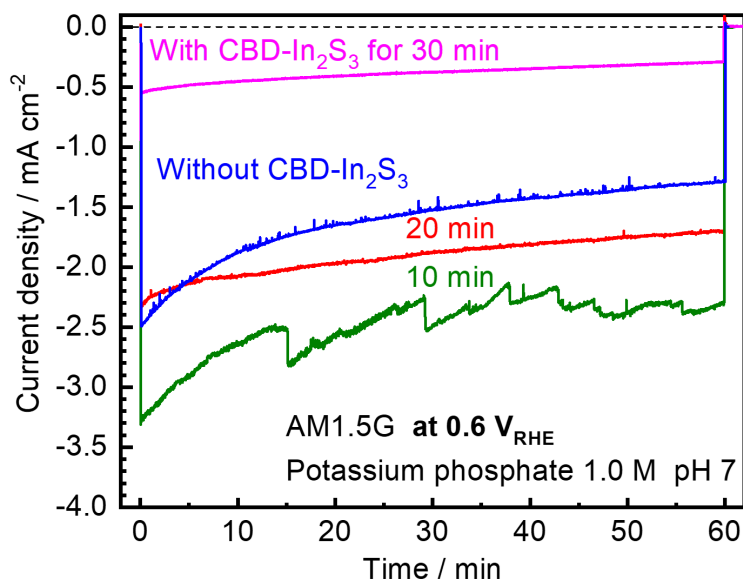


Figure 4-2-3. Current-time curves for the Pt/Mo/Ti/CdS/(ZnSe)_{0.85}(CIGS)_{0.15} photocathode (blue) and the photocathodes modified with In₂S₃ using CBD for 10 min (green), 20 min (red) and 30 min

Chapter 4. Development of Flexible ZnSe:Cu(In,Ga)Se₂ Photocathodes for Construction of Stirring-Free Photoelectrochemical Cells

(pink) at 0.6 V_{RHE}. It should be noted that the vibration of photocurrent is because of the absorption and desorption of hydrogen bubbles.

4-3-3 Construction of a Comb-Like Photoelectrochemical Cell Composed of the ZnSe:Cu(In,Ga)Se₂ Photocathode and a BiVO₄ Photoanode

Using the flexible (ZnSe)_{0.85}(CIGS)_{0.15} photocathodes, *i*-PEs were fabricated as exhibited in Figure 4-3-1. The photocathodes and photoanodes with the widths of 1 and 2-3 mm, respectively, were arranged like a comb. As discussed in section 1-3-4, the diffusion layer thickness is typically 0.1 to several millimeters. Therefore, the interval between each photoelectrode is narrow enough to eliminate the effect of mass transport in the electrolyte bulk. In other words, effect of electrolyte convection can be removed from the reaction system. The numerical simulation of mass transport for the comb-like cell has also been detailed in elsewhere by co-workers of the author.^[23]

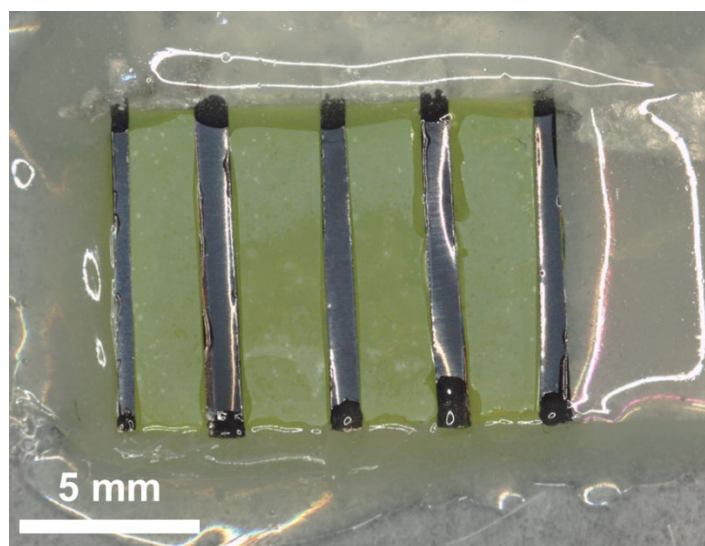


Figure 4-3-1. A Photographic image of the *i*-PEs composed of the (ZnSe)_{0.85}(CIGS)_{0.15} photocathode and a BiVO₄ photoanode.

Chapter 4. Development of Flexible ZnSe:Cu(In,Ga)Se₂ Photocathodes for Construction of Stirring-Free Photoelectrochemical Cells

Figure 4-3-2 shows time-courses of evolved gases over the *i*-PEs under irradiation of a 300 W Xe lamp equipped with a cutoff filter (L42, Hoya) without and with stirring the electrolyte. For a few hours after the beginning of the reaction, the *i*-PEs without stirring showed almost the same amount of hydrogen and oxygen as those with stirring. Compared with the case of the conventional parallel PEC cell shown in Figure 2-4-1, the indifference in the reaction speed suggests that the *i*-PEs are not affected by the convection of the electrolyte. It should be noted that the ratio of evolved hydrogen and oxygen was almost 2:1, which means the cell drives overall water splitting reaction without meaningful self-reaction of the electrode. Interestingly, the cell without stirring electrolyte showed better stability than that with stirring. A possible reason of the difference in the stability is that the deposition speed and/or mechanism of impurities to Pt surface of the photocathode can differ between with and without forced convection of the electrolyte, which is discussed layer.

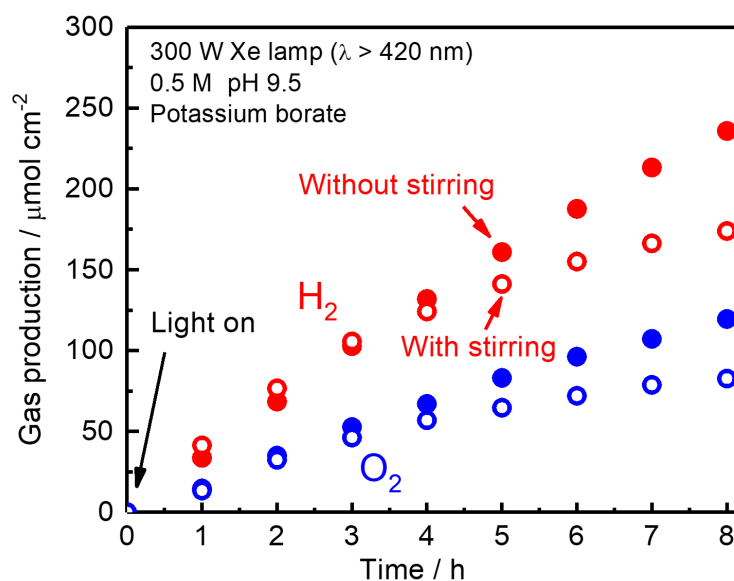


Figure 4-3-2. Evolved hydrogen (red) and oxygen (blue) gases over time using the *i*-PEs composed of the (ZnSe)_{0.85}(CIGS)_{0.15} photocathode and a BiVO₄ photoanode with (colored dots) and without (outlined dots) stirring the electrolyte.

Chapter 4. Development of Flexible ZnSe:Cu(In,Ga)Se₂ Photocathodes for Construction of Stirring-Free Photoelectrochemical Cells

In an attempt to evaluate further the effect of electrode integration onto the mass transport, metal electrodes composed of a couple of a Pt (99.95%, Nilaco) and IrO₂-coated Ti (Japan Carlit) electrodes were employed as model cells for the parallel cell and the *i*-PEs. Table 4-3-1 shows the relationship between rotating speed of a magnetic stirrer (length of 4 cm) and flow rate in the vicinity of the sampling point in a glass beaker (inner diameter of 75 mm) containing and 250 mL of 0.5 M potassium borate with pH 9.5, which was measured by observing the speed of colored resin particles (Chelex[®] 200-400, Bio-Rad). The observed flow rates, v , were proportional to the rotating speeds, ω , under 300 rpm, obtaining an approximate equation of

$$v = 0.071\omega - 3.1 \quad (4-1)$$

which gave the estimated flow rates at ω of higher than 300 rpm. The Reynolds number Re was derived from v , the kinetic viscosity of water ($9 \times 10^{-3} \text{ cm}^2 \text{ s}^{-1}$) and the characteristic length of the electrode L (set to 1 cm). It should be noted that the obtained Re of < 4000 suggests the laminarity of the flow or possibly transition region. Therefore, the Sherwood number Sh can be described as

$$Sh = 0.664 \frac{v^{0.33}}{D} Re^{0.5} \quad (4-2)$$

where D stands for the diffusion coefficient of H⁺, which was assumed to be $9.31 \times 10^{-5} \text{ cm}^2 \text{ s}^{-2}$.^[23–25] Furthermore, the thickness of diffusion boundary layer, δ , is obtained according to the expression of Sh ($= L/\delta$) as listed in the table.

Chapter 4. Development of Flexible ZnSe:Cu(In,Ga)Se₂ Photocathodes for Construction of Stirring-Free Photoelectrochemical Cells

Table 4-3-1. Relationship between the rotation speed of the magnetic stirrer, measured flow rate in the vicinity of the sampling point and estimated thickness of diffusion boundary layer on the electrodes. The parameters at the rotating speed of 400 rpm or higher (*italic*) were determined by extrapolation of the data at the speed of lower than 400 rpm and assuming laminar flow.

Rotating speed ω [rpm]	Linear flow rate v [cm s ⁻¹]	Reynolds number Re	Sherwood number Sh	Diffusion boundary layer thickness δ [mm]
0	0	0	0	-
100	4.0	4.0×10^2	6.4×10^1	1.6×10^{-1}
150	7.5	8.0×10^2	8.8×10^1	1.1×10^{-1}
200	11	1.2×10^3	1.1×10^2	9.4×10^{-2}
250	15	1.6×10^3	1.2×10^2	8.0×10^{-2}
300	18	2.0×10^3	1.4×10^2	7.3×10^{-2}
<i>400</i>	<i>25</i>	<i>2.8×10^3</i>	<i>1.6×10^2</i>	<i>6.2×10^{-2}</i>
<i>500</i>	<i>32</i>	<i>3.6×10^3</i>	<i>1.8×10^2</i>	<i>5.5×10^{-2}</i>

The metal photoelectrodes (the total geometric surface area of approximately 1 cm²) conducted electrolysis water at the current densities of 0.7 mA cm⁻² and 4 mA cm⁻² under various rotation speeds. The error bars stand for each width of data section, which is caused by formation and detachment of bubbles. At the current density of 0.7 mA cm⁻², the difference in current between the stirring-free and saturated conditions was 5 and 12% for the comb-like cell and the conventional parallel cell, respectively, which is consistent with the results obtained above and in section 2-3-4. The comb-like cell showed saturation of operation current at $\delta = 0.1$ mm, at which H⁺ transport at the center of each electrode stripe into the bulk electrolyte was facilitated because the width is approximately 0.5-1 mm. It should be noted that the comb-like cell showed a slight but considerable decrease in the current density at the rotation speed of 100 rpm, which is possibly due to suppression of reverse reactions such as hydrogen oxidation and oxygen reduction reactions by facilitating removal of products, although further investigation is required to reveal the origin. In the case of the current density of 4 mA cm⁻²,

Chapter 4. Development of Flexible ZnSe:Cu(In,Ga)Se₂ Photocathodes for Construction of Stirring-Free Photoelectrochemical Cells

both the comb-like and parallel cells showed severe decreases in the current density value by 15% at the stirring-free condition, while the comb-like cell readily reached the saturation of the operation current as the convection was forced. This is because the estimated boundary layer thickness needed for the saturation is only $\sim 60\ \mu\text{m}$ as written in Table 4-3-1, which is much smaller than the width of each electrode on the comb-like cell, although the change in the H^+ by OER on the anode surface and natural convection by bubble removal make it difficult to discuss the relationship between δ and operation current by extracting mass transport coefficient. Despite that, it has been revealed that further refinement of *i*-PEs is required for realization of such a high operation current.

Chapter 4. Development of Flexible ZnSe:Cu(In,Ga)Se₂ Photocathodes for Construction of Stirring-Free Photoelectrochemical Cells

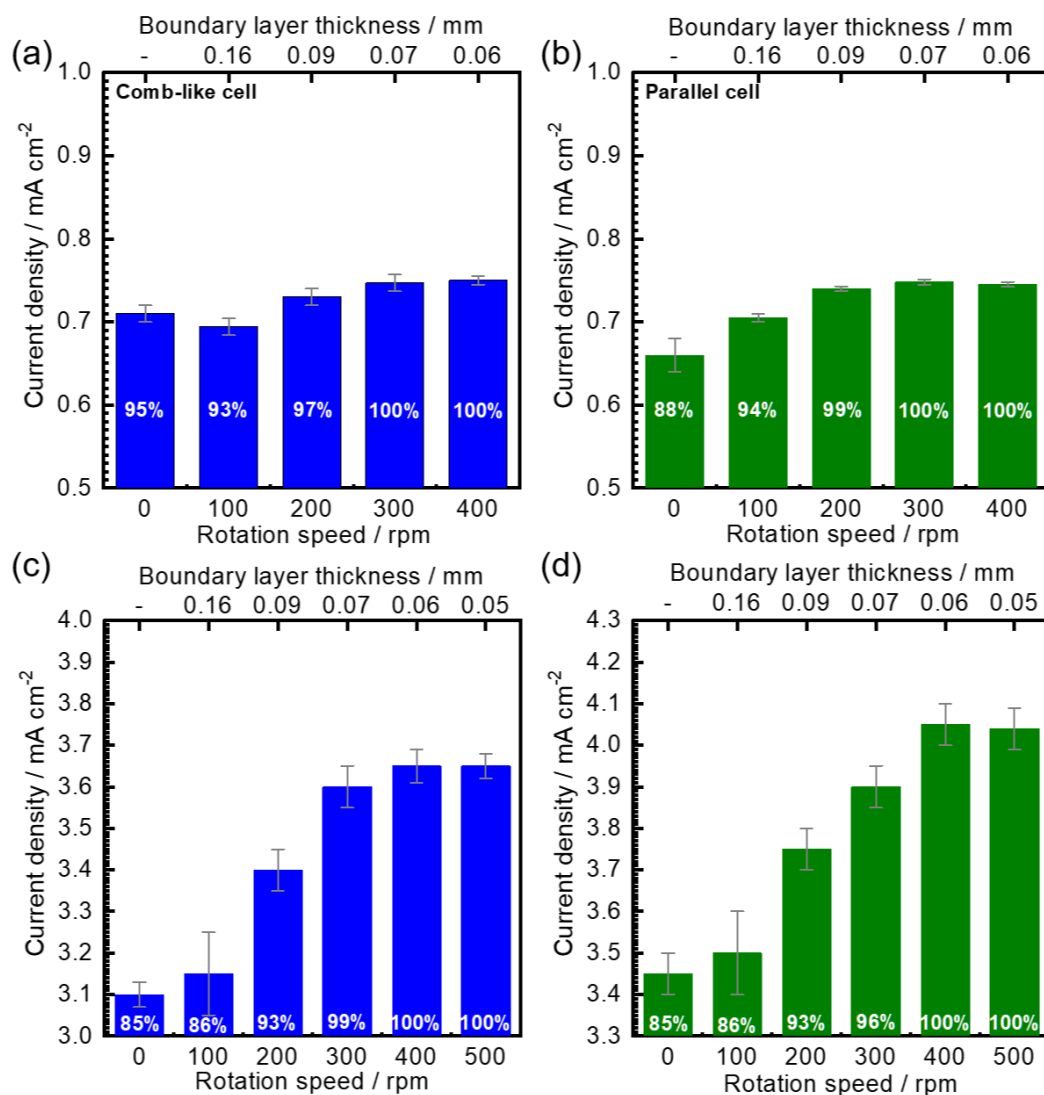


Figure 4-3-3. The relationship between rotation speed of the magnetic stirrer and operation current in chronoamperometry using the comb-like (a, c) and parallel (b, d) two-electrode cells. The percentages and error bars stand for each ratio of the current to the saturated value and data section, respectively.

Another set of *i*-PEs were fabricated and illuminated by simulated sunlight to measure the STH. The plots of evolved gas were shown in Figure 4-3-4. The STH 0.5 h after the initiation of reaction was found to be 1.0% without stirring. The average STH value for the reaction period of 2.5 h was calculated to be 0.6%. To the best of the author's knowledge, this is the first report on spontaneous overall water splitting using a PEC cell without stirring the electrolyte for hours. Although the rate

Chapter 4. Development of Flexible ZnSe:Cu(In,Ga)Se₂ Photocathodes for Construction of Stirring-Free Photoelectrochemical Cells

of gas evolution continuously decreased, the speed of decrease is much slower than that reported in chapter 3, which is probably attributed to the effect of the CBD-In₂S₃. It is very interesting that the production rate of gases dramatically recovered after interrupting the reaction for 15 min; the STH 0.5 h after the restart of reaction was approximately 0.9%. Figure 4-3-5 shows XPS spectra obtained from the photocathode before and after reaction in a PEC cell. A conventional parallel cell was employed so as to eliminate the possibility of unintentional contamination by BiVO₄. The result clearly revealed that the Bi species was deposited on the surface of the photocathode, suggesting that the surface of Pt HER catalysts was poisoned, resulting in the degradation of reaction rate. Moreover, the recovery of the cell performance by interruption of light irradiation can be explained by the dissolvment of Bi species from photocathode surface in the dark. This is why the reaction rate regained at the second run in Figure 4-3-4. Furthermore, the difference in stability between the *i*-PEs without and with stirring the electrolyte exhibited in Figure 4-3-2 can be attributed to the difference in the deposition condition of the Bi species; forced convection should promote the transport of the Bi species from the photoanode surface to the photocathode surface. Investigation on the control of impurity species to prevent the HER catalyst from surface poisoning is reported in chapter 6.

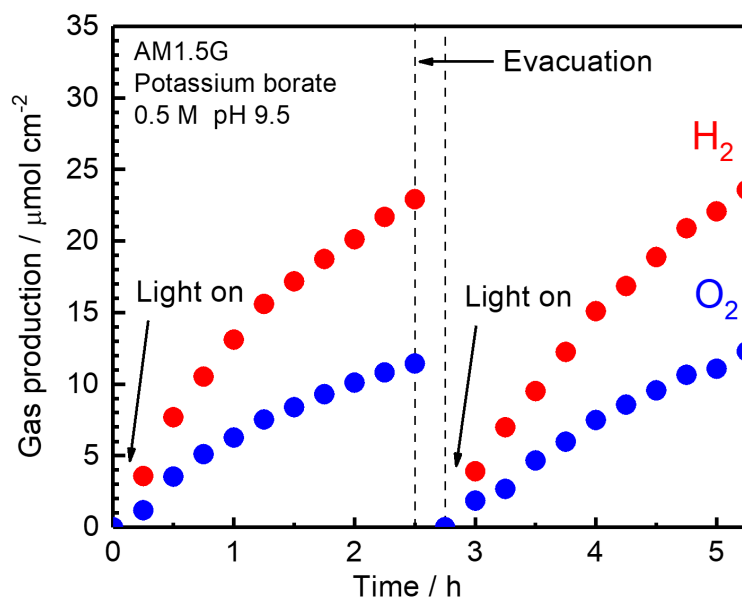


Figure 4-3-4. Evolved hydrogen (red) and oxygen (blue) gases over time using the *i*-PEs composed of the (ZnSe)_{0.85}(CIGS)_{0.15} photocathode (geometric area of 0.33 cm²) and a BiVO₄ photoanode (0.88 cm²) under simulated sunlight without stirring the electrolyte.

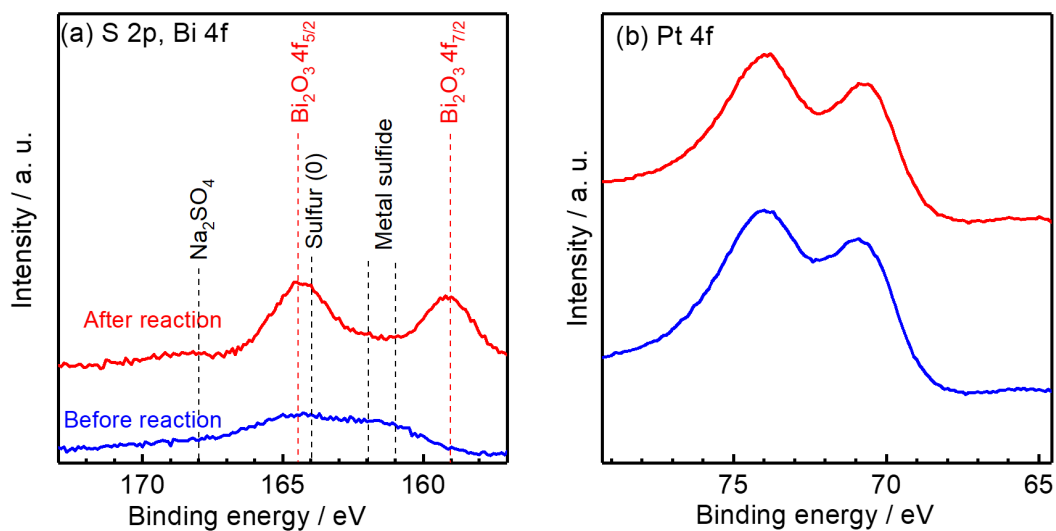


Figure 4-3-5. XPS spectra obtained for S and Bi (a), and Pt (b) from the surface of (ZnSe)_{0.85}(CIGS)_{0.15} photocathodes before (blue) and after (red) overall water splitting reaction in a PEC cell with a BiVO₄ photoanode for 1.7 h.

4-4 Conclusions

Effects of substrates onto the PEC properties of the (ZnSe)_{0.85}(CIGS)_{0.15} photocathodes were investigated. A Na species in the substrate was found to be indispensable for the (ZnSe)_{0.85}(CIGS)_{0.15} photocathodes to show sufficient photocurrent values and onset potentials. Sputtering of a thin SLG layer on the Ti foil for fabrication of the flexible (ZnSe)_{0.85}(CIGS)_{0.15} photocathode resulted in a comparable photocurrent value with the conventional photocathode deposited on the Mo-coated SLG substrate. The flexible photocathode deposited on the Ti foil is relatively easy to cut and bend, which enabled construction of comb-like PEC cells with BiVO₄ photoanodes. Moreover, the easiness in manipulating can be applied to further fabrications of semiconductor electrodes such as membrane electrode assembly.^[26]

Treating the CdS layer with CBD of In₂S₃ was found to be effective to improve the durability at a positive potential without significant corrosion. The decrement of photocurrent after 55 min of continuous PEC reaction at 0.6 V_{RHE} was alleviated from 39% to 20%, although there was still considerable degradation observed.

The *i*-PEs composed of the flexible (ZnSe)_{0.85}(CIGS)_{0.15} photocathode and a BiVO₄ photoanode were fabricated and their water splitting activity was measured. The cell showed almost no difference in the STH between with and without stirring the electrolyte. That means that the structure of *i*-PEs is advantageous in terms of scalability and efficiency compared with the conventional PEC cells. The initial STH recorded 1.0% without the stirring, while reversible degradation in the activity due to surface poisoning on photocathode by Bi species was also observed, which is addressed in chapter 6.

References

- [1] F. Pianezzi, P. Reinhard, A. Chirila, B. Bissig, S. Nishiwaki, S. Buecheler, A. N. Tiwari, *Phys. Chem. Chem. Phys.* **2014**, *16*, 8843.

Chapter 4. Development of Flexible ZnSe:Cu(In,Ga)Se₂ Photocathodes for Construction of Stirring-Free Photoelectrochemical Cells

- [2] A. Sadono, T. Ogihara, M. Hino, K. Yamamoto, K. Nakada, A. Yamada, *Jpn. J. Appl. Phys.* **2017**, *56*, 08MC15.
- [3] A. Chirilă, P. Reinhard, F. Pianezzi, P. Bloesch, A. R. Uhl, C. Fella, L. Kranz, D. Keller, C. Gretener, H. Hagendorfer, D. Jaeger, R. Erni, S. Nishiwaki, S. Buecheler, A. N. Tiwari, *Nat. Mater.* **2013**, *12*, 1107.
- [4] C. P. Muzzillo, *Sol. Energy Mater. Sol. Cells* **2017**, *172*, 18.
- [5] B. L. Kronik, D. Cahen, H. W. Schock, *Adv. Mater.* **1998**, *10*, 31.
- [6] S. Ishizuka, A. Yamada, K. Matsubara, P. Fons, K. Sakurai, S. Niki, *Appl. Phys. Lett.* **2008**, *93*, 124105.
- [7] F. Jiang, Gunawan, T. Harada, Y. Kuang, T. Minegishi, K. Domen, S. Ikeda, *J. Am. Chem. Soc.* **2015**, *137*, 13691.
- [8] H. Kumagai, T. Minegishi, N. Sato, T. Yamada, J. Kubota, K. Domen, *J. Mater. Chem. A* **2015**, *3*, 8300.
- [9] M. Moriya, T. Minegishi, H. Kumagai, M. Katayama, J. Kubota, K. Domen, *J. Am. Chem. Soc.* **2013**, *135*, 3733.
- [10] D. Yokoyama, T. Minegishi, K. Maeda, M. Katayama, J. Kubota, A. Yamada, M. Konagai, K. Domen, *Electrochem. Commun.* **2010**, *12*, 851.
- [11] Gunawan, W. Septina, S. Ikeda, T. Harada, T. Minegishi, K. Domen, M. Matsumura, *Chem. Commun.* **2014**, *50*, 8941.
- [12] M. Zhong, T. Hisatomi, T. Minegishi, H. Nishiyama, M. Katayama, T. Yamada, K. Domen, *J. Mater. Chem. A* **2016**, *4*, 9858.
- [13] C. D. Wagner, W. M. Riggs, L. E. Davis, J. F. Moulder, G. E. Mullenberg, *Handbook of X Ray Photoelectron Spectroscopy*; Eden Prairie, Minn., 1979.
- [14] S. Niki, M. Contreras, I. Repins, M. Powalla, K. Kushiya, S. Ishizuka, K. Matsubara, *Prog. Photovoltaics Res. Appl.* **2010**, *18*, 453.

Chapter 4. Development of Flexible ZnSe:Cu(In,Ga)Se₂ Photocathodes for Construction of Stirring-Free Photoelectrochemical Cells

- [15] Zinc Selenide (ZnSe). *Crystran Ltd.* **2012**, <https://www.crystran.co.uk/optical-materials/>.
- [16] P. Hidnert, *J. Res. Natl. Bur. Stand. (1934)*. **1943**, *30*, 101.
- [17] S. Chen, X. G. Gong, A. Walsh, S. H. Wei, *Appl. Phys. Lett.* **2010**, *96*, 021902.
- [18] P. Blösch, S. Nishiwaki, L. Kranz, C. M. Fella, F. Pianezzi, T. Jäger, C. Adelhelm, E. Franzke, S. Buecheler, A. N. Tiwari, *Sol. Energy Mater. Sol. Cells* **2014**, *124*, 10.
- [19] H. Stange, S. Brunken, H. Hempel, H. Rodriguez-Alvarez, N. Schäfer, D. Greiner, A. Scheu, J. Lauche, C. A. Kaufmann, T. Unold, D. Abou-Ras, R. Mainz, *Appl. Phys. Lett.* **2015**, *107*, 152103.
- [20] Y. Kageshima, T. Minegishi, Y. Goto, H. Kaneko, K. Domen, *Sustain. Energy Fuels* **2018**, *2*, 1957.
- [21] T. Moeller, *J. Am. Chem. Soc.* **1941**, *63*, 2625.
- [22] T. P. Dirkse, *IUPAC SDS Vol. 23*; 1983.
- [23] T. Higashi, H. Kaneko, T. Minegishi, H. Kobayashi, M. Zhong, Y. Kuang, T. Hisatomi, M. Katayama, T. Takata, H. Nishiyama, T. Yamada, K. Domen, *Chem. Commun.* **2017**, *53*, 11674.
- [24] H. Huang, F. Haghighat, *Build. Environ.* **2002**, *37*, 1127.
- [25] F. M. White, *Heat Transfer*; 1st ed.; Reading, Mass. : Addison-Wesley, 1988.
- [26] Y. Kageshima, T. Minegishi, T. Hisatomi, T. Takata, J. Kubota, K. Domen, *ChemSusChem* **2017**, *10*, 659.

Chapter 5

Effects of RuO₂-Coating onto the Durability of the

ZnSe:Cu(In,Ga)Se₂ Photocathode

5-1 Introduction

Through chapter 2-4, the photoelectrochemical (PEC) properties of (ZnSe)_{0.85}(CuIn_{0.7}Ga_{0.3}Se₂)_{0.15} (abbreviated as (ZnSe)_{0.85}(CIGS)_{0.15} herein) photocathodes were investigated. The (ZnSe)_{0.85}(CIGS)_{0.15} photocathodes showed a relatively long absorption edge of 850-900 nm and positive onset potential of 0.89 V_{RHE}. The photocathode modified with a combination of metal nanolayers (Mo and Ti) and metal sulfides (CdS and In₂S₃) improved the photocurrent value up to 12 mA cm⁻² under simulated sunlight in a neutral electrolyte of phosphate buffer solution. Moreover, as the case of other Cu-chalcopyrite-based photocathodes, the stability at negative potentials of <0.5 V_{RHE} is good enough for practical use. At an oxidative potential, however, a significant corrosion of the surface CdS layer was observed, causing severe degradation of the PEC cell. Moreover, although BiVO₄ photoanodes employed in this thesis require weak alkaline electrolytes, many other photoanodes reported so far use strong alkaline media, and such a harsh condition should increase the speed of CdS corrosion.^[1-6]

Surface coating with metal oxides has been reported as a promising means to stabilize semiconductor photoelectrodes.^[2,7-9] The most commonly used material is TiO₂, which requires a high temperature of >300°C for sufficient stabilization of itself by crystallization.^[10,11] However, such a high temperature often damages underlying layers, and another report has pointed out that pinholes in the TiO₂ layer are also generated by the change in density.^[12] This is a main reason why successful stabilization of Cu-chalcopyrite-based photocathodes using TiO₂ layers has not been reported yet. In other words, development of a protection layer which conformally covers the surface without any pinhole and which doesn't require heat treatment to get stabilized is indispensable to demonstrate durable PEC hydrogen evolution reaction (HER) for the (ZnSe)_{0.85}(CIGS)_{0.15} photocathodes.

Chapter 5. Effects of RuO₂-Coating onto the Durability of the ZnSe:Cu(In,Ga)Se₂ Photocathode

In this chapter, RuO₂ is focused on as a promising coating layer for (ZnSe)_{0.85}(CIGS)_{0.15} photocathodes. It has been reported that photo(electro)reduction of RuO₄⁻ can directly deposit a stable RuO₂ layer onto semiconductor materials without heat treatment.^[13,14] Moreover, RuO₂ is known as a relatively active HER catalyst, which means that additional deposition of Pt on the RuO₂ layer is not mandatory to drive efficient PEC HER. Tilley et al. have recently demonstrated stable PEC HER using a RuO₂-coated photocathode composed of metal oxides of Cu₂O, Al:ZnO and TiO₂ as the photoabsorber, n-type layer and protection layer, respectively. Nevertheless, investigation on usage of RuO₂ for a protection layer, especially at a positive potential, has not been reported yet. Furthermore, RuO₂ shows relatively high conductivity of electrons in spite of being oxide, which suggests that the RuO₂ layer can also act as conductive layer like a binary of Mo and Ti (Mo/Ti).^[15] The RuO₂ layer was, in summary, expected to function as a protection layer, HER catalyst and surface conductive layer in place of another metal oxide, Pt and Mo/Ti (Pt/Mo/Ti).

In this chapter, characterization and PEC properties of RuO₂-coated (ZnSe)_{0.85}(CIGS)_{0.15} photocathodes were investigated so as to demonstrate a highly durable water splitting using the PEC cell. Also, the relationship between the surface state of the RuO₂ layer and its activity on HER was revealed using angle-resolved X-ray photoelectron spectroscopy (AR-XPS).

5-2 Experimental Section

Preparation of (ZnSe)_{0.85}(CIGS)_{0.15} Thin Films

(ZnSe)_{0.85}(CIGS)_{0.15} thin films were deposited on substrates of Mo-coated soda-lime glass. The Mo-coated substrates were fabricated by RF magnetron sputtering of a Mo target (99.9%, Kojundo) onto each soda-lime glass plate heated at 573 K. Prior to the Mo deposition, a 30 nm thick Ti was deposited by the sputtering of a Ti target (99.9%, Kojundo) so as to improve the adhesion. The thickness of Mo and Ti are about 500 and 30 nm, respectively.

Chapter 5. Effects of RuO₂-Coating onto the Durability of the ZnSe:Cu(In,Ga)Se₂ Photocathode

The substrate was loaded into a deposition chamber equipped with Knudsen cells containing elemental Cu, In, Ga, Zn and Se (99.9999%, Asahi Metal or Furuuchi Chemical). The substrate temperature was set at 623 K for 5 min and then reset to 723 K for 35 min. The (ZnSe)_{0.85}(CIGS)_{0.15} thin films were deposited using the bilayer method (see chapter 3); the typical deposition rates for Cu, In, Ga, Zn and Se were 0.042, 0.095, 0.028, 0.4 and 1 nm s⁻¹, respectively. In and Ga were absent for the first and last 20 min, respectively, followed by 10 min-annealing in a Se atmosphere. The rates were monitored by using a quartz crystal microbalance sensor (Q-POD, INFICON). The pressure in the chamber was kept at $<2 \times 10^{-5}$ Pa during deposition. Following the film deposition processes, each sample was cooled from 723 to 573 K with exposure to Zn and Se vapor to alleviate the formation of a Zn-poor surface.

KCN Etching

After deposition, the samples were immersed into an etching solution containing 0.1 M KCN (98.0%, FUJIFILM Wako Pure Chemical) and 0.8 M KOH (8 M, FUJIFILM Wako Pure Chemical) for 1 min in room temperature. This etching process removed excess Cu from the (ZnSe)_{0.85}(CIGS)_{0.15} thin films. Energy dispersive X-ray spectroscopy (EDS; EMAX-7000, Horiba) analysis revealed that the atomic ratio of Cu/(In+Ga) was 0.9 to 1.0 after the process.

Characterization

The (ZnSe)_{0.85}(CIGS)_{0.15} thin film samples were analyzed using scanning electron microscopy (SEM; Hitachi), scanning transmission electron microscopy (STEM; JEM-2800, JEOL) equipped with an SDD detector for STEM-EDS mapping (X-Max 100 TLE, Oxford Instruments), AR-XPS (JPS-9000, JEOL) and electron-beam-induced current (EBIC) mapping conducted together with SEM (JSM-7000F, JEOL) at an acceleration voltage of 5 kV. Prior to the EBIC measurement, a 100 nm-thick Mo layer was additionally deposited onto the surface of (ZnSe)_{0.85}(CIGS)_{0.15} photocathodes by RF magnetron sputtering. The light transmittance of K₂RuO₄ solutions in quartz cells was measured using a dual beam UV-vis spectrometer (V-670, JASCO) with a reference cell filled with pure water.

Surface Modification with an CdS Layer

A CdS layer was formed on the surface of each (ZnSe)_{0.85}(CIGS)_{0.15} thin film using chemical bath deposition (CBD) method.^[15–17] The CBD solution with a volume of 50 mL contained 14 wt% ammonia (28 wt%, FUJIFILM Wako Pure Chemical), 25 mM of Cd(CH₃COO)₂ (98.0%, FUJIFILM Wako Pure Chemical) and 0.375 M of SC(NH₂)₂ (98.0%, Kanto Chemical). The bath temperature was gradually increased from room temperature to 325–326 K over the span of about 8 min. The samples were taken out from the bath and immediately washed with pure water 14 min after the initiation of heating, followed by annealing at 473 K for 1 min in air.

Chemical bath deposition treatment of In₂S₃

The CdS-modified (ZnSe)_{0.85}(CIGS)_{0.15} thin film was treated with additional CBD treatment of In₂S₃.^[18,19] The CBD solution with a volume of 50 mL contained 100 mM of CH₃COOH (99.7%, FUJIFILM Wako Pure Chemical), 25 mM of In₂(SO₄)₂ (FUJIFILM Wako Pure Chemical) and 100 mM of CH₃CSNH₂ (98.0%, FUJIFILM Wako Pure Chemical). The bath temperature was heated at 343 K. The samples were taken out from the bath and immediately washed with pure water 10 min after the initiation of heating.

Surface Modification with Thin Metal Layers

A binary of Mo/Ti with each thickness of 3 nm was deposited by successive RF magnetron sputtering of a Ti and Mo target in room temperature.^[15] Subsequently, a Pt layer with a thickness of a few nanometers was deposited on it by thermal evaporation of Pt wire (99.98%, Nilaco) in a high vacuum of $<4 \times 10^{-3}$ Pa.

Preparation of BiVO₄ Photoanodes

A BiOI precursor was prepared on an indium tin oxide (ITO)-coated soda-lime glass substrate (0051, Geomatec) by electrodeposition method in a three-electrode cell with an Ag/AgCl reference electrode in a saturated aqueous KCl solution and with a Pt wire counter electrode. Subsequently, a dimethyl sulfoxide solution containing VO(C₅H₇O₂)₂ (98%, Sigma-Aldrich) was drop-cast onto the precursor,

Chapter 5. Effects of RuO₂-Coating onto the Durability of the ZnSe:Cu(In,Ga)Se₂ Photocathode

followed by calcination at 723 K for 1 h in air. As oxygen evolution reaction (OER) catalyst, NiFeO_x-Bi was deposited onto the prepared BiVO₄ electrode (NiFeO_x-Bi/BiVO₄) by photoelectrodeposition method.^[20] The potential of the electrode was held at -0.16 V vs. Ag/AgCl until saturation of the photocurrent (typically requiring 10-20 min) under simulated sunlight (XES-40S2-CE, SAN-EI Electric) in a 0.5 M aqueous potassium borate solution containing 4 μM NiSO₄ (99.9%, FUJIFILM Wako Pure Chemical) and 40 μM FeSO₄ (99%, FUJIFILM Wako Pure Chemical) with the pH adjusted to 9.5 by KOH addition. It should be noted that a previous report describes the fabrication process of the BiVO₄-based photoanode in more detail.^[21]

Photoelectrochemical deposition of a RuO₂ layer

The (ZnSe)_{0.85}(CIGS)_{0.15} photocathodes treated by CBD of CdS and In₂S₃ were fixed and the region not intended for measurement was coated using epoxy resin (Araldite Rapid, Nichiban). Afterwards, they are exposed to simulated sunlight produced by a solar simulator (XES-40S2-CE, SAN-EI Electric) in a 1.3 mM K₂RuO₄ (98%, Strem Chemicals) solution for 3-5 min unless noted otherwise.^[13] A current density of -28 μA cm⁻² was applied during the exposure.

Photoelectrochemical Measurements

A three-electrode cell equipped with a magnetic stirrer under an Ar atmosphere using an aqueous solution of 1.0 M potassium phosphate buffer solution (pH 7.0 or 13.0, adjusted by adding KOH) as the electrolyte was set up and connected to a potentiostat (HSV-110, Hokuto Denko), unless otherwise noted. A solar simulator producing AM1.5G was employed as the light source. In the current-potential measurements, the applied potential, expressed relative to a reversible hydrogen electrode (RHE), was swept at 5 mV s⁻¹ from 0 V_{RHE} under intermittent irradiation with a period of 6 s. Mott-Schottky plots were obtained in the dark using a potentiostat (VersaSTAT 3, Princeton Applied Research) with applied potential perturbation at the amplitude of 20 mV applying the frequency of 2 kHz.

The wavelength dependence of the incident photon-to-current conversion efficiency (IPCE) was evaluated under monochromatic light from a 300 W Xe lamp equipped with a monochromator (CT-10, JASCO), where the light intensity was measured using a Si photodiode (S2281-01, Hamamatsu Photonics).

5-3 Results and Discussion

5-3-1 Characterization of the Photoelectrodeposited RuO₂ Layers

Figure 5-1-1 shows cross-sectional STEM-EDS elemental maps for the interfaces between the photoelectrodeposited RuO₂, In₂S₃, CdS and (ZnSe)_{0.85}(CIGS)_{0.15}. For the sample used in the measurement, the photoelectrodeposition time of RuO₂ was set to 15 min. The elemental maps suggest that the ruthenium oxide layer densely and conformally coats the surface of the underlying layer. As discussed in chapter 4, the In₂S₃ layer was too thin to be identified, but the existence of In species between RuO₂ and CdS can be identified from Figure 5-1-2 as the line profiles acquired along the red line shown in the image. Figure 5-1-3 shows high-resolution TEM (HRTEM) images and corresponding diffraction patterns at each part of the interface, although the boundary between CdS and (ZnSe)_{0.85}(CIGS)_{0.15} was very difficult to identify in the image because of the small lattice mismatch. The RuO₂ region is relatively uniform but the diffraction pattern suggests to be amorphous, while that of the underlying layer is crystalline as can be seen from the lattice fringes due to electron beam interference. This is supported by selected area electron diffraction patterns shown in Figure 5-1-4. The amorphous structure is preferable for the conformality without pinholes or voids between crystal grains, which are often formed in a polycrystalline protection layer.

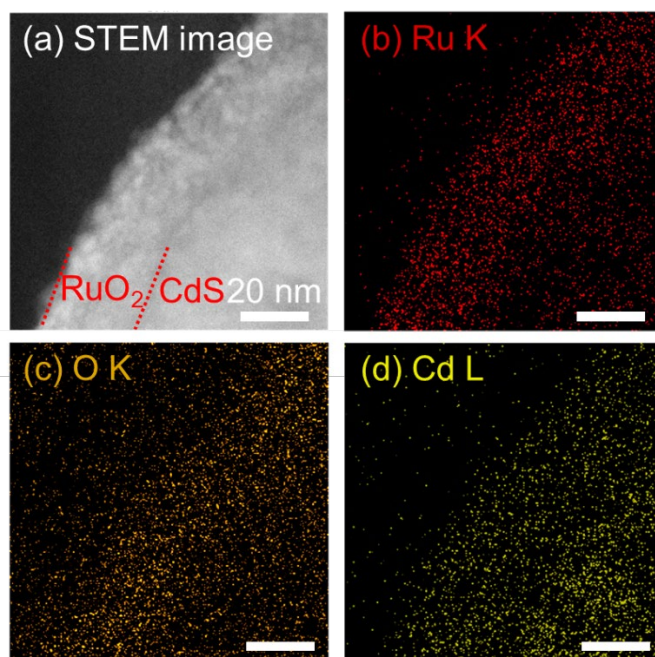


Figure 5-1-1. A cross-sectional STEM image (a) and the corresponding STEM-EDS elemental maps for (b) Ru, (c) O and (d) Cd at the interfaces between RuO_2 , In_2S_3 , CdS and $(\text{ZnSe})_{0.85}(\text{CIGS})_{0.15}$.

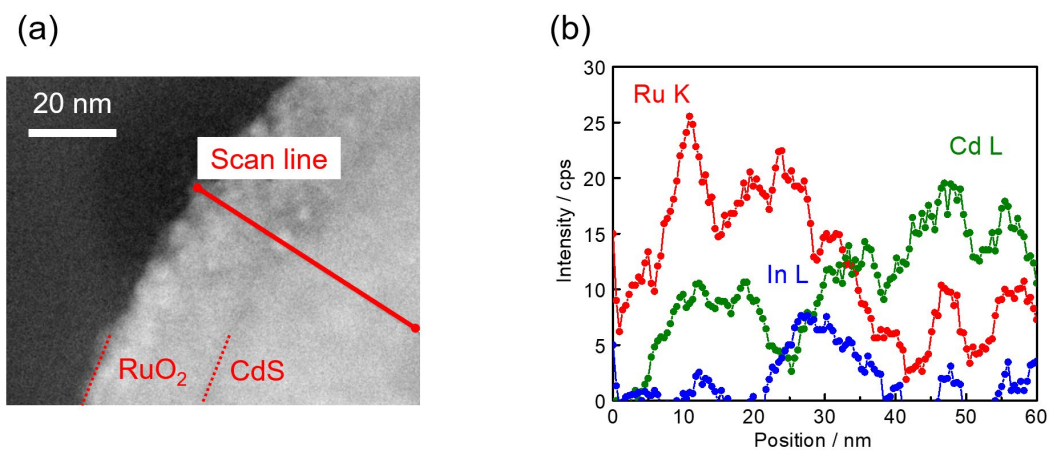


Figure 5-1-2. A cross-sectional STEM image (a) and the corresponding line profiles (b) acquired along the red line at the interfaces between RuO_2 , In_2S_3 , CdS and $(\text{ZnSe})_{0.85}(\text{CIGS})_{0.15}$.

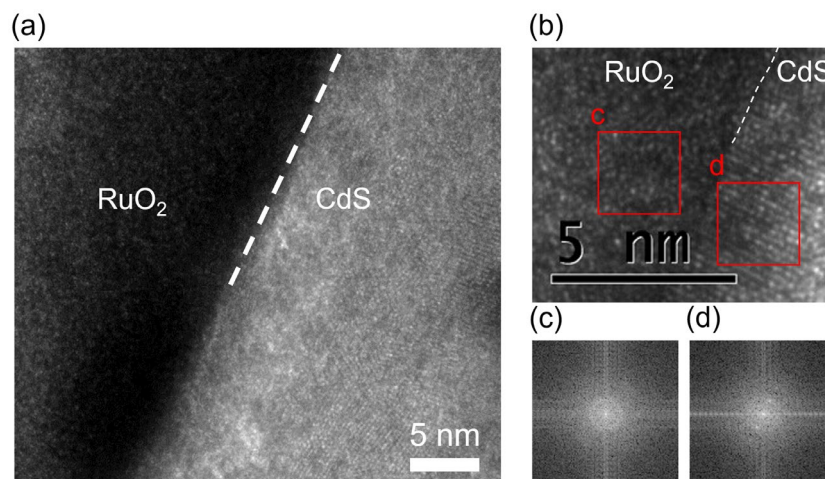


Figure 5-1-3. (a, b) HRTEM images at the interfaces between RuO_2 , In_2S_3 , CdS and $(\text{ZnSe})_{0.85}(\text{CIGS})_{0.15}$, and (c, d) fast-Fourier-transformed images of the domains shown in red squares.

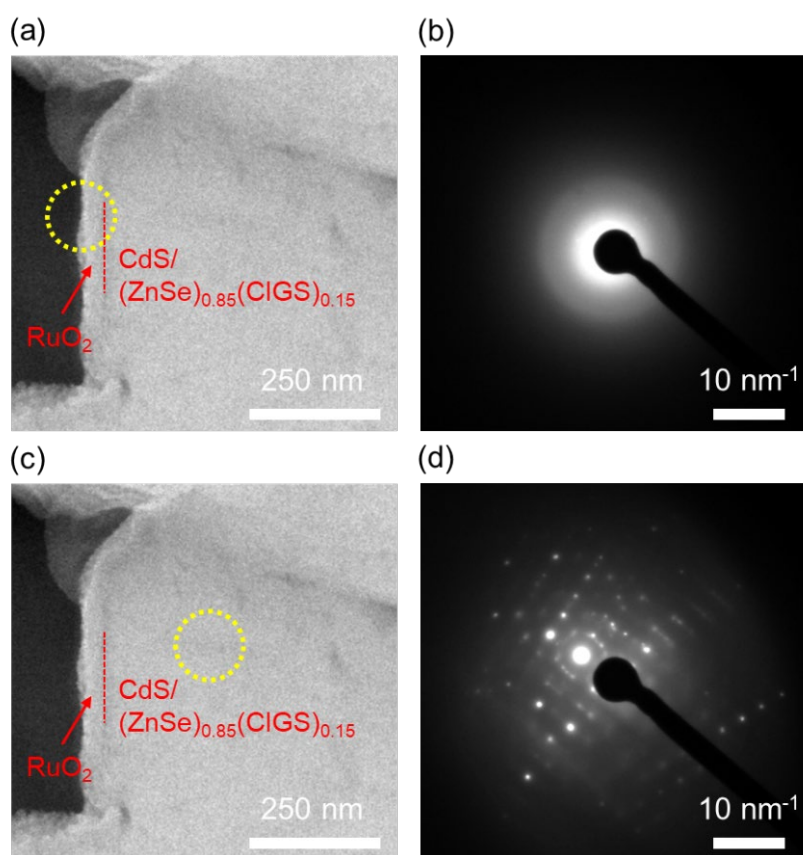


Figure 5-1-4. (a, c) Cross-sectional STEM images at the interfaces between RuO_2 , In_2S_3 , CdS and $(\text{ZnSe})_{0.85}(\text{CIGS})_{0.15}$, and (b, d) selected area electron diffraction patterns of the domains shown in yellow circles in (a, c).

The work function of the photoelectrodeposited RuO₂ layer was measured using PESA as shown in Figure 5-1-5. It has been found that the estimated work function, 5.4-5.5 eV vs. the vacuum level, is consistent with the reported value and quite similar between the commercially available RuO₂ powder and the prepared RuO₂ layer deposited on an FTO glass, which suggests that the RuO₂ layer doesn't consist of significant impurity phases such as metallic Ru (work function of 4.7 eV).^[22]

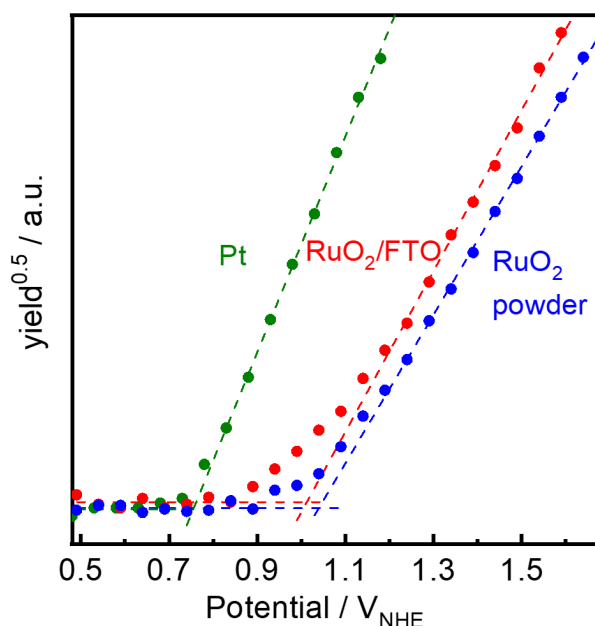


Figure 5-1-5. PESA spectra for a Pt plate (99.95%, Tanaka Kikinzoku Kogyo), RuO₂ powder (FUJIFILM Wako Pure Chemical) and a RuO₂ layer photoelectrodeposited onto an FTO glass (RuO₂/FTO).

The in-plane electric conductivity of the RuO₂/FTO was measured by preparing indium electrode at both ends of the specimen by vacuum evaporation. By comparing the resistivity with that of a bare FTO glass assuming a parallel circuit of two resistors, the resistivity of the RuO₂ layer was estimated to be 1.4 $\mu\Omega$. The resistivity is comparable with that of a Mo/Ti binary (1.2 $\mu\Omega$), which is a conventional conductive layer reported by Kumagai et al.^[15] Hence, the RuO₂ layer itself is able to

Chapter 5. Effects of RuO₂-Coating onto the Durability of the ZnSe:Cu(In,Ga)Se₂ Photocathode

function as a good electron mediator from the sulfide layer to reaction sites thanks to the conformality and low resistivity.

The cross-sectional characterizations have also revealed a significant difference between the estimated deposition rate and the actual value; the theoretical deposition rate was 1.1 nm⁻¹ by considering the density of crystalline RuO₂ (6.97 g cm⁻³), the applied current (-28 μA cm⁻²) and Eq. (5-1),^[23] which is the reduction reaction of RuO₄⁻.



However, the Figure 5-1-1 showed the RuO₂ layer with a thickness of 25-30 nm, meaning the actual deposition rate of 2 nm⁻¹. Considering the roughness of the photocathode surface, the difference can be even larger. It is noted that the Figure 5-1-3 suggests the layer is obviously dense, so the layer structure doesn't contribute to the difference in the deposition rates.

It is suggested that electroless decomposition of RuO₄⁻ species to RuO₂ promotes the deposition process. Figure 5-1-6 shows the photographs of KRuO₄ aqueous solutions before and after photoelectrodeposition procedures. The deposition process clearly changes the color of the solution from yellow to dark green, which is attributed to formation of RuO₂ without any electrode reaction. To the best of the author's knowledge, such a phenomenon has not been reported on a H₂PtCl₆ aqueous solution, a commonly-used precursor for photoelectrodeposition of Pt. Time-courses of transmittance spectra of the solution treated with and without continuous light irradiation were shown in Figure 5-1-7. Given that the Lambert-Beer's law holds true for the product (RuO₂ particles), its production rate was suggested to be (pseudo-) zero-order, which can be attributed to the photoinduced decomposition of RuO₄⁻. A possible reaction formula for the electroless decomposition is suggested in Eq. (5-2).^[14]

Chapter 5. Effects of RuO₂-Coating onto the Durability of the ZnSe:Cu(In,Ga)Se₂ Photocathode



Typical photoelectrodeposition process can often be site-selective if the photoelectrode surface is not uniform because the process is strongly affected by the potential at the outermost surface.^[24] The feature in turn can disturb formation of a conformal and monolithic layer. On the other hand, the electroless photodeposition of RuO₂ can proceed upon the entire surface to support formation of the conformal thin layer as shown in Figure 5-1-1 and 5-1-3. The high coverage of the RuO₂ layer is expected to realize sufficient durability of the (ZnSe)_{0.85}(CIGS)_{0.15} photocathode, which is investigated in the next section.

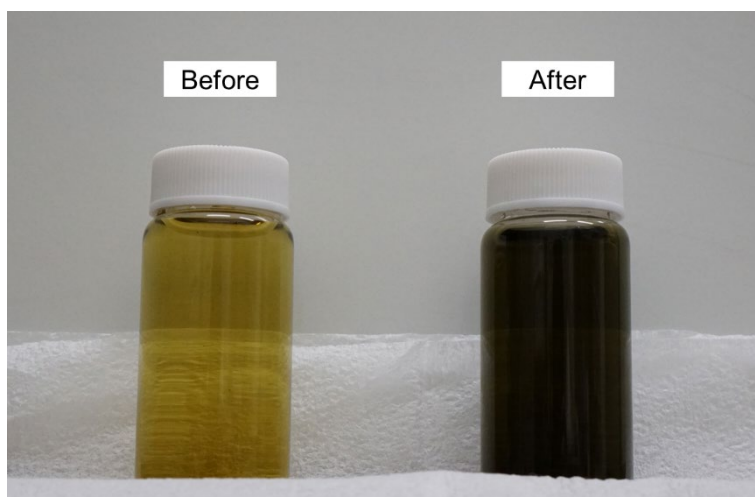


Figure 5-1-6. A photographic image of aqueous solutions of containing 1.3 mM KRuO₄ before (left) and after (right) several photoelectrodeposition procedures.

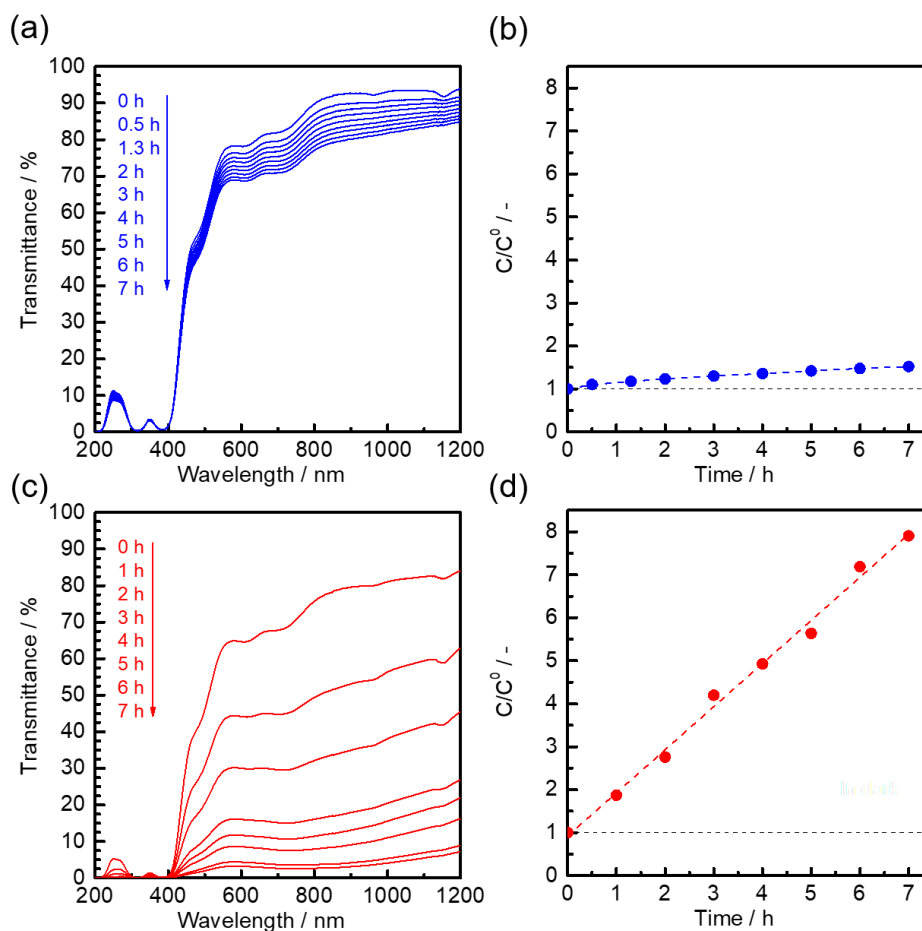


Figure 5-1-7. (a, c) Time-courses of the transmittance spectra of aqueous solutions of containing 1.3 mM K₂RuO₄ in quartz cells left in dark (a) and under continuous light irradiation from a 300 W Xe lamp equipped with filters (420-800 nm) (c), and (b, d) the corresponding relative concentrations (C/C^0) of nanoparticles in the solutions left in the dark (b) and under light irradiation (d), assuming the Lambert-Beer's law for the product using the transmittance at 600 nm.

5-3-2 Photoelectrochemical Properties of RuO₂-Coated ZnSe:Cu(In,Ga)Se₂ Photocathodes

Figure 5-2-1 shows current-time curves for the (ZnSe)_{0.85}(CIGS)_{0.15} photocathodes at 0.6 V_{RHE} under simulated sunlight. The initial photocurrent values were 0.1 and 1.2 mA cm⁻² in the phosphate electrolytes at pH 7 and 13, respectively. These values are clearly lower than the values of photocathodes modified with the conventional layers, Pt/Mo/Ti (see chapter 3). However, they

gradually increased up to almost three times as large as the initial values over the span of several hours under light irradiation. Herein, the phenomenon is called activation, and some other works have reported similar effects in HER.^[25,26] The phenomenon is further investigated in the next section. After the end of the activation, the photocathodes showed no clear decrease in the photocurrent for longer than 10 h at both conditions. In contrast, the conventional photocathodes showed a rapid decrease to one tenth of the initial value in just a few hours because of the high potential and the pH 13 electrolyte. Figure 5-2-2 compares surface SEM images of each photocathode before and after the current-time measurements in the pH 13 electrolyte. The RuO₂-coated (ZnSe)_{0.85}(CIGS)_{0.15} photocathode was found to exhibit no clear change in the surface morphology and remain as a dense layer after the long-term PEC HER for 17 h. The photoelectrodeposited RuO₂ layer functions as a stable protection layer even in a pH 13 electrolyte without any heat treatment. On the other hand, severe cracks at the surface were observed within 7 h of the PEC reaction due to the corrosion in the case of the photocathode modified with Pt/Mo/Ti.

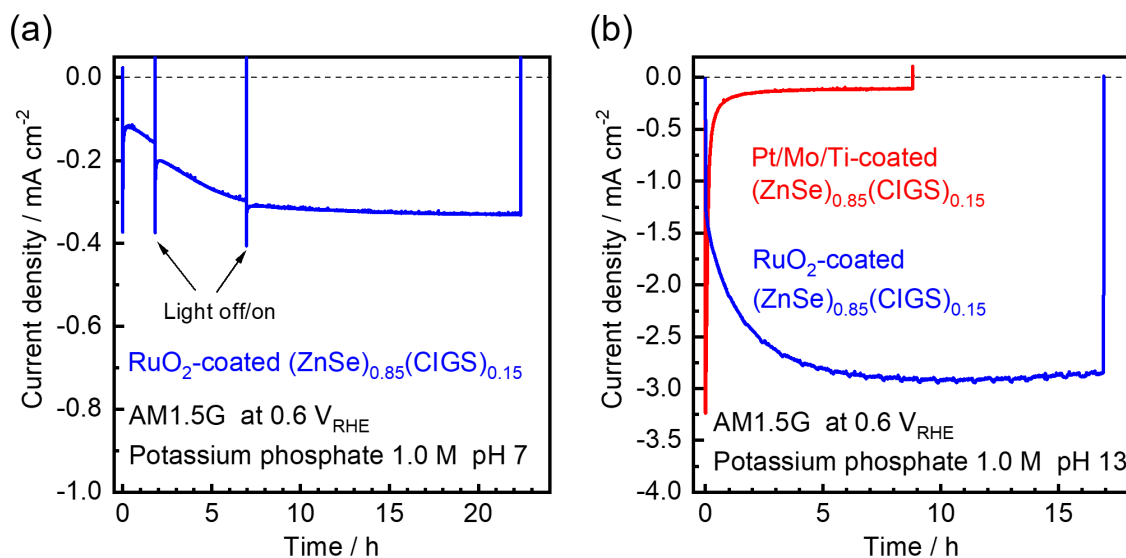


Figure 5-2-1. Current-time curves for the (ZnSe)_{0.85}(CIGS)_{0.15} photocathodes modified with RuO₂ (blue) and combination of Mo/Ti binary and Pt (Pt/Mo/Ti, red) at 0.6 V_{RHE}.

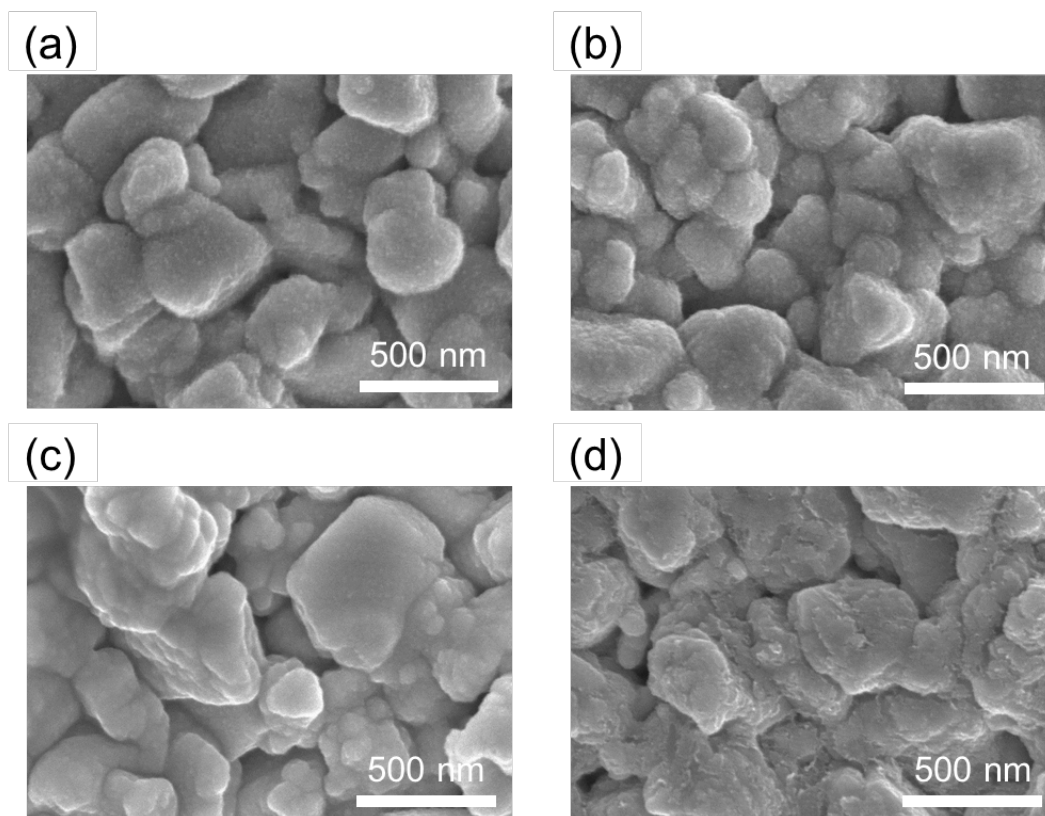


Figure 5-2-2. Surface SEM images of the (ZnSe)_{0.85}(CIGS)_{0.15} photocathodes coated with RuO₂ (a, b) and Pt/Mo/Ti (c, d) before (a, c) and after (b, d) the measurements in Figure 5-2-1 (b).

Figure 5-2-3 shows current-potential curves for the RuO₂-coated (ZnSe)_{0.85}(CIGS)_{0.15} photocathodes before and after activation. The activation process clearly increased the photocurrent at the potentials below the onset. The photocurrent value in the pH 13 electrolyte reached 9.1 mA cm⁻² at 0 V_{RHE} under simulated sunlight, while the value in the pH 7 electrolyte was relatively low, 4.6 mA cm⁻². The reason for the remarkable difference in the photocurrent is discussed in the next section. Furthermore, the pH difference also resulted in the shift in the onset potential of approximately 0.15 V. This can be explained by the change in the pinning potentials of the band edges at the electrode-electrolyte interface. The measurement of Mott-Schottky plots exhibited in Figure 5-2-4 revealed a significant increase in the estimated flat-band potential vs. RHE, while it showed little shift if compared with the Ag/AgCl electrode. This is not the case with another metal

oxide, TiO₂, reported by Watanabe et al. possibly due to the difference in the surface protonation mechanism or permeance of ions,^[27] which should be addressed in the future. In any case, the relatively high onset potential of the RuO₂-coated photocathode is preferable for construction of photoanodes based on a highly alkaline solution. The linearity of the plots at around the onset potential also suggested existence of a meaningful depletion layer at the electrode-electrolyte interface without a significant potential barrier undesirable for smooth charge transfer from CdS to RuO₂.

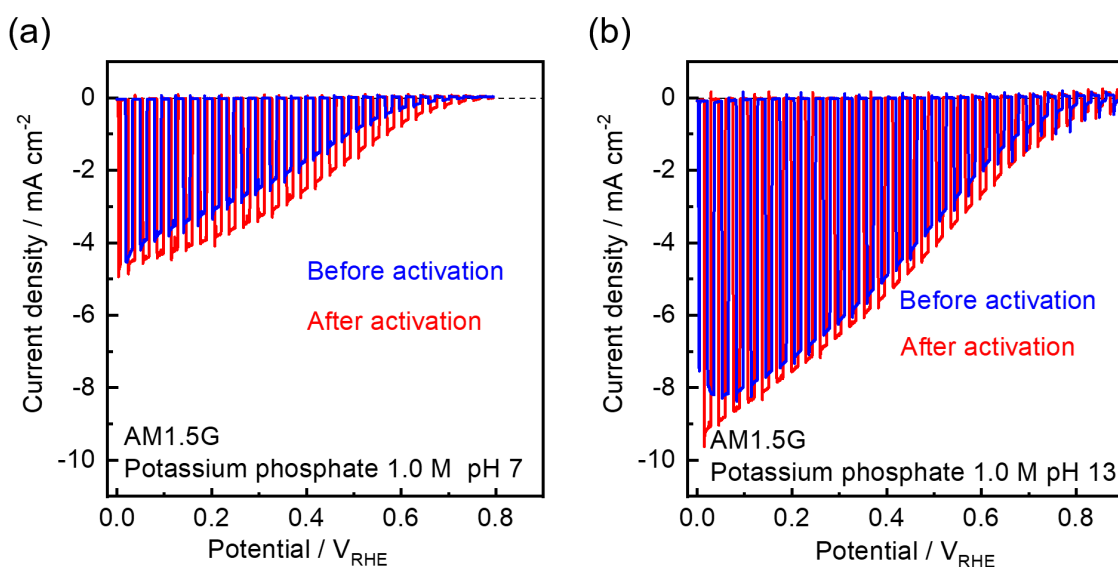


Figure 5-2-3. Current-potential curves for the RuO₂-coated (ZnSe)_{0.85}(CIGS)_{0.15} photocathodes before (blue) and after (red) the activation.

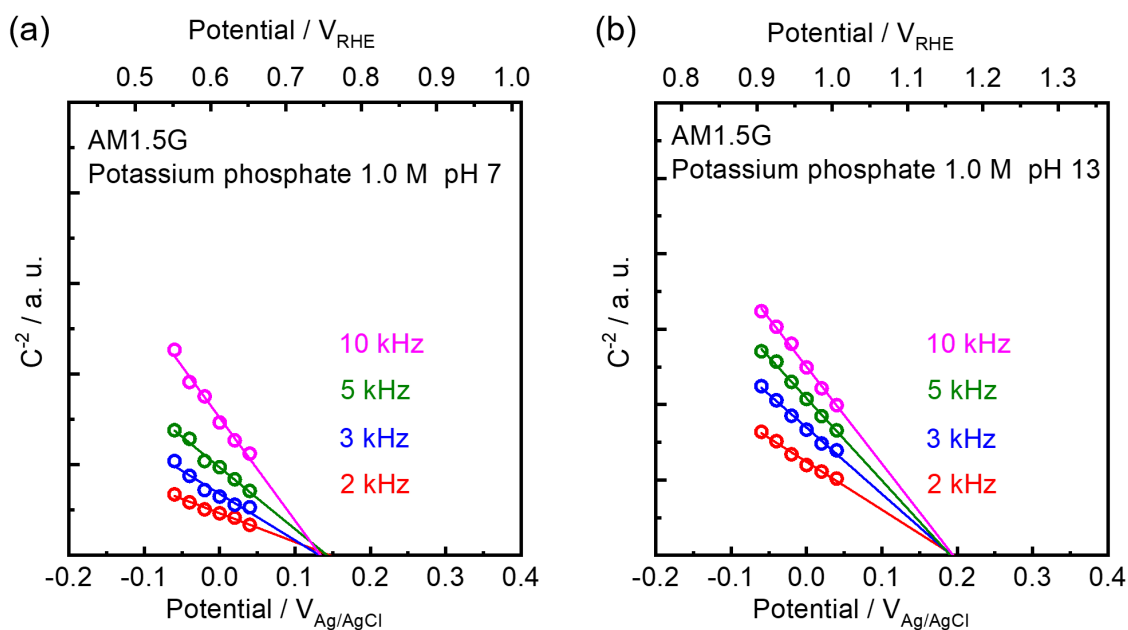


Figure 5-2-4. Mott-Schottky plots for the RuO₂-coated (ZnSe)_{0.85}(CIGS)_{0.15} photocathodes measured in 1.0 M potassium phosphate buffer solutions at pH 7 (a) and 13 (b). The potential perturbation was applied at various frequencies.

As discussed above, the RuO₂-coated (ZnSe)_{0.85}(CIGS)_{0.15} photocathodes showed a unique phenomenon called activation by long-term PEC reaction. Mapping of EBIC signals was conducted by forming a 100 nm-thick Mo layer on the surface of the photocathode before and after the activation process. The details about the EBIC measurements are described in chapter 3. As shown in Figure 5-2-5, EBIC signals were detected in the vicinity of the interface between CdS and (ZnSe)_{0.85}(CIGS)_{0.15}, although the distribution is slightly different from the results for the Mo/Ti-deposited sample shown in Figure 3-2-3 possibly due to existence of the RuO₂ layer. It is difficult to find any appreciable difference in the signal distribution by the activation process. To conclude, the effect of the activation process is not attributed to the change in the inside of the photocathode. Instead, it is highly possible that the change in the surface RuO₂ layer caused the increase in photocurrent. In the next section, the RuO₂ layers before and after activation are analyzed in detail.

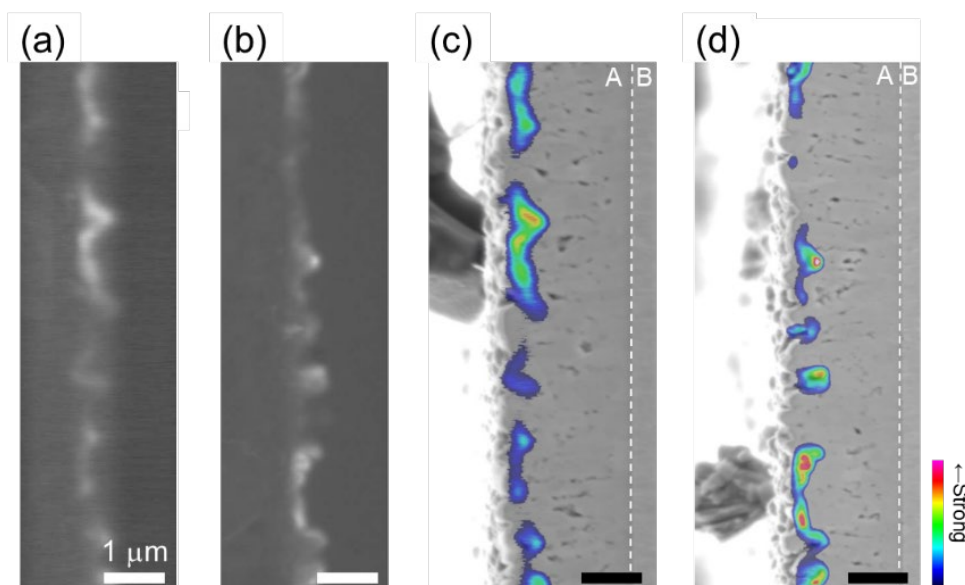


Figure 5-2-5. Maps of EBIC signals for the RuO₂-coated (ZnSe)_{0.85}(CIGS)_{0.15} photocathodes before (a, c) and after (b, d) activation. The signal intensity was normalized in each map (a, b), and then colorized maps (c, d) were generated according to the normalized values. The designations A and B stand for the (ZnSe)_{0.85}(CIGS)_{0.15} and back side Mo, respectively.

The decrease in the photocurrent value due to the absence of Pt, which is highly active for HER, can be recovered by sequential photoelectrodeposition, which has recently been reported by co-workers of the author using particulate (ZnSe)_{0.85}(CIGS)_{0.15} photocathodes.^[28] Existence of Pt on the RuO₂ layer (Pt/RuO₂) generates photocurrent as high as that of Pt-modified photocathodes, but it showed a relatively poor durability due to detachment of Pt, which was possibly caused by the hydroxylation and structure change during the activation process. On the other hand, further deposition of RuO₂ over Pt/RuO₂ (RuO₂/Pt/RuO₂) maintained both high photocurrent and sufficient durability of Pt-modified and RuO₂-modified (ZnSe)_{0.85}(CIGS)_{0.15} photocathodes, respectively. The investigation demonstrated facilitation of HER activity of the RuO₂ layer by additional modification.

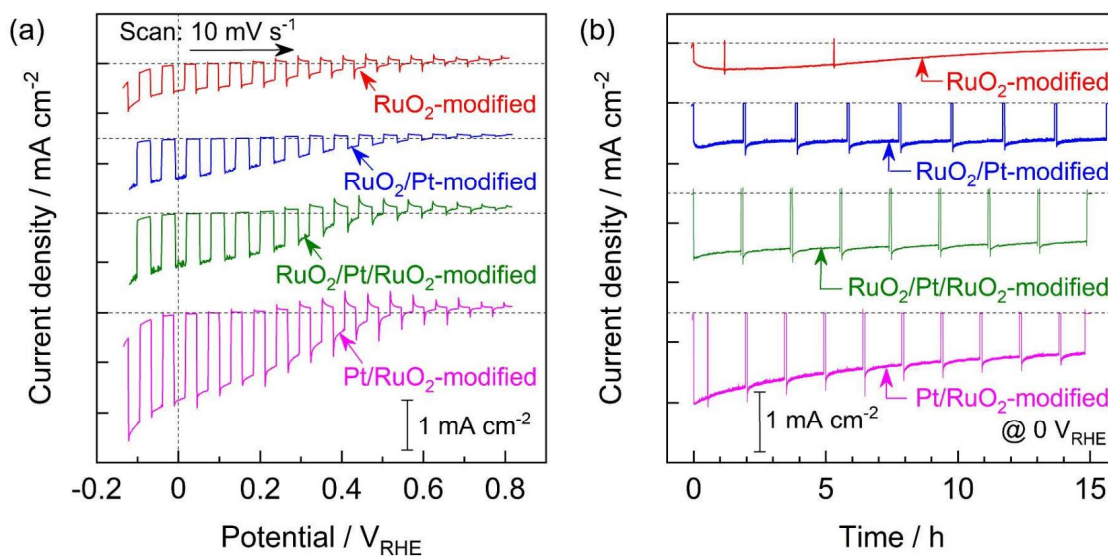


Figure 5-2-6. Current-potential curves for the particulate (ZnSe)_{0.85}(CIGS)_{0.15} photocathodes under simulated sunlight modified with RuO₂ and/or Pt by sequential photoelectrodeposition. A 1.0 M potassium phosphate solution (pH 13) was used as the electrolyte. Reprinted with permission from ref. [28] - Published by The Royal Society of Chemistry.

Figure 5-2-7 represents the PEC properties of the thin-film (ZnSe)_{0.85}(CIGS)_{0.15} photocathode modified with RuO₂/Pt/RuO₂. The deposition condition was the same with the literature.^[28] As is the case with the particulate photocathode, employment of RuO₂/Pt/RuO₂ resulted in the larger photocurrent values of (ZnSe)_{0.85}(CIGS)_{0.15} photocathodes than that of monolayer RuO₂. Moreover, the current-time curve revealed that there was no detriment in the durability at 0.6 V_{RHE}. The maximum photocurrent after the activation was increased from 2.8 mA cm⁻² to 4.3 mA cm⁻². Although further investigation on reaction mechanism of RuO₂/Pt/RuO₂ is required, the application was found to be suitable for the thin film photocathode as well as the particulate photocathode.

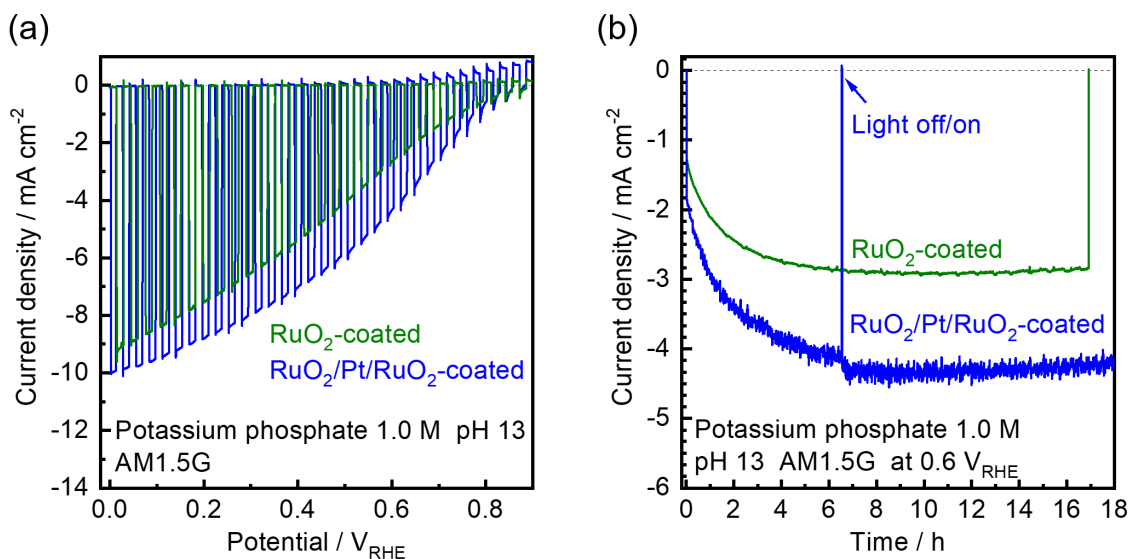


Figure 5-2-7. (a) Current-potential curves for the (ZnSe)_{0.85}(CIGS)_{0.15} photocathodes coated with RuO₂ (green) and RuO₂/Pt/RuO₂ (blue) under simulated sunlight after the activation, and (b) the current-time curves for each photocathode at 0.6 V_{RHE}.

5-3-3 Analysis of the RuO₂ Layers Using Angle-Resolved X-ray Photoelectron Spectroscopy

AR-XPS was employed to study the activation mechanism of RuO₂, at which Ru 3p_{3/2} peaks were repeatedly obtained by changing the takeoff angles of photoelectrons. In principle, a low takeoff angle leads to a shallow detection depth of photoelectrons. The spectra before and after the activation process are shown in Figure 5-2-6 to discuss the chemical states of Ru. Each peak was fitted to reveal superpositions of the peaks attributed to metallic Ru⁰ (binding energy of 461.5 eV), RuO₂ (463.7 eV) and hydroxylated or hydrated RuO₂ (466.1 eV), which is termed as RuO_xH_y herein.^[29] The spectra before the activation process showed no difference in the relative peak intensities between each takeoff angle, which suggests that the chemical state of the Ru species did not vary with depth. As the activation process progressed, however, the relative peak area of RuO_xH_y became higher than the others, while the chemical states in the bulk layer hardly varied by the activation process. Therefore, the origin of activation is attributed to alternation of the outermost surface of the RuO₂ layer to RuO_xH_y.

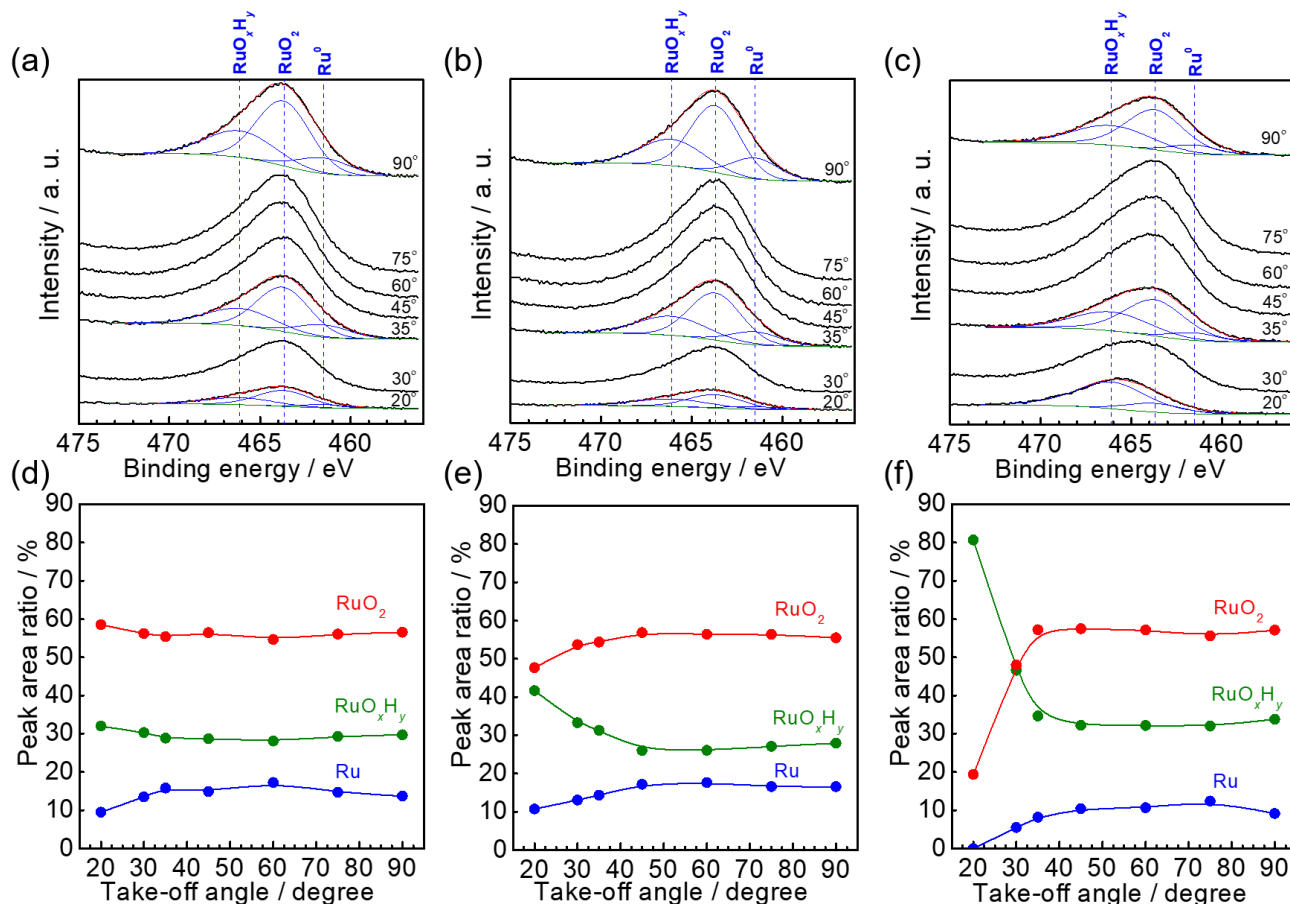


Figure 5-3-1. (a-c) AR-XPS spectra of Ru 3p_{3/2} obtained from the surface of the RuO₂-coated photocathodes before the activation process (a) and after the process for 0.5 h (b) and 3 h (c) in a 1.0 M potassium phosphate buffer solution at pH 7. (d-f) Changes in the peak area ratios of Ru metal, RuO₂ and RuO_xH_y with takeoff angle before the activation process (d), and after the activation process for 0.5 h (e) and 3 h (f).

Blouin and Guay reported that RuO₂ electrocatalyst for HER is greatly activated by cathodic polarization due to H-chemisorption within the RuO₂ layer, resulting in an increase in the density of active sites, while there was no evidence of metallic Ru formation.^[25] Karlsson et al. concluded that hydrogen enters RuO₂ crystal lattice during HER, which results in the formation of hydroxides.^[30] The results of PEC measurements and AR-XPS analyses are consistent with these reports and strongly suggest that RuO_xH_y species, likely to be hydroxides, play an important role during the PEC HER.

Chapter 5. Effects of RuO₂-Coating onto the Durability of the ZnSe:Cu(In,Ga)Se₂ Photocathode

Furthermore, the experimental fact that a pH 13 electrolyte gives higher photocurrent values than pH 7 can be explained by the difference in the concentration of hydroxyl species at the photocathode surface at equilibrium.

Watanabe et al. simulated the interface between water and rutile RuO₂ (110) surface using DFT calculations at various potentials to suggest that the O atoms bridging two Ru atoms can be hydroxylated at the potential at which HER is expected to occur, while the other O atoms connecting three Ru atoms are not hydroxylated.^[31,32] Also, the calculated Pourbaix diagram suggests that oxidation state of Ru is maintained at 4+ or at least 3.5+ on average in the potentials between -0.2 to 1.2 V_{RHE} at pH 13, which should attribute to the high stability of RuO₂ as a protection layer.

By using Penn algorithm,^[33] the inelastic mean free path (IMFP) of photoelectrons generated during XPS measurement was estimated to be 1.3 nm in the case of the kinetic energy of 788 eV, which corresponds to a binding energy of 466 eV in the case of the Mg K α line. Since the proportion of the signal obtained from RuO_xH_y increased by about 10% after the activation process, this thickness of the RuO_xH_y layer was roughly calculated to be 0.1-0.2 nm, based on an assumption that the IMFP in RuO_xH_y is the same as in RuO₂. The calculation suggests that the hydroxylation occurred within the outermost surface region.

The structure of ruthenium hydroxide, which was estimated using X-ray absorption fine structure analysis by Yamaguchi et al., was suggested to be composed of one-dimensional chainlike structure and doesn't consist of the O atoms connecting three Ru atoms.^[34] Instead, the O atoms bridge two Ru atoms or form -OH species, where the arrangement of RuO₆ octahedra is one-dimensional. Hence, there is a high possibility that the hydroxylation (i.e. activation) of RuO₂ needs to be accompanied with the rearrangement of the network structures of RuO₆ octahedra. Also, this can explain the reason why the activation process takes several hours, even though the RuO₂ layer employed in this work is suggested to be amorphous.

Chapter 5. Effects of RuO₂-Coating onto the Durability of the ZnSe:Cu(In,Ga)Se₂ Photocathode

Recently, Fang et al. has demonstrated DFT calculations on single molecules of RuO₂·H₂O and RuO(OH)₂, which stand for RuO₂ physisorped with water and the subsequent product by water dissociative chemisorption, respectively, as well as the transition state between them. They calculated the enthalpies relative to anhydrate RuO₂ at 298 K to be -21.9, -0.5 and -26.3 kcal mol⁻¹ for RuO₂ · H₂O, the transition state and RuO(OH)₂, respectively.^[35] Using the thermodynamic parameters, a rough estimation of transformation rate was conducted herein. Since the transformation of RuO₂ · H₂O to RuO(OH)₂ can be considered as the first order reaction, the preexponential factor for the Arrhenius equation can be written as $k_B T/h$, where k_B , T and h stand for the Boltzmann's constant, temperature and the Planck constant, respectively.^[36] Hence, by assuming unity of the transmission coefficient and equality of partition functions between the reactant and the transition state, the rate constant k_n can be described as

$$k_n = \frac{k_B T}{h} e^{-\frac{E_a}{RT}} \quad (5-3)$$

for the reaction



where E_a and R mean the activation energy and the gas constant, respectively. Herein, E_a is equal to the difference in the enthalpy values because the entropy change by the reaction is considered to be zero. Accordingly, k_1 and k_{-1} in the Eq. (5-4) at 298 K were calculated to be 2.27×10^{-4} and $1.34 \times 10^{-7} \text{ s}^{-1}$, respectively, suggesting that the reaction (5-4) can be considered as irreversible. Moreover, further stabilization to form RuO(OH)₂·H₂O makes the reverse reaction more energetically difficult. Figure 5-3-2 shows the time-course of the RuO₂ · H₂O concentration under these parameters. It was estimated to take 3 h for 90% of RuO₂ (·H₂O) to transform to the hydroxide, which is consistent with the result of AR-XPS. Even though the calculated enthalpy should be different between a single molecule and crystal surface and the negative potential during HER possibly facilitates the deprotonation of the physisorped water molecule, the simulation also explains why the activation

process takes a relatively long period and supports the possibility that the hydroxide plays an important role in HER on the RuO₂ layer. It must be noted that the real case shows a considerable difference in the partition function between the reactant and the activated complex. Therefore, further investigation based on the transition state theory is still required to support the discussion described above.

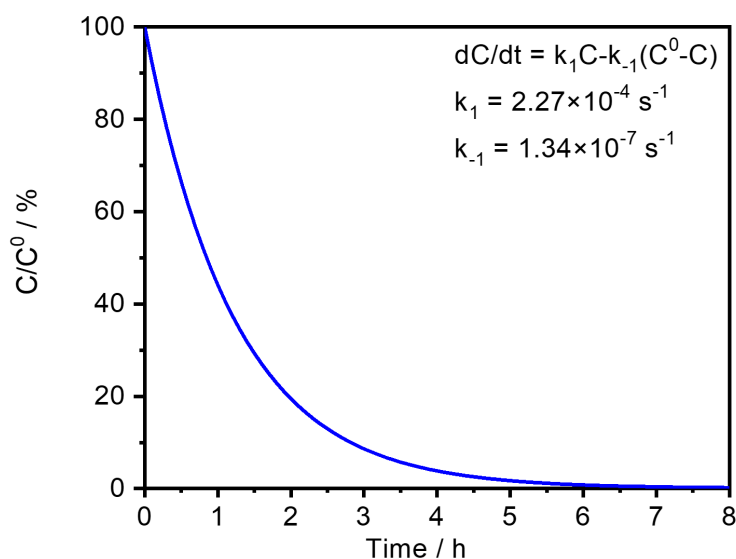


Figure 5-3-2. Time-course of the relative concentration of RuO₂ · H₂O (C/C^0) during the reaction of Eq. (5-4).

5-3-4 Overall Water Splitting Using the RuO₂-Coated ZnSe:Cu(In,Ga)Se₂ Photocathode and a BiVO₄ Photoanode

A PEC cell was again constructed using the RuO₂-coated (ZnSe)_{0.85}(CIGS)_{0.15} photocathode, a BiVO₄ photoanode modified with NiFeO_x-Bi as OER catalyst (NiFeO_x-Bi/BiVO₄) and a 0.5 M potassium borate buffer solution as an electrolyte. As in the case of chapter 3, tandem-type cell was employed to maximize the net solar-to-hydrogen conversion efficiency (STH). Figure 5-4-1 shows the current-potential curves of the photocathodes with and without BiVO₄ filter. The RuO₂-coated

photocathode showed considerable photocurrent even under the BiVO₄ photoanode, presenting the estimated working current of approximately 1.0 mA cm⁻² at 0.5 V_{RHE}.

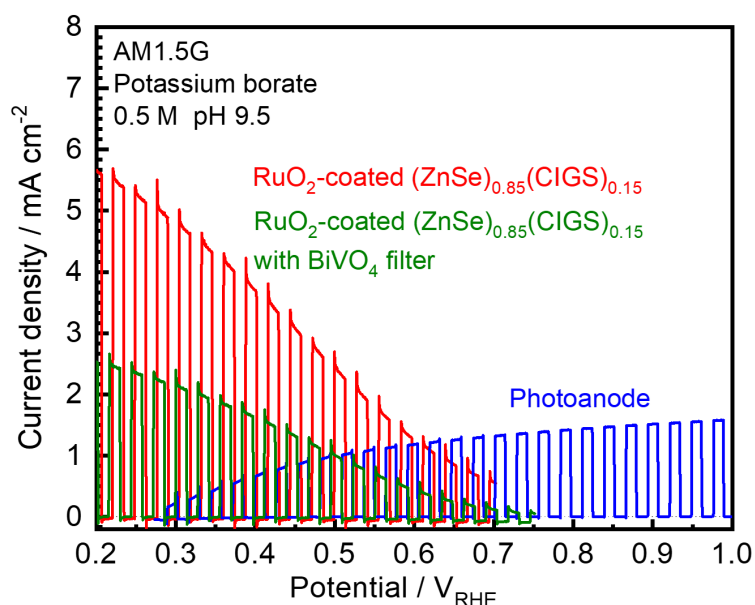


Figure 5-4-1. Current-potential curves for the RuO₂-coated (ZnSe)_{0.85}(CIGS)_{0.15} photocathode (red) and the photocathode under BiVO₄ filter (green) and a NiFeO_x-Bi/BiVO₄ photoanode (blue).

Figure 5-4-2 compares the current-time curves for the tandem cell composed of the RuO₂-coated (ZnSe)_{0.85}(CIGS)_{0.15} photocathode with the conventional photocathode modified with Pt/Mo/Ti. The initial STH reached 1.2%, which is comparable with the previous efficiency. The degradation of working current was greatly alleviated by introduction of the RuO₂ layer; the decrease in the photocurrent after the first 1 h was by approximately 70% and 20% in the cases of Pt/Mo/Ti- and RuO₂-coated photocathodes, respectively. However, there was still significant decrease observed under the continuous irradiation. The interval of light irradiation recovered the photocurrent to 80-85% of the initial value, as is the case for the results in chapter 4.

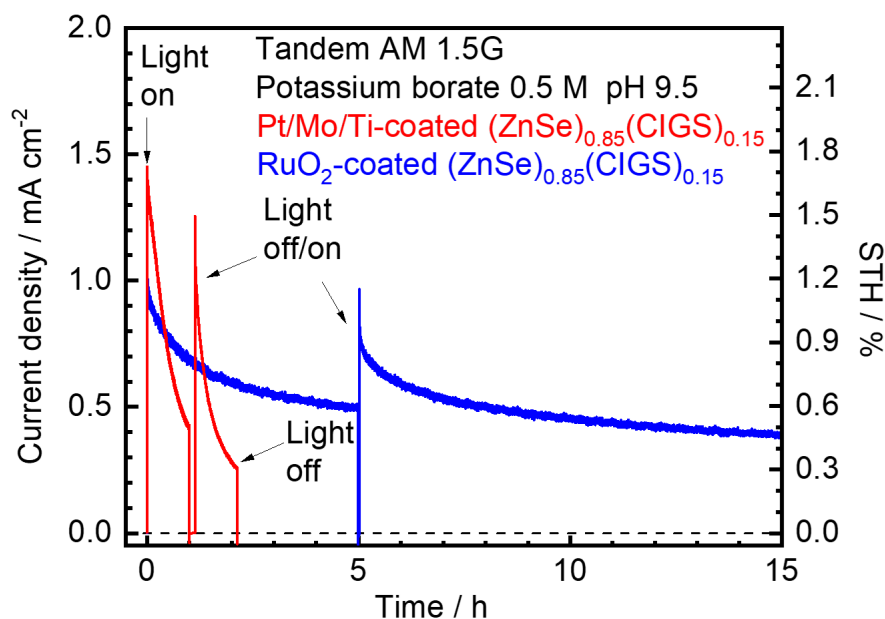


Figure 5-4-2. A current-time curve for the tandem two-electrode cell composed of a NiFeO_x-Bi/BiVO₄ photoanode and a (ZnSe)_{0.85}(CIGS)_{0.15} photocathode coated with Pt/Mo/Ti (red, geometric area of 0.47 cm²) and that coated with RuO₂ (blue, geometric area of 0.79 cm²) under simulated sunlight.

To conclude, suppression of catalyst poisoning on the photocathode surface was found to be indispensable for further improvement in the durability of the PEC cell. The next chapter addresses the problem by controlling metal cation impurities such as Bi³⁺.

5-4 Conclusions

Effects of photoelectrodeposition of RuO₂ layers onto (ZnSe)_{0.85}(CIGS)_{0.15} photocathode on the PEC properties were investigated. The RuO₂ layer was also expected to function as a surface conductive layer and HER catalyst because of its high electron conductivity and activity for HER, respectively. The photoelectrodeposition method successfully formed an amorphous, conformal and dense RuO₂ layer. The RuO₂-coated (ZnSe)_{0.85}(CIGS)_{0.15} photocathode showed no degradation,

Chapter 5. Effects of RuO₂-Coating onto the Durability of the ZnSe:Cu(In,Ga)Se₂ Photocathode

which is often caused by corrosion of photocathode surface, for longer than 10 h in potassium phosphate buffer solutions at pH 7 and 13. Analyses using SEM images revealed that the surface of RuO₂-coated (ZnSe)_{0.85}(CIGS)_{0.15} photocathode exhibited no evidence of corrosion.

The RuO₂ layer was found to exhibit a phenomenon of gradual increase in its catalytic activity in PEC HER. AR-XPS measurements suggested that hydroxylation of the outermost surface of the RuO₂ layer is the origin of the activation process. After the activation process, the RuO₂-coated photocathode showed a photocurrent value of 9.1 mA cm⁻² at 0 V_{RHE} under simulated sunlight, which is comparable with the conventional surface modification with Pt/Mo/Ti.

Overall water splitting using a PEC cell composed of the RuO₂-coated (ZnSe)_{0.85}(CIGS)_{0.15} photocathode and a NiFeO_x-Bi/BiVO₄ photoanode was demonstrated to show an improved stability by employment of RuO₂. However, as reported in chapter 4, surface poisoning by impurities dissolved from the BiVO₄ photoanode disturbed highly durable operation of the PEC cell. In the next chapter, the problem concerning the metal cation impurity is addressed.

References

- [1] J. Seo, H. Nishiyama, T. Yamada, K. Domen, *Angew. Chemie Int. Ed.* **2018**, 57, 2.
- [2] H. Kaneko, T. Minegishi, K. Domen, *Chem. Eur. J.* **2018**, 24, 5697.
- [3] F. F. Abdi, S. P. Berglund, *J. Phys. D Appl. Phys* **2017**, 50, 193002.
- [4] Y. Chen, X. Feng, M. Liu, J. Su, S. Shen, *Nanophotonics* **2016**, 5, 524.
- [5] T. Hisatomi, J. Kubota, K. Domen, *Chem. Soc. Rev.* **2014**, 43, 7520.
- [6] D. Lee, A. Kvit, K.-S. Choi, *Chem. Mater.* **2018**, 30, 4704.
- [7] S. Hu, N. S. Lewis, J. W. Ager, J. Yang, J. R. McKone, N. C. Strandwitz, *J. Phys. Chem. C* **2015**, 119, 24201.
- [8] N. Guijarro, M. S. Prévot, K. Sivula, *Phys. Chem. Chem. Phys.* **2015**, 17, 15655.

Chapter 5. Effects of RuO₂-Coating onto the Durability of the ZnSe:Cu(In,Ga)Se₂ Photocathode

- [9] T. Yao, H. Han, J. Q. Chen, C. Li, *Adv. Energy Mater.* **2018**, 8, 1800210.
- [10] B. Seger, T. Pedersen, A. B. Laursen, P. C. K. Vesborg, O. Hansen, I. Chorkendor, *J. Am. Chem. Soc.* **2013**, 135, 1057.
- [11] J. Liu, T. Hisatomi, M. Katayama, T. Minegishi, K. Domen, *ChemPhotoChem* **2018**, 2, 234.
- [12] L. Kavan, L. Steier, M. Grätzel, *J. Phys. Chem. C* **2017**, 121, 342.
- [13] S. D. Tilley, M. Schreier, J. Azevedo, M. Stefik, M. Grätzel, *Adv. Funct. Mater.* **2014**, 24, 303.
- [14] A. Mills, P. A. Duckmanton, J. Reglinski, *Chem. Commun.* **2010**, 46, 2397.
- [15] H. Kumagai, T. Minegishi, N. Sato, T. Yamada, J. Kubota, K. Domen, *J. Mater. Chem. A* **2015**, 3, 8300.
- [16] M. Moriya, T. Minegishi, H. Kumagai, M. Katayama, J. Kubota, K. Domen, *J. Am. Chem. Soc.* **2013**, 135, 3733.
- [17] D. Yokoyama, T. Minegishi, K. Jimbo, T. Hisatomi, G. Ma, M. Katayama, J. Kubota, H. Katagiri, K. Domen, *Appl. Phys. Express* **2010**, 3, 101202.
- [18] F. Jiang, Gunawan, T. Harada, Y. Kuang, T. Minegishi, K. Domen, S. Ikeda, *J. Am. Chem. Soc.* **2015**, 137, 13691.
- [19] Gunawan, W. Septina, S. Ikeda, T. Harada, T. Minegishi, K. Domen, M. Matsumura, *Chem. Commun.* **2014**, 50, 8941.
- [20] A. M. Smith, L. Trotochaud, M. S. Burke, S. W. Boettcher, *Chem. Commun.* **2015**, 51, 5261.
- [21] Y. Kuang, Q. Jia, H. Nishiyama, T. Yamada, A. Kudo, K. Domen, *Adv. Energy Mater.* **2016**, 6, 1501645.
- [22] E. V Jelenkovic, S. To, *ECS Solid State Lett.* **2013**, 2, P42.
- [23] Y. Du, C. Wang, J. Zhou, W. Zhang, J. Ji, L. Han, Y. Li, *ECS J. Solid State Sci. Technol.* **2017**, 6, P521.

Chapter 5. Effects of RuO₂-Coating onto the Durability of the ZnSe:Cu(In,Ga)Se₂ Photocathode

- [24] G. Ma, J. Liu, T. Hisatomi, T. Minegishi, Y. Moriya, M. Iwase, H. Nishiyama, M. Katayama, T. Yamada, K. Domen, *Chem. Commun.* **2015**, 51, 4302.
- [25] M. Blouin, D. Guay, *J. Electrochem. Soc.* **1997**, 144, 573.
- [26] L. Chen, D. Guay, F. H. Pollak, F. Levy, *J. Electroanal. Chem.* **1997**, 429, 185.
- [27] T. Watanabe, A. Fujishima, K. Honda, *Chem. Lett.* **1974**, 3, 897.
- [28] Y. Kageshima, T. Minegishi, S. Sugisaki, Y. Goto, H. Kaneko, M. Nakabayashi, N. Shibata, K. Domen, *ACS Appl. Mater. Interfaces* **2018**, DOI: acsami.8b14814.
- [29] S. Armenise, L. Roldán, Y. Marco, A. Monzón, E. García-Bordejé, *J. Phys. Chem. C* **2012**, 116, 26385.
- [30] R. K. B. Karlsson, A. Cornell, L. G. M. Pettersson, *J. Phys. Chem. C* **2016**, 120, 7094.
- [31] E. Watanabe, J. Rossmeisl, M. E. Björketun, H. Ushiyama, K. Yamashita, *J. Phys. Chem. C* **2016**, 120, 8096.
- [32] E. Watanabe, H. Ushiyama, K. Yamashita, Y. Morikawa, D. Asakura, M. Okubo, A. Yamada, *J. Phys. Chem. C* **2017**, 121, 18975.
- [33] D. R. Penn, *J. Electron Spectros. Relat. Phenomena* **1976**, 9, 29.
- [34] K. Yamaguchi, T. Koike, J. W. Kim, Y. Ogasawara, N. Mizuno, *Chem. Eur. J.* **2008**, 14, 11480.
- [35] Z. Fang, M. A. Outlaw, D. A. Dixon, *J. Phys. Chem. A* **2017**, 121, 7726.
- [36] R. C. Baetzold, G. A. Somorjai, *J. Catal.* **1976**, 45, 94.

Chapter 6

Control of Cation Impurities in the Electrolyte for Long-Term Operation of Photoelectrochemical Cells

6-1 Introduction

Through chapter 5, the photoelectrochemical (PEC) properties of RuO₂-coated (ZnSe)_{0.85}(CuIn_{0.7}Ga_{0.3}Se₂)_{0.15} (abbreviated as (ZnSe)_{0.85}(CIGS)_{0.15} herein) photocathodes were investigated. The RuO₂-coated (ZnSe)_{0.85}(CIGS)_{0.15} photocathodes showed a high durability for longer than 10 h at an oxidative potential of 0.6 V_{RHE} in the electrolytes at the pH 13 as well as 7. Thus, the photocathode is suitable for construction of a stable PEC cell combined with another photoanode.

BiVO₄ photoanodes have also been reported to show a sufficient stability for longer than 10 h at 0.6 V_{RHE}.^[1-3] Therefore, a PEC cell composed of the RuO₂-coated (ZnSe)_{0.85}(CIGS)_{0.15} photocathode and BiVO₄ photoanode was expected to demonstrate a high durability in overall water splitting reaction. However, the PEC cell still exhibited considerable degradation under continuous light irradiation as shown in Figure 5-4-2, although the improvement in the stability to a certain degree was achieved. The origin of the degradation was catalyst poisoning on the photocathode surface due to deposition of Bi species as revealed in chapter 4. The heavy metal cations dissolved from the photoanode are readily reduced on the photocathode surface because the reduction potential of Bi³⁺/Bi is more positive than that of H⁺/H₂ by approximately 0.3 V. It should be noted that other metal cation species which possesses reduction potentials more negative than that of H⁺/H₂ also can cause a similar kind of poisoning via underpotential deposition.^[4-6] Therefore, the surface poisoning of the photocathode can be a general problem among not only the combination of (ZnSe)_{0.85}(CIGS)_{0.15} and BiVO₄ but also many of the other combinations of photoelectrodes.

In this chapter, prevention of Bi deposition on the photocathode surface was investigated using two techniques: dispersing chelating resin and surface-coating with anion-conducting ionomers. Firstly, commercially-available chelating resin beads (Chelex[®] 100, Bio-Rad) was employed for the sake of absorbing the heavy metal cations from the electrolyte in the PEC cell. Chelating group supported

Chapter 6. Control of Cation Impurities in the Electrolyte for Long-Term Operation of Photoelectrochemical Cells

on the resin selectively absorbs multivalent metal cations in the solution but monovalent cations are not affected.^[7] The kind of chelating resin has already been applied to purification of electrolyte reagents for electrochemical reduction of CO₂,^[7,8] but application to a PEC cell for this purpose has not been reported yet. Secondly, coating the surface of BiVO₄ photoanodes with an anion-conducting ionomer, which is also a commercially-available (AS-4[®], Tokuyama), was investigated. Since the layer allows anions to pass but blocks cations, the heavy metal cations dissolved from the photoanode surface are accumulated in the vicinity of the surface. The situation not only alleviates the Bi deposition on photocathode surface but also improves the stability of the BiVO₄ photoanode. This is because the high concentration of Bi³⁺ (and V⁵⁺) suppresses further decomposition of BiVO₄ via Le Châtelier's principle.^[2] Herein, effects of the two modifications were investigated using two- and three-electrode cells in conjunction with analyses on (photo)cathode surface so as to demonstrate a highly durable overall water splitting using the PEC cell.

6-2 Experimental Section

Preparation of (ZnSe)_{0.85}(CIGS)_{0.15} Thin Films

(ZnSe)_{0.85}(CIGS)_{0.15} thin films were deposited on substrates of Mo-coated soda-lime glass. The Mo-coated substrates were fabricated by RF magnetron sputtering of a Mo target (99.9%, Kojundo) onto each soda-lime glass plate heated at 573 K. Prior to the Mo deposition, a 30 nm thick Ti was deposited by the sputtering of a Ti target (99.9%, Kojundo) so as to improve the adhesion. The thickness of Mo and Ti are about 500 and 30 nm, respectively.

The substrate was loaded into a deposition chamber equipped with Knudsen cells containing elemental Cu, In, Ga, Zn and Se (99.9999%, Asahi Metal or Furuuchi Chemical). The substrate temperature was set at 623 K for 5 min and then reset to 723 K for 35 min. The (ZnSe)_{0.85}(CIGS)_{0.15} thin films were deposited using the bilayer method (see chapter 3); the typical deposition rates for Cu,

Chapter 6. Control of Cation Impurities in the Electrolyte for Long-Term Operation of Photoelectrochemical Cells

In, Ga, Zn and Se were 0.042, 0.095, 0.028, 0.4 and 1 nm s⁻¹, respectively. In and Ga were absent for the first and last 20 min, respectively, followed by 10 min-annealing in a Se atmosphere. The rates were monitored by using a quartz crystal microbalance sensor (Q-POD, INFICON). The pressure in the chamber was kept at $<2 \times 10^{-5}$ Pa during deposition. Following the film deposition processes, each sample was cooled from 723 to 573 K with exposure to Zn and Se vapor to alleviate the formation of a Zn-poor surface.

KCN Etching

After deposition, the samples were immersed into an etching solution containing 0.1 M KCN (98.0%, FUJIFILM Wako Pure Chemical) and 0.8 M KOH (8 M, FUJIFILM Wako Pure Chemical) for 1 min in room temperature. This etching process removed excess Cu from the (ZnSe)_{0.85}(CIGS)_{0.15} thin films. Energy dispersive X-ray spectroscopy (EDS; EMAX-7000, Horiba) analysis revealed that the atomic ratio of Cu/(In+Ga) was 0.9 to 1.0 after the process.

Surface Modification with an CdS Layer

A CdS layer was formed on the surface of each (ZnSe)_{0.85}(CIGS)_{0.15} thin film using chemical bath deposition (CBD) method.^[9-11] The CBD solution with a volume of 50 mL contained 14 wt% ammonia (28 wt%, FUJIFILM Wako Pure Chemical), 25 mM of Cd(CH₃COO)₂ (98.0%, FUJIFILM Wako Pure Chemical) and 0.375 M of SC(NH₂)₂ (98.0%, Kanto Chemical). The bath temperature was gradually increased from room temperature to 325-326 K over the span of about 8 min. The samples were taken out from the bath and immediately washed with pure water 14 min after the initiation of heating, followed by annealing at 473 K for 1 min in air.

Chemical bath deposition treatment of In₂S₃

The CdS-modified (ZnSe)_{0.85}(CIGS)_{0.15} thin film was treated with additional CBD treatment of In₂S₃.^[12,13] The CBD solution with a volume of 50 mL contained 100 mM of CH₃COOH (99.7%, FUJIFILM Wako Pure Chemical), 25 mM of In₂(SO₄)₂ (FUJIFILM Wako Pure Chemical) and 100 mM of CH₃CSNH₂ (98.0%, FUJIFILM Wako Pure Chemical). The bath temperature was heated

Chapter 6. Control of Cation Impurities in the Electrolyte for Long-Term Operation of Photoelectrochemical Cells

at 343 K. The samples were taken out from the bath and immediately washed with pure water 10 min after the initiation of heating.

Photoelectrochemical deposition of a RuO₂ layer

The (ZnSe)_{0.85}(CIGS)_{0.15} photocathodes treated by CBD of CdS and In₂S₃ were fixed and the region not intended for measurement was coated using epoxy resin (Araldite Rapid, Nichiban). Afterwards, they are exposed to simulated sunlight produced by a solar simulator (XES-40S2-CE, SAN-EI Electric) in a 1.3 mM K₂RuO₄ (98%, Strem Chemicals) solution for 3-5 min unless noted otherwise.^[14] A current density of -28 $\mu\text{A cm}^{-2}$ was applied during the exposure.

Preparation of BiVO₄ Photoanodes

A BiOI precursor was prepared on an indium tin oxide (ITO)-coated soda-lime glass substrate (0051, Geomatec) by electrodeposition method in a three-electrode cell with an Ag/AgCl reference electrode in a saturated aqueous KCl solution and with a Pt wire counter electrode. Subsequently, a dimethyl sulfoxide solution containing VO(C₅H₇O₂)₂ (98%, Sigma-Aldrich) was drop-cast onto the precursor, followed by calcination at 723 K for 1 h in air. As oxygen evolution reaction (OER) catalyst, NiFeO_x-Bi was deposited onto the prepared BiVO₄ electrode (NiFeO_x-Bi/BiVO₄) by photoelectrodeposition method.^[15] The potential of the electrode was held at -0.16 V vs. Ag/AgCl until saturation of the photocurrent (typically requiring 10-20 min) under simulated sunlight (XES-40S2-CE, SAN-EI Electric) in a 0.5 M aqueous potassium borate solution containing 4 μM NiSO₄ (99.9%, FUJIFILM Wako Pure Chemical) and 40 μM FeSO₄ (99%, FUJIFILM Wako Pure Chemical) with the pH adjusted to 9.5 by KOH addition. It should be noted that a previous report describes the fabrication process of the BiVO₄-based photoanode in more detail.^[1]

Surface Modification with an Anion-Conducting Ionomer Layer

After deposition of NiFeO_x-Bi, anion-conducting ionomer was deposited by dipping the electrodes into a 1-propanol solution containing 5 wt% of the ionomer (AS-4, Tokuyama), followed by the application of a vacuum for 3 min to remove residual air between the BiVO₄ nanoworms. Subsequently, the

Chapter 6. Control of Cation Impurities in the Electrolyte for Long-Term Operation of Photoelectrochemical Cells

electrodes were affixed to a spin coater and the solution was added by drop-casting so as to prevent drying. The spin coater immediately rotated the sample first at 500 rpm for 10 s and then at 3000 rpm for 25 s at room temperature. The ionomer-coated electrodes were heated at 140 °C for 20 min under vacuum.

Characterization

The samples were analyzed using scanning electron microscopy (SEM; Hitachi) and X-ray photoelectron spectroscopy (XPS; JPS-9000, JEOL). The light transmittance of the dispersion of chelating resin beads and the ionomer layer coated on a soda-lime glass plate were measured using a dual beam UV–vis spectrometer (V-670, JASCO) equipped with quartz cells having the volume and path length of 3.5 mL and 10 mm, respectively.

Photoelectrochemical Measurements

A three-electrode cell equipped with a magnetic stirrer under an Ar atmosphere using an aqueous solution of 0.5 M potassium borate buffer solution (pH 9.5, adjusted by adding KOH) as the electrolyte was set up and connected to a potentiostat (HSV-110 or HZ-7000, Hokuto Denko). Chelating resin beads (Chelex[®] 100 sodium form, Bio-Rad, 50-100 mesh) were dispersed in the electrolyte at a concentration of 0.5 wt%. A solar simulator producing AM1.5G was employed as the light source. In the current-potential measurements, the applied potential, expressed relative to a reversible hydrogen electrode (RHE), was swept at 5 mV s⁻¹ from 0 V_{RHE} under intermittent irradiation with a period of 6 s.

Analysis of the evolved gases was conducted using an airtight glass cell under an Ar flow. The airtight cell was connected to a gas chromatograph (490 Micro GC, Agilent Technologies) and a potentiostat.

6-3 Results and Discussion

6-3-1 Effects of Chelating Resin Dispersion onto the Stability of the Photoelectrochemical Cells

Figure 6-1-1 shows the photograph and transmittance spectrum of the chelating resin dispersed in the electrolyte. The resin beads are highly transparent in the aqueous solution, which means that the optical loss caused by the dispersion is inconsiderable. Therefore, a PEC cell employing the dispersion is expected to show a solar-to-hydrogen conversion efficiency (STH) value comparable to conventional PEC cells. Current-time curves for the tandem-type PEC cells under simulated sunlight with and without the chelating resin were exhibited in Figure 6-1-2. Both cells showed the STH of higher than 1.0% (c.a. 1.1 to 1.2 %) on the initiation of light irradiation. Without the chelating resin, the STH continuously decreased for several hours under light irradiation as already discussed in section 5-3-4. On the other hand, the cell containing the resin reached a steady state of the photocurrent following 8-10 h of light irradiation, and then there was no meaningful decrease for longer than 40 h. It is noteworthy that this demonstration over about two days is the longest stable operation of a PEC cell ever reported (see Table 1-4-1). Quantification of the evolved gases revealed that the photocurrent was attributed to overall water splitting with a Faradaic efficiency close to 100%, and it wasn't affected by presence of the chelating resin as shown in Figure 6-1-3.

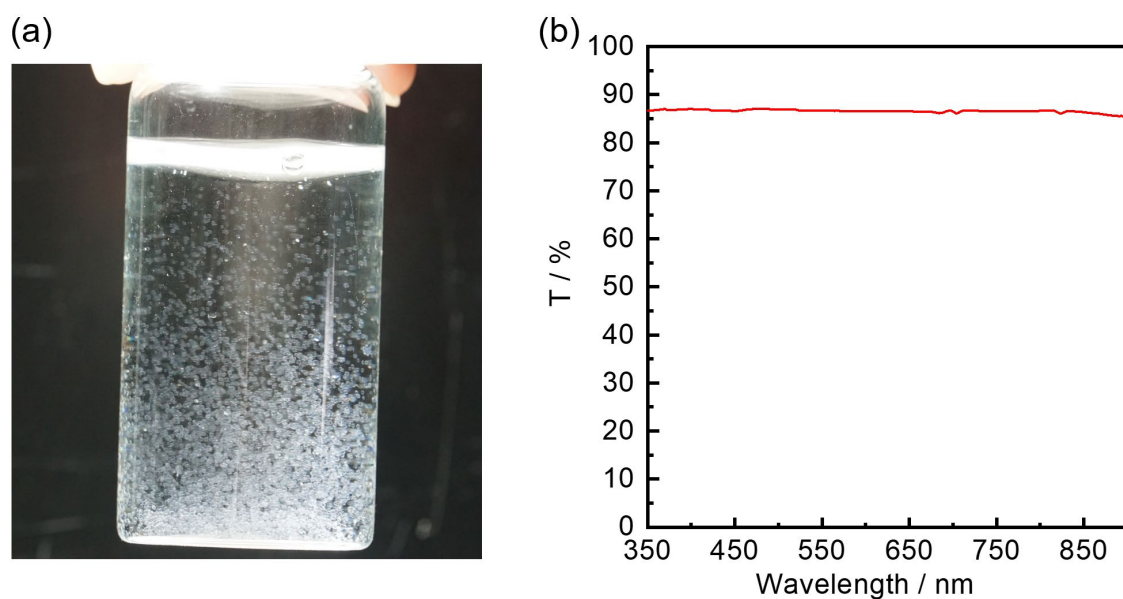


Figure 6-1-1. (a) A photographic image of the chelating resin dispersion. (b) A transmittance spectrum of the chelating resin dispersed in an aqueous 0.5 M potassium borate solution (pH 9.5, adjusted by adding KOH) in a quartz cell. The reference cell was filled with the potassium borate solution without the chelating resin.

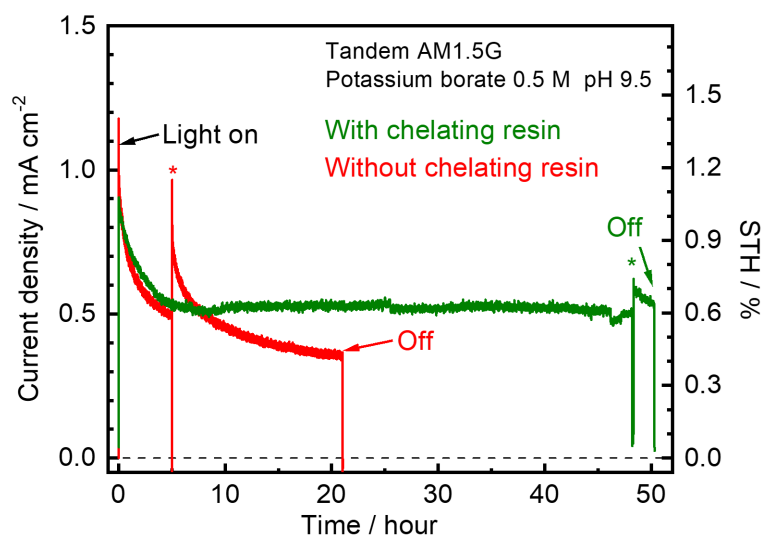


Figure 6-1-2. Current-time curves for the tandem two-electrode cells composed of the BiVO_4 photoanodes and RuO_2 -coated $(\text{ZnSe})_{0.85}(\text{CIGS})_{0.15}$ photocathodes under simulated sunlight with (green, geometric area of the photocathode surface of 0.60 cm^2) and without (red, 0.79 cm^2) chelating

resin beads in electrolyte. Illumination was stopped temporarily at the time points marked by asterisks. Right Y-axis shows the corresponding STH.

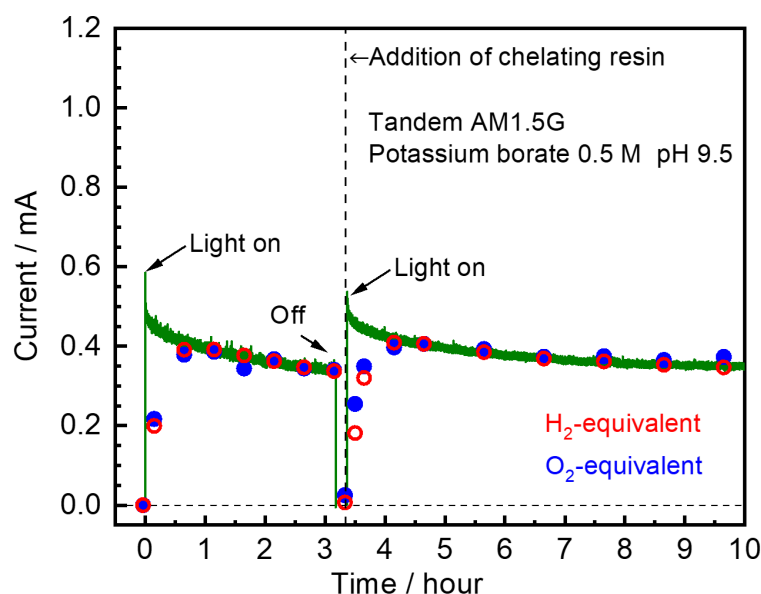


Figure 6-1-3. Current-time curve for the two-electrode tandem cell composed of the BiVO_4 photoanodes and RuO_2 -coated $(\text{ZnSe})_{0.85}(\text{CIGS})_{0.15}$ photocathodes under simulated sunlight (green), and the amounts of evolved hydrogen (red dots) and oxygen (blue dots) based on the photocurrent values determined by the gas chromatography.

Simultaneous monitoring of working potentials of the PEC cells can identify the origin of decrease in the photocurrent as the degradation in the photocathode/photoanode because the working potential is determined by the intersection of each current-potential curve.^[16] Figure 6-1-4 compares time-courses of the working potentials. In both cases, positive shifts after initiation of light irradiation were observed, which means that degradation of the photoanode occurred. Moreover, introduction of chelating resin resulted in a relatively large shift due to the enhanced dissolvment of BiVO_4 via Le Châtelier's principle,^[2] while the dissolvment seemed to stop possibly because the outermost surface of the photoanode was covered by any stable phase or plane. Without the chelating resin beads, the

potential shift gradually turned to positive 5 h after the beginning of reaction, indicating the catalyst poisoning on the photocathode surface.

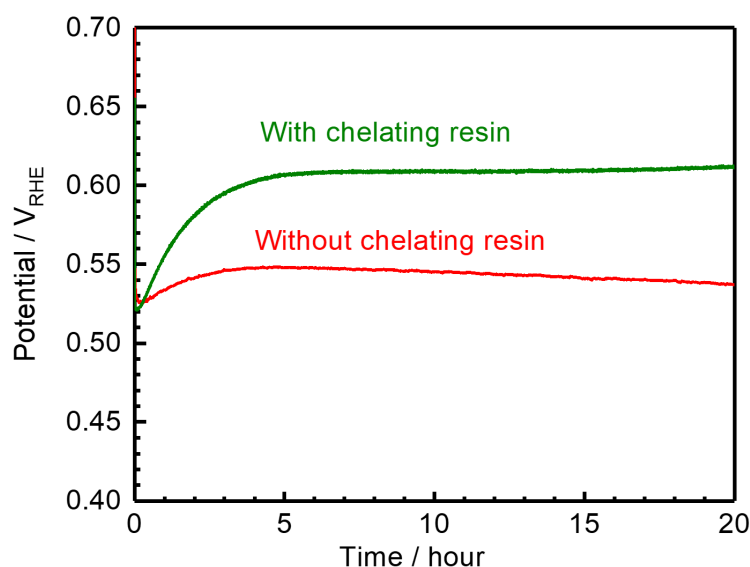


Figure 6-1-4. Potential-time curves acquired from two-electrode tandem cells composed of the BiVO_4 photoanodes and RuO_2 -coated $(\text{ZnSe})_{0.85}(\text{CIGS})_{0.15}$ photocathodes under simulated sunlight with (green) and without (red) chelating resin beads in electrolyte.

The photocathode surfaces before and after the long-term reaction for two days were analyzed using XPS measurements as exhibited in Figure 6-1-5. It should be noted that RuO_2 has been reported as relatively less sensitive catalyst to surface poisoning by heavy metal cations,^[17] but a Bi peak significantly appeared after the long-term reaction without chelating resin, which is consistent with the result shown in section 4-3-3. In contrast, addition of the chelating resin beads dramatically suppressed the deposition of Bi species on the photocathode surface, decreasing the Bi-to-Ru peak area ratios to less than one-tenth.

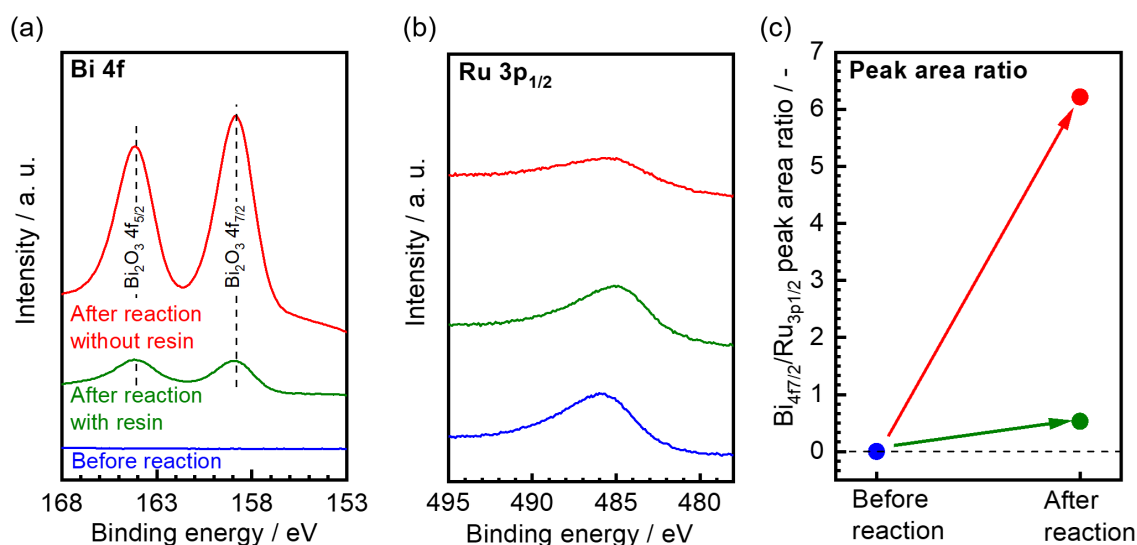


Figure 6-1-5. XPS spectra of Bi 4f (a) and Ru 3p_{1/2} (b) obtained from surfaces of photocathodes before overall water splitting reaction (blue) and after reaction without (red) and with (green) resin. (c) Changes in ratio of Bi 4f_{7/2} to Ru 3p_{1/2} XPS peak areas after reaction without (red) and with (green) resin.

The consistent data was obtained in the measurements using a three-electrode cell, where a Pt plate with a geometric area of 2 cm² was employed as a model counter electrode. The time-courses of photocurrent and overpotential applied to the Pt counter electrodes with and without chelating resin beads were shown in Figure 6-1-6. In both cells, the BiVO₄ photoanodes showed a certain decrease in the photocurrent after initiation of light irradiation. In absence of chelating resin, the photocurrent reached a plateau, while the resin-introduced cell showed continuous decrease due to the non-stopping dissolution. The increase in the overpotential for HER after 7 h of measurement was significantly decreased from 0.20 V to 0.09 V by introduction of the chelating resin, which suggests that the poisoning of Pt surface was dramatically alleviated. XPS spectra obtained from the surfaces of Pt plates also revealed that the Bi deposition was suppressed by dispersing the chelating resin as shown in Figure 6-1-7.

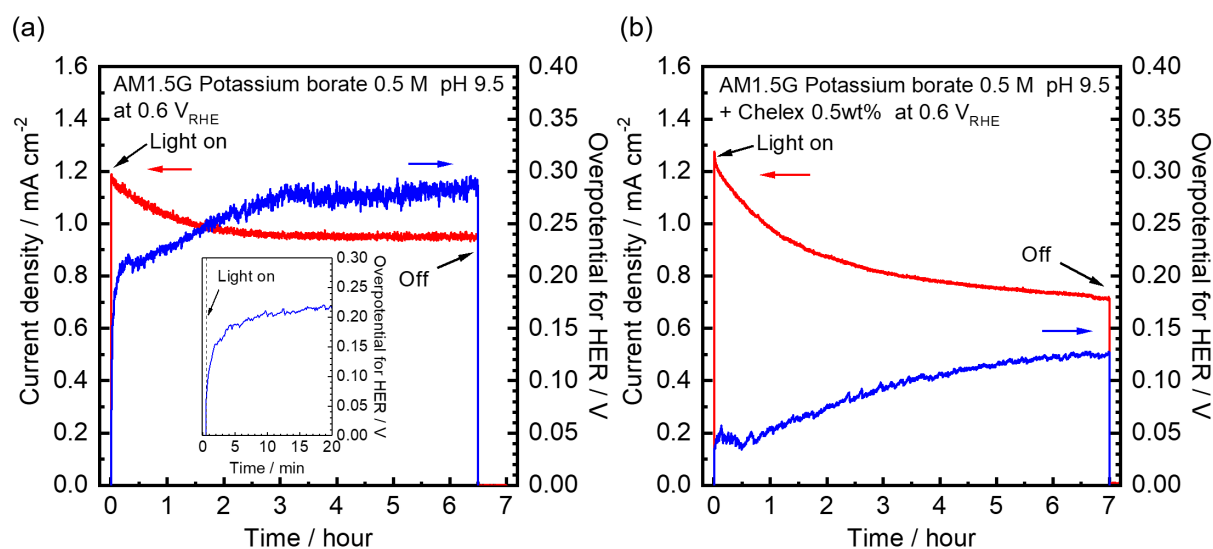


Figure 6-1-6. Current-time curves for the BiVO₄ photoanodes at 0.6 V_{RHE} under simulated sunlight (red) and time curves for overpotential applied to Pt counter electrodes (blue) without (a) and with (b) chelating resin beads in the electrolyte.

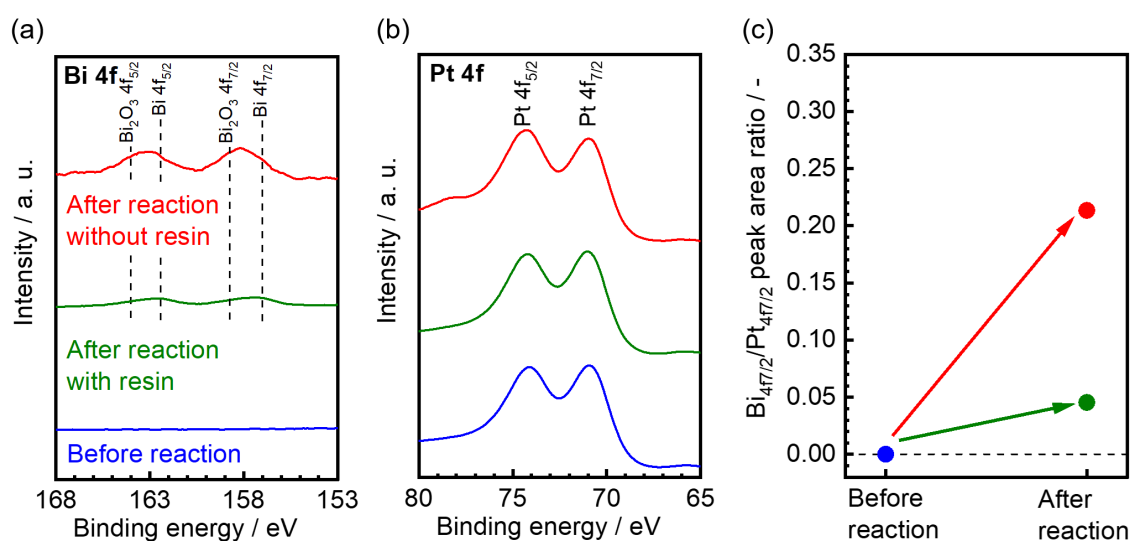


Figure 6-1-7. XPS spectra of (a) Bi 4f and (b) Pt 4f obtained from the surfaces of Pt plate counter electrodes before the measurement (blue) and after measurement of Figure 6-1-6 without (red) and with (green) chelating resin beads in the electrolyte. (c) Changes in ratio of Bi 4f_{7/2} to Pt 4f_{7/2} XPS peak areas after the measurements without (red) and with (green) the resin.

Chapter 6. Control of Cation Impurities in the Electrolyte for Long-Term Operation of Photoelectrochemical Cells

These results concluded that employment of chelating resin dispersion slows down the surface poisoning of the photocathode but also deteriorates the durability of BiVO₄ photoanodes by shifting the chemical equilibrium. The latter feature will not appear if a PEC cell uses other photoanodes whose stability doesn't matter with the chemical equilibrium. Even though, further development of surface modification using an anion-conductive ionomer was investigated in order to solve the dilemma. It was expected that the surface modification contributes to suppression of decomposition by accumulating Bi species in the vicinity of the BiVO₄-ionomer interface, as well as alleviation of poisoning the photocathode surface.

6-3-2 Effects of an Anion-Conductive Ionomer Layer onto the Stability of the Photoelectrochemical Cells

Figure 6-2-1 shows SEM images of the BiVO₄ photoanodes before and after surface-coating with the anion-conductive ionomer by the spin coating technique explained in the experimental section. The ionomer densely covered the photoanode surface with a thickness of approximately 100 nm, penetrating into the nanoworm-like rods of BiVO₄. The dense layer was expected to prevent metal cations generated on the BiVO₄ surface from migrating into the electrolyte sufficiently. Furthermore, the ionic conductivity of the ionomer has been reported to be 13 mS cm⁻¹ at room temperature,^[18] which means that the resistance for hydroxide ions passing through a 100 nm-thick ionomer layer was less than 0.1 μΩ. Therefore, the surface-coating technique theoretically doesn't affect the PEC property of the BiVO₄ photoanode.

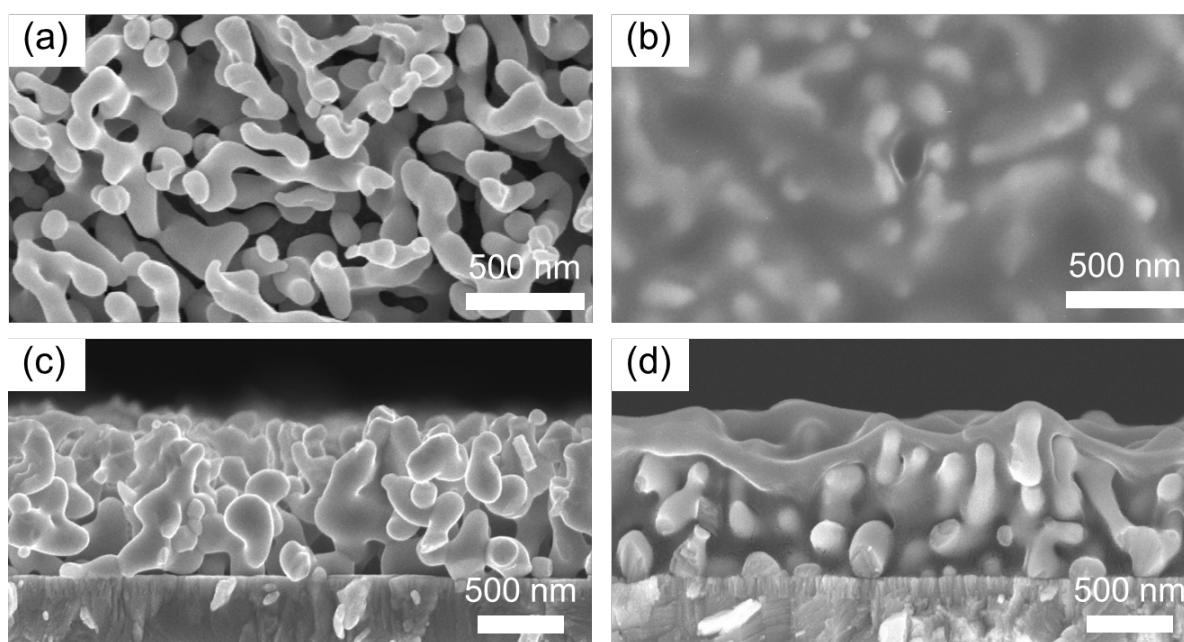


Figure 6-2-1. Surface (a, b) and cross-sectional (c, d) SEM images of $\text{NiFeO}_x\text{-Bi/BiVO}_4$ photoanodes before (a, c) and after (b, d) ionomer coating.

Using a Pt plate counter electrode as the case of the previous section, the rate of Bi deposition was measured again. Figure 6-2-2 exhibits the current- and overpotential-time curves for the ionomer-coated BiVO_4 photoanode and the Pt counter electrode, respectively. The photoanode showed no clear decrease in the photocurrent for about 7 h of measurement at 0.6 V_{RHE} , even though the initial photocurrent was slightly smaller than that of the conventional photoanode (see Figure 6-1-6 (a)). It should be noted that the fluctuations in the photocurrent were caused by continuous accumulation and detachment of oxygen bubbles formed at the photoanode surface. The increase in the overpotential after the measurement was approximately 0.08 V, which was clearly smaller than the case of the conventional photoanode shown in Figure 6-1-6. The result and XPS spectra exhibited in Figure 6-2-3 suggest that the deposition speed of Bi species onto the (photo)cathode surface was effectively slowed down by the ionomer layer; the Bi-to-Pt peak area ratio decreased to one-fourth.

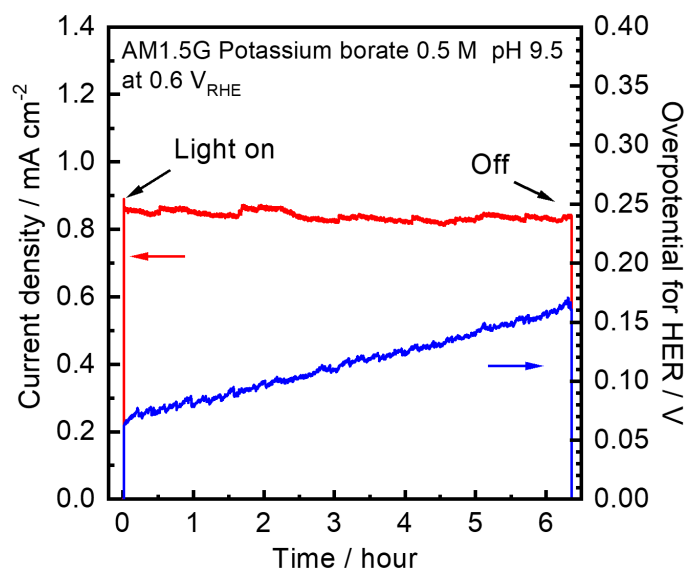


Figure 6-2-2. Current-time curves for the ionomer-coated BiVO_4 photoanodes at $0.6 V_{\text{RHE}}$ under simulated sunlight (red) and time curves for overpotential applied to Pt counter electrodes (blue) without chelating resin beads in the electrolyte.

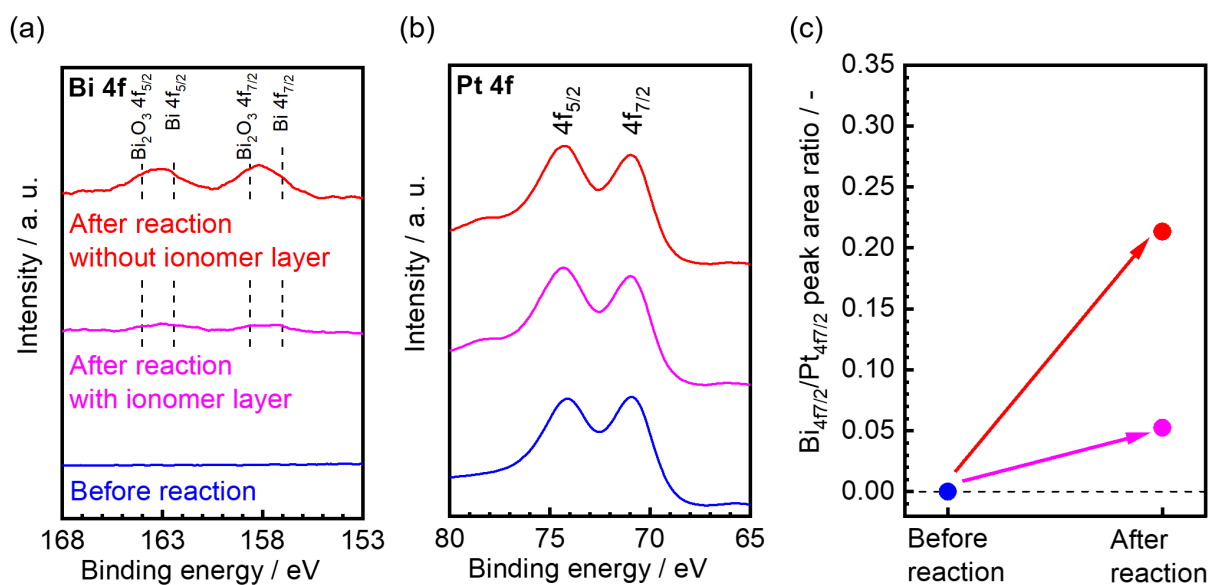


Figure 6-2-3. XPS spectra of (a) Bi 4f and (b) Pt 4f obtained from the surfaces of Pt plate counter electrodes before (blue) and after the measurements of Figure 6-1-6 and 6-2-2 without (red) and with (pink) ionomer layer without chelating resin beads in the electrolyte. (c) Changes in ratio of Bi $4f_{7/2}$ to Pt $4f_{7/2}$ XPS peak areas after the corresponding measurements.

Chapter 6. Control of Cation Impurities in the Electrolyte for Long-Term Operation of Photoelectrochemical Cells

The surface and cross-sectional SEM images after the current-time measurement were exhibited in Figure 6-2-4. The photoanode surface was still covered with the ionomer without any evidence in collapse or decomposition of the layer. Also, quantification of the evolved hydrogen and oxygen gases revealed the Faradaic efficiency of almost unity as shown in Figure 6-2-5. Therefore, the ionomer layer was found to be stable in the aqueous solution of potassium borate during PEC OER without appreciable oxidation at the electrode-electrolyte interface by the holes formed by photoexcitation.

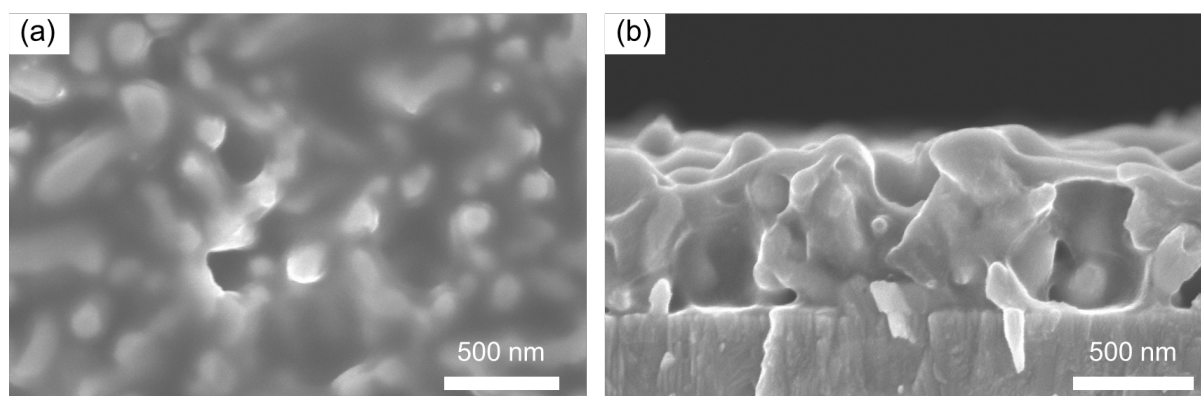


Figure 6-2-4. Surface (a) and cross-sectional (b) SEM images of the ionomer-coated BiVO₄ photoanodes after the measurement in Figure 6-2-2.

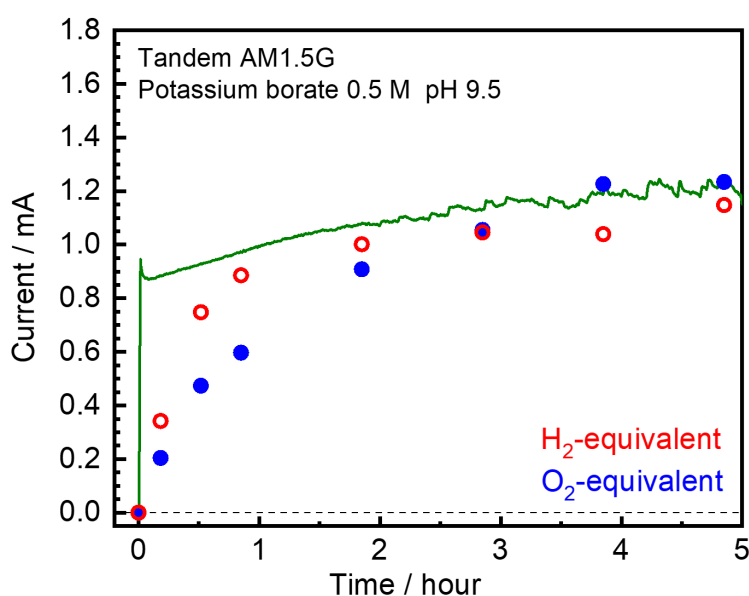


Figure 6-2-5. A current-time curve for the ionomer-coated BiVO₄ photoanode at 0.6 V_{RHE} under simulated sunlight (green), and the amounts of evolved hydrogen (red dots) and oxygen (blue dots) based on the photocurrent values determined by the gas chromatography.

Unlike most of the other surface modifiers such as metal oxide,^[19–22] the ionomer layer is not conductive for electrons or holes but permeable to chemical reactants and products of water splitting reaction, and therefore the OER occurs on the surface of NiFeO-Bi catalyst under the ionomer layer. Hence, the mechanism of the stabilization effect is estimated to be different from the conventional modifiers. Lee et al., reported that a high concentration of V⁵⁺ species in the electrolyte, which was realized by adding V₂O₅ into the electrolyte up to the saturation, slows down the ionization of BiVO₄ during PEC reaction, demonstrating a significant stability in a three-electrode cell.^[2] In the present case, Bi³⁺ and/or V⁵⁺ cations generated via initial decomposition accumulated at the interface between the ionomer and BiVO₄, rapidly reaching saturation because of the limited volume of the interface. Consequently, further decomposition of BiVO₄ was suppressed as the report by Lee et al., realizing the improved durability of the photoanode.

Chapter 6. Control of Cation Impurities in the Electrolyte for Long-Term Operation of Photoelectrochemical Cells

Tandem-type PEC cells were constructed again using the ionomer-coated BiVO_4 photoanodes and RuO_2 -coated $(\text{ZnSe})_{0.85}(\text{CIGS})_{0.15}$ photocathodes. Figure 6-2-6 shows the time-courses of the photocurrent obtained from the tandem cells for the initial 5 h of light irradiation. Employment of both the ionomer layer and chelating resin successfully suppressed the decrease in the photocurrent, resulting in the small fluctuation in the working potential (between 0.50 and 0.55 V_{RHE}) under continuous light irradiation. Absence of the chelating resin causes a severe decrease in the photocurrent due to the degradation of the photocathode, shifting the working potential negatively up to 0.43 V_{RHE} in a few hours. These results demonstrate that stabilization of both photocathode and photoanode in the PEC cell can be achieved by introducing the two techniques. It should be noted that a slow but continuous decrease in the photocurrent was observed during long-term measurement in the scale of days as shown in Figure 6-2-7, which indicates that further investigations (e.g. optimization of the deposition condition and ionomer material, especially frameworks of the support) are still required. Also, the ultimate photocurrent was slightly decreased by introduction of the ionomer, which is possibly attributed to existence of a meaningful resistance of mass transfer in the ionomer layer. Nevertheless, the study should assist the realization of durable PEC cells even when they employ semiconductor materials which easily dissolves into the electrolyte.

Chapter 6. Control of Cation Impurities in the Electrolyte for Long-Term Operation of Photoelectrochemical Cells

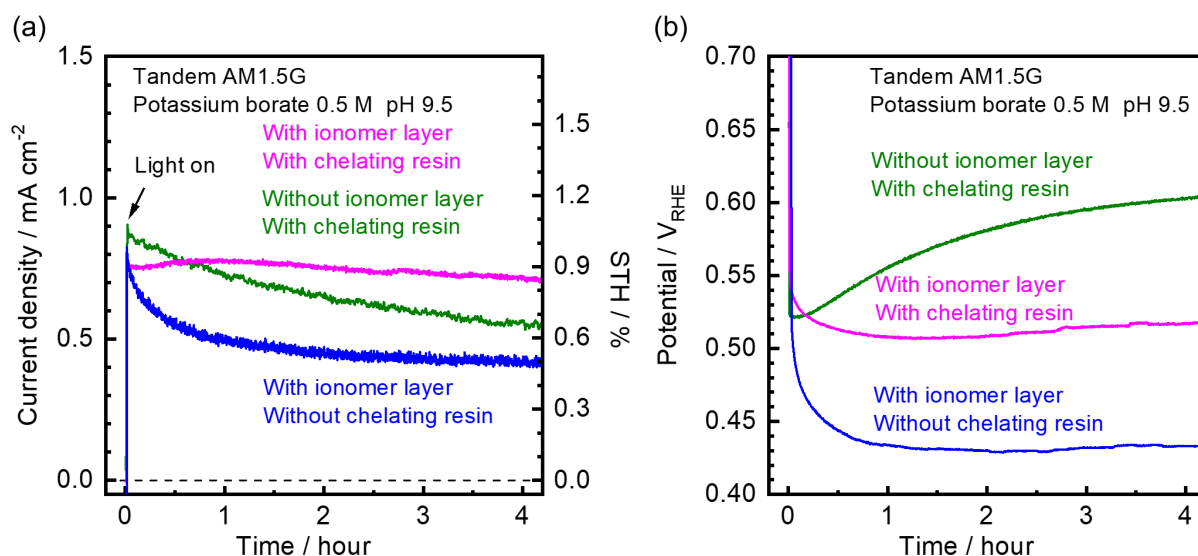


Figure 6-2-6. Current-time (a) and potential-time (b) curves for the tandem two-electrode cells composed of the BiVO₄ photoanodes and RuO₂-coated (ZnSe)_{0.85}(CIGS)_{0.15} photocathodes under simulated sunlight with (green, geometric area of the photocathode surface of 0.60 cm²) chelating resin beads in electrolyte, the cell with ionomer layer under simulated sunlight with (pink, 0.60 cm²) and without (blue, 0.72 cm²) addition of chelating resin beads to electrolyte. Right Y-axis shows the corresponding STH.

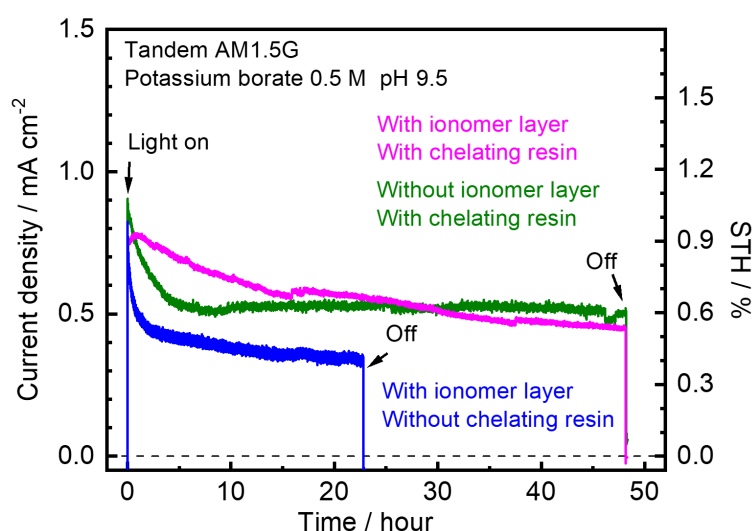


Figure 6-2-7. Current-time curves for the tandem two-electrode cells composed of the BiVO₄ photoanodes and RuO₂-coated (ZnSe)_{0.85}(CIGS)_{0.15} photocathodes under simulated sunlight with (green, geometric area of the photocathode surface of 0.60 cm²) chelating resin beads in electrolyte,

the cell with ionomer layer under simulated sunlight with (pink, 0.60 cm²) and without (blue, 0.72 cm²) addition of chelating resin beads to electrolyte. Right Y-axis shows the corresponding STH.

6-4 Conclusions

This chapter investigated effects of modifying the electrolyte with chelating resin beads and surface modification of BiVO₄ photoanodes with anion-conductive ionomer layers onto the PEC properties of both of the photocathodes and photoanodes. Without the chelating resin, the Bi species gradually deposited onto the (photo)cathode surface to cause a severe catalyst poisoning. Introduction of a dispersion of the resin beads slowed down the Bi deposition process by adsorbing the Bi³⁺ ions in the electrolyte. On the other hand, the low concentration of Bi³⁺ in the solution facilitates decomposition of BiVO₄ based on a shift in the chemical equilibrium. Therefore, the approach is effective especially for photoelectrode materials which don't show a meaningful solubility in the aqueous solution employed in the PEC cell. The PEC cell composed of the RuO₂-coated (ZnSe)_{0.85}(CIGS)_{0.15} photocathode and BiVO₄ photoanode showed a high durability for two days after the photocurrent reached plateau.

Coating the surface of BiVO₄ photoanodes with anion-conductive ionomer layers was found to efficiently block the migration of metal cations into the electrolyte. The blocking-effect of metal cations not only alleviates the catalyst poisoning but also improves durability of the BiVO₄ photoanode via accumulation of metal cations at the electrode-ionomer interface. Therefore, the decomposition of BiVO₄ can be suppressed even in the presence of chelating resin in the electrolyte. The ionomer layer remains stably without any evidence in oxidation of itself during PEC OER for hours. The PEC cell demonstrated suppression of initial decrease in the photocurrent, resulting in the improved durability of the overall water splitting reaction. Although there is room for investigations on the

Chapter 6. Control of Cation Impurities in the Electrolyte for Long-Term Operation of Photoelectrochemical Cells

coating material/process for further stabilization, the key techniques to establish the high durability of PEC cells for overall water splitting were successfully demonstrated in the chapter.

References

- [1] Y. Kuang, Q. Jia, H. Nishiyama, T. Yamada, A. Kudo, K. Domen, *Adv. Energy Mater.* **2016**, 6, 1501645.
- [2] D. K. Lee, K.-S. Choi, *Nat. Energy* **2018**, 3, 53.
- [3] T. W. Kim, K.-S. Choi, *Science* **2014**, 343, 990.
- [4] Y. Zhang, L. Huang, T. N. Arunagiri, O. Ojeda, S. Flores, O. Chyan, R. M. Wallace, *Electrochem. Solid-State Lett.* **2004**, 7, C107.
- [5] L. H. Mendoza-Huizar, C. H. Rios-Reyes, *J. Solid State Electrochem.* **2011**, 15, 737.
- [6] T. J. Schmidt, B. N. Grgur, R. J. Behm, N. M. Markovic, P. N. Ross, *Phys. Chem. Chem. Phys.* **2000**, 2, 4379.
- [7] A. Wuttig, Y. Surendranath, *ACS Catal.* **2015**, 5, 4479.
- [8] E. L. Clark, J. Resasco, A. Landers, J. Lin, L. T. Chung, A. Walton, C. Hahn, T. F. Jaramillo, A. T. Bell, *ACS Catal.* **2018**, 8, 6560.
- [9] M. Moriya, T. Minegishi, H. Kumagai, M. Katayama, J. Kubota, K. Domen, *J. Am. Chem. Soc.* **2013**, 135, 3733.
- [10] D. Yokoyama, T. Minegishi, K. Maeda, M. Katayama, J. Kubota, A. Yamada, M. Konagai, K. Domen, *Electrochem. Commun.* **2010**, 12, 851.
- [11] H. Kumagai, T. Minegishi, N. Sato, T. Yamada, J. Kubota, K. Domen, *J. Mater. Chem. A* **2015**, 3, 8300.
- [12] F. Jiang, Gunawan, T. Harada, Y. Kuang, T. Minegishi, K. Domen, S. Ikeda, *J. Am. Chem. Soc.* **2015**, 137, 13691.

Chapter 6. Control of Cation Impurities in the Electrolyte for Long-Term Operation of Photoelectrochemical Cells

- [13] Gunawan, W. Septina, S. Ikeda, T. Harada, T. Minegishi, K. Domen, M. Matsumura, *Chem. Commun.* **2014**, 50, 8941.
- [14] S. D. Tilley, M. Schreier, J. Azevedo, M. Stefik, M. Grätzel, *Adv. Funct. Mater.* **2014**, 24, 303.
- [15] A. M. Smith, L. Trotochaud, M. S. Burke, S. W. Boettcher, *Chem. Commun.* **2015**, 51, 5261.
- [16] M. G. Walter, E. L. Warren, J. R. McKone, S. W. Boettcher, Q. Mi, E. A. Santori, N. S. Lewis, *Chem. Rev.* **2010**, 110, 6446.
- [17] E. R. Kötz, S. Stucki, *J. Appl. Electrochem.* **1987**, 17, 1190.
- [18] P. K. Shen, C.-Y. Wang, S. P. Jiang, X. Sun, J. Zhang, *Electrochemical Energy: Advanced Materials and Technologies*; CRC Press, 2017.
- [19] S. Hu, N. S. Lewis, J. W. Ager, J. Yang, J. R. McKone, N. C. Strandwitz, *J. Phys. Chem. C* **2015**, 119, 24201.
- [20] H. Kaneko, T. Minegishi, K. Domen, *Chem. Eur. J.* **2018**, 24, 5697.
- [21] P. Neuderth, P. Hille, J. Schörmann, A. Frank, C. Reitz, S. Martí-Sánchez, M. de la Mata, M. Coll, J. Arbiol, R. Marschall, M. Eickhoff, *J. Mater. Chem. A* **2018**, 6, 565.
- [22] N. Guijarro, M. S. Prévot, K. Sivula, *Phys. Chem. Chem. Phys.* **2015**, 17, 15655.

Chapter 7

Summary and Outlooks

7-1 General Conclusions of This Thesis

In the present study, development of a novel photocathode composed of $(\text{ZnSe})_{0.85}(\text{CuIn}_{0.7}\text{Ga}_{0.3}\text{Se}_2)_{0.15}$ (abbreviated as $(\text{ZnSe})_{0.85}(\text{CIGS})_{0.15}$ herein) thin films and construction of photoelectrochemical (PEC) cells were investigated aiming for efficient and durable overall water splitting. The results and discussion obtained from each chapter were summarized as follows.

In chapter 2, effects of ZnSe introduction into $\text{CuIn}_{0.7}\text{Ga}_{0.3}\text{Se}_2$ thin films were investigated. The $\text{ZnSe}:\text{Cu}(\text{In},\text{Ga})\text{Se}_2$ formed complete solid solution without formation of any impurity phase. ZnSe mole fraction of 85% has been found to be optimum because it shows a sufficiently long absorption edge wavelength of 900 nm in the near-infrared region and a significantly deeper valence band maximum (VBM) than $\text{CuIn}_{0.7}\text{Ga}_{0.3}\text{Se}_2$ by 0.25 V, resulting in a high onset potential of 0.89 V_{RHE} . Relatively low deposition temperature and Cu-rich condition were suitable for preparation of p-type $(\text{ZnSe})_{0.85}(\text{CIGS})_{0.15}$ without significant re-evaporation of crystals nor formation of Zn_{Cu} defects. Moreover, post-deposition treatment of the films with Zn vapor effectively compensate the Zn species evaporated from the surface. Overall water splitting using a PEC cell was demonstrated using the $(\text{ZnSe})_{0.85}(\text{CIGS})_{0.15}$ photocathode and a BiVO_4 photoanode under simulated sunlight without applying any external bias voltage. The cell showed a solar-to-hydrogen conversion efficiency (STH) of 0.91%, while the cell showed a continuous degradation due to corrosion of CdS surface modifier. Existence of significant mass transport resistance in the electrolyte was also revealed by changing the forced convection of the solution.

In chapter 3, effects of multistage deposition process of the $(\text{ZnSe})_{0.85}(\text{CIGS})_{0.15}$ thin films were investigated so as to improve quantum efficiency of the photocathode. Annealing process for 10 min was found to eliminate Cu_xSe impurities from the inside of thin films. The bilayer structure composed of a Ga-rich layer and In-rich layer on the back-side and front-side, respectively, showed a photocurrent value almost twice as high as the monolayer sample, which was investigated in chapter 2. Incident photon-to-current conversion efficiency values reached greater than 60% at a wide range

Chapter 7. Summary and Outlooks

of wavelength of 400-600 nm. Mapping of electron beam-induced current (EBIC) was employed for the photoelectrodes for the first time ever reported, whose consistency with the condition in the electrolyte was supported by numerical simulation of band bending at the interfaces using the Poisson's equation. The mapping of EBIC signals revealed that the uniform distribution of active region in the bilayer sample was a highly probable reason for the improvement. A PEC cell recorded the initial STH of 1.6%, although the degradation was still observed due to corrosion of photocathode surface.

In chapter 4, effects of substrates for the $(\text{ZnSe})_{0.85}(\text{CIGS})_{0.15}$ photocathodes onto their PEC properties were investigated. As is the case of $\text{Cu}(\text{In,Ga})\text{Se}_2$, a source of Na species was found to be indispensable to show sufficient carrier concentration in the thin film. The photocathode deposited on a Mo-coated Ti foil with a nanolayer of soda-lime glass showed a PEC property comparable with the conventional photocathode developed in Chapter 2. Because the photocathode is easy to cut and bend, construction of a comb-like PEC cell composed of the integrated photoelectrodes was realized, which doesn't require to stir the electrolyte. The cell exhibited almost no difference in the STH between with and without the stirring and recorded the STH of 1.0%. Hence, the cell is advantageous in terms of scalability and efficiency compared with the parallel and tandem PEC cells.

In chapter 5, stabilization of the $(\text{ZnSe})_{0.85}(\text{CIGS})_{0.15}$ photocathodes at a potential which is expected to be the working potential of a PEC cell, $0.6 V_{\text{RHE}}$, was investigated. Photoelectrodeposition of RuO_2 forms a dense, conformal and stable protection layer on the photocathode. Moreover, RuO_2 shows sufficient catalytic activity for hydrogen evolution reaction (HER) and conductivity, which enables substitution of Pt and Mo/Ti binary from the photocathode surface. The RuO_2 -coated $(\text{ZnSe})_{0.85}(\text{CIGS})_{0.15}$ photocathode showed a high durability in the electrolytes at pH 13 as well as pH 7, which means that the photocathode can be combined with the other photoanodes which employs strong alkaline electrolyte. Interestingly, the RuO_2 layer showed a phenomenon called activation during PEC HER. Angle-resolved X-ray photoelectron spectroscopy analyses suggested that hydroxylation

Chapter 7. Summary and Outlooks

of the outermost surface of the RuO_2 layer contributes to the increase in the catalytic activity. A PEC cell constructed using the RuO_2 -coated $(\text{ZnSe})_{0.85}(\text{CIGS})_{0.15}$ photocathode and BiVO_4 photoanode showed a dramatical alleviation of efficiency degradation: $70\% \text{ h}^{-1}$ to $20\% \text{ h}^{-1}$. The degradation still observed was attributed to catalyst poisoning of the photocathode due to Bi deposition via the electrolyte.

In chapter 6, effects of modifying the electrolyte and the photoanode surface were investigated aiming for suppression of the surface poisoning on the photocathode. Dispersing chelating resin beads into the electrolyte was found to effectively adsorb the dissolved Bi species before poisoning the photocathode surface, resulting in a stable overall water splitting for approximately two days. On the other hand, a relatively low concentration of Bi^{3+} facilitates decomposition of BiVO_4 due to a shift in the chemical equilibrium. Then, spin-coating of anion-conductive ionomer onto the surface of the BiVO_4 photoanode was investigated to slow down the decomposition. Because the ionomer layer blocks metal cations, the dissolved ions are accumulated in the vicinity of photoanode surface. Consequently, decomposition of BiVO_4 was significantly suppressed, which led to further stabilization of the PEC cell.

7-2 Future Prospects

The current study focused on a quinary compound of $(\text{ZnSe})_{0.85}(\text{CIGS})_{0.15}$ to demonstrate band engineering by element substitution. As discussed in chapter 2, the carrier concentration in the $(\text{ZnSe})_{0.85}(\text{CIGS})_{0.15}$ crystal is affected by the relative amount of Cu during deposition, which makes application of multistage deposition process difficult. More simple material systems such as II-VI compounds should be easy to introduce the multistage deposition with engineering the band-edge potential(s). For example, CdTe, which has the absorption edge of 1.5 eV, is a promising candidate as a target material of band engineering.

Chapter 7. Summary and Outlooks

It was also found that there is still room for further development of photoanodes in terms of absorption edge, choice of electrolyte and stability in the aqueous solution. The work recorded the maximum STH of 1.6%, which should not be high enough to commercialize the PEC devices. In addition to improvement of the photocathode as described above, development of photoanodes which utilizes a wider range of the sunlight spectrum than BiVO_4 and shows a sufficient onset potential is demanded according to this work. Moreover, the BiVO_4 photoanode employed in this work can work stably and efficiently only in the weak-alkaline borate buffer solution. The RuO_2 -coated photocathode prefers a strong alkaline solution to a neutral one, so development of a photoanode working in such a condition should result in a significant progress in the STH.

Analyses on the photocathode surface after overall water splitting in a PEC cell revealed the existence of element transfer from the photoanode to photocathode surface, poisoning the HER catalyst. Even though chapter 6 demonstrated suppression of the poisoning, it is also concluded that photoanode should avoid employing materials which easily dissolve into the electrolyte. Instead, employment of a highly insoluble compounds as the photoanode material or covering the photoanode surface with some insoluble materials is expected to realize practical durability of a PEC cell.

Figure 7-2-1 illustrates a scheme for scalable water splitting using a tandem cell. An advantage of the module is that simple electric wires and conductive poles can expand the photoelectrodes horizontally, no matter how the size of each cell is small. It has been reported that the size of semitransparent BiVO_4 photoanodes which exhibits considerable photocurrent has been limited up to 25 cm^2 so far,^[1] while monolithic thin films of Cu-chalcopyrites such as $\text{Cu}(\text{In,Ga})(\text{S,Se})_2$ with the aperture area of approximately 800 cm^2 have already been available, which are prepared by sputtering of metal precursors followed by selenization and sulfurization.^[2] Hence, it is necessary to adjust the difference in the scalability between photocathodes and photoanodes, and the wiring is a promising technique to compensate the gap in the sizes. A significantly larger photoanode also should be developed after realizing practical performance of solar energy conversion in the future. Furthermore,

the ion exchange membrane, which prevents mixing of evolved hydrogen and oxygen gases and catalyst poisoning on the photoelectrode, is required to be not only durable but also highly transparent so as to feed enough photons to the underlying photoelectrode. Development of the durable and highly transparent membrane is also an on-going challenge.^[3]

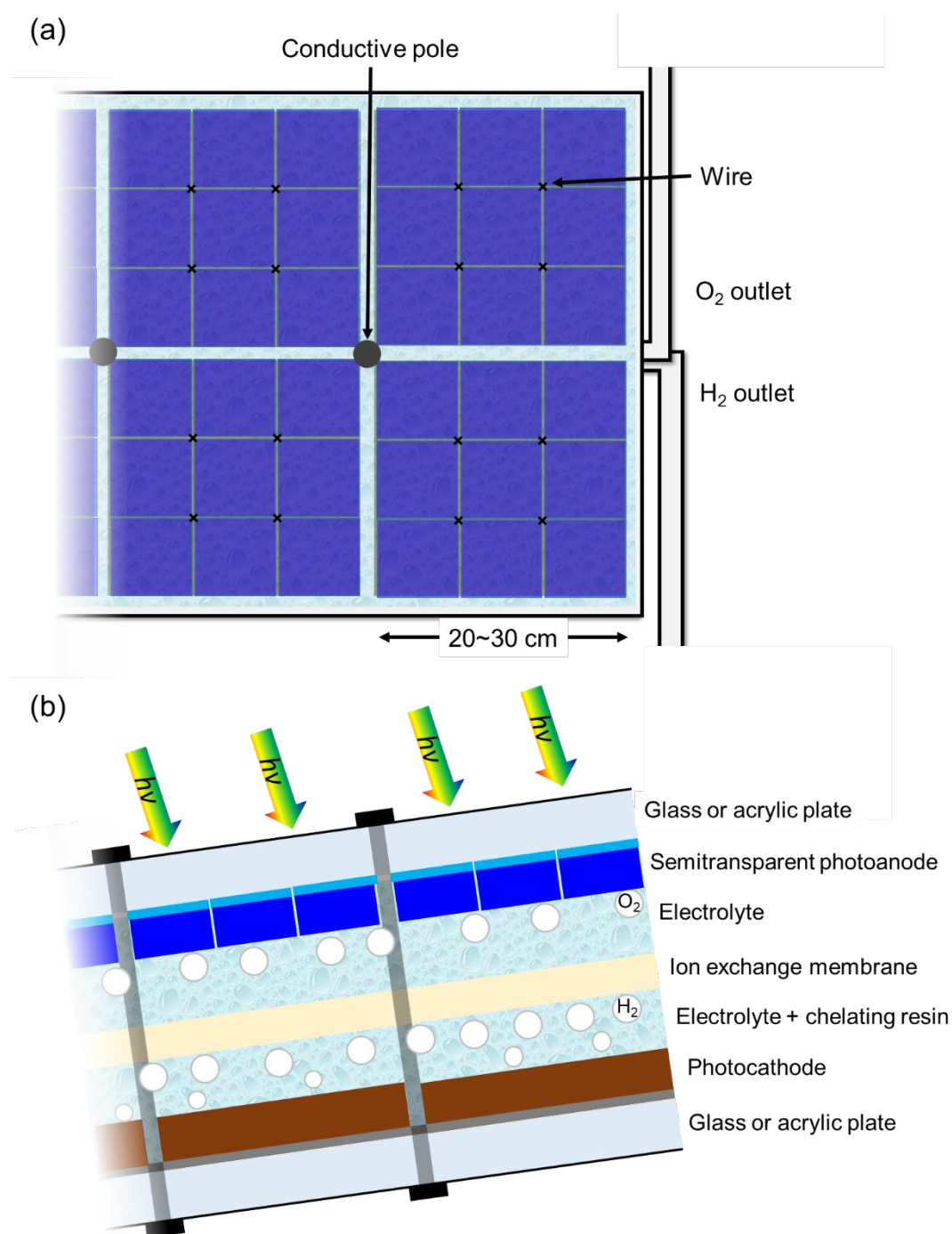


Figure 7-2-1. (a) Top and (b) cross-sectional illustrations of a scalable tandem-type PEC cell.

Chapter 7. Summary and Outlooks

The author is confident that this work extended the knowledge concerning PEC water splitting and gave useful information for construction of PEC cells for efficient and durable overall water splitting driven by sunlight.

References

- [1] X. Yao, D. Wang, X. Zhao, S. Ma, P. S. Bassi, G. Yang, W. Chen, Z. Chen, T. Sritharan, *Energy Technol.* **2018**, 6, 100.
- [2] T. Kato, *Jpn. J. Appl. Phys.* **2017**, 56, 04CA02.
- [3] *Photoelectrochemical Solar Fuel Production: From Basic Principles to Advanced Devices*; Giménez, S.; Bisquert, J., Eds.; 1st ed.; Springer, 2016.

List of Publications (Peer Reviewed Papers)

[Chapter 2]

1. **Hirovuki Kaneko**, Tsutomu Minegishi, Mamiko Nakabayashi, Naoya Shibata, Yongbo Kuang, Taro Yamada and Kazunari Domen, “A Novel Photocathode Material for Sunlight-Driven Overall Water Splitting: Solid Solution of ZnSe and Cu(In,Ga)Se₂” *Adv. Funct. Mater.*, 26, 4570-4577, 2016. (0.9)
2. Ayako Kubo, **Hirovuki Kaneko**, Tsutomu Minegishi, Kazunari Domen, Koichi Yamashita, “A Theoretical Investigation on Crystal Defects in (ZnSe)_{0.85}(CuIn_{0.7}Ga_{0.3}Se₂)_{0.15} Photocathodes for Solar Hydrogen Production” *in preparation*.

[Chapter 3]

3. **Hirovuki Kaneko**, Tsutomu Minegishi, Mamiko Nakabayashi, Naoya Shibata and Kazunari Domen, “Enhanced Hydrogen Evolution under Simulated Sunlight from Neutral Electrolytes on (ZnSe)_{0.85}(CuIn_{0.7}Ga_{0.3}Se₂)_{0.15} Photocathodes Prepared by a Bilayer Method” *Angew. Chem. Int. Ed.*, 55, 15329-15333, 2016. (0.4)

[Chapter 4]

4. Tomohiro Higashi, **Hirovuki Kaneko**, Tsutomu Minegishi, Hirovuki Kobayashi, Miao Zhong, Yongbo Kuang, Takashi Hisatomi, Masao Katayama, Tsuyoshi Takata, Hiroshi Nishiyama, Taro Yamada and Kazunari Domen, “Overall Water Splitting by Photoelectrochemical Cells Consisting of (ZnSe)_{0.85}(CuIn_{0.7}Ga_{0.3}Se₂)_{0.15} Photocathodes and BiVO₄ Photoanodes”, *Chem. Comm.*, 53, 11674-11677, 2017. (0.3)

List of Publications

[Chapter 5]

5. **Hiroyuki Kaneko**, Tsutomu Minegishi, Tomohiro Higashi, Mamiko Nakabayashi, Naoya Shibata, and Kazunari Domen, “Stable Hydrogen Production from Water on an NIR-Responsive Photocathode under Harsh Conditions”, *Small Methods*, 2, 1800018, 2018. (0.9)

[Chapter 6]

6. **Hiroyuki Kaneko**, Tsutomu Minegishi, Hiroyuki Kobayashi, Yongbo Kuang and Kazunari Domen, “Suppression of Poisoning of Photocathode Catalysts in Photoelectrochemical Cells for Highly Stable Sunlight-Driven Overall Water Splitting”, *J. Chem. Phys.*, 150, 041713, 2019. (0.9)

[Papers in relation to this thesis but not included]

7. Jin Hyun Kim, **Hiroyuki Kaneko**, Tsutomu Minegishi, Jun Kubota, Kazunari Domen and Jae Sung Lee, “Overall Photoelectrochemical Water Splitting using Tandem Cell under Simulated Sunlight” *ChemSusChem*, 9, 61-66, 2016.
8. Yosuke Goto, Tsutomu Minegishi, Yosuke Kageshima, Tomohiro Higashi, **Hiroyuki Kaneko**, Yongbo Kuang, Mamiko Nakabayashi, Naoya Shibata, Hitoshi Ishihara, Toshio Hayashi, Akihiko Kudo, Taro Yamada and Kazunari Domen, “A particulate $(\text{ZnSe})_{0.85}(\text{CuIn}_{0.7}\text{Ga}_{0.3}\text{Se}_2)_{0.15}$ photocathode modified with CdS and ZnS for sunlight-driven overall water splitting”, *J. Mater. Chem. A*, 5, 21242-21248, 2017.
9. Ying Fan Tay, **Hiroyuki Kaneko**, Sing Yang Chiam, Stener Lie, Qiusha Zheng, Bo Wu, Shreyash Sudhakar Hadke, Zhenghua Su, Prince Saurabh Bassi, Douglas Bishop, Tze Chien Sum, Tsutomu Minegishi, James Barber, Kazunari Domen and Lydia Helena Wong, “Solution-Processed Cd-Substituted CZTS Photocathode for Efficient Solar Hydrogen Evolution from Neutral Water”, *Joule*, 2, 537-548, 2018.

List of Publications

10. Yosuke Kageshima, Tsutomu Minegishi, Yosuke Goto, **Hiroyuki Kaneko** and Kazunari Domen, “Particulate photocathode composed of $(\text{ZnSe})_{0.85}(\text{CuIn}_{0.7}\text{Ga}_{0.3}\text{Se}_2)_{0.15}$ synthesized with Na_2S for enhanced sunlight-driven hydrogen evolution”, *Sustainable Energy Fuels*, 2, 1957-1965, 2018.
11. Hiroyuki Kobayashi, Naotoshi Sato, Masahiro Orita, Yongbo Kuang, **Hiroyuki Kaneko**, Tsutomu Minegishi, Taro Yamada and Kazunari Domen, “Development of highly efficient $\text{CuIn}_{0.5}\text{Ga}_{0.5}\text{Se}_2$ -based photocathode and application to overall solar driven water splitting”, *Energy Environ. Sci.*, 11, 3003-3009, 2018.
12. Yosuke Kageshima, Tsutomu Minegishi, Sho Sugisaki, Yosuke Goto, **Hiroyuki Kaneko**, Mamiko Nakabayashi, Naoya Shibata and Kazunari Domen, “Surface protective and catalytic layer consisting of RuO_2 and Pt for stable production of methylcyclohexane using solar energy”, *ACS Appl. Mater. Interfaces*, 10, 51, 2018.
13. Jiao Zhao, Tsutomu Minegishi, **Hiroyuki Kaneko**, Guijun Ma, Miao Zhong, Mamiko Nakabayashi, Takashi Hisatomi, Masao Katayama, Naoya Shibata, Taro Yamada and Kazunari Domen, “Efficient hydrogen evolution from water on $(\text{CuInS}_2)_x(\text{ZnS})_{1-x}$ solid solution-based photocathode under simulated sunlight”, *Chem. Commun.*, 55, 470-473, 2019.
14. **Hiroyuki Kaneko**, Ying Fan Tay, Stener Lie, Wenjie Li, Mamiko Nakabayashi, Naoya Shibata, Lydia Helena Wong, Tsutomu Minegishi and Kazunari Domen, “Structural and electrical investigations on $(\text{ZnSe})_x(\text{Cu}(\text{In,Ga})\text{Se}_2)_{1-x}$ ($x = 0.85$) thin films for photovoltaic applications”, *in preparation*.

List of Publications (Review Articles - Related to Chapter 1)

1. **Hiroyuki Kaneko**, Tsutomu Minegishi and Kazunari Domen, “Chalcopyrite Thin Film Materials for Photoelectrochemical Hydrogen Evolution from Water under Sunlight” *Coatings*, 5, 293-311, 2015.

List of Publications

2. **Hiroyuki Kaneko**, Tsutomu Minegishi and Kazunari Domen, “Recent Progress in the Surface Modification of Photoelectrodes toward Efficient and Stable Overall Water Splitting” *Chem. Eur. J.*, 23, 1-11, 2017.

List of Publications (Books)

1. Miao Zhong, **Hiroyuki Kaneko**, Taro Yamada and Kazunari Domen, “Photoanodic and Photocathodic Materials Applied for Free-Running Solar Water Splitting Devices” In D. Wang and G. Cao (Eds.) “Nanomaterials for Energy Conversion and Storage” *World Scientific Publishing*, November 14, pp. 251-289, 2017
2. **兼古寛之** “光電気化学的水分解による高効率な水素製造を目指して” 水素エネルギーシステム, Vol.42, No.2, pp.119-120, 2017.